

Design of high-torque-density synchronous drives for propulsion of rotary-wing aircraft

Sanabria von Walter, Christian

DOI

[10.4233/uuid:fc614c24-420a-45f2-8d47-78e9dd4c750b](https://doi.org/10.4233/uuid:fc614c24-420a-45f2-8d47-78e9dd4c750b)

Publication date

2016

Document Version

Final published version

Citation (APA)

Sanabria von Walter, C. (2016). *Design of high-torque-density synchronous drives for propulsion of rotary-wing aircraft*. [Dissertation (TU Delft), Delft University of Technology]. <https://doi.org/10.4233/uuid:fc614c24-420a-45f2-8d47-78e9dd4c750b>

Important note

To cite this publication, please use the final published version (if applicable).
Please check the document version above.

Copyright

Other than for strictly personal use, it is not permitted to download, forward or distribute the text or part of it, without the consent of the author(s) and/or copyright holder(s), unless the work is under an open content license such as Creative Commons.

Takedown policy

Please contact us and provide details if you believe this document breaches copyrights.
We will remove access to the work immediately and investigate your claim.

**Design of High-Torque-Density
Synchronous Drives for Propulsion of
Rotary-Wing Aircraft**

Design of High-Torque-Density Synchronous Drives for Propulsion of Rotary-Wing Aircraft

PROEFSCHRIFT

ter verkrijging van de graad van doctor
aan de Technische Universiteit Delft,
op gezag van de Rector Magnificus prof.ir. K.C.A.M. Luyben,
voorzitter van het College voor Promoties,
in het openbaar te verdedigen op woensdag 18 mei 2016 om 15.00 uur
door

Christian David SANABRIA von WALTER

Master of Science in Elektrotechnik, Technische Universität Hamburg-Harburg
geboren te Bogotá, Colombia

Dit proefschrift is goedgekeurd door de promotor:
Prof.dr.-Eng. J.A. Ferreira

Copromotor:
Dr.ir. H. Polinder

Samenstelling promotiecommissie:
Rector Magnificus, voorzitter
Prof.dr.-Eng. J.A. Ferreira, Technische Universiteit Delft, promotor
Dr.ir. H. Polinder, Technische Universiteit Delft, copromotor
Prof.dr. R. Nilssen, Norges Teknisk-Naturvitenskapelige Universitet
Dr. A. Gangoli Rao, Technische Universiteit Delft
Prof.dr.ir. A.H.M. Smets, Technische Universiteit Delft
Prof.dr. E. Lomonova, Technische Universiteit Eindhoven
Prof.dr. J.J. Smit, Technische Universiteit Delft



This research was supported by the Airbus Group and the European Union's Seventh Framework Program (FP7) through the Clean Sky Joint Technology Initiative

Printed by Gildeprint Drukkerijen, Enschede, The Netherlands

ISBN 978-94-6186-648-6
Copyright © 2016 by Christian Sanabria von Walter

All rights reserved. No part of the material protected by this copyright notice may be reproduced or utilized in any form or by any means, electronic or mechanical, including photocopying, recording or by any information storage or retrieval system without permission from the author.

to the Sanabria von Walter and Robl families

Acknowledgements

These pages are the culmination of a journey, the journey of a curious child trying to figure out how technology works. In 2004 this curiosity led me to Germany, the country that I now call home, and where in 2010 I began my doctoral research at EADS Innovation Works, now Airbus Group Innovations (AGI) in Munich. In this quest, I was privileged enough to count with the support and guidance of the Electrical Power Processing (EPP) group of the Delft University of Technology (TU Delft) in The Netherlands. These particular circumstances brought me in contact with many different individuals from many different backgrounds from which I profited enormously in my personal and professional growth. Some of them, through their contributions, influence and example have been determinant in the development of who I am today. For their support and guidance I am ever grateful.

In first place, I would like to thank my AGI supervisor, Markus Christmann, whose support and fairness were vital for the realization of this work. It was because of his guidance and trust that I was able to come to a successful conclusion of this research. As my superior he always found the best balance between the objectives of his team and those of my research. For this I will always be in debt with him.

Equally important during this time was my TU Delft co-promoter and supervisor, Henk Polinder. He took me in as his PhD candidate and offered me nothing but the best academic guidance. His advice and friendship always accompanied and motivated me to persevere and see this project through. His involvement in my work as a professional, friend and human being were a true privilege.

My gratitude also goes out to my TU Delft promoter, Prof. Braham Ferreira. He always asked the right questions and highlighted the key aspects that insured the quality and sharpness of my work.

To my fellow doctoral candidates Johannes Kirn, Tim Hilden and Sebastian Seemann: I thank you for your contributions and friendship. We always worked in an atmosphere of comradeship characterized by its positive energy. That our respective fields were different from one another was never a disadvantage but an immediate source of knowledge, fresh ideas and points of view. I specially thank Johannes Kirn who was crucial in my understanding of structural and materials engineering, a very important aspect in my research. He was always unconditional and willing to offer his time and patience to answer my questions.

I also thank my AGI team colleagues Alexander Kaiser, Gerhard Steiner, Stefan Friedl and Konrad Lentner whose sound technical knowledge was an invaluable help more than

once. In particular I would like to thank Frank Hermle, for his active support and participation in the successful development of the experimental setup, and Michael Hofmann, a key person in the planning of the next steps of my career.

At this point I would like to make special mention of the people who are personally closest to me and who have a very special place in my life.

My deepest gratitude and love goes to Oswald and Ingrid Robl. They constitute what I have come to call my family in Germany, took me into the core of their home like a son and entrusted me with their most valuable treasure. They have been by my side since before the beginning of this project and have given me their unconditional and unmatched support. It is very difficult to imagine how any of this would have come to be without them.

To my mother and father: physical separation over long periods of time has not been easy for any of us. But you can be sure that your love and memory are much more powerful than any uncertainty, fear and solitude that might unsettle me. It is this love what has always given me the strength to keep pursuing, to keep persevering, to keep dreaming. To you I simply owe my existence.

To Gabriela: no one has been most affected by distance and separation more than you have. It is my dream not to be absent anymore and I will never cease to work for this ideal, I will never cease working for your well-being. I dedicate this achievement also to you; it takes us one step closer to that dream.

To Pablo: the journey has been longer than what we planned, but at last we are seeing the light at the end of the tunnel, this time brighter than ever. This is only because you were always there to remind me why we came here, to remind me in which direction we are going, to remind me there was still some road ahead of us. Whatever the future may bring, only one thing is certain: you are the only one I could always call “my family” here, you are my blood, you are my truest friend. This achievement is as much yours as it is mine.

Finally, to the commander in chief of my “state of love and trust”: Christina. You seem so fragile, yet you seem to be the only one able to endure a dark day with me. I have simply lost count of the lessons you have repeatedly taught me in matters of love, humility and respect. Thank you for your resilience and for your love, thank you for enduring this time with me. Nothing could have ever prepared me for the happiness and greatness you have brought into my life. I am more than looking forward to spending the rest of my life with you.

Christian Sanabria von Walter
Munich, April 2016

Table of Contents

Acknowledgements	i
Table of Contents	iii
Symbols and Abbreviations	ix
Chapter 1 Introduction	1
1.1 General Motivation.....	1
1.2 Conventional and Alternative Aircraft Propulsion	2
1.3 Problem description	4
1.3.1 State of the art of electrical machines	4
1.3.2 Research Question.....	6
1.3.3 Thesis Objectives	7
1.3.4 Experimental Setup:	7
1.4 Thesis Outline.....	7
Chapter 2 Problem Background and Definition	11
2.1 Clean Sky JTI	11
2.2 Next-Generation Aircraft Demonstrators	13
2.2.1 Hybrid Fixed-Wing Aircraft.....	14
2.2.2 Battery-Powered Fixed-Wing Aircraft.....	15
2.2.3 Fuel-Cell-Powered Fixed-Wing Aircraft.....	17
2.2.4 Solar-Cell-Powered Fixed-Wing Aircraft	17
2.2.5 Hybrid Rotary-Wing Aircraft: Eurocopter AS350 Hybrid.....	18
2.2.6 Battery-Powered Rotary-Wing Aircraft: Sikorsky Firefly.....	18
2.3 Feasibility Studies and Future Concepts.....	18
2.3.1 Fixed-Wing-Oriented Studies.....	19

2.3.2	Rotary-Wing-Oriented Studies.....	22
2.4	The Idea of a Hybrid Helicopter.....	22
2.4.1	Hybrid Aircraft Concept.....	23
2.4.2	Requirement Definition.....	25
2.4.3	Volumetric Torque Density and Shear Stress as Figures of Merit.....	27
2.5	Chapter Summary.....	28
Chapter 3	Current Technology Status.....	31
3.1	Material Considerations for Aerospace Electrical Machine Designs.....	31
3.1.1	Magnetic Materials.....	32
3.1.2	Electrical Materials.....	33
3.1.3	Structural Materials.....	34
3.2	Fault Tolerance Considerations for Aerospace Electrical Machine Designs.....	35
3.3	Conventional Electrical Machine Architectures.....	37
3.3.1	Induction Machines (IM).....	37
3.3.2	Switched Reluctance Machines (SRM).....	37
3.3.3	Permanent Magnet (PM) Machines.....	37
3.4	High Temperature Superconducting (HTS) Machines.....	45
3.4.1	Superconductivity.....	45
3.4.2	Critical Surface.....	45
3.4.3	Superconducting Wire Material.....	46
3.4.4	Superconducting Bulk Material.....	48
3.4.5	HTS Machines' Specifics and Topologies.....	48
3.5	Aerospace Specific Electrical Machines.....	51
3.5.1	Conventional Machines.....	51
3.5.2	Conceptual HTS Machine Designs for Aerospace.....	53
3.6	Starting Point.....	54
3.6.1	Topology Selection.....	54
3.6.2	Radial Flux PM Machine vs. Axial Flux PM Machine.....	56
3.7	Chapter Summary.....	59

Chapter 4	Surface Permanent Magnet Machines as a Benchmark.....	61
4.1	Analytical Model	61
4.1.1	Main Parameters	62
4.1.2	Dimensions, Loading and Performance Calculation	63
4.1.3	Weight	68
4.1.4	Electromagnetic Model Verification	68
4.2	Winding factors and Slot/Pole Combinations.....	69
4.3	Topology comparison	70
4.3.1	Basic Assumptions	70
4.3.2	Aluminum vs. Copper Windings.....	70
4.3.3	Comparison between Topologies	72
4.4	Analysis of 12/16 as Base Configuration	77
4.4.1	168/224 Machine Characteristics and Mechanical Considerations.....	77
4.4.2	Potential for Mass Reduction	78
4.5	Chapter Summary	80
Chapter 5	Flux Switching Permanent Magnet Machines.....	83
5.1	Analytical-Numerical Hybrid Model.....	83
5.1.1	Airgap and Magnet Flux Density	85
5.1.2	Magnetic Equivalent Circuit	87
5.1.3	Nonlinear Permeances.....	89
5.1.4	Electromagnetic Model Verification	91
5.2	Electrical Loading, Torque and Weight.....	93
5.3	Topology Selection: Winding Factor and Slot/Pole Combinations.....	94
5.4	Topology Comparison	94
5.4.1	Basic Assumptions	94
5.4.2	Comparison between Topologies	95
5.5	Analysis of 6/13 C-Core Machine as Base Configuration.....	96
5.5.1	84/182 Machine Characteristics and Mechanical Considerations.....	97
5.5.2	Potential for Mass Reduction	97
5.6	Halbach-FSPM Machine	99

5.6.1	Flux Enhancement Principle	99
5.6.2	Halbach Arrays in Free Space	101
5.6.3	Use of Halbach Arrays with Wavelength λ_2 on FSPM Machines	102
5.7	Analysis of a 84/182 Halbach-FSPM Machine	105
5.7.1	Use of Flux Enhancement and Further Mechanical Considerations	105
5.7.2	Final Machine Parameters	107
5.8	Chapter Summary	108
Chapter 6 High Temperature Superconducting Synchronous Machines		111
6.1	Simplified Machine Model and Assumptions	111
6.1.1	HTS Operating Temperature and Cryostat	112
6.1.2	HTS Material: YBCO vs. MgB ₂	112
6.1.3	Simplified Machine Model	113
6.1.4	Armature Winding and Mechanical Airgap	114
6.2	Optimization Problem	115
6.2.1	Figure of Merit	115
6.2.2	Problem Formulation	116
6.2.3	Optimization Results	117
6.3	Best-case Performance Prediction	118
6.4	Chapter Summary	120
Chapter 7 Comparison, Experimental Validation and Conceptual Structure		121
7.1	Design Comparison and Selection	121
7.2	Halbach-FSPM Machine: Electromagnetic Analysis and Implementation	124
7.2.1	Stator Segmentation and Use of Air Bearings	124
7.2.2	Further Electromagnetic Characterization	126
7.3	Experimental setup	128
7.3.1	Full Machine vs. Experimental setup: Segment Differences	129
7.3.2	Support Structure	131
7.3.3	Air Cooling Scheme	134
7.4	Experimental Validation	137
7.4.1	Phase 1: Static Torque Measurements	138

7.4.2	Phase 2: Cooling and Temperature Measurements	142
7.4.3	Phase 3: Back-EMF and Structural Support Testing.....	146
7.5	Conceptual Stator Support Structure	149
7.5.1	Design Methodology	149
7.5.2	Stiffness and Weight	151
7.5.3	Deformation Study	152
7.5.4	Thermal Expansion.....	153
7.5.5	Weight Estimation Model	154
7.6	Chapter Summary	160
Chapter 8	Conclusions and Recommendations	161
8.1	Considerations for Electrical Main Aircraft Propulsion.....	161
8.2	Topology Selection and Comparison.....	163
8.3	Distributed Design Approach	165
8.4	Contributions	166
8.5	Recommendations.....	169
References	173
Summary	187
Samenvatting	191
List of Publications	195
Journal Publications	195
Conference Publications	195
Patents	195
Biography	197

Symbols and Abbreviations

Abbreviations

2D	Two-Dimensional
3D	Three-Dimensional
AC	Alternate Current
ACARE	Advisory Council for Aeronautics Research in Europe
AEA	All-Electric Aircraft
AFPM	Axial Flux Permanent Magnet
BiSCCO	Bismuth Strontium Calcium Copper Oxide
BLDC	Brushless DC
CAD	Computer-Aided Design
CFD	Computational fluid dynamics
CPMG	Cycloid Permanent Magnet Gear
DC	Direct Current
EMF	Electro-Motive Force
EU	European Union
FEM	Finite-Element Method
FP7	Seventh Framework Program
FSCW	Fractional-Slot Concentrated Winding
FSPM	Flux-Switching Permanent Magnet
HAI	Homopolar Alternator Inductor
HTS	High Temperature Superconductor/Superconducting
ICE	Internal Combustion Engine
IM	Induction Machine
IPM	Interior Permanent Magnet
ITD	Integrated Technology Demonstrators
ITER	International Thermonuclear Experimental Reactor
JTI	Joint Technology Initiative
LH ₂	Liquid Hydrogen
LHC	Large Hadron Collider
LHe	Liquid Helium
LN ₂	Liquid Nitrogen
LTS	Low Temperature Superconductor/Superconducting
MEA	More-Electric Aircraft
MgB ₂	Magnesium Diboride
MGPM	Magnetically-Geared Permanent Magnet

MTOW	Maximum Take-Off Weight
NASA	National Aeronautics and Space Administration
Nb3Sn	Niobium Tin
NbTi	Niobium Titanium
OECD	Organization for Economic Co-operation and Development
PM	Permanent Magnet
PMSM	Permanent Magnet Synchronous Machine
RFPM	Radial Flux Permanent Magnet
R&D	Research & Development
RMS	Root Mean Square
SPM	Surface Permanent Magnet
SRM	Switched Reluctance Machine
TOW	Take-Off Weight
TFPM	Transverse-Flux Permanent Magnet
UAV	Unmanned Aerial Vehicle
YBCO	Yttrium Barium Copper Oxide

Latin letters

a_{mvr}	Perceived acceleration by rotor during maneuvers	[m/s ²]
A_s	RMS linear current density	[A _{RMS} /m]
A_s^*	Maximum allowable RMS linear current density	[A _{RMS} /m]
b_1	Slot opening	[m]
B_1	Flux density of Halbach array (array type 1)	[T]
B_2	Flux density of Halbach array (array type 2)	[T]
B_c	Superconductor critical magnetic field	[T]
B_g	Airgap flux density	[T]
B_{g1}	Airgap fundamental peak flux density	[T]
b_m	Magnet coverage	[m]
B_m	Magnet flux density at magnet surface	[T]
B_{m1}	Fundamental peak flux density at magnet surface	[T]
$B_{max,\perp}$	Maximum magnetic field perpendicular to HTS tape	[T]
$B_{peak,1}$	Peak flux density of Halbach array (array type 1)	[T]
$B_{peak,2}$	Peak flux density of Halbach array (array type 2)	[T]
B_{\parallel}	Magnetic field component parallel to HTS	[T]
B_{\perp}	Magnetic field component perpendicular to HTS tape	[T]
B_r	Magnetic remanent flux density	[T]
B_{ry}	Rotor yoke flux density	[T]
B_{sat}	Saturation magnetic flux density	[T]
b_s	Slot width	[m]
B_{sy}	Stator yoke flux density	[T]
b_t	Stator tooth width	[m]
B_t	Tooth peak flux density	[T]
B_t^*	Maximum allowable tooth peak flux density	[T]
b_{tp}	Tip overlength	[m]

b_{tr}	FSPM machine rotor tooth width	[m]
b_{ts}	FSPM machine stator tooth width	[m]
B_y^*	Maximum allowable yoke peak flux density	[T]
C	Carter factor	[-]
C_i	Cross-section of component i	[m ²]
D	Thickness of Halbach array	[m]
d	Clearance around support holes for SPM machines	[m]
D_g	Airgap diameter	[m]
d_i	Depth of component/feature i (radial direction)	[m]
d_m	Magnet coverage of pole pitch in pu	[-]
D_o	Outer machine diameter	[m]
d_{ring}	Air bearing ring radial thickness	[m]
E	Longitudinal voltage drop across superconductor	[V/m]
E_0	Superconductivity electric field criterion	[V/m]
\hat{e}_{ph}	Peak phase back-EMF	[V]
F	Figure of merit for the optimization of HTS machines	[Nm·m/kgA _{RMS}]
f	Frequency	[kHz]
$F_{m,AB}^*$	Air bearing force density per unit mass	[N/kg]
$F_{s,AB}^*$	Air bearing surface force density	[N/m ²]
$F_{n,seg}$	Normal force per segment	[N]
g	Equivalent airgap	[m]
g_{acc}	Gravitational acceleration	[m/s ²]
h	Convective heat transfer coefficient	[W/m ² K]
h_{AB}	Height of air bearing unit	[m]
h_{ay}	HTS machine armature yoke height	[m]
h_{br}	Support bracket height	[m]
h_c	Height of coil-head-cooling region	[m]
$h_{d,HTS}$	HTS machine field winding depth	[m]
h_{fly}	Air bearing fly height	[m]
h_{ft}	HTS machine field tooth half width	[m]
h_{fy}	HTS machine field yoke thickness	[m]
h_j	Dimension of HTS machine feature j	[m]
h_k	HTS machine cryostat wall thickness	[m]
h_{ry}	Rotor yoke height	[m]
h_{sy}	Stator yoke height	[m]
h_t	Stator tooth height	[m]
$h_{w,HTS}$	HTS machine field winding width	[m]
I_c	Superconductor critical current	[A]
i_d	d-axis current	[A]
I_{ph}	RMS phase current	[A _{RMS}]
\hat{i}_{ph}	Peak phase current	[A]
i_q	q-axis current	[A]
J	RMS conductor current density	[A _{RMS} /m ²]
J_c	Superconductor critical current density	[A/m ²]

J_{eng}	Superconductor engineering current density	[A/m ²]
k_{air}	Air conduction coefficient	[W/K]
k_{ay}	Optimization variable for armature yoke height	[-]
k_d	Distribution factor	[-]
$k_{d,HTS}$	Optimization variable for HTS field winding depth	[-]
k_{end}	End-effect factor	[-]
k_f	Slot fill factor	[-]
$k_{f,HTS}$	HTS coil fill factor	[-]
k_{ft}	Optimization variable for field tooth half width	[-]
k_{fy}	Optimization variable for field yoke thickness	[-]
k_j	Optimization variable for HTS machine feature j	[-]
k_m	Conventional/C-Core FSPM differentiation factor	[-]
k_p	Pitch factor	[-]
k_{red}	Redundancy factor	[-]
k_s	Slot opening factor	[-]
k_{safe}	General modeling safety factor	[-]
k_{σ}	Pole leakage factor	[-]
k_{σ}^*	Pole leakage factor in the presence of Halbach array	[-]
$k_{\sigma,array}$	Halbach array leakage factor	[-]
$k_{s,HTS}$	HTS wire safety factor	[-]
k_{sk}	Skewing factor	[-]
k_T	Torque constant	[Nm/A]
k_w	Winding factor	[-]
$k_{w,HTS}$	Optimization variable for HTS field winding width	[-]
L	Active length	[m]
L_{axial}	AFPM machine axial length	[m]
L_c	Circumferential path length of circulating air	[m]
L_d	d-axis Inductivity	[H]
l	Base value for feature dimensions of HTS machine	[m]
l_e	End-winding length	[m]
l_g	Airgap length	[m]
$l_{g,av}$	Average airgap length	[m]
$l_{g,max}$	Maximum airgap length	[m]
$l_{g,min}$	Minimum airgap length	[m]
l_i	Depth of component/feature i (axial direction)	[m]
l_m	Magnet height	[m]
l_{seg}	Circumferential span per segment	[m]
L_q	q-axis Inductivity	[H]
L_{tot}	HTS machine total axial length	[m]
l_{tr}	FSPM machine rotor yoke thickness	[m]
l_w	Winding turn average length	[m]
L_w	Phase wire length	[m]
m	Total mass	[kg]
m_{act}	Active mass	[kg]

m_{AB}	Air bearing units total mass	[kg]
$m_{AB,rot}$	Rotor air bearing units total mass	[kg]
m_i	Mass of component i	[kg]
m_{ph}	Number of phases	[-]
N	N value of superconductor sample/coil	[-]
n	Rotational speed	[rpm]
N_c	Number of turns per coil	[-]
n_n	Nominal rotor speed	[rpm]
N_{ph}	Turns per phase	[-]
N_r	Number of rotor poles in FSPM machine	[-]
N_s	Number of slots	[-]
N_{seg}	Number of stator segments	[-]
$Nu_{Lc,av}$	Nusselt number over length L_c	[-]
P	Power	[W]
p	Number of pole pairs	[-]
P^*	Volumetric loss density	[W/m ³]
P_{Al}	Conduction loss (using aluminum windings)	[W]
P_e	Electrical power	[W]
P_{Fe}	Core loss	[W]
P_M	Magnet eddy current loss	[W]
$P_{M,array}$	Array eddy current loss	[W]
Pr	Prandtl number	[W]
\mathcal{P}_g	Airgap permeance	[Wb/A]
\mathcal{P}_m	Magnet permeance	[Wb/A]
\mathcal{P}_{par}	Parallel nonlinear permeance	[Wb/A]
\mathcal{P}_{ser}	Series nonlinear permeance	[Wb/A]
Re_{Lc}	Reynolds number over length L_c	[-]
R_{fo}	HTS machine field circuit outer radius	[m]
R_g	Airgap radius	[m]
r_h	Support bolt radius for SPM machines	[m]
R_i	Machine/Rotor inner radius	[m]
R_o	Machine outer radius	[m]
R_{ro}	Rotor outer radius	[m]
R_{ry}	Rotor yoke outer radius	[m]
R_{sy}	Stator yoke inner radius	[m]
$S_{AR,g}$	Aspect ratio of airgap permeance in FSPM machine	[-]
$S_{AR,m}$	Aspect ratio of magnet permeance in FSPM machine	[-]
S_c	Area of one conductor	[m ²]
SR	Split Ratio	[-]
SR_{new}	Split ratio after addition of Halbach array	[-]
S_s	Total conductor area per slot	[m ²]
T_e	Electromagnetic Torque	[Nm]
T_c	Superconductor critical temperature	[K]
THD	Total Harmonic Distortion	[-]

T_n	Nominal torque	[Nm]
UTS	Ultimate Tensile Stress	[Pa]
V_{act}	Active volume	[m ³]
V_i	Volume of component i	[m ³]
V_m	Total magnet volume	[m ³]
V_{rt}	Total rotor teeth volume	[m ³]
V_{ry}	Rotor yoke volume	[m ³]
V_{st}	Total stator teeth volume	[m ³]
V_{sy}	Stator yoke volume	[m ³]
V_w	Total winding volume	[m ³]
w_f	HTS machine total field coil width	[m]
w_i	Width of component/feature i (azimuth direction)	[m]
x	x-coordinate along Halbach array wavelength	[m]
y	Perpendicular distance to surface of Halbach array	[m]

Greek letters

β	Half the magnet pole-arc for SPM machines	[rad]
γ	Half the pole-arc for HTS machines	[deg]
δ	Angle between rotor and stator fields	[deg]
δ_{dist}	Airgap distortion	[m]
ε	Complement of half the pole-arc for HTS machines ε	[deg]
η	Efficiency	[-]
λ	Dimensioning factor for HTS machine features	[-]
λ_1	Halbach array wavelength (array type 1)	[m]
λ_2	Halbach array wavelength (array type 2)	[m]
λ_m	Number of machine modules	[-]
μ	Free stream velocity	[m/s]
μ_o	Permeability of vacuum	[H·m]
μ_{rm}	Magnet relative recoil permeability	[-]
ν	Air kinematic viscosity	[m ² /s]
ν_l	Winding type	[-]
ρ	Mass density	[kg/m ³]
ρ_{av}	Average mass density	[kg/m ³]
ρ_e	Electrical resistivity	[Ω·m]
ρ_i	Mass density of component i	[kg/m ³]
σ_t	Airgap shear stress	[Pa]
τ_p	Pole pitch	[m]
τ_u	Slot pitch	[m]
φ	Phase shift angle	[deg]
ϕ_{array}	Halbach array magnetic flux	[Wb]
$\phi_{array,1}$	Halbach array magnetic flux (array type 1)	[Wb]
$\phi_{array,2}$	Halbach array magnetic flux (array type 2)	[Wb]
ϕ_g	Peak flux linkage per turn / airgap magnetic flux	[Wb]
$\phi_{g,new}$	Airgap magnetic flux after flux enhancement	[Wb]
ϕ_m	Magnet operational flux	[Wb]

ϕ_r	Magnet remanent flux	[Wb]
ω_e	Electrical angular frequency	[rad/s]
ω_m	Rotor angular speed	[rad/s]

Chapter 1

Introduction

1.1 General Motivation

Preserving the environment is the main motivation for the gaining importance of environmentally friendly technologies. Nevertheless, achieving the technological development stage necessary for this preservation is not only important from a social point of view. The dependence of the economy's momentum on oil prices and oil availability calls for the development of technologies with low use of oil and its derivatives.

Political initiatives encompass this philosophy in most developed countries. Within the EUs global objectives for the short, medium and long term, a comprehensive environmental policy has been endorsed to limit the influence of human population on climate. For the short term, the objectives for the year 2020 are summarized in the "20-20-20 targets":

- 20% reduction of EU greenhouse gas emissions from 1990 levels
- 20% of EU energy consumption from renewable resources
- 20% increase in energy efficiency

Medium term goals for the year 2030 have also been proposed to keep the EUs economy and energy system more competitive with the "2030 framework":

- At least 40% reduction of EU greenhouse gas emissions from 1990 levels
- At least 27% energy consumption from renewable resources
- At least 27% improvement in energy efficiency

Finally, for the long term (year 2050), the EU considers clean technologies as the future for Europe's economy. With the "2050 Roadmap" it looks beyond the short term and sets out plans towards a low-carbon society. The roadmap suggests that, by 2050, the EU should cut its emissions to 80% below 1990 levels through domestic reductions alone.

This climate and energy package offers an integrated approach to climate and energy policy. It aims to combat climate change and increase the EUs energy security while strengthening its competitiveness [1]. The afore-mentioned policies provide kick-start incentives and guidelines for the same process in the different industry sectors, e.g.

automotive, aerospace, etc. Industry specific R&D policies derived from them are automatically aligned with EU policy. The seriousness of this approach is such that the European Commission has even proposed binding legislation for its implementation [1].

1.2 Conventional and Alternative Aircraft Propulsion

In the European aerospace industry, achieving such reductions requires intensive innovation in the topics of All-Electric- and More-Electric-Aircraft (AEA and MEA). This is currently a top priority that cascaded down from the EU policies mentioned above.

The increase in innovation can be summarized as the intensive search for solutions that minimize their environmental footprint and increase aircraft operational efficiency in the fields of:

- Aeronautics, space and mechanical engineering: with composite materials, lightweight structures, electromechanical actuation, more efficient jet and turboprop propulsion, among others.
- Electronics and electrical engineering: with breakthroughs in instrumentation and control, efficient solid-state control and power electronics, powerful portable computing, high-quality satellite communications and efficient navigation, among others.

The aerospace industry has been 2nd in research intensity steadily behind the biotechnology and pharmaceutical industries according to the OECD [2]. Yet, despite this, propulsion is still based on conventional propellant combustion: a fossil fuel is ignited to produce work in a gas turbine with only a moderate thermal efficiency of 30% to 40% under ideal conditions [3]. This approach is also subject to other well-known disadvantages: potentially limited availability of oil, plus undesirable combustion by-products and emissions. On the other hand, the main advantage of the traditional kerosene-fed gas turbine as an aero engine is its gravimetric power density. Measured in thrust-to-weight ratio or power-to-weight ratio, this figure is one order of magnitude higher than for most piston engines and electrical motors [4, 5, 6].

Indeed, the core of a gas turbine can be twenty times as powerful as a piston engine of equal size. This is because of the continuous combustion cycle and the large, open flowpath of a gas turbine, which can admit 70 times as much air as an equivalently sized piston engine over the same time period [7]. This also indicates a low weight, i.e. a low material content per unit volume. Most of the volume is destined for the flowpath of the working fluid with little volume being used by actual components. This is in contrast to piston engines, where heavy hardware occupies most of the space, similarly to electrical motors.

Additionally, the propellant itself (kerosene) also exhibits one of the best compromises of energy content per unit mass *and* per unit volume (see Figure 1-1). When compared to alternative energy sources, kerosene does not have the high energy content per mass of hydrogen. However, compared to kerosene, hydrogen requires three and a half times more volume to store the same amount of energy. When compared to electrical energy storage means, kerosene is around one order of magnitude energy-richer than electrochemical batteries both in terms of weight and volume [8, 9, 10, 11].

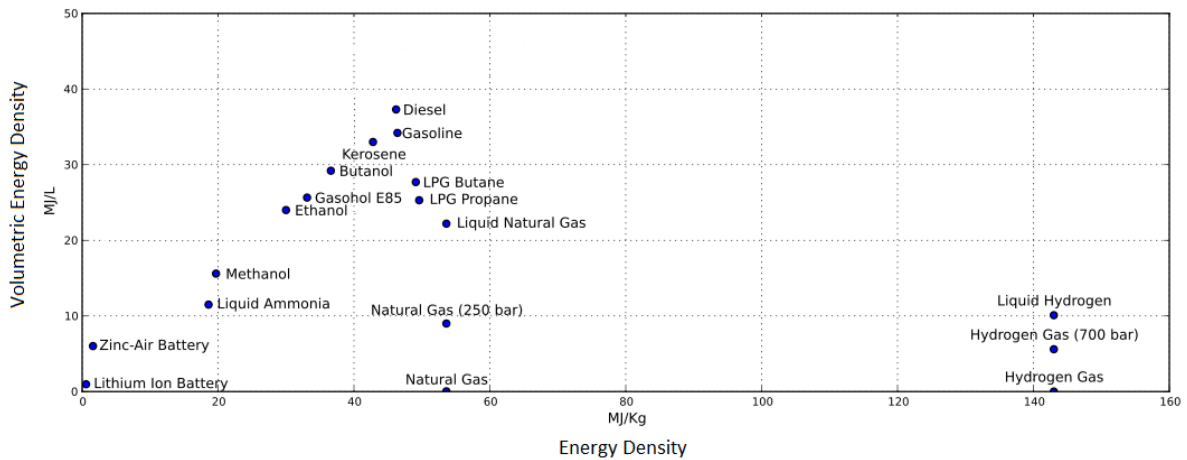


Figure 1-1: Energy densities from different fuels and energy sources [9]

Regarding weight and storage space, it is then reasonable to use the combination gas-turbine-kerosene as cornerstone of the aircraft propulsion architecture: its performance-to-weight compromise seems to offset the advantages of a more efficient alternative. Nevertheless, new policies and strategies revolve around a “reduced and more efficient fuel burn”. This means that alternative propulsion systems are worth considering, if the advantage in efficiency is considerable and the weight penalty involved is acceptable.

Among gas turbines, a higher efficiency than the traditional 30% to 40% is only achieved by rocket engines: due to their higher peak cycle temperatures and pressures an efficiency of 60% is achievable. Also possible, an electrical motor powered by batteries can have an even higher efficiency: ca. 90%. As an additional alternative involving internal combustion, Diesel engines have typical efficiencies of 45% [11, 12, 13] and are known to go as high as 55% [14, 15]. Their theoretical maximum lies at around 80% according to the limit set by Carnot’s efficiency limit.

The three afore-mentioned approaches still need an energy source, and in that aspect only oil derivatives can currently provide the appropriate energy density. Based on this, hydrogen-powered gas turbines and battery-powered electrical motors must be ruled out. An alternative based solely on Diesel engines, however, offers a better efficiency. They are in fact already used for rotary-wing aircraft propulsion, but limited to aircraft with low to moderate TOWs. This is because Diesel engines for large aircraft would require considerable installation space and would have a high weight. In the same manner of gas turbines, they are also limited to operation in a narrow rpm range and have a limited architectural and integration flexibility [16, 17].

An additional more viable alternative, a combination of all-electric and all-chemical, is a hybrid architecture: a full serial hybrid drivetrain. In such architecture, Diesel engines generate the electrical energy required while operating efficiently at their sweet spot. Following, the generated energy flows into electrical machines that drive the main aircraft propulsor(s). This eliminates the mechanical coupling between the energy source and propellers/rotors, and potentially enhances the efficiency of the drivetrain. It allows a more flexible operation and integration than using Diesel engines alone, but also has a lower weight than an all-electric solution.

1.3 Problem description

With a hybrid drivetrain, a more-electric propulsion system has a higher probability of success. Among its components, Diesel engines are already a tested technology in aircraft. Electrical machines have been investigated for aircraft propulsion mostly at a conceptual level, however with the same known problem: insufficient power-to-weight ratio [4, 10].

For electrical machines, the problem is critical: 0,5kW/kg in average for a power class of 1MW [4, 6]. Machines with higher gravimetric power density (3-5kW/kg) do exist, but are limited to high-speed applications ($n \gg 1000\text{rpm}$) where most of the power is achieved through rotational speed. For aircraft electrical propulsion many application and sizing studies have been performed as seen for example in [16, 17, 18, 19, 20, 21]. Nevertheless, very little experimental work has been carried out and the usually reached conclusion points at an excessive size/weight [22]. As a comparison, aerospace propulsion powerplants are expected to achieve at least 5kW/kg. It is also common to find examples providing as much as 10kW/kg for a 1MW power class and propeller speeds below 1000rpm.

Furthermore, most studies assume an electrical-machine-gearbox constellation to reduce rotational speed and increase torque. Gearboxes are undesired components due to cost and reliability reasons, although a direct-drive machine for rotorcraft propulsion has also shown to be heavier [11, 21]. Nevertheless, based on the figures below, the cost reduction in construction and operation is still a stronger motivation to look into direct-drive machines:

- Propulsion-system-related costs can amount from 30% to 50% of the total manufacturing costs, and from 30% to 60% of the total operational costs [11].
- From a safety perspective, 60% of all first occurrences leading to accidents and incidents occur during Take-Off/Climb, Approach/Landing and Maneuver/Hover phases. 50% of these events can be associated to loss of control and engines. For these flight phases, transmission systems are under significant dynamic loads and their connection to engines and aircraft control deems their reliability vital [11].

All of the mentioned studies use either off-the-shelf electrical machines or approximate calculations based on general design equations. None however, perform a detailed design based on requirements of a particular aircraft propulsion application. Also, it is unclear if the machine topology can have a significant influence on the performance of a final design, since many new topologies are constantly being reported and investigated.

1.3.1 State of the art of electrical machines

Conventional Machines

Three types of electrical machines are mainly used in energy conversion applications: permanent magnet synchronous machines (PMSM), induction machines (IM), and switched reluctance machines (SRM). All three have been extensively researched to determine their advantages and disadvantages for different drive applications (traction/propulsion, actuation, generation). It has been determined that PMSMs have the upper hand in terms of torque and power capability, and efficiency [8, 23, 24]. Contrary to PMSMs, IMs and

SRMs lack a built-in excitation directly affecting their performance: they require larger magnetization currents and machine volumes to achieve comparable ratings.

Simple and robust in their design, IMs and SRMs have begun to lose terrain to PMSMs in applications, where they were usually considered as the main workhorse: medium- and heavy-duty traction, high-speed rail, off-highway vehicles and ship propulsion [8, 23]. Regarding fault tolerance, favorable feature of IMs and SRMs [25], PMSMs have shown potential in this area with additional features: auxiliary windings, mechanical flux weakening and inherently fault-tolerant topologies [26] are some examples.

Also, direct-drive PMSM designs are of particular interest for aerospace use. Currently they are mainly employed in low-speed high-torque applications. The most relevant is probably wind power generation where the efficiency and reliability benefits are exploited [27, 28]. Other fields such as actuation and vehicle traction/propulsion are gaining importance as well [24, 29, 30, 31, 32, 33]. They are also favored for aircraft propulsion as discussed in [11], although preliminary analyses indicate a severe weight penalty when implementing a direct-drive system [27, 28].

In weight-critical applications, PMSMs with fractional-slot concentrated windings (FSCW) are the best chance for a low weight with conventional materials. Seriously considered only until recently, FSCW machines have a similar number of stator slots and rotor poles. Their non-overlapping windings offer inherent phase fault tolerance [34, 35], but can also result in some parasitic effects: enhanced torque ripple, unbalanced magnetic forces and rotor losses and less sinusoidal back-EMF waveforms. At the same time, it gives the possibility to build a slimmer machine with a high pole number, short end-windings and high slot fill factors [35, 36]. Assuming an equal shear stress for two machines, one with distributed and one with concentrated windings, the latter can be designed to deliver the same performance at a smaller size [35, 37, 38, 39]. This is particularly useful for applications where a high pole number results in a high speed machine from the electromagnetic point of view, but with a low mechanical speed.

Designs based on these topologies can be implemented in a compact manner yielding high gravimetric ($\sim 40\text{Nm/kg}$) [40] and volumetric torque densities ($\sim 40\text{kNm/m}^3$). Using torque density gives a better measure of a machine's capability independent of speed [41]. With the use of high-energy permanent magnet material, high-grade electrical steels and efficient cooling, these machines achieve high airgap shear stress values ($\sim 40\text{kPa}$).

Superconducting Machines

Additional to machines based on conventional materials, superconducting materials open new possibilities for electrical machines. They can carry considerably higher current densities when compared to traditional conductors (at least an order of magnitude higher) [42]. Consequently, much higher airgap flux densities and current loadings can be potentially generated, but at the expense of a more complex cryogenic cooling system [43]. This complexity increases with decreasing operating temperature of the superconductor (allowing in turn even higher current densities).

Some working machine prototypes have been manufactured with a superconducting rotor (superconducting material used in the field windings only). These were designed for power generation and ship propulsion [43, 44], which are currently the two main fields driving the technology. As for fully superconducting machines (superconducting material

used in both armature and field windings), only one implementation attempt is currently known concluding that further material and operation maturity is still required [45]. Although theoretically more power-dense than conventional machines by one order of magnitude, no definite figures exist for superconducting machines due to the infancy of the technology [4, 42, 46]. These are up to now only comparable to figures achieved by conventional machines.

1.3.2 Research Question

This thesis considers both conventional and superconducting machines as candidate topologies for electrical aircraft propulsion. Its main goal is to take into account specific requirements and machine topologies and examine them in a specific context: as case study the main rotor drive of a civilian helicopter of the EC135 class will be used as target application. The feasibility of a solution based on direct-drive electrical machines is analyzed and a detailed design is performed. This work should help further understand the aspects and limitations that require consideration in the design of such drive systems.

No direct-drive electrical machine specifically designed for rotorcraft propulsion is known, and gravimetric torque density studies for different topologies are scarce. It is therefore not clear if such performance is achievable or even realistic with conventional materials. Also, if a design is plausible using superconducting materials, it's unclear if such design would be ironless or would require core material. Some is expected to be necessary in order to contain the magnetic field within the machine volume. Additionally, the mass density of the highest-performing superconducting material (YBCO) is comparable to that of electrical steel, magnet material or copper; something not usually discussed. For a certain target weight, any use of heavy active materials reduces the available weight for structural and/or cooling purposes, quickly leading to a weight penalty.

In [4] an overview of the topic of aircraft propulsion is given, although in terms of gravimetric power density, but contemplating the usual operational envelope of jet turbines: *there, the capabilities of electrical machines are placed one order of magnitude below turbofan engines for any given weight*. Due to the power-torque relationship, the same can be assumed for the torque capability. However, without further information regarding rotational speeds a more accurate assertion cannot be made.

For the case study at hand, a required gravimetric power density of 5kW/kg can be assumed between 300rpm and 400rpm. Considering the above, an electrical machine can be initially expected to have a gravimetric power density of 0,5kW/kg. The improvement needed is then considerable, and the research question can be formulated as follows:

Given the current state of the art of electrical machines and the possibility to use superconducting materials, is it possible to propel a civilian helicopter (TOW: 3t) using a direct-drive electrical synchronous machine?

The feasibility assessment should focus on alternative or new construction principles and/or materials offering any improvement, even if only incremental. Regardless of the purpose (electromagnetic, thermal, structural or miscellaneous), possibilities should be considered keeping in mind that their use/implementation should be aerospace certifiable.

Finding a definitive answer to the research question probably goes beyond the scope of this thesis. On the other hand, the considerations presented here will serve as first steps in the right direction, in the case that the interim answer is “no”. Also, even if the ultimate goal is not achieved, this thesis brings awareness to the machine topologies studied. Their potential for other high-torque applications within or outside aerospace engineering can contribute to the development of More- and All-Electric applications in all industries.

1.3.3 Thesis Objectives

As a summary of the problem description above, this thesis has the following goals:

- Identify the key performance indicators for the evaluation of electrical machine performance for aerospace propulsion
- Perform a selection of candidate topologies based on the already defined performance indicators
- Make a comparison of the candidate topologies through preliminary modelling, that fulfills the performance requirements of the target application
- Perform a detailed electromagnetic design using the selected topology
- Make initial design considerations regarding lightweight structural design for the selected topology
- Implement a partial experimental set-up for model and performance validation

1.3.4 Experimental Setup:

As a culmination of the intended comparison, an experimental setup was produced to validate methodology and results obtained from the detailed design. A thorough design explanation is given in Chapter 7, while here only the main broad features are mentioned.

Given the nature and size of the application a test setup of a complete machine was not produced in order to reduce risk and costs. Instead, a partial implementation was done, where enough segments of the machine were fabricated, so that static performance measurements could be carried out.

The mentioned segments were manufactured on a scale 1:1 with the objective of integrating them in a realistic test bench. On such test bench further mechanical features for structural support and positioning were implemented. The test bench uses aerostatic bearings and stainless steel support parts meant as a proof of concept and not as a final lightweight design.

1.4 Thesis Outline

Chapter 2 – Problem Background and Definition

This chapter focuses on the specific background of electrical aerospace propulsion. The Clean Sky Joint Technology Initiative (JTI) is explained in more detail while highlighting the demonstrators and technologies relevant for the development of this thesis. A thorough

review of actual demonstrators and concept studies is made, in which electrical propulsion is implemented at least in some degree. Relevant aspects are the electrical machine type employed, its maximum gravimetric power density and maximum take-off weight (MTOW) of the aircraft. Within this context the concept of a hybrid helicopter is presented in detail, and the requirements for the main rotor drive are defined. These are compared to the figures observed in the other demonstrators reviewed in a first attempt to assess the feasibility of a solution.

Chapter 3 – Current Technology Status

This chapter examines electrical machines from the basics, starting with materials employed not only in the active part but also for structural purposes. Guidelines for fault tolerance, relevant for aerospace applications, and the most important PMSM and superconducting machine topologies are reviewed. This is done with the purpose of identifying incremental advantages and synergies for the following designs. Some examples of aerospace specific machines for future civilian transport are presented, which reflect the preceding guidelines. In the final part of the chapter, candidate topologies are chosen for further analysis, and a first design decision is made by choosing a radial flux machine architecture. Such choice is made by using generic modelling of the gravimetric torque density for both cases, allowing a direct comparison.

Chapter 4 – Surface Permanent Magnet Machines as a Benchmark

This chapter concentrates on surface permanent magnet (SPM) machines, and studies their performance for the target application through a FEM-validated analytical model. The model incorporates the most important physical parameters that allow a simple but precise performance and weight calculation. Different design scenarios are examined: using copper and aluminum windings, different slot/pole combinations, structural support provisions, etc. This allows identifying the most relevant design drivers to achieve high torque densities, and quantifies the impact of structural support on the overall active mass. With the insights won, a final design is proposed and roughly optimized in order to make a prediction of the achievable performance.

Chapter 5 – Flux Switching Permanent Magnet Machines

This chapter examines the second choice of iron-based machines: FSPM machines. With the working principle and main features presented in Chapter 3, this chapter focuses on the machine modelling. Based on a one-time initial input from FEM simulations, the proposed principle makes a performance estimation based on input parameters and a simplified 1-phase model. For candidate configurations, this allows a detailed but quick investigation of the sensitivity to split ratio and airgap length of the performance-to-weight ratio. Also, a topology variation is proposed and analyzed: the Halbach-FSPM machine. A final design including the studied features is made and optimized making considerations for structural support. The final result is a prediction of the gravimetric torque density.

Chapter 6 – High Temperature Superconducting Synchronous Machines

This chapter turns to the study of superconducting machine design based on a synchronous salient pole machine configuration. It focuses on the study of the material distribution

within the machine, which yields the highest gravimetric torque density using a simplified 2D machine model. The objective is to find the highest magnetic loading possible per overall unit mass for a fixed pole pair number. The result indicates how much iron and superconducting material is needed and where. With the resulting 2D profile a best-case performance and weight prediction is made.

Chapter 7 – Experimental Validation and Conceptual Structural Support

In this chapter the designs from the previous chapters are revisited and compared based on performance and a preliminary estimation of efficiency. Centered on the final selection, a mechanical support design based on air bearings is introduced and explained together with the air cooling strategy. The partial experimental setup as mentioned in 1.3.4 is developed parting from the proposed construction principle. With such experimental setup the most relevant performance parameters are validated, giving way for a conceptual design of a complete prototype. Such design delivers a final weight prediction and serves as starting point for future recommendations and work.

Chapter 8 – Conclusions and Recommendations

In the last chapter, theoretical and practical work presented in the thesis is revisited and evaluated. Important conclusions are drawn with respect to the validation of the developed designs, the models used and the limits on gravimetric torque density for the helicopter main rotor drive application. Lastly, it discusses the final conceptual design and lists the main thesis contributions and recommendations for future work.

Chapter 2

Problem Background and Definition

This chapter sets the aerospace-specific problem background by giving a more detailed explanation about Clean Sky JTI and its main objectives. Afterwards, it goes on to list the main electrical and hybrid demonstrators built at present, mainly consisting of light aircraft with low TOWs. This review then turns to some important feasibility studies and future concepts proposed, which are more oriented towards mass civilian transport.

The chapter then continues to present the concept aircraft considered in this study: a hybrid helicopter. The drivetrain architecture is presented together with a parallel between the conventional and hybrid configurations. A focus is made on the main rotor drive for which its main requirements and constraints are presented. Given the application requirements, figures of merit are chosen for the initial assessment of electrical machines. Lastly, the hybrid helicopter main rotor drive is compared to the other demonstrator drives in terms of performance-to-weight ratio in order to establish a possible starting point.

2.1 Clean Sky JTI

Major aerospace companies within the EU have developed a public-private cooperation, together with the European Commission to foster research and innovation. This agreement focuses on complying with the top-level objectives explained in Chapter 1 at an aerospace industry level. The initiative is contained within the EU's Seventh Framework Program (FP7) for Research and Technological Development, and was named Clean Sky Joint Technology Initiative (JTI). Clean Sky is the main contributor to the targets set by ACARE for the year 2020. It is also in charge of formulating the research roadmap for aviation beyond 2020 for the horizon towards 2050 [47].

Clean Sky's main objective is to speed up technological breakthrough in clean air developments and shorten the time to market for new solutions [47]. To achieve this at a European level, the initiative emphasizes on an effective coordination of aeronautics research and improvement of the generation of knowledge. Also necessary are a guaranteed use of research findings and a set-up of an innovative and competitive air transport system.

Qualitatively, the expected outcome of this venture will be quieter and more fuel efficient aircraft; quantitatively the strived achievements are summarized as follows [47]:

- 50% reduction of CO₂ emissions through drastic reduction of fuel consumption
- 80% reduction of NO_x (nitrogen oxide) emissions
- 50% reduction of external noise

The challenge of reducing emissions, while improving performance and efficiency, can be tackled with better results by identifying fields of interest. In total six Integrated Technology Demonstrators (ITDs) and their respective deliverables have been defined, so that research areas can be clearly set, coordinated and managed [47]:

- **SMART Fixed Wing Aircraft:** active wing technologies and new aircraft configuration
- **Green Regional Aircraft:** low-weight aircraft using smart structures, low-noise configurations and technology integration from other ITDs.
- **Green Rotorcraft:** innovative rotor blades, alternative engine installation for reduced noise and drag, and advanced electromechanical systems
- **Sustainable and Green Engines:** low-noise high-efficiency lightweight cores and low-pressure systems, and novel configurations (open rotors, intercoolers)
- **Systems for Green Operations:** AEA equipment and system architectures, thermal management, "green" trajectories and improved ground operations
- **Eco-Design:** green design and production, minimization of environmental impact of the product life cycle and optimal withdrawal and recycling of aircraft

Within each ITD, advancements in diverse engineering disciplines have originated new products, which are the first steps to complying with the afore-mentioned. These first achievements have in turn encouraged own development in industry players not part of Clean Sky JTI. For example, in American industry players, as a competitive response but also out of own initiative, consequently driving the process within Clean Sky JTI further.

Green Rotorcraft

While most ITDs are destined for fixed-wing aircraft, the Green Rotorcraft Demonstrator aims at minimizing the impact of the predicted increase in rotorcraft traffic [47]. For this purpose, emphasis is made in two principles: efficiency increase in energy and material use, and drastic reduction of noise and greenhouse emissions for the complete flight envelope. Six technologies, or GRCs, are proposed to guarantee meeting the targets [47]:

- GRC1.** Innovative Rotor Blades: active blade control (active twist, control surfaces) combined with design optimization
- GRC2.** Drag Reduction: outer shape optimization and active flow control for aerodynamic drag reduction (rotor hub, fuselage body, etc.); optimized turboshaft design, manufacturing and installation (air intakes and nozzles)
- GRC3.** Innovative on-board electrical systems: hydraulic fluid elimination and optimization of on-board energy use through a more-electrical concept

- GRC4.** Lean power plant: low CO₂ emissions demonstration with a Diesel-powered light helicopter
- GRC5.** Environment-Friendly Flight Paths: flight management that enables noise and gas emissions reduction (NO_x, CO₂) within controlled and uncontrolled air space
- GRC6.** Eco-Design Demonstrators for Rotorcraft: use of “economic” (“green”) materials and processes to manufacture, test and recycle typical components

Relevant points for the development of this thesis are concentrated in GRC3 and GRC4. For both all-electric and more-electric aircraft propulsion, innovative electrical machine concepts are needed to match the performance requirements of conventional propulsion. Also, in the case of a hybrid system, the main energy source would be a combustion engine, conventionally a gas turbine, or as GRC4 suggests, a diesel engine.

The gas turbines usually powering rotorcraft, also called turboshafts, are built with centrifugal compressors and turbines, which are particularly compatible with reverse-flow combustors. These two features result in a very compact design, critical for helicopter engines [7], capable of achieving gravimetric power densities between 5kW/kg to 8kW/kg. Hence, the main goal in adapting Diesel engines and electrical machines for helicopter drivetrain use is minimizing their weight penalty. Current gravimetric power densities of high performance turbo-charged Wankel Diesel engines lie between 1,5kW/kg and 2kW/kg [48, 49]. For electrical machine concepts for aerospace, a lower specific power of the order of 1kW/kg can be expected, caused predominantly by the highly dense materials needed.

Judging by the difference between gas turbines and the most power-dense Diesel engines and electrical motors, the replacement of the former with the latter two is not straightforward. Although some demonstrators have been built and operated successfully, these are only low-TOW-cases. For high-TOW-aircraft with powerplants showing 10kW/kg or more, gas turbines are not replaceable at present. However, for intermediate-TOWs, the hybrid drivetrain might be possible. To find a clearer answer, a breakdown of a hybrid propulsion system for rotorcraft and its power conversion elements must be made and compared to the conventional system. But before further elaboration of the concept, a review of the state of the art of more-electric and all-electric propulsion is given, to appreciate better what is currently achieved, and at which TOWs.

2.2 Next-Generation Aircraft Demonstrators

The following is a review of the most important demonstrators and studies produced in recent years, which implement a complete or partial electrification of the drivetrain. For each part of the review, a distinction between fixed-wing and rotary-wing aircraft is made, and the electrification type is specified (hybrid, battery powered, etc). For each demonstrator a brief explanation of the development background and involved parties is presented. Besides this, the maximum take-off weight is listed, together with the maximum gravimetric power density and rotational speed of the electrical machine installed in the drivetrain. This information is presented for the cases where it is readily available. For the feasibility studies and future concepts, only the major propositions are briefly discussed, since it is not possible to go further into detail at present.

2.2.1 Hybrid Fixed-Wing Aircraft

e-Star

Presented in 2011 by Diamond Aircraft, the DA36 e-Star 2 is a hybrid small aircraft (see Figure 2-1) [50]. Based on a HK36 Dimona glider, it employs a serial direct-drive hybrid system with a 70kW electric motor and a 30kW ICE coupled to a generator.

The battery pack provides the electric motor with extra power during take-off. During cruise flight it is recharged since only a portion of the available 30kW from the ICE is required. This setup achieves fuel savings of up to 25% compared to an equivalent non-hybrid.

- $MTOW$: 770kg
- $P/m|_{max}$: 5.4kW/kg @5800rpm



Figure 2-1: DA-36 e-Star 2 serial hybrid aircraft [50]

Flight Design C4

The Flight Design C4 is a 4-seat light aircraft employing a 116kW-parallel-hybrid powerplant (see Figure 2-2). The supplementary electric motor installed provides boost power for a short time during take-off and climb phases. It also provides safety back-up power for greater control and a milder descent in the event of an engine failure [51, 52].

The permanent magnet electric motor is fed by lithium iron phosphate batteries providing a total of 30kW during the mentioned phases. The batteries are recharged during flight, while the ICE provides the remaining 86kW during cruise flight. Battery charge also takes place during descent, when the windmilling propeller serves as a regenerative brake.

- $MTOW$: 1200kg
- $P/m|_{max}$: 2.3kW/kg @7000rpm



Figure 2-2: Flight Design C4 [53] (left) and parallel hybrid powerplant [54] (right)

2.2.2 Battery-Powered Fixed-Wing Aircraft

Elektra 1 and Elektra 2

The PC-Aero Elektra 1 and Elektra 2 small all-electric planes are flight-certified in Germany and commercially available [55].

The Elektra 1 (see Figure 2-3) is a plug-in 1-seater aircraft with a 400km range, a cruise speed of 160km/h and a payload of 100kg. It is powered by a 100kg battery pack through a 16kW 1400rpm BLDC motor. The Elektra 2 comes with a combination of battery pack and solar cells laminated in the wing structure, which can provide up to 20 hours of flight time and a range of 2000km.



Figure 2-3: Elektra 1 aircraft [183]

- *MTOW*: 300kg (Elektra 1), 350kg (Elektra 2)
- $P/m|_{max}$: 3.4kW/kg @2200rpm [56] (Elektra 1, Elektra 2)

Antares 20E and Antares 23E

Another all-electric plug-in aircraft is the Antares 20E glider manufactured by LANGE aviation [57] seen in Figure 2-4.

The glider is equipped with an outer rotor 38.5kW BLDC direct-drive motor that develops a maximum torque of 216Nm, and is powered with Li-ion batteries [58]. The motor is however used only during take-off. Once the desired height is reached, it is turned-off and the propeller is folded into the fuselage to avoid unnecessary drag during gliding.



Figure 2-4: Antares 20E [58]

- *MTOW*: 660kg
- $P/m|_{max}$: 1.32kW/kg @1700rpm [59]

Universität Stuttgart e-Genius

The e-Genius is an all-electric 2-seater glider aircraft designed and constructed by the Institut der Flugzeugbau of Universität Stuttgart. The purpose of the aircraft is competing in the Green Flight Challenge aircraft-fuel-saving competition organized by NASA [60]. It is powered by a 60kW BLDC motor and a 56kWh Li-ion battery pack that provide an all-electric flight autonomy of 400km.

- *MTOW*: 850kg
- $P/m|_{max}$: 3.5kW/kg @2000rpm [61]



Figure 2-5: e-Genius aircraft [62] (left) and propeller with electrical motor [60] (right)

Taurus Electro G2 and Taurus G4

The Taurus Electro G2 by Pipistrel is a 2-seat fully electric glider commercially available. Like other all-electric solutions, its powertrain consists of lithium ion batteries and a 40kW BLDC motor. The Taurus G4 is a 4-seat special twin-fuselage version made to compete in the Green Flight competition. It is created by merging two Taurus fuselages with a 5 meter spar whilst the 145kW BLDC motor and propeller are mounted in between [63].

- *MTOW*: 550kg (Taurus Electro G2)
- $P/m|_{max}$: 3.6kW/kg @1800rpm (Taurus Electro G2) [64]



Figure 2-6: Taurus Electro G2 (left) and Taurus G4 (right) [64]

Airbus Group E-Fan

The E-Fan is an all-electric all-composite 2-seater aircraft developed by the Airbus Group in 2013 intended for pilot training [65, 66]. While most electric concepts are retrofitted or modified gliders, the E-Fan's body is designed especially to accommodate an all-electric powertrain. It is powered by two 30kW electric motors installed in variable pitch ducted fans, and has a cruise and maximum speed of 160km/h and 220km/h respectively. With two 65kg battery packs, with 19.2kWh of total capacity, a 45-60min flight autonomy is reached.

- *MTOW*: 580kg
- $P/m|_{max}$: Not available

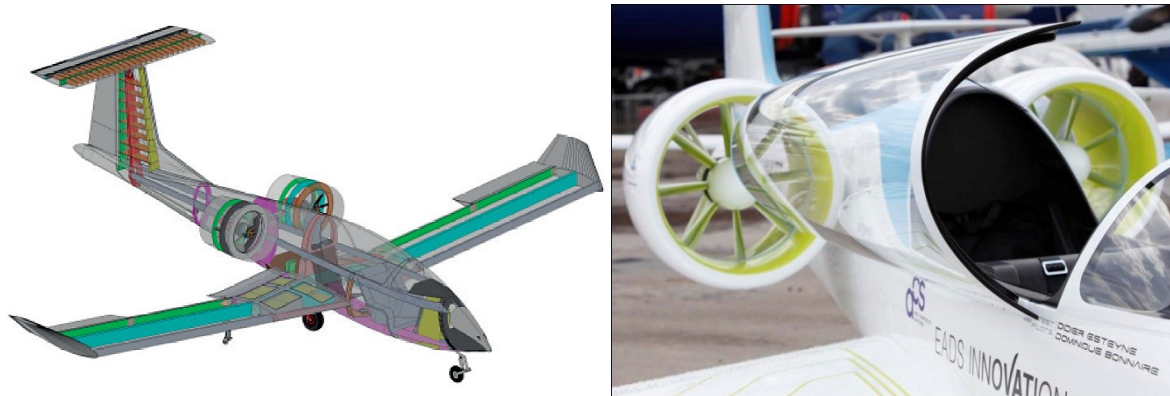


Figure 2-7: E-fan CAD model [65] (left) and E-fan prototype [67] (right)

2.2.3 Fuel-Cell-Powered Fixed-Wing Aircraft

Boeing Fuel-cell Electric Airplane

Successfully tested by Boeing in 2008 [68], the 1-seat fuel-cell-powered aircraft, was based on the Diamond Super Dimona HK36 glider like the DA36 serial hybrid. It was however modified for a fuel cell and battery-powered drivetrain. The variable-pitch propeller is directly driven by a 30kW BLDC motor, and powered directly from the fuel cell during flight. The lithium-ion battery is connected to provide the extra power needed during take-off, and during landing as an emergency backup. The average power consumption during cruise flight was measured at 20kW, which is translated into a maximum flight autonomy of 1 hour.

- $MTOW$: 860kg
- $P/m|_{max}$: 1.83kW/kg @3000rpm [69]

Enfica FC

The Enfica is a small fuel-cell powered airplane constructed by Politecnico di Torino, that in 2010 accomplished its maiden flight [70]. It is powered by a 40kW BLDC motor, in turn powered by a 20kW fuel-cell and a 20kW lithium-polymer battery. Maximum autonomy was estimated at 1 hour at 150km/h cruise speed. The plane is considered as a proof of concept that fuel-cell-powered airplanes are feasible for small aircraft.

- $MTOW$: 560kg
- $P/m|_{max}$: 1.05kW/kg @2200rpm [70]

2.2.4 Solar-Cell-Powered Fixed-Wing Aircraft

Zephyr Solar UAV

The Zephyr is a zero-emission solar/battery powered UAV plane designed for long endurance flights [71]. The aircraft is powered during the day by a solar-cell array placed on the wings and by an onboard battery pack at night. Propulsion is achieved with 2 custom-designed direct-drive FSCW SPM BLDC motors each delivering a maximum

power output of 500W at 1400rpm. The main design goal of the motor was maximum efficiency, considering that a slight decrease in it would result in increased battery mass.

- $MTOW$: 30kg
- $P/m|_{max}$: 0.84kW/kg @1400rpm [71]

2.2.5 Hybrid Rotary-Wing Aircraft: Eurocopter AS350 Hybrid

Eurocopter's hybrid version of the AS350 helicopter [72] is a parallel hybrid system equipped with a supplementary electrical motor powered by lithium ion batteries. The supplementary system provides safety back-up power for greater control and milder descent in the event of an engine failure. It does however not contribute to other flight phases, during which a 630kW turboshaft provides all propulsion power.

- $MTOW$: 2250kg
- $P/m|_{max}$: Not available



Figure 2-8: Eurocopter AS350 Hybrid [72]

2.2.6 Battery-Powered Rotary-Wing Aircraft: Sikorsky Firefly

The all-electric Sikorsky Firefly is based on the S-300C™. The conventional drivetrain was replaced by a 250kW BLDC electrical motor, power and control electronics and lithium-ion battery packs. In its current configuration, it can hold the pilot only and fly for 12 to 15 minutes at a top speed of 80 knots [73]. According to the manufacturer the total propulsion efficiency of the all-electric drivetrain is of 75% (a 300% increase from baseline value).

- $MTOW$: 930kg
- $P/m|_{max}$: 1.77kW/kg @3200rpm [73]



Figure 2-9: The Sikorsky Firefly [73]

2.3 Feasibility Studies and Future Concepts

“Alternative propulsion methods for the aviation industry” is a topic researched for many years now. Some of the alternatives considered are hydrogen-powered turbofan propulsion, fuel-cell- or battery-based all-electric propulsion, and hybrid concepts like the ones proposed by the automotive industry. Each of these can offer advantages in terms of fuel

consumption, operating cost reduction and protection of the environment, with significant challenges needed to be faced first.

In the following sections, the key points of some of the most recent studies in alternative propulsion concepts are presented. Most of the research up to this point is focused on the ability to implement these concepts on commercial aircraft. Some research regarding application in helicopters is also published but the interest seems to be lower.

2.3.1 Fixed-Wing-Oriented Studies

Alternative Propulsion Feasibility with Conventional Frames, NASA

In 2009 NASA published the research results on the feasibility of a zero and near-zero emissions aircraft [74]. The study predicts the weight of components such as fuel cells, radiators, superconducting motors and other accessories in the near future. A graph showing the power densities for different key technologies is shown in Figure 2-10.

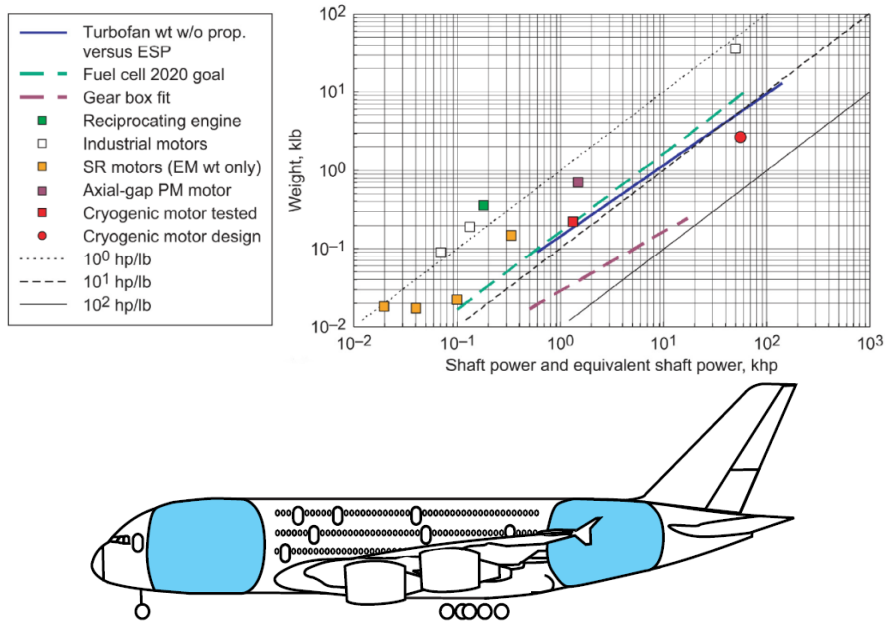


Figure 2-10: Aircraft component weight trends [74] (top), impression of modified commercial airliner to fit hydrogen tanks (in light blue) in fuselage [75] (bottom)

Different powerplant setups were compared on existing standard *medium-sized passenger aircraft* frames. The baseline was a turbofan kerosene-burning configuration, and the alternatives included hybrid and fully electric fuel-cell configurations. Results indicated that the most viable solution for the near future would be a change to a LH₂ turbofan powerplant, which proved to have a lower take-off weight and reduced NO_x emissions. The results regarding the LH₂ powered airplane (see Figure 2-10) are in agreement with another very recent study by the University of Sydney on the feasibility of long-range hydrogen-powered aircraft [75]. A hybrid solution on the other hand was deemed *not viable* by NASA, as it would still require most of the technology weight reductions that a fully electric fuel-cell aircraft would require.

N3-X Hybrid Wing Body Turboelectric Concept, NASA

In order to meet NASA's 2030 goals for propulsive efficiency and noise, a turboelectric aircraft concept is proposed based on the Boeing N2 Hybrid-Wing-Body design [22]. These goals dictate a 60% reduction on energy consumption from the current generation aircraft.

The powertrain consists of two wing-tip-mounted turboshaft engines powering two 40MW superconducting generators. The aircraft is propelled by 14 fans mounted on the rear of the fuselage (see Figure 2-11), each powered by a 5,8MW superconducting motor. All machines are driven by cryogenic-temperature non-superconducting converters. The power is transferred through a superconducting grid. The turboshafts are either powered by LH₂, first used to cool the superconducting parts, or by jet fuel or liquid methane. In the latter two scenarios, cryocoolers would be used to keep all parts at cryogenic temperatures, where superconductivity is possible.

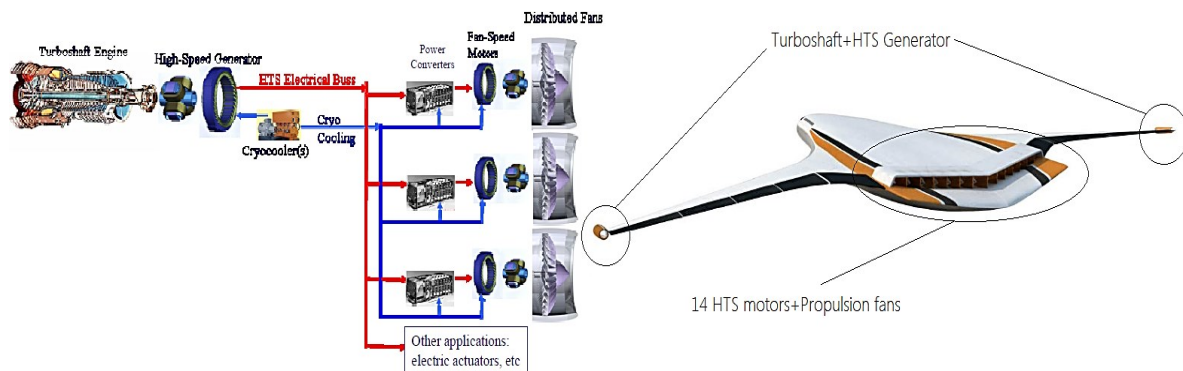


Figure 2-11: Turboelectric propulsion system (left), and outside view of the N3-X hybrid wing body (right) [22]

Some of the advantages this system offers are fuel save, lower noise, optimal rpm and maximum efficiency for all components. A first estimate indicated that the system would be more efficient than a mechanically-gearred concept, with an efficiency of 99.8% using LH₂ as fuel. In a later study, a more in-depth analysis of weights and efficiencies was conducted considering the technology improvements that took place in the meantime [76]. Results indicated slightly higher motor weights, but significantly lower cryocooler weight and constant system efficiency. Compared to a conventional powertrain, fuel savings were estimated between 8.5% and 10% before optimization.

Hybrid-Electric Propulsion for Aircraft, University of Cambridge

This research includes the design and sizing process of a parallel hybrid propulsion system for a small aircraft demonstrator. The results are then scaled down to a small size UAV and up to an intercity airliner [20]. Instead of focusing on full serial hybrid systems, it examines the application of a parallel system that assists the internal combustion engine during take-off and cruise phases, and regenerates energy during the landing phase. The serial configuration was considered too heavy, since it needs a motor and a generator of higher power rating. A SOUL SDR microlight aircraft with an engine power of 15kW was used. The piston motor was then replaced with a 7.5kW internal combustion engine, and a 12kW 2.8kg BLDC electric motor. The added weight of the hybrid system with the required fuel

was 11kg more than the standard TOW of 113kg. A number of simulations conducted for different flight scenarios, using experimental data obtained from engine and motor testing, indicated fuel savings from 12% to 30% depending on speed and battery charge.

An interesting part of this study was the up-scaling of the base system described up to an intercity airliner, e.g. a Boeing 737-800. Assuming an annual 5.5% increase in battery energy density, and an electric motor power density of 4.6kW/kg, such a step is considered viable in the year 2038. The power savings were estimated to be around 10% for a total installed electric motor power of 4MW.

Small Plane Electrical Drivetrain, Brno University of Technology

One of the most recently published studies describes the basic drivetrain components of the all-electric aircraft and the interaction between them [77]. The suggested aircraft is a typical setup consisting of a battery pack of lithium-ion batteries, a 3-phase direct-drive 10-pole permanent magnet motor and a DC-AC converter. The whole system is controlled by a main computer that gathers data from all battery cells, converter and power system. This computer further controls DC-bus voltage, battery operation and converter operation.

The main purpose of the study was not only to design a simple all-electric drivetrain, but to also analyze the potential faults that may occur along with their consequences and possible solutions in the framework of electric flight. The result was a drivetrain with a combination of software and hardware protections, instead of duplicate parts for redundancy and safety. The main failure modes are summarized in Table 2-1, together with possible causes, consequences and solutions. The importance of such research lies in the study of reliability of electrical aircraft propulsion systems, when the level of electrification becomes dominant (higher than 50%).

Table 2-1: Possible failures and causes, effects and solutions

<i>Failure</i>	<i>Possible cause</i>	<i>Consequences / Possible solution</i>
Motor overheating	Prolonged overloaded operation, extreme climatic conditions	Motor output power automatically decreased, signal sent to the pilot / Motor service recommended
DC/AC inverter overheating	Cooling fan failure / fan control failure while taxiing	Drivetrain switched off, crew informed / Fan replacement
Battery cell overheating	Battery cell damage	Total battery capacity decrease / Cell replacement
Activation of battery emergency protection	Excessively deep discharge of battery, battery monitoring circuit failure	Aircraft drivetrain immediate power down / Battery monitoring circuits verification
Auxiliary source / monitoring computer / monitor panel failure	Hardware failure, cable lead failure	Short standard flight continuation possible / Cables, monitoring computer, onboard monitor panel replacement.
Main computer failure	Hardware failure, cable lead failure	Drivetrain stopped and battery disconnected / Cables, main computer replacement
DC/AC inverter failure	Hardware failure, cable lead failure (short circuit, break)	Drivetrain stopped / Repair required

2.3.2 Rotary-Wing-Oriented Studies

Alternative Propulsion Systems in Conventional Helicopters, University of Southampton

A similar study as [77] was conducted in [11] on the capability of conventional helicopters to adapt more electric and alternative transmission technologies. In all the configurations examined, it was assumed that the main rotor was driven by a turboshaft engine powered either by kerosene or LH₂. The tail rotor on the other hand was either coupled mechanically to the main engine through a gearbox, or it was moved by a superconducting or conventional SR electric motor powered by a superconducting generator. All the combinations were evaluated according to the ratio of useful load to gross weight.

The results indicated that only the combination of turboshaft with worm gearbox and kerosene was more efficient than the conventional kerosene one. The best hybrid combination was a kerosene-powered hybrid drive with cryocoolers for the superconducting generator and tail rotor drive. It should be however noted that no combination assumed full electric direct-drive propulsion or alternative ICEs, e.g. Diesel.

Requirements for Hydrogen All-Electric Rotorcraft, NASA Ames Research Center

This study [19] focused on the feasibility of substituting the 100kW piston combustion powertrain of a small 650kg helicopter, with a fully electric one powered by either a fuel cell, a battery or a combination of the two. The best currently available technologies in the fields of fuel cells, lithium-ion batteries and electric motors were considered to synthesize the power plants. The study concluded that the specific power of the powertrain would be at the levels of 1950's piston engines. Fuel efficiency would, on the other hand, be almost twice of piston engines. Of the 3 examined options, the best results were achieved with the fuel-cell-battery hybrid combination.

An important barrier that was identified is the low gravimetric torque density of available electrical machines, which makes them unattractive for rotorcraft applications. An order of magnitude higher gravimetric torque density is required compared to the most demanding applications of the automotive world. Novel direct-drive machines were finally suggested as a possible solution to bypass this issue.

2.4 The Idea of a Hybrid Helicopter

Some of the disadvantages of a helicopter's conventional propulsion system have been briefly discussed: poor thermal efficiency of gas turbines, and gearbox mechanisms that decrease reliability and increase maintenance costs. Others have not been addressed yet:

- Low drivetrain efficiency
- Low design flexibility (due to rigid mechanical linkage between moving parts)
- Twice the required power installed for redundancy (leading to partial loading)

All these issues become secondary next to the low-weight advantage of the overall system. To increase overall system efficiency the sole use of piston engines can be considered, which have been well established as helicopter drive systems over a long period of time.

They are however restricted to low and moderate TOWs ($< 2t$). As mentioned before, for larger helicopters piston engines become a more unlikely solution due to:

- **Large volume and weight needed:** difficult integration of a single bulky engine in the fuselage due to the rigid link between motor and gearbox
- **Gearbox and engine location constrained to main rotor immediate vicinity:** large system changes require high development and integration efforts

Also, a full electrical drivetrain, as proposed by Sikorsky (see 2.2.6), shows a high efficiency at the cost of very limited payload and flight autonomy. Although energy storage technology is a quick developing field, it is not yet mature enough for practical full electric flight. However, the possibility to save fuel and achieve a more-electric helicopter can lay in a hybrid drivetrain using diesel engines. Reduced electrical energy storage is used to guarantee fail-safe power in case of a complete engine failure, and to provide boosting capabilities for sudden maneuvers. The inclusion of electric flight features requires redesign effort, without the possibility of simply retrofitting the present drivetrain. For example, for the mild hybrid presented in 2.2.5 the pre-existing drivetrain is still used to develop an intermediate product [78].

Using standard off-the-shelf components for this concept proves insufficient for meeting the required performance, mass, and volume requirements [21]. A custom solution is necessary, and at first glance most of the development must concentrate on two main areas:

- **Drivetrain:** emphasis on the use of power-dense ICEs and electrical machines
- **Energy Storage:** emphasis on high specific power *and* energy batteries

The main goal of the concept is therefore to develop the technologies required to replace the conventional helicopter drivetrain with a hybrid drivetrain. A detailed description of the drivetrain type and component equivalence between both systems is presented below.

2.4.1 Hybrid Aircraft Concept

Definition

Depending on the level of hybridization, a hybrid drivetrain is classified in three different types. This is a crucial aspect for the overall architecture, since the higher the degree of electrification, the bulkier and heavier the battery pack must be. Table 2-2 presents an overview of the hybridization degree.

Table 2-2: Hybrid systems classification according to degree of hybridization

<i>Type</i>	<i>Main application</i>
Micro hybrid	Mainly start-stop systems for automatic shut down and restart of internal combustion engines during idling
Mild hybrid	Typically parallel systems to combustion engines with start-stop, modest levels of engine assist or energy-regeneration features. Generally unable to provide all-electric propulsion
Full hybrid	Systems capable of all-electric, all-engine operation or a combination of both. Electric vehicle, cruise, over-boost and battery-charge operational modes are possible

A hybrid helicopter with a drivetrain capable of all-electric-, all-engine-flight, or a combination of the two, automatically falls in the category of “Full hybrid”. Within this category, a further distinction according to the division of the power sources is given:

- **Full-parallel hybrid:** ICE and electrical motor coupled in parallel at some mechanical axis. Propulsion power comes mainly from the ICE while the remaining reserve/boost comes directly from the electrical machine.
- **Full-serial hybrid:** Mechanical power delivered by the ICE is converted to electrical power, and either stored in batteries, or fed to the propelling electrical motors. Stored battery power provides the reserve/boost power.

Full-parallel hybrid architecture is not further considered due to the mechanical linkage required, leaving the “Full-serial hybrid” as the intended system for the hybrid helicopter. The combination Diesel-engine/electrical-generator/power-electronics is dubbed a Generator Set or GenSet. Assuming the main rotor requires P kilowatts of nominal power and n GenSets are used, each GenSet must provide a nominal power between 100% and 125% of P/n . The discretization of the power generation through the use of GenSets is an important feature of the concept. It provides design flexibility, easier upgrading and flexible weight distribution. Electrical power not stored in batteries is fed to power converters that drive the electrical machines in the main and tail rotors (see Figure 2-12).

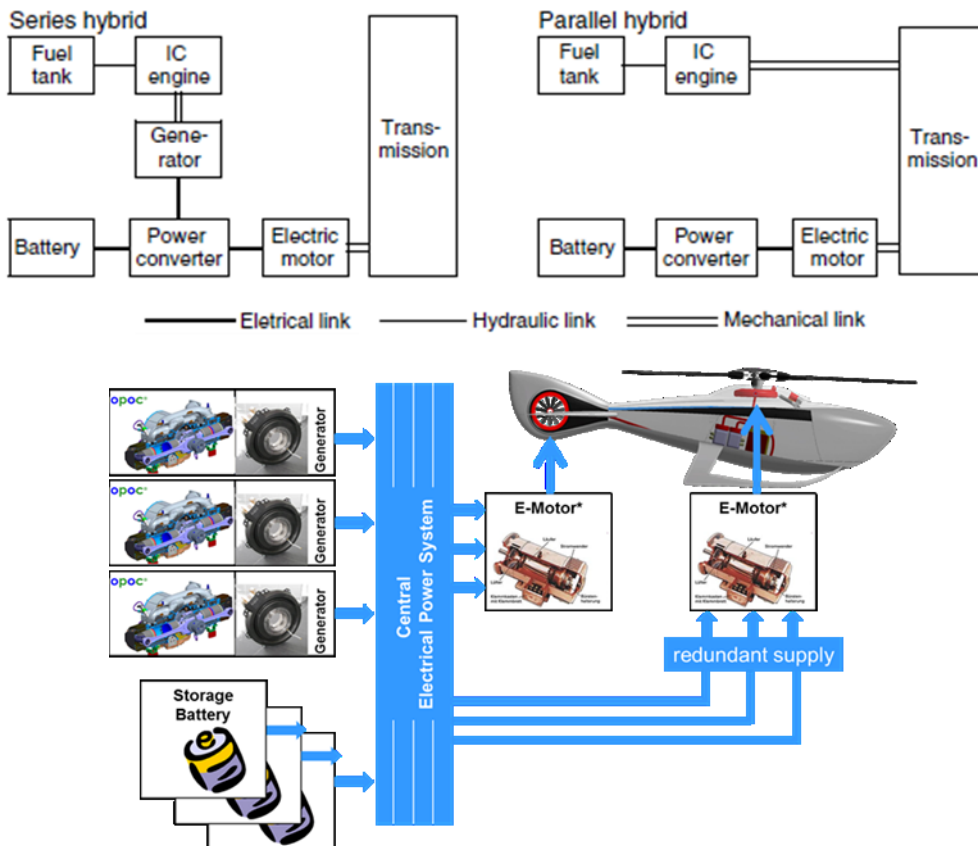


Figure 2-12: Full-serial hybrid and full-parallel hybrid architectures [78] (top) and hybrid helicopter full-serial hybrid system architecture (bottom)

Conventional Drivetrain vs. Hybrid Drivetrain

A next step in the concept definition is to identify the main components of a conventional drivetrain. Afterwards the analogy to the components in a hybrid drivetrain is made. This sets the base to perform a mass balance between the two alternatives.

Table 2-3: Conventional drive components vs. hybrid drive components

<i>Conventional Drivetrain</i>	<i>Full-Serial Hybrid Drivetrain</i>
Main gearbox Tail rotor drivetrain	Electrical network Power electronics
Fuel space	Battery
Turbines	Diesel engines Main rotor electrical machine Tail rotor electrical machine

The disadvantages of increased amount of components and weight in the hybrid drivetrain can be outweighed by its advantages:

- **Optimum main rotor speed:** electrical main rotor drive allows reduced and optimum power requirement and an adaptable noise profile
- **Reduced fuel burn and emissions:** high-performance turbo-charged Diesel engines operating at their “sweet spot” can require up to 40% less fuel
- **Power boost, partial-electric take-off and landing possible:** increased performance during transient maneuvers and quieter flight phases
- **Configuration and design flexibility:** non-mechanical non-rigid electrical links between components allow a better aircraft weight distribution
- **Improved aerodynamic:** adjustable position of electrical main rotor with respect to fuselage, since there is no mechanical connection to other components, results in optimum alignment with airstream
- **Flight-phase-dependent operation of electrical tail rotor drive:** complete or partial stopping of the electrically driven tail rotor during cruise flight. Tail rotor would be operational strictly during take-off, landing and hovering.

The lower Diesel fuel burn is especially valuable for missions of uncertain duration where a reserve must be available (law enforcement, rescue). Additionally, Diesel engines offer a better efficiency than gas turbines even in hot and high altitude conditions.

2.4.2 Requirement Definition

The target aircraft for which the full serial hybrid architecture is defined, is a **civilian helicopter of the EC135 class. It has a payload of 7 to 8 persons (including flight crew), an empty weight of 1.5t, and a maximum take-off weight (MTOW) of 3t.** This section presents a set of performance requirements and physical constraints that define the operational envelope of the aircraft’s main rotor drive.

Performance

For the feasibility assessment of electrical machines for the main rotor drive, its power, torque and speed requirements have to be defined. They depend on specific vehicle design parameters and mission profile, but for the EC135 class a **base nominal power of 600kW** can be defined. This is based on a fuel tank weight of ca. 480kg, 700km flight autonomy or 2.5 hours flight at 83% MTOW [17].

For the time being different scenarios with operation at different rotational speeds are not examined. As a requirement a mean value of **350rpm** is taken. Since the objective is to replace a gas turbine, power requirements for take-off and transient maneuvers can be defined from the technical data of the EC135 [79]. Regardless of twin or single engine operation, 110% of the nominal power is required for aircraft take-off during 5 minutes [80]. For transient maneuvers 115% of the nominal power is required for a period of 30 seconds. The resulting power and torque ratings are summarized in Table 2-4.

Table 2-4: Main rotor drive power and torque requirements

<i>Flight Phase/Maneuver</i>	<i>Power (pu)</i>	<i>Power (kW)</i>	<i>Torque (kNm)</i>
Maximum Continuous Power (Nominal operation)	1.00	600	16.4
Take-Off maneuver Power (5 Min.)	1.10	660	18.0
Transient Maneuver Power (30 Sec.)	1.15	690	18.8

Weight & Volume

Regarding the mechanical constraints, an approximate weight and physical dimensions are also defined. For the calculation of the weight requirement, a mass balance of conventional vs. hybrid drivetrain is made (See Table 2-5).

Table 2-5: Conventional drivetrain weight distribution [17]

<i>Component</i>	<i>Weight (kg)</i>
Engines, Gearbox, Tail Rotor Drivetrain	450
2 Starter/Generator, Power Box, Battery	90
Fuel weight (from 45% fuel burn reduction)	270
Total Weight available for Hybrid drivetrain	750

With some assumptions about the weight of other drivetrain components, the available mass for the main electrical motor is estimated according to [16] and [17]. For electrical power storage, electrical network and ICEs, the weight is approximated as follows:

- ICEs expected power density: ca. 2kW/kg ➔ $m_{\text{tot,diesel}} \approx 350\text{kg}$
- Battery energy density: ca. 400Wh/kg ➔ $m_{\text{tot,batt}} \approx 100\text{kg}$
 Battery power density: ca. 2kW/kg
- High voltage system / Power electronics ➔ $m_{\text{tot,misc}} \approx 100\text{kg}$

The remaining 200kg are intended for electrical machines, from which 75% is allocated to the main rotor exclusively, and the remaining 25% to the tail rotor (not object of this

investigation) [17]. Finally, the maximum physical dimensions allowed for the active region of the machine are given. These complete the physical envelope specification:

Table 2-6: Maximum machine dimensions and weight

<i>Parameter</i>	<i>Value</i>
Weight (kg)	150
Diameter (mm)	1400
Axial length (mm)	250

With these specifications, performance-to-weight and performance-to-volume ratios are calculated for the main rotor machine under nominal operating conditions. These are used as key performance indicators for the later assessment of electrical machine topologies. They are listed together with additional mechanical and cooling requirements in Table 2-7.

Table 2-7: Main rotor electrical machine final requirements

<i>Parameter</i>	<i>Value</i>
Gravimetric Power Density (kW/kg)	4
Gravimetric Torque Density (Nm/kg)	110
Volumetric Torque Density (kNm/m ³)	43
Gearbox gear ratio	1 (Direct-drive)
Cooling type	Air-cooled
Efficiency	> 95%

2.4.3 Volumetric Torque Density and Shear Stress as Figures of Merit

Contrary to automotive applications, volumetric power density and volumetric torque density are secondary for an electrical machine designed for aerospace applications. For automotive vehicles, the higher the electrical machine weight, the higher the energy loss from rolling resistance. In stand still there is however no other disadvantage than the reduced loading capacity. A hovering helicopter, the analogy of a car in standstill, requires constant use of energy to keep its mass in the air. Any additional weight increases the energy needed per unit time to maintain that mass airborne. Due to this, the aircraft's low mass is of utter importance, with the volume playing a minor role. This is opposed to ground vehicles, where the compactness has a higher priority.

Depending on the application (low- or high-speed), it is also important to make a distinction between gravimetric torque density and gravimetric power density. For a low-speed application such as the one at hand, the gravimetric torque density is more relevant. Most of the power will be achieved through the developed torque. Therefore, a candidate machine should be evaluated using an indicator that relates directly to the machine's torque capability. It is not common to find values for the gravimetric torque density of electrical machines in literature, and only limited references address such comparison. Since different machines are constructed in different ways, with different number of phases and slot/pole combinations, etc., their final gravimetric torque density can vary greatly. Therefore, it is not a suitable indicator for an initial assessment.

On the other hand, the rotor volume is directly proportional to the torque capability. Based on [81], for most machine designs the following is a reasonable assumption, when the pole number is high (> 10) and the windings are concentrated or nearly concentrated:

$$0.65 < SR < 0.7 \quad (2-1)$$

where SR is the split ratio or ratio of rotor radius to stator radius. The total machine volume is then roughly twice the rotor volume, which results in proportionality of the total volume to the torque rating. Under the assumption of (2-1), the volumetric torque density is a valid performance indicator that is characteristic of a machine topology. As an indicator, **volumetric torque density** is often encountered in literature: from the reviews presented in [82] and [41] an **average of 40kNm/m³ can be identified for PM machines**, a value very close to the required for the target application. Additionally, a more absolute performance measure of different machine types is the **airgap shear stress**. This is a well-studied parameter in literature, and although values still vary somewhat from topology to topology, an **average of 40kPa for PM machines** can be assumed as specified in [83].

These values of volumetric torque density and airgap shear stress are used as the state of the art of electrical machines. They help setting the context for the formulation of the research question of this thesis.

2.5 Chapter Summary

The goals defined in Clean Sky JTI were proposed with the objective of motivating research towards the use of cleaner technologies for aviation. In this chapter, they have been broken down to a level, at which their feasibility can be concretely evaluated. The resulting assessment indicates very ambitious goals and, as a consequence, the need for technological breakthrough in different areas.

Cleaner aircraft propulsion is one of those areas where major breakthrough is needed. In this regard, several demonstrators have been already developed and tested, most of them solely for research purposes. The ultimate motivation however, is to achieve the commercialization of such aircraft. Current demonstrators use iron-based permanent magnet machines, while future studies focus mostly on the potential use of superconducting machines. From the current demonstrators, only aircraft with low MTOWs ($< 1.5t$) are in place, and only for general aviation with a focus on fixed-wing aircraft. These use without exceptions electrical motors with rotational speeds above 1000rpm. This allows for a high gravimetric power density, even if the gravimetric torque density is not higher than 20Nm/kg, as is shown in Figure 2-13.

Only one relevant rotary-wing aircraft demonstrator, the Sikorsky Firefly, could be identified (All-Electrical with low MTOW, payload and flight autonomy). Its characteristics permit highlighting a key point directly related to the hybrid helicopter concept: Implementing a serial hybrid drivetrain is a reasonable intermediate step. For the time being All-Electrical flight is still not viable due to insufficient energy density of the different battery technologies. When comparing a conventional drivetrain with the proposed architecture, the main advantage in efficiency of the latter arises mainly from the lower Diesel fuel burn. Additionally, architectural flexibility resulting from the absence of

rigid mechanical links between components makes optimal operation of the different parts possible. Nevertheless, considerable losses (ca. 10%) still arise from the mechanical-electrical-mechanical energy conversion [16].

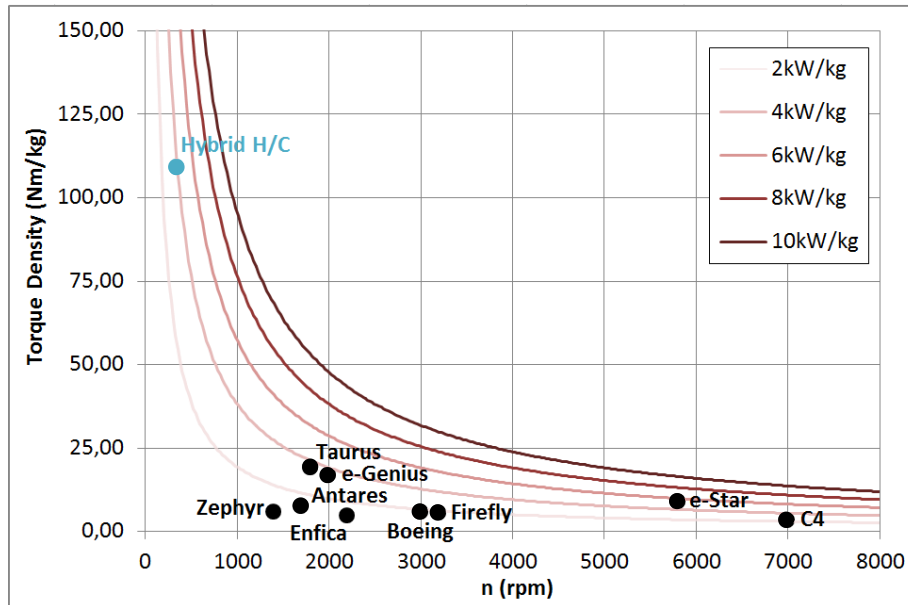


Figure 2-13: Gravimetric torque and power density as function of rotational speed for the different aircraft reviewed in 2.2 and for the hybrid helicopter defined in 2.4

In the last part of the chapter, key requirements were given for the main rotor drive, allowing the comparison with the reviewed aircraft in 2.2 (see Figure 2-13). Although no application with such a high gravimetric torque density has been realized yet, the gravimetric power density is comparable to that of other demonstrators. This hints at the possibility, that such an electrical machine is still realizable with conventional electrical machine materials. Nevertheless, this question cannot be answered at this point, since a dedicated study and subsequent design have to be carried out first. The study takes the volumetric torque density and shear stress as initial assessment parameters, in order to analyze the torque capability of electrical machines.

Chapter 3

Current Technology Status

In the previous chapter, some examples of applications using electrical propulsion in light aircraft were presented, together with a detailed definition of the problem. Figure 2-13 suggests that a machine for the problem at hand is plausible, although no similar examples are encountered currently for aerospace applications. Because of this, this chapter goes deeper and into the basics of electrical machines with the purpose of approaching the problem from scratch. In order to consider as many incremental advantages as possible that could contribute to a successful design, a review of the state of the art is done in terms of:

- Materials used in the design of conventional iron-based machines
- Relevant design guidelines for aerospace-specific machines
- Electrical machine topologies and their performance

Consequently, some examples of aerospace-specific electrical machines intended for middle to high MTOWs are given, as these are the target segment. With this comprehensive overview, a starting point for the designs presented in the following chapters is defined. This starting point focuses on two aspects:

- Selection of machine topologies for further study
- Selection of radial or axial flux architecture as a design principle

3.1 Material Considerations for Aerospace Electrical Machine Designs

Three types of materials are mostly found in electrical machines: Magnetic, electrical and structural. For each type, options with different performance characteristics exist, along with the respective cost differentiation. The following is a review of these material types along with a summary of their most relevant properties. For the sake of simplicity only the properties related to their main function are mentioned, e.g. for magnetic material only magnetic properties, for structural materials only structural properties, etc.

3.1.1 Magnetic Materials

Their main function is of magnetic nature, i.e. to produce or guide magnetic flux. Of importance are properties like the magnetic permeability, coercivity, remanent flux density (for hard magnetic materials) and saturation flux density (for soft magnetic materials).

Hard Magnetic

Hard magnetic materials or permanent magnets have an impressed magnetic field, and act as sources of magnetic flux used for the machine excitation. The amount of flux produced depends on a number of factors:

- Permeance seen by the magnet
- Remanent or “short circuit” flux density
- Recoil permeability (close to that of air)
- Operating temperature.

Mainly two types of magnets are used in high performance applications due to their energy content and temperature sensitivity:

- **Neodymium Iron Boron alloys (NdFeB)**: characterized by a high remanent flux densities B_r (and high energy content or BH-product)
- **Samarium Cobalt alloys (SmCo)**: known for their low temperature sensitivity and high maximum operating temperatures.

Table 3-1: Magnet material main properties and typical values

<i>Material</i>	B_r (T)	<i>Max. Op. Temp.</i> (°C)	B_r <i>Temp. coeff.</i> (%/°C)	<i>Mass Density</i> (g/cm ³)
NdFeB	1.1 – 1.4	50 – 230	~ 0.1	~ 7.7
SmCo	0.9 – 1.1	250 – 350	~ 0.035	8.4

While NdFeB-magnets can reach the highest remanent flux density, this is only for magnet types with the lowest maximum operating temperatures. Also, with a temperature coefficient three times that of SmCo-magnets, the performance change with temperature is more pronounced. This makes a good temperature management of the magnets necessary.

NdFeB is 10% lighter than SmCo, and together with the high energy content, it makes a reasonable choice, if their temperature is regulated correctly. A reduced performance is also acceptable if the overall performance of the application is not affected considerably.

Soft Magnetic

Soft magnetic materials have a high permeability necessary to guide the magnetic flux without significant magnetomotive force absorption. This way the magnetomotive force can be focused at the airgap to produce a high flux density. This last feature is crucial to produce a high airgap shear stress. The amount of flux that can be carried is limited by the saturation flux density of the material. Consequently, the saturation flux density determines

the cross section needed to guide a certain amount of flux, which in turn determines the amount of material. Further properties describing loss behavior are dependent on the exact composition of the material and lamination thickness used.

Focusing on the saturation flux density, two material types come to mind:

- **Silicon steel (SiFe)**
- **Cobalt steel (CoFe)**

The use of the latter is established for aerospace applications. Figure 3-1 shows two typical magnetization curves where the advantage of cobalt steel can be appreciated.

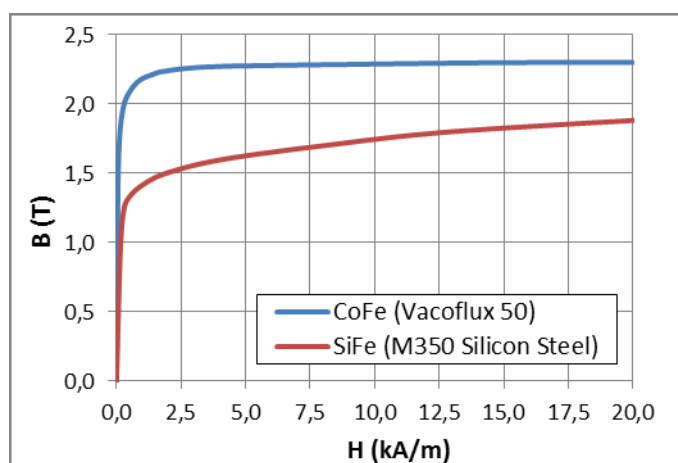


Figure 3-1: Typical DC magnetization curves for cobalt and silicon steels

With 30% more saturation flux density in average, cobalt steel allows the construction of lighter machines, albeit at a higher cost. With a 4% higher mass density, the overall weight advantage for a machine with similar design comes down to 25%.

Table 3-2: Core material main properties and typical values

<i>Material</i>	<i>B_{sat}</i> <i>(T)</i>	<i>Mass Density</i> <i>(g/cm³)</i>
SiFe	1.6 – 1.8	7.8
CoFe	2.25 – 2.35	8.12

3.1.2 Electrical Materials

These materials are used for winding construction. They carry the electrical current, therefore generating losses. The volumetric rate of loss generation is defined as the resistivity times the square of the current density flowing through it. This resistivity is low but finite, and increases along with operating temperature, further increasing the losses.

In this aspect, copper is overwhelmingly the most popular material and the only practical choice for the majority of cases. However, it does not have good aging and mechanical properties, but it does have a high mass density. Due to this, aluminum is also considered here, since it is already used in aerospace as a wiring solution in aircraft. On the downside,

aluminum has a higher resistivity than copper, which is compensated to a degree by its much lower mass density. A summary of material properties is presented below:

Table 3-3: Conductor material main properties and typical values

<i>Material</i>	<i>Resistivity at 20°C (Ωmm)</i>	<i>Resistivity Temp. Coeff. ($^{\circ}\text{C}^{-1}$)</i>	<i>Max. Op. Temp. ($^{\circ}\text{C}$)</i>	<i>Mass Density (g/cm^3)</i>
Copper	1.68×10^{-5}	0.003862	180	8.9
Aluminum	2.82×10^{-5}	0.0039	500	2.7

From Table 3-3, aluminum has 67% higher resistivity than copper at one third of the mass density, plus a much higher maximum operating temperature. An anodized aluminum winding built with the same resistance as a copper winding, weighs only half as much. Furthermore, despite the higher loss, they are easier to cool due to their higher heat capacity and higher thermal conductivity of the anodization [84]. Due to these reasons, aluminum windings are considered as a possibility as well as copper windings.

3.1.3 Structural Materials

Given the mass and torque requirements, the design of the structural support for the active mass is an important point. The expected loads, in particular the normal forces between rotor and stator, require a stiff support to avoid deformation and deflection of the active parts. The mechanical stress that a statically loaded structure can withstand without presenting irreversible plastic deformation is determined by the tensile yield strength. Additionally, the mechanical stress at which structural failure can be expected is given by the ultimate tensile strength *UTS*. Alternatively, under cyclic load conditions, e.g. pulsating forces, the stress limit is determined by a *suggested* endurance limit. This is the stress limit under which, there is a 50% probability of fatigue related failure [85, 86]. The endurance limit is defined as a percentage of the ultimate strength. Such percentage is always less than the material's yield strength.

Furthermore, an important property is the Young's modulus or modulus of elasticity. It characterizes the amount of deformation a material undergoes when stressed, and determines the stiffness of a structure: the higher the value of the Young's modulus, the stiffer the structure and the lesser the material deformation. These properties are summarized in Table 3-4 for the most relevant alloys. It is expected that the presented designs undergo cyclic loading, making them susceptible to fatigue. Therefore, the tensile yield strength is not presented since it always has a higher value than fatigue limits.

The strongest and stiffest materials, i.e. the ones with the highest ultimate tensile strengths and elasticity modules, also tend to be the densest ones. Exceptions in this sense are beryllium alloys (very stiff but moderately strong) and titanium (as strong as stainless steel but with half the mass density). For aerospace applications, the materials normally used have a high strength-to-mass density ratio. This feature is a determinant factor more important than costs of raw material and manufacture. This is in contrast to traditional electrical machine applications: the choice of stainless steels, or similar, results in lower costs at the expense of higher weight. Given the secondary role of the capital expenditure,

materials can be selected, which would otherwise not be considered in electrical machine design.

Table 3-4: Structural material main properties and typical values [87, 88]

<i>Alloy Type</i>	<i>Young's Modulus (GPa)</i>	<i>UTS (MPa)</i>	<i>Endurance Limit (% of UTS)</i>	<i>Mass Density (g/cm³)</i>	<i>Th. Expansion Coeff. (10⁻⁶/K)</i>
Aluminum	~70	150 – 420	0.5 ^{*1}	~2.7	23.1
Titanium	100 – 115	900 – 1000	0,4	~4.5	8.6
Beryllium	~200	200 – 400	0.5 ^{*1}	~2.2	13.2
St. Steel	190 – 210	500 – 1500	0.5	~8.0	16

^{*1} For these materials no endurance limit exists. Instead, a fatigue stress is defined at which failure occurs after a pretested number of cycles, usually 10^7

3.2 Fault Tolerance Considerations for Aerospace Electrical Machine Designs

Apart from the figures of merit discussed in 2.4.3, a further aspect is also of high relevance: fault tolerance. This is crucial in all propulsion and actuation components found in aircraft. Systems must not only be reliable, but must also withstand faults and continue to operate with reduced capabilities at least. Achieving a high level of reliability in aerospace applications is very challenging, since the performance must be kept high and the weight low at the same time.

In order to make a design fault tolerant, the causes of faults and their consequences need to be known first. Identifying possible failure scenarios of an electrical drive is the first step in designing a fault tolerant electrical propulsion system. According to [89] the main *electromagnetic* faults that may occur within an electrical machine are the following:

- Winding open circuit
- Winding short circuit (phase to ground or phase to phase)
- Winding short circuit at the terminals
- Power device open circuit
- Power device short circuit
- DC link capacitor failure

A successful handling of the above failures can be achieved by making provisions for those scenarios through the following derived requirements:

- **Electrical isolation between phases (at power electronics level):**
 - Independent converters per phase
 - Two or more converters per phase
 - Twice the number of switches needed

- **Fault current limiting:**
 - Low per unit inductance to allow high fault currents. This causes open circuit due to subsequent heating
 - 1pu d-axis inductance to limit the fault current to the nominal current. Subsequent operation is safe from the thermal point of view
- **Magnetic isolation between phases:**
 - One-layer concentrated windings to prevent flux linkage between faulted and healthy phases. Linkage would hinder control of the healthy windings
- **Thermal isolation between phases:**
 - One-layer concentrated windings to prevent overheating of healthy windings placed adjacently
- **Electrical isolation between phases (at winding level):**
 - One- or two-layer concentrated windings to prevent a phase-to-phase fault
- **Number of phases/machine modules:**
 - High number of phases or machine modules to avoid less overrating per phase. This helps maintain rated performance during faults

Statistical data for machine failures is unfortunately relatively hard to find. This is true especially in areas such as aerospace, where the use of electrical machines for actuation and propulsion is a relatively recent trend. According to a survey conducted for electrical machines in the petrochemical industry [90] (oil rigs, refineries etc.), the main cause of failure was bearing failure. Other frequent causes were insulation failure in the windings, overheating, and failure of external devices such as the power electronic converter. Although the study is focusing on induction machines, the findings indicate that reliability of the mechanical structures and bearings can be of equal importance to electromagnetic reliability (See Figure 3-2).

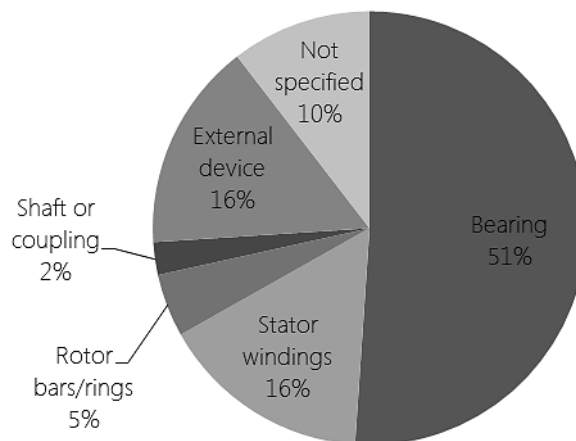


Figure 3-2: Statistical data for electrical machine failure in the petrochemical industry, data from [90]

3.3 Conventional Electrical Machine Architectures

Having reviewed the materials used in electrical machines and the guidelines to build them, the attention is now turned to the actual machine types. In the following subsections a brief performance review of the most important types is presented: switched reluctance machines, induction machines and permanent magnet machines.

3.3.1 Induction Machines (IM)

Induction machines have been used in a variety of applications over the years, ranging from industrial to automotive, with a number of studies conducted for potential aerospace applications [91, 92, 93, 94]. Apart from the torque density, that is usually lower compared to PM machines [24, 95], another issue arises from the inability to sustain a short-circuit fault. A property summary in different areas of interest is presented in Table 3-5. The lower torque density, efficiency and fault tolerance compared with its competitors make it an unattractive alternative for electric helicopter propulsion.

3.3.2 Switched Reluctance Machines (SRM)

Very simple in their construction, the main advantages of the SRM are robustness, low cost and inherent fault tolerance due to the lack of magnets. This results in the absence of an excitation field and a very low mutual inductance between phases [96]. In the case of a short circuit, no currents are induced, as there is no induced voltage in the faulted winding. Additionally, in terms of converter topology, SRMs require very simple power electronics.

SRMs have been suggested as alternatives to PM drives in electric vehicles [97, 98] but have not been adopted in production up to this time. Most designs are usually focused on high-speed applications. Little literature is available on high-power direct-drive applications, where PM drives are the standard [99]. In terms of torque density, the SRM is considered inferior to PM machines, which can offer higher volumetric torque densities with the same cooling effort [96, 100] (see Table 3-5).

3.3.3 Permanent Magnet (PM) Machines

Given the inferior performance achieved by SRMs and IMs, the focus is put predominantly on the PM machines, from which some topologies are addressed. Their operation is based on the interaction between the excitation and armature magnetic fields. Traditionally, the AC armature field is produced by a winding placed on the stator, and the excitation field by permanent magnets placed in the rotor. Alternatively, armature and excitation circuits can be placed on rotor and stator respectively. In such case, AC current has to be fed to the rotor through slip rings, brushes or wireless power transmission. From this point on, and unless otherwise specified, it is assumed that the armature winding is placed on the stator and the permanent magnets are placed in the rotor. The excitation circuit in PM machines produces a magnetic field in the air-gap (see Figure 3-3). This field has either a sinusoidal or trapezoidal profile depending on magnet shape and positioning.

In order for the machine to operate, a rotating magnetic field is created by the stator winding. This is a poly-phase winding (usually 3-phase) with the phases spatially displaced

from one another. Due to the spatial displacement, a rotating magnetic field is created at the airgap when the windings are fed with symmetric sinusoidal currents, which are also temporally displaced. This rotating magnetic field is of alternating nature, with the same number of poles as the rotor. Therefore, the two magnetic fields of rotor and stator tend to align, thus developing torque needed. The electromagnetic torque depends on the intensity of both fields and the angle between them, which is controlled by the magnitude of the d - and q -currents. The torque produced by a permanent magnet machine is given as [101]:

$$T_e = \frac{1}{2\sqrt{2}} \pi D_g^2 L B_{g1} k_w A_s \sin \delta \quad (3-1)$$

where:

- D_g : airgap diameter
- L : active length
- B_{g1} : Airgap fundamental peak flux density
- k_w : winding factor
- A_s : RMS linear current density
- δ : angle between the rotor and stator fields

From equation (3-1), the output torque is therefore proportional to the rotor volume, the winding factor, and the magnetic and electrical loading. The fundamental of the rotor field depends on permanent magnet type, geometric configuration, air-gap length and materials used on the stator and rotor. The linear current density reflects the magnitude of the electrical loading, and is usually limited by the thermal factors. In equation (3-1), the current loading *does not* include the winding factor as it usually does in literature. The reason for this is because in this study the current loading is also used as a thermal loading guideline. *The inclusion of the winding factor in A_s may lead to an underestimation of the thermal loading if the winding factor is too low.*

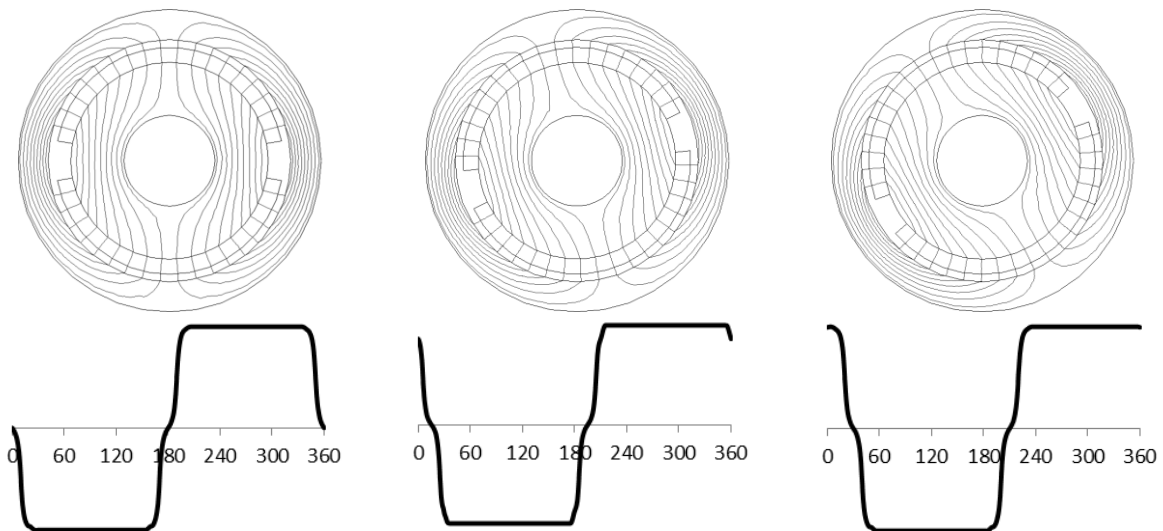


Figure 3-3: Surface permanent magnet rotor with non-slotted stator, in no-load conditions for 3 different positions 15° apart: magnetic flux lines (top), and flux density profile along airgap circumference (bottom)

Furthermore, equation (3-1) only gives the electromagnetic torque, which is maximized when the angle between both fields is 90 electrical degrees. At this angle the armature current is completely aligned with the q -axis in what is called i_q -control, i.e. i_d equals zero. This mode of operation is the one assumed from now on for the synchronous permanent magnet machines investigated here. The reluctance torque makes no contribution to the total torque. To summarize, Table 3-5 presents a comparison of the three main electrical motor technologies reviewed up to now.

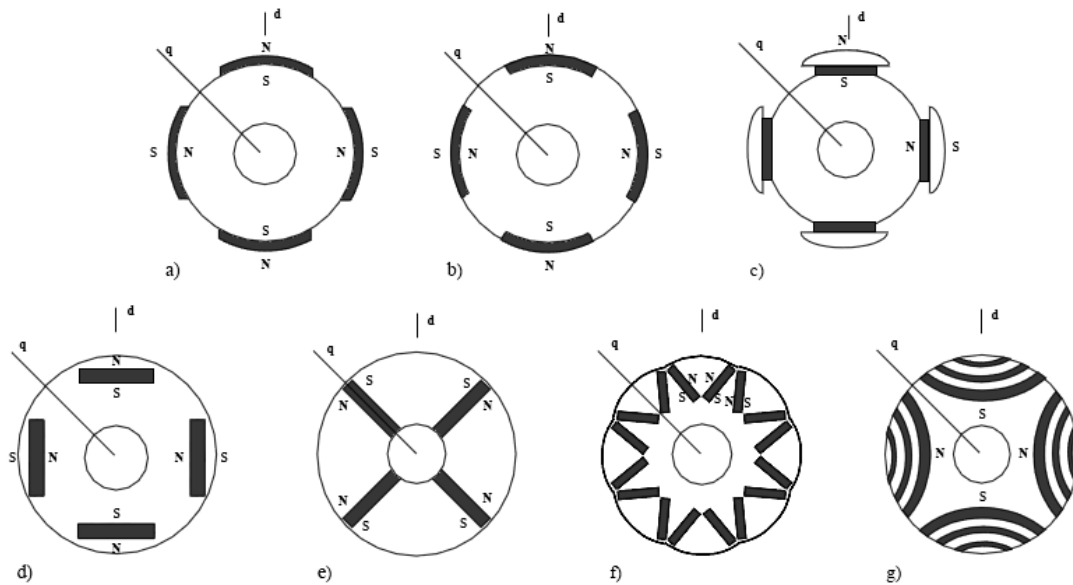


Figure 3-4: Different rotor types with: (a) surface mounted magnets, (b) inset surface magnets, (c) surface magnets and pole shoes, (d) embedded tangential magnets, (e) embedded radial magnets, (f) embedded V-shaped magnets with 1/cosine-shaped air-gap, (g) PM-assisted synchronous reluctance motor [102]

Table 3-5: Performance comparison of motor technologies adapted from [91]

<i>Performance/Feature</i>	<i>IM</i>	<i>SR</i>	<i>PM</i>
Fault tolerance	-	++	+
Power density	Moderate	Moderate	High
Robustness	Yes	Yes	No
Efficiency	Moderate	High	High
Cost	Low	Low	High
Wide speed range	No	Yes	Yes
Open loop control	Yes	No	No
Closed loop simplicity	Yes	Yes	Yes
Torque ripple	No	High	Low
Acoustic noise	No	Moderate	Low

Surface Permanent Magnet (SPM) Machines

Surface Permanent Magnet machines are probably the simplest type of PM machines. In them, magnet material is brought onto the rotor surface using glue. In some cases, a retaining can as a means of containment is used, if centrifugal forces are too high. Figure 3-4 a) depicts the rotor of an SPM machine, where the absence of reluctance torque is clear due to the same inductivity of the d - and q -axis ($L_d = L_q$).

For high performance operation, SPM machines with fractional slot concentrated windings (FSCW) are gaining importance with respect to machines with distributed windings. They allow a high torque and power density due to short end turns and a thin back-iron both in stator and rotor. Further advantages also include high efficiency, high slot fill factor, low cogging torque and fault tolerance [35]. Concentrated windings allow electrical isolation and. They potentially allow full magnetic and thermal isolation between phases, although at the expense of some torque capability [83, 103, 104, 105]. Also, enhanced controllability and segmentation of machine structures is possible. Due to these advantages, only SPM machines with fractional slot concentrated windings are considered from this point on for this study. Specifically machines for which:

$$|N_s - 2p| = 1 \text{ and } |N_s - 2p| = 2 \quad (3-2)$$

where N_s is the number of slots and p the number of pole-pairs. The reason for this selection is the maximization of flux-linkage and volumetric torque density. These conditions are achieved when the coil pitch is as close as possible to the pole pitch [106].

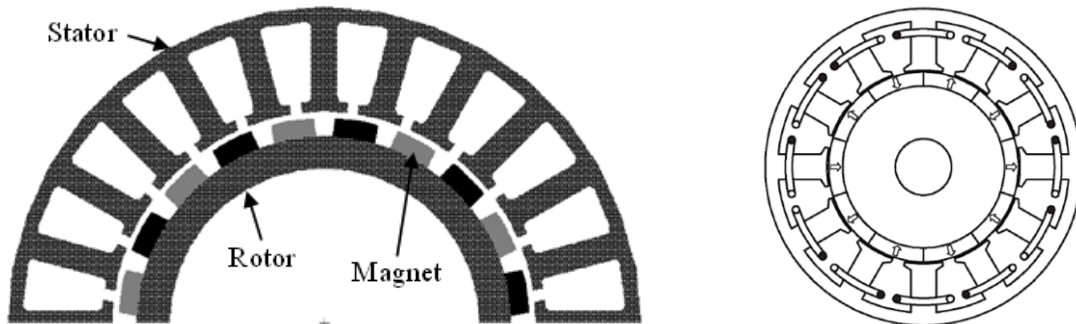


Figure 3-5: 24/20 [103] (left) and 12/10 [107] (right) slot/pole motor geometries

Regarding their performance, SPM machines are known to achieve different values of shear stress depending on the cooling type. The peak airgap flux density is usually around 0.9T, and the performance depends mostly on the current loading. Since SPM machines have a high electromagnetic airgap length, armature reaction is usually low and saturation becomes pronounced only at high current loading values. From literature, the following average performance values using standard materials were put together for the purpose of comparison [82, 41, 81, 83, 108, 109, 110]. These are to be revisited at the end of the chapter once other PM machine topologies are reviewed:

- Shear stress: 35-45kPa
- Volumetric torque density: 35-45kNm/m³ under the assumption of (2-1)

Flux Switching Permanent Magnet (FSPM) Machines

Flux-Switching Permanent Magnet machines belong to the topologies with permanent magnets on the stator. Unlike conventional PM machines, they produce both the armature and excitation field in the stator. The armature influences the flux distribution within the stator over electric cycle, so that shear stress is produced at the airgap. Shear stress is only produced in the vicinity of the stator poles with no contribution from the slot regions. Also, while the double saliency of the machine is responsible for torque generation, the torque is electromagnetic in nature with negligible reluctance torque, i.e. $L_d = L_q$.

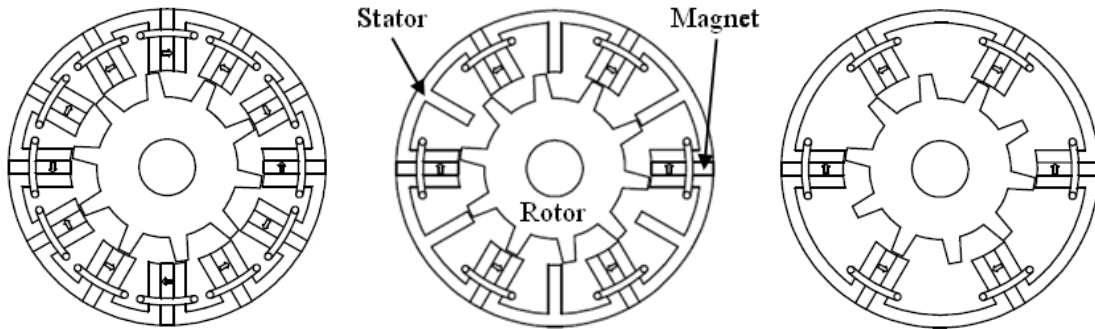


Figure 3-6: Conventional FSPM machines with all poles wound (left), E-core FSPM machine (center), and C-core FSPM machine (right) [111]

In Figure 3-6, some FSPM machine variations are shown: rotor and stator show resemblance to a SRM, with non-overlapping concentrated windings around each stator pole. In each stator pole a magnet is sandwiched between two U-, C- or E-shaped laminated segments, depending on the machine type. The magnetization direction is circumferential and alternates from one magnet to the next [112].

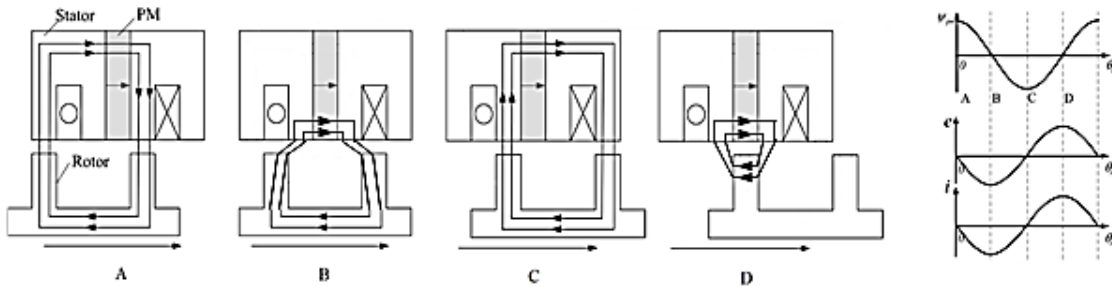


Figure 3-7: Flux linkage mechanism in a FSPM machine

With a sinusoidal back-EMF it's not necessary to skew or shape magnets or core material, which allows the use of conventional converters [113]. Nevertheless, the flux linkage of a single coil has a significant even-order harmonic content, due to asymmetry between positions d and $-d$ (positions A and C in Figure 3-7) and q and $-q$ (positions B and D in Figure 3-7). The sinusoidal back-EMF stems from the series connection of two coils electrically displaced from each other by 180 electrical degrees. This cancels out even-order harmonic components, especially the 2nd harmonic, resulting in a back-EMF with a low Total Harmonic Distortion (THD). From Figure 3-7, one rotor pole passing in front of

a stator pole results in one electrical period. Therefore, the rotor pole number in an FSPM machine is equal to the pole pair number in a conventional FSCW PM machine [114].

The placement of the magnets in the stator facilitates their temperature management, but makes them susceptible to magnet eddy current loss due to flux density excursions [111]. Regarding fault tolerance, the use of concentrated windings allows implementing the features explained in 3.2, e.g. inherent electrical isolation between phases. Magnetic and complete thermal isolation can be implemented in a conventional FSPM machine with alternate poles wound, or in E-core FSPM machines. Further guidelines for fault tolerance are given in [115], and fault behavior is also studied showing no considerable differences to conventional machines. In [116] it was shown that fault-tolerant alternate-pole-wound FSPM designs exhibit equally high output torque as designs without these features. This comes at the expense of increased torque ripple, which can be mitigated with a skewed or twisted rotor [117].

From a performance perspective, due to flux concentration at the stator poles, high airgap flux densities are achieved using traditional silicon steel [112]: about 1.8T in the d position, and as high as 2T at the tooth corners in the q position. Studies such as [118, 119, 120] suggest a superior performance of FSPM machines in comparison to SPM and IPM machines *under similar electrical loading conditions*. This results in a shear stress and torque density improvement of between 15% and 20%:

- Shear stress: 40-50kPa
- Volumetric torque density: 40-50kNm/m³ under the assumption of (2-1)

Depending on the FSPM machine, the amount of magnet material can be reduced by half also decreasing the overall weight (e.g. with C-core or E-core FSPM machines). The trade-off is the increased susceptibility to core material saturation: the number of turns per slot increases and so does the slot area, but at the expense of half the stator teeth. This implies higher flux density at the teeth at lower phase currents than for the conventional FSPMs.

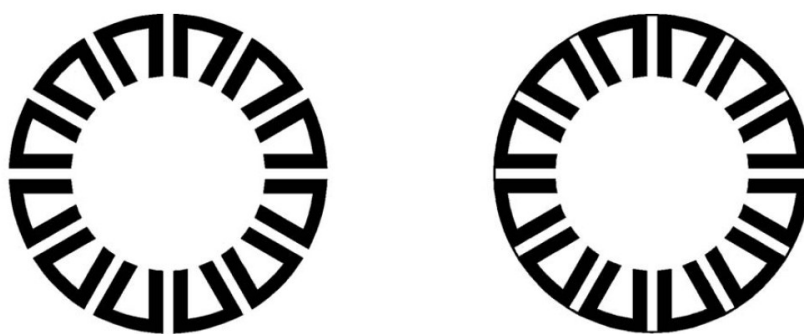


Figure 3-8: Core laminations for a conventional FSPM machine: Completely separated (left) and joint together by thin bridges (right) [107]

Finally, from a manufacturing and robustness perspective, FSPM machines have a very simple rotor that offers the same advantages of a SRM rotor: robustness and ease of manufacture. The stator is composed of single separate iron cores that can be manufactured separately, or in a single lamination to enhance stability and ease of assembly. In such a case, all cores are joined together through thin bridges (see Figure 3-8).

Magnetically-Geared Permanent Magnet (MGPM) Machines

One of the newest high-torque-density drives proposed is the MGPM machine. This novel design combines a magnetic gearbox [121] and a brushless PM machine in the same housing to achieve compactness and high torque density [122].

An MGPM machine consists of a typical 3-phase stator, and a high-speed PM rotor that form a traditional PM machine. The magnetic gearing is implemented by modulating the magnetic field through a low-speed rotor placed between the stator and the high-speed rotor. This low-speed rotor consists of an array of soft-magnetic bars. The modulated field couples with a second stationary magnet array located on the stator teeth. The field locking forces the movement of the secondary rotor, therefore producing torque.

An example of such a machine is presented in Figure 3-9. The 6-slot 3-phase stator has 21 magnet pole-pairs laid on its inner surface. The low-speed rotor consisting of 23 field-modulating soft magnetic bars is found afterwards. Finally, the high-speed rotor is a typical 4-pole SPM rotor. The design has been tested achieving a torque density of 60kNm/m^3 , with a current density lower than $2A_{\text{RMS}}/\text{mm}^2$ and natural cooling. In [123] the torque capabilities of inner stator and outer stator configurations are examined and compared with a typical FSCW PM configuration. The inner-stator topology displayed a torque density of 73kNm/m^3 , more than double the 30kNm/m^3 of the SPM machine used for comparison. Recent publications [124, 125] have presented an already tested axial flux generator and a motor with a volumetric torque density of 100kNm/m^3 .

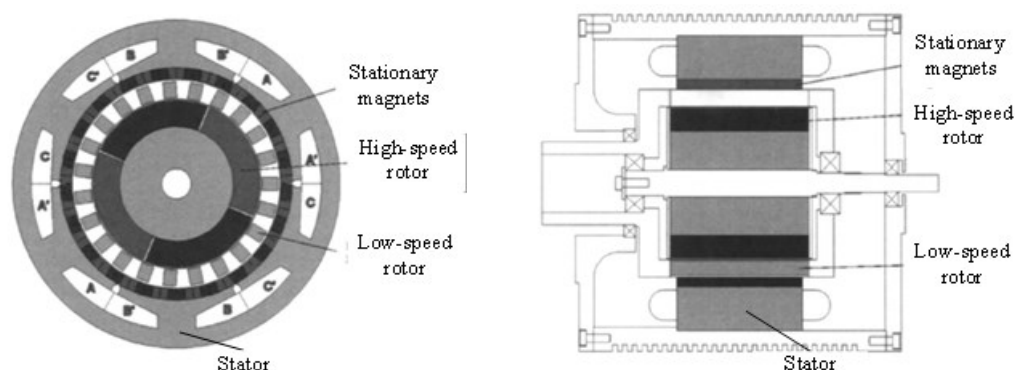


Figure 3-9: MGPM machine: Radial view (left) and axial view (right) [122]

Due to the magnetic gear ratio, an airgap flux density lower than 1T can be transformed into an *equivalent* peak flux density of more than 6T as explained in [82]. This is more than 6 times the peak airgap flux density achieved by SPM machines, and 3 times that of FSPM machines. This is, nevertheless, at the expense of more moving components, which brings a higher complexity into the design. This results in a high mass yielding a gravimetric torque density of a few newton-meters per kilogram [123, 125, 126, 127]. This was noted in [11], where magnetic gearboxes were studied to replace conventional helicopter gearboxes. The advantages in terms of maintenance, vibrations, noise, reliability and overload protection were outweighed by the excessive weight: the best alternative, the Cycloid Permanent Magnet Gear (CPMG), is still 3 times as heavy as a conventional helicopter gearbox.

Although examples with volumetric torque densities from 80kNm/m^3 to a 100kNm/m^3 were mentioned, these are exclusively outer-rotor configurations. For the purpose of

comparison, inner rotor machines with a split ratio close to 0.7 are considered [82, 122, 128]. This is to establish comparability to the machines considered before:

- *Equivalent* shear stress: $\sim 60\text{kPa}$
- Volumetric torque density: $\sim 60\text{kNm/m}^3$

Transverse-Flux Permanent Magnet (TFPM) Machines

Transverse Flux Permanent Magnet machines receive their name from the flux path within the stator core, which is transverse to the direction of rotor movement. This feature makes the 3D modeling of TFPM machines mandatory for reliable results [129], and implies prolonged simulation times for design and optimization. This topology allows having a very high pole number, with short pole pitches along the airgap. This means very good airgap area utilization for force production, and a very high gravimetric torque density. Nevertheless, this is at the expense of increased sensitivity to airgap length variations and strong leakage between poles, when compared to traditional machines [130].

Similar to conventional PM machines, TFPM machines can make use of surface mounted magnets in the rotor or flux concentrators. Also, designs with single or double airgap, moving or stationary magnets, etc. have been proposed and reviewed [40, 109, 131, 132] (see Figure 3-10). From the many configurations, the following characteristics can be summarized from a comparison to traditional radial or axial PM machines [40]:

- Higher force density
- Lower copper losses
- Simpler winding

TFPM machines can develop considerably higher values of airgap shear stress, with a simple concentrated winding configuration that reduces copper losses. On the other hand, due to complex path of the magnetic flux, they cannot be manufactured using laminations. Instead, single cores or pieces have to be manufactured separately and supported individually. Alternatively, sintered metal composites can be used to manufacture the complex structures through molding. In such case, decreased mechanical stability and reduced overall permeability must be expected.

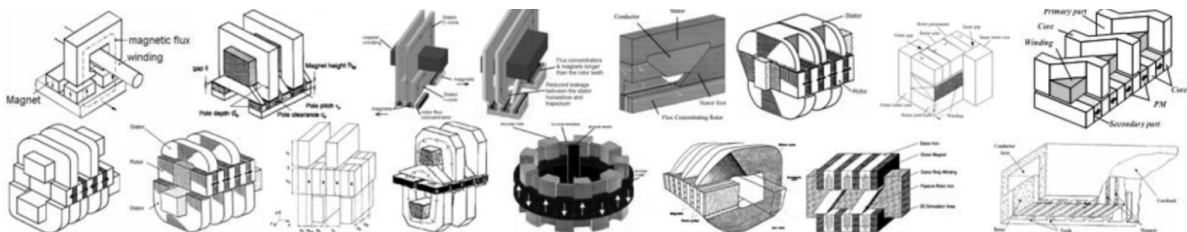


Figure 3-10: Different TFPM machines [40]

In terms of performance, peak flux densities are not higher than the values presented for the other topologies. However, the high pole density along the airgap results in very high shear stress values and volumetric torque densities. From [82, 41, 131, 132] the following figures were compiled for the purpose of comparison:

- Shear stress: 70-100kPa
- Volumetric torque density: 60-80kNm/m³

3.4 High Temperature Superconducting (HTS) Machines

This section covers the theory of superconductivity, focusing on properties and effects relevant for the design process. Superconductor types, operating theory and coil construction methods are described. The cooling alternatives are briefly discussed together with the system complexity involved.

3.4.1 Superconductivity

Theories of superconductivity have been developed in the past 100 years after the discovery of superconductors. There is however no unified theory explaining their behavior. New High Temperature Superconductors (HTS) are displayed as blue dots in Figure 3-11. They have been discovered in the past 30 years, mostly by trial and error, since they do not fit in the traditional theories.

Currently accepted theories like the BCS theory and Beans model give an in-depth quantum physical explanation of the phenomena. Yet for the purpose of this work only the relevant engineering theory needed for electrical machine design is considered.

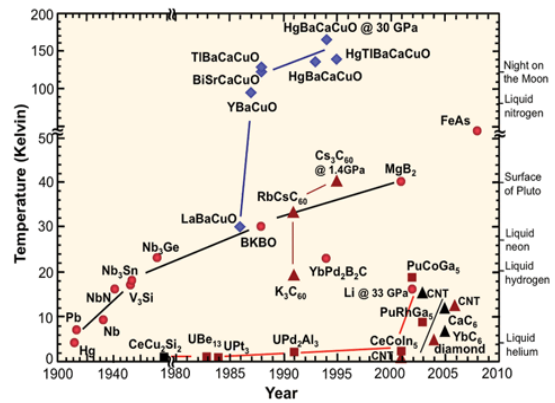


Figure 3-11: Superconductivity timeline [184]

3.4.2 Critical Surface

Next to a critical temperature T_C , a critical field H_C and a critical current density J_C describe the “operational surface” below which superconductivity can exist (see Figure 3-12). When the operating point of the material is above the critical surface, the material ceases to be superconducting. Every superconductor has a different surface, which can be somewhat influenced using advanced processing techniques like material doping [133].

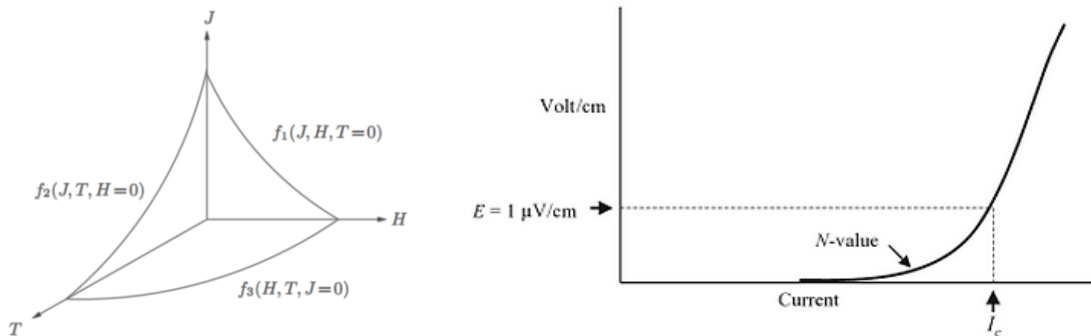


Figure 3-12: Superconductor critical surface [133] (left) and I-V curve [134] (right)

The critical current is an important measure of the performance of a superconducting wire. It is not a physical parameter of the material but an industry-defined standard. Since the transition from superconducting to normal state is gradual and not sharp, a critical voltage drop must be defined first. The critical current is then defined as the current at which the voltage drop across the wire exceeds the specified field E_0 (typically $1\mu\text{V}/\text{cm}$):

$$E = E_0 \left(\frac{I}{I_C}\right)^N \quad (3-3)$$

where I_C is the critical current and the N value depends on the construction of the tested sample. The N value defines the transition steepness between superconducting and normal state (see Figure 3-12). The I-V curve is used to determine I_C experimentally on a wire in self-field (the field produced by the straight wire itself), or in wound coil configurations.

3.4.3 Superconducting Wire Material

Superconductors can be classified based on two properties: the transition type and the critical temperature. Categorization according to transition is based on the material phase transition from superconducting to normal state with two types defined:

- **Type I:** instant transition from superconducting state (Meissner state or with no flux penetration) to normal state, with a high N value mostly independent of the geometry of the tested sample.
- **Type II:** gradual transition from fully superconducting (no flux penetration), to a mixed state (partial flux penetration) and finally to normal state [133]. While in mixed state, the material gradually loses its superconducting properties, and a voltage/loss can be measured due to the flux penetration.

Classification by the critical temperature is more widely used. It is based on the temperature range in which a material shows superconductivity. Since this is a directly measurable quantity, this system is the one considered from this point on for this work. Two classes of superconducting materials are also defined in this categorization:

- **Low Temperature Superconductors (LTS):** these show a critical temperature of about 30K and lower, and are usually type I superconductors [133]. LTS materials are pure metals with low critical values T_C , H_C and J_C .
- **High Temperature Superconductor (HTS):** usually type II superconductors, these are metal alloys, ceramic compounds or oxides [133]. HTSs make everyday application of superconductors more possible due to higher critical values. Also, cooling systems are less complex and more affordable. Critical values depend on crystal orientation, material doping, etc., so optimization according to the desired application is possible.

From the many different superconductors known, few have critical values that are practical. Therefore, further development is still needed on these materials before they can be used widely for high performance applications. Only five materials are considered mature enough at present or in the near future: NbTi, Nb₃Sn, MgB₂, BiSCCO and YBCO. An overview of their basic properties is presented in Table 3-6.

Table 3-6: Overview of practical superconductors and their basic properties [135]

<i>Material</i>	T_c (K)	<i>Anisotropy</i>	J_c (A/mm ²) * ¹	B_c (T) * ¹	ρ_e (Ω mm) * ²
NbTi	9	Negligible	$\sim 10^4$	11 – 12	6×10^{-4}
Nb ₃ Sn	18	Negligible	$\sim 10^4$	25 – 29	5×10^{-5}
MgB ₂	39	1.5 – 5	$\sim 10^4$	15 – 20	0.4×10^{-5}
Bi-2223	110	20 – 200	$\sim 10^5$	> 100	$4 - 6 \times 10^{-4}$
YBCO	93	5 – 7	$\sim 10^4$	> 100	$15 - 80 \times 10^{-4}$

*¹ At 4.2K*² In normal state

NbTi and Nb₃Sn are LTS materials easy and cheap to produce in long wires, reason why there is considerable industrial experience with their use in coil construction (ITER, LHC, etc.) [135]. Very powerful magnets can be made with them at the expense of cooling system complexity, since liquid helium is required. Due to low working temperature, these materials are not considered at this point for aerospace applications.

Discovered rather recently, magnesium diboride MgB₂ is not really considered a HTS, but very easy and cheap to produce in various shapes. Its sharp phase transition resembles that of LTSs more than HTSs. More practical to cool than other LTSs, it still requires a very low temperature for good performance. Its strength lies mostly in the feasible production of stranded wires, making them more resilient to AC losses than HTSs.

Among HTSs, of most interest are the cuprate materials, from which two major families are considered for commercial application: yttrium barium copper oxide or YBCO and bismuth strontium calcium copper oxide or BiSCCO. These HTSs have high critical temperatures above 77K, and can be cooled with LN₂. Because of their high critical values they are chosen for most high-performance electrical machines and magnets *in literature*.

Compared to the LTSs, the cuprates are much more difficult to produce, and considerable research is being carried out in order to make the material commercially available. Both HTS materials are used in literature for building coils, however most projects involve BiSCCO taped coils because of its currently higher availability. YBCO, however, is superior in terms of mechanical robustness and magnetic field critical values.

The most important difference between BiSCCO and YBCO is the critical current dependence on magnetic field direction or anisotropy (see Table 3-6). This results in maximum and minimum critical current of the HTS tape. Shown in Figure 3-13, the perpendicular field corresponds to 0 degrees, while the parallel field to 90 degrees. This causes a critical current difference of 2 to 3 times between both field orientations for the example in Figure 3-13. The anisotropy effect is much higher in BiSCCO, where the difference in critical currents can be of up to two orders of magnitude. This means that e.g. with a parallel critical field of 2T, the perpendicular critical field is 0.2T or lower. This direction dependency has to be taken into account when designing HTS coils.

For coil design, HTSs offer the best compromise between performance and cooling complexity. Both HTS materials are similar, but due to better mechanical performance and anisotropy, YBCO is the material of choice among the cuprates. Besides YBCO, MgB₂ is also considered for further analysis. It also offers weight advantages that could be interesting for aerospace applications, despite the comparably low critical temperature.

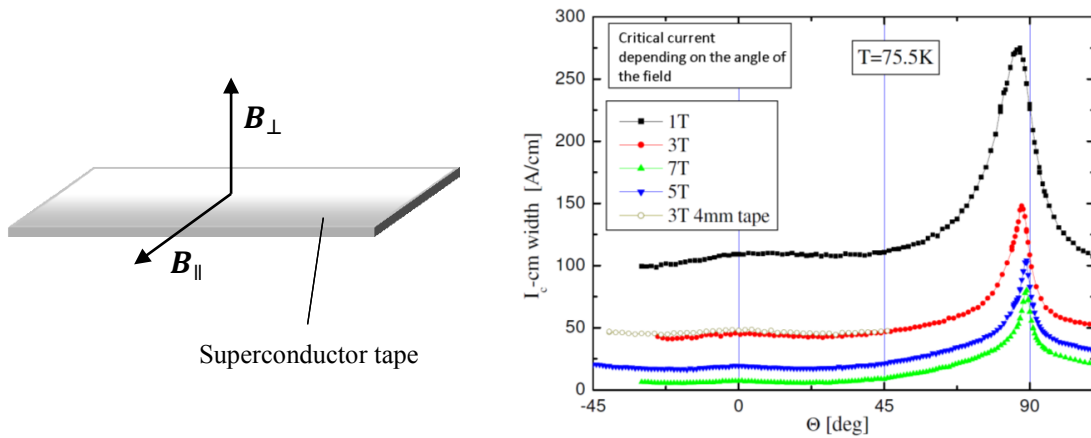


Figure 3-13: Normal and parallel field direction (left), and critical current dependence on magnetic field direction for YBCO tape (courtesy of SuperPower Inc.)

3.4.4 Superconducting Bulk Material

Aside from wires or tapes also superconductor bulk material is of interest. These bulks are made with a different production process that is much easier and cheaper but less mature. By using the Meissner effect, field isolators can be made in an existing DC field. Also, by using flux pinning an external field can be trapped inside the material creating a “superconducting permanent magnet”. It can be produced in round and square shapes, with diameters varying from 20mm up to 75mm. Some bulk products can be seen in Figure 3-14.

The main challenges in bulk material production are increasing flux pinning and material strength. Material strength is important to withstand high forces present inside *and* outside of the material.



Figure 3-14: Samples of bulk material manufactured by THEVA [185]

3.4.5 HTS Machines’ Specifics and Topologies

From the many principles proposed for HTS machine construction, it is not clear which ones could deliver the best performance for the target application. Before going into these designs in detail, some advantages of HTS machines are briefly discussed:

- **High current densities:** three orders of magnitude higher than copper are common [136]. High airgap field, armature loading, etc. are possible
- **Possibility to build air-core machines:** high fields are possible without active heavy iron, also eliminating saturation [137]
- **Improved efficiency:** copper and iron losses are not present [137]. The removed copper losses are typically greater than the required cryogenic-cooling power

- **Possibility to use bulk material:** through flux trapping and flux shaping, different potentially lighter designs are possible

The use of superconductors also comes with some disadvantages stemming mainly from the required operating temperatures:

- **Cryocooling system:** heavy and potentially maintenance-intensive equipment necessary, possibly counteracting the weight advantages of HTS use
- **Cryostat:** well-designed cryostat needed for HTS storage and efficient insulation. In partially superconducting machines the cryostat vacuum wall contributes to the electromagnetic airgap, increasing it to several centimeters
- **Coolant transport:** in designs with rotating cryostat, a special rotating coupling required to transport coolant in and out of it
- **Additional failure modes:** superconductor quench caused by exceeding critical values or cooling system failure. Scenarios and reliability are barely researched. Safety back-up solutions needed, e.g. safety torque squirrel cage [138].

A superconducting electrical machine is made by replacing its copper/aluminum coils with superconducting variants. In literature, mostly the field windings that produce the stationary airgap field are replaced, whereas the armature coils remain conventional. Using superconductors for the armature coils would increase armature loading, yielding an even higher possible gravimetric torque density. However, few designs consider replacing the armature coils with superconducting windings due to considerable AC-losses. These losses have led to the failure of one of the first fully superconducting concepts [139].

Concepts with superconducting armature windings are proposed using MgB₂ helix windings for wind turbine applications and aerospace concepts [140]. These designs require long axial lengths and are therefore not suitable for the current application. Furthermore, recent implementations such as [45] have shown the difficulty of a fully superconducting machine. Due to the numerous challenges, a partly superconducting variant is adopted for this research. Armature coils are conventional while field windings are superconducting.

Many conventional electrical machines can be “upgraded” with superconductors. There are also several design methods for field coils for a partly superconducting machine. However, for aerospace applications, superconducting machine research is scarce and with goals differing from the ones in this thesis. Finding a good compromise between advantages and disadvantages is a great challenge for the design phase. A list of the currently reviewed machines gives an overview of the possibilities:

- | | |
|--|--|
| • Hysteresis machine | • Trapped flux machine |
| • DC-Excited Synchronous mach. | • Homopolar DC machine |
| • Bulk flux-concentrating machine | • Homopolar alternator inductor (HAI) |

From these, the hysteresis and homopolar DC machines are not actively researched. The trapped flux topology is currently too underperforming and the HIA, although considered for aerospace, only performs well at high speeds (> 10.000rpm). The remaining topologies are considered for this thesis and are described in the following sections.

DC-Excited Synchronous Machines

The most popular synchronous machine topology is the separately excited synchronous machine. For the superconducting variant the rotor field copper coils are replaced with superconducting coils, while the stator remains unchanged. This machine type is considered for almost every application, from direct-drive wind turbines to electric vehicle propulsion.

The great amount of research on this topology plus the high number of concept demonstrators and the promising performance favor this topology. Progress is still to be made to reach full maturity, but the DC-excited synchronous machine could offer good success potential for the hybrid helicopter application.

From literature, the most interesting designs are the ones that made it to the demonstrator phase. Although all of them were built using BiSCCO wire, they show what is possible in practice with current technology:

- **American Superconductor ship propulsion motor:** air-core stator windings, 36.5MW at 120rpm, 75t and $90kNm/m^3$ of volumetric torque density [141]
- **Siemens 400kW and 4MVA generators:** air-core stator winding, operation at 1500 rpm and 3600rpm respectively. Operated for three years without major issues [142]

Bulk Flux-concentrating Machines

For this topology the inductor construction principle differs somewhat from most conventional machines. The excitation field is created with one or more HTS coils that produce a DC magnetic field at the airgap. By inserting HTS bulks between the coils, the DC field is concentrated and suppressed at certain points. The magnetic field inside the HTS bulks is reduced because of the Meissner effect. The flux is then concentrated on the spaces between the bulks, creating magnetic poles along the airgap (see Figure 3-16).

This topology is considered both for wind turbines and aerospace applications. In [143] a superconducting wind turbine using this principle was proposed (see Figure 3-15). The superconducting rotor consists of several HTS coils wound around the whole rotor with superconducting bulks between them. The needed currents are illustrated in Figure 3-16 together with the resulting field distributions: high airgap flux densities are achievable, but the field rapidly decreases with distance from the coils. From [143] a volumetric torque density of about $130kNm/m^3$ can be achieved in theory with such a design.

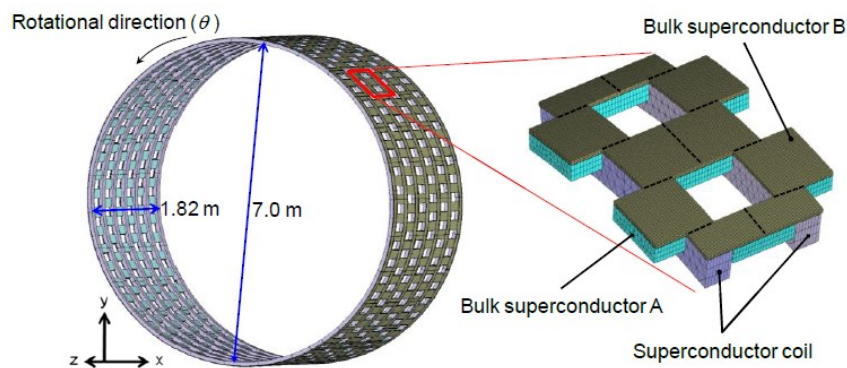


Figure 3-15: Wind turbine design using a bulk concentrating-flux design [143]

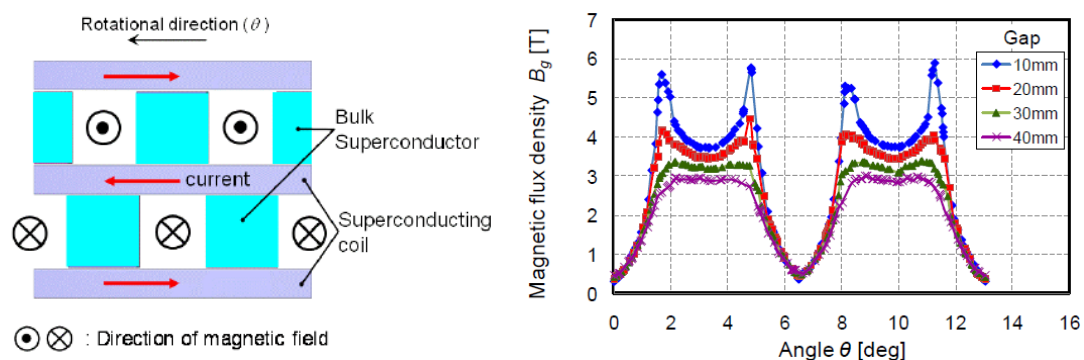


Figure 3-16: Fields and currents in the axial plane (left) and field along airgap for different radial distances from the coils at 20K [143] (right)

3.5 Aerospace Specific Electrical Machines

The following sections make a brief review of electrical machine developments and studies intended for massive civilian transport in the future. Unlike the machines used in the demonstrators reviewed in 2.2, which present rather conventional and established designs, these concepts are more likely to be used in the applications presented in 2.3.

3.5.1 Conventional Machines

Non-superconducting Cryogenic SRM by NASA

Using LH_2 fuel could also make non-superconducting cryogenic motors feasible for aircraft propulsion. Without the supply of a cryogenic coolant, a cryocooler would be required to compensate for all copper losses, which would lower efficiency and increase weight.



Figure 3-17: Cryogenic non-superconducting SRM stator [144] (left) with stator and rotor submerged in LN_2 [145] (right)

Conventional stator windings are cooled by LH_2 , lowering their resistivity and permitting current densities up to $50\text{A}_{\text{RMS}}/\text{mm}^2$ [144]. Coolant is made to flow through the copper layers of the loosely packed end windings, therefore removing the heat. The NASA Glenn Research Center has tested a SRM with copper windings cooled with LN_2 according to this principle. A gravimetric power density of $10.8\text{kW}/\text{kg}$ was achieved at 20krpm, and higher performance is expected with LH_2 .

Direct PM Fan-tip Drive by NASA

Another concept proposed in [145] is a tip-drive motor for a thrust fan rotating at 10krpm. Here, an axial-flux PM drive with an epoxy-impregnated stator disk is surrounded on both sides by the rotor permanent magnets. The magnets are surface-mounted, and are protected from centrifugal forces by the tip of the stator laminations (see top of Figure 3-18). The attractiveness of the design lies in the high gravimetric torque density expected, and easy cooling due to machine size and positioning.

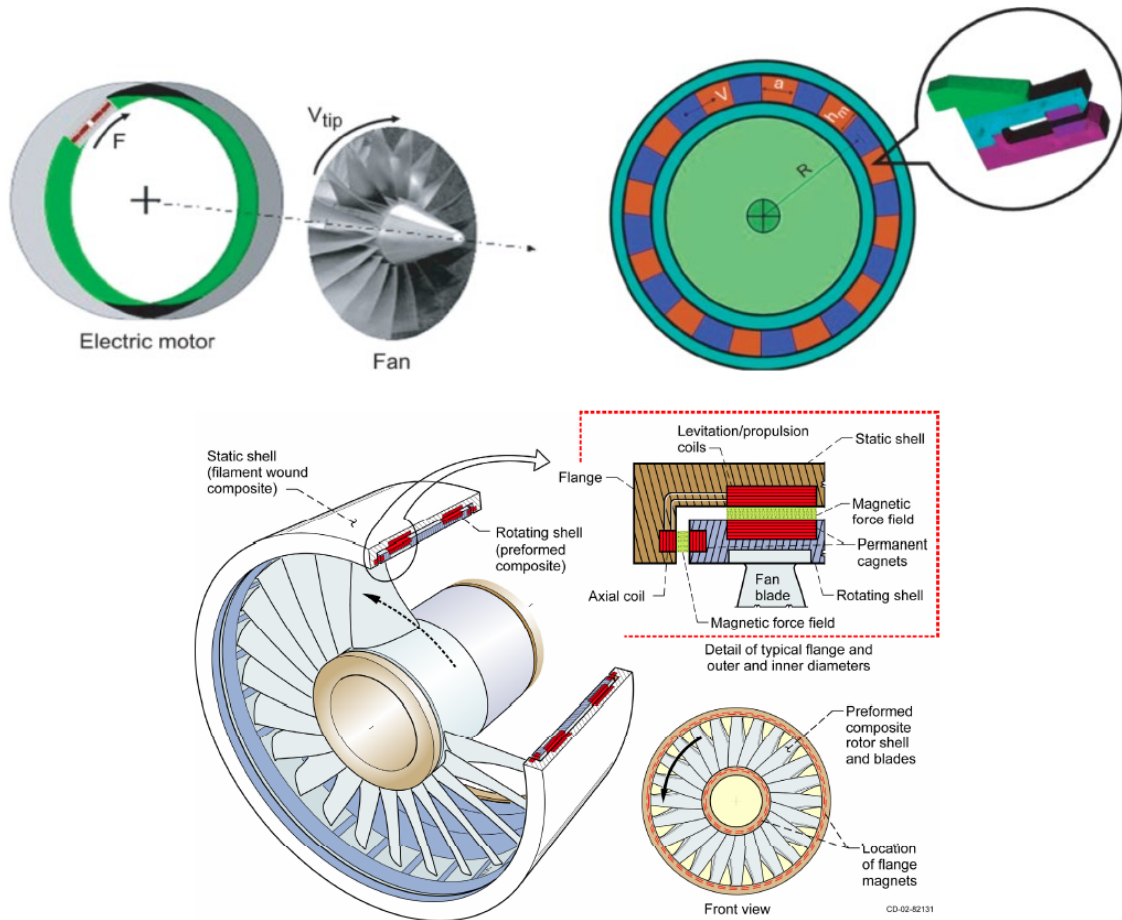


Figure 3-18: Fan-tip drive motor integration in fan housing (top left), and view of permanent-magnet axial-flux rotor [145] (top right). Magnetically levitated ducted-fan drive with construction details [146] (bottom)

Magnetically Levitated Direct Ducted-fan Drive by NASA

Similar to the previous concept, the levitated ducted-fan is a high power density integrated drive [146]. It consists of a drum rotor with blades attached at the outer diameter and supported by a stress tuner ring on the inside. Axially and radially placed Halbach arrays on the rotor, combined with passive coils in the stator provide the rotor levitation. The arrays also provide the excitation for the propulsion coils, mounted on the stator inner periphery. The stator airgap winding is held together by a low-weight nanocomposite material, while the support structure and the blades are made from carbon fiber.

A model of the design with some construction details is shown at the bottom part of Figure 3-18. The total power output is estimated at 685kW with a total weight of 241kg. According to the related publication, a small scale prototype has been constructed and successfully tested, verifying the concept (test results not yet published).

Yokeless Segmented Stator Axial (YASA) motor

The YASA motors were first introduced in 2007 as a high torque density alternative for electric vehicle direct-drive applications [147]. In contrast to other axial flux designs, the stator is segmented, each segment having a copper coil wound around it. With this approach, coils can have a rectangular cross-section and can be tightly wound separately from each other (see Figure 3-19). Besides the high fill factor, the double-rotor yokeless configuration allows the flux path to close through the second rotor. Already commercially available, they offer a maximum volumetric and gravimetric torque density of 60kNm/m^3 and 15Nm/kg respectively (400Nm, 200kW). Design studies for large scale applications, e.g. multi-megawatt wind turbines, have resulted in a more compact and lightweight design, when compared to modern radial and axial flux designs [148].



Figure 3-19: YASA configuration [147] (left) and YASA-750 model [149] (right)

3.5.2 Conceptual HTS Machine Designs for Aerospace

200HP HTS for Cessna

A 150kW HTS radial-flux machine designed to power a Cessna 172 [4, 150] is a concept suggested for direct-drive propulsion applications. The concept is a bulk flux-concentrating HTS machine. The armature is mechanically connected to the propeller while the superconducting inductor is stationary. The inductor comprises a series of pancake coils and YBCO bulk plates. (see Figure 3-20). The coils, centered on the axis of rotation, are fed with opposing currents to produce outwardly driven radial magnetic flux through the space between the coils. By cooling down the YBCO plates, while immersed in the coil-created field, high flux density trapped-flux magnets are created. After bulk magnetization, the coil current is reversed to produce an opposing field, and therefore a bipolar field profile.

The eventual motor concept operates at 2700rpm and 30K. The gravimetric power density of 6kW/kg is achieved mostly with high rotational speed. The gravimetric torque density is a moderate 21Nm/kg , but the volumetric torque density reaches up to 100kNm/m^3 . These figures are only for the motor without the weight of the cryocooler.

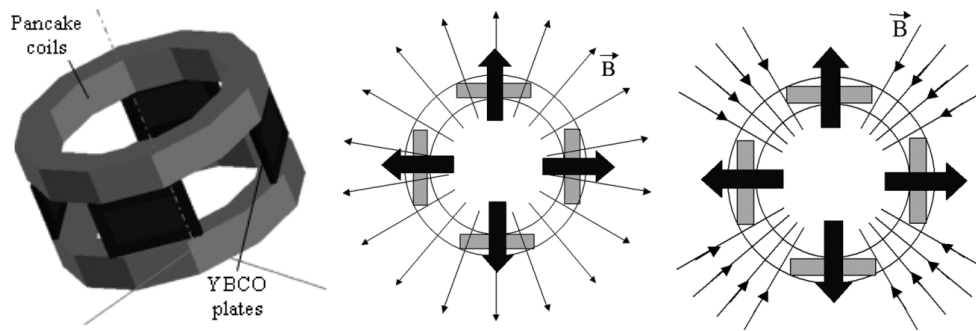


Figure 3-20: HTS rotor with bulk YBCO plates and pancake coils (left), flux density during magnetization with bold arrows indicating the trapped flux (middle), and flux density after coil current reversal (right) [150]

Axial flux HTS Machine for Larger Aerospace Applications

A further bulk flux-concentrating HTS motor, this concept provides a gravimetric power density of 7.5kW/kg. The gravimetric and volumetric torque densities are 17.7Nm/kg and 290kNm/m³ respectively. Only active material and a temperature of 20K are considered in these figures [151].

The YBCO bulk magnetization is achieved with two cylindrical HTS coils on the outer and inner periphery of the machine (see Figure 3-21). They allow a no-load airgap flux density of 3T. The machine is brought to superconducting temperatures by a flow of LH₂, which also serves as main aircraft fuel. The authors assume LH₂-powered aircraft would be feasible with gas turbines for power generation. For propulsion, scaled versions of the HTS machines presented in [150, 151] would be employed [152].

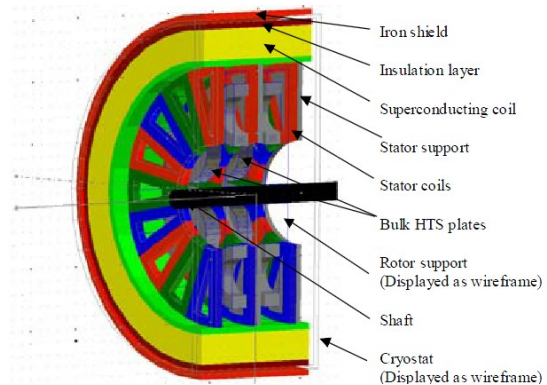


Figure 3-21: Axial flux HTS machine with cylindrical coils [151]

3.6 Starting Point

3.6.1 Topology Selection

From Chapter 2, volumetric torque density and airgap shear stress are chosen as representative figures of the torque capability of a machine topology. In the previous sections, average numbers for these figures were reviewed from literature. They are summarized in Table 3-7 along with some observations about the respective topologies.

For both conventional and HTS machines, there are topologies that are very promising in terms of electromagnetic performance. At the same time, they require additional implementation effort compared to more traditional machines. Besides torque capability, the topology selection must also consider the implementation feasibility of a test setup. Considering this reduces the risks associated with mechanical and structural requirements.

For conventional machines, experience favors SPM machines, since they are well studied and can serve as a benchmark for comparison. From the remaining conventional machine topologies, MGPM machines were already deemed too heavy for this particular application as discussed in 3.3.3. Between FSPM and TFPM machines, there is a clear performance difference, as TFPM machines offer about 50% higher performance than FSPM machines. On the other hand, choosing TFPM machines involves high computational design effort plus structural integrity concerns due to manufacturing and airgap sensitivity. FSPM machines still offer some drawbacks in terms of stator manufacturing complexity, and saturation susceptibility due to the low machine reluctance. Nevertheless, the stator can still be manufactured in a conventional laminated manner and the rotor is inherently robust. They use concentrated windings, bringing some inherent fault tolerance, and they also seem to have a slightly better performance than SPM machines under similar conditions. This shows a good performance/risk compromise, favoring FSPM machines as the second choice from the conventional machine topologies.

Table 3-7: Summary of reviewed electrical machine topologies

<i>Topology</i>		<i>Shear Stress (kPa)</i>	<i>Torque Density (kNm/m³)</i>	<i>Observations</i>
Conventional	SPM	35 – 45	35 – 45	+ Simple and very well known – Lowest performance of reviewed machines
	FSPM	40 – 50	40 – 50	+ Enhanced performance, robustness and fault tolerance – Saturation susceptibility, stator complexity
	MGPM	60	60	+ High performance at low thermal loading – Weight, mechanical complexity
	TFPM	70 – 100	60 – 80	+ Very high performance and low weight – Design complexity, mech. Robustness, airgap sensitivity
HTS	Sync.	-	90	+ Proven operation and design – Still experimental
	Bulk	-	> 100	+ Very promising performance – Mainly conceptual and highly experimental

Regarding HTS machines, the choice is based on the same reasoning and actual practical experience plays a very important role. The bulk flux-concentrating machine topology promises very high torque densities, particularly as an axial flux machine with trapped flux magnets. Its downside is the complicated inductor construction and magnetization scheme needed to realize a prototype. The lack of hands-on experience and complexity is an obstacle as seen in [45], where the magnetization technique of the rotor proved to be less mature than anticipated. For a HTS DC-excited synchronous machine, on the other hand, there is available and sufficient evidence of its operability, despite still being experimental. This is crucial since an eventual implementation is more likely to succeed.

Summarizing the choices, two conventional and one superconducting machine topologies were selected for further study:

- **SPM machines**
- **FSPM machines**
- **HTS DC-Excited Synchronous machines**

Based on these topologies, design studies are performed in the next chapters with the SPM design as benchmark. Designs based on the other two topologies are compared to the baseline to assess their suitability for this application. This evaluation focuses mainly on the gravimetric torque density, but without neglecting mechanical and thermal feasibility.

3.6.2 Radial Flux PM Machine vs. Axial Flux PM Machine

From the machines and concepts presented in 3.5, some are radial flux machines, some others axial flux machines. Some examples like the YASA motors and the axial flux HTS machine for larger aerospace applications in 3.5.2 use axial flux architecture with a very high volumetric torque density. On the other hand, the other examples in 3.5.1 are for very similar applications, yet one is a radial flux machine and the other an axial flux machine. Given that the space envelope of the problem resembles a thick disk (long radius and short axial length), an axial flux machine could be instinctively chosen. Though to make an informed decision, a short analysis on the most appropriate type is made.

Table 3-8: Main materials density and average mass density

<i>Material</i>	<i>Density (g/cm³)</i>	<i>Average density (g/cm³)</i>
Electrical steel	7.6 - 8.1	8
Copper	8.9	
Neodymium Iron Boron	7.7	

Conventional electrical machine topologies use iron and materials with a similarly high mass density, e.g. neodymium iron boron and copper. Given the weight and volume constraints of this application (see Table 2-6), an average mass density can be assumed to calculate the maximum active volume occupied by the machine materials (see Table 3-8):

$$\frac{\text{Expected Machine Weight}}{\text{Average Material Density}} = 5\% \text{ of total volume}$$

This volume is regardless of the machine built, and is used to determine which construction principle is more likely to yield the highest gravimetric torque density. To find an answer, the *approximate* ratio of the gravimetric torque density for both cases is calculated subject to spatial and weight constraints. Due to the low mass, a high pole number is assumed: a minimum of 50 and a maximum determined by the maximum electrical frequency of 1kHz are set. Furthermore, the active mass is assumed to be between half and two thirds of the total mass. Since only machines with fractional-slot concentrated windings are being considered, the number of poles is assumed equal to the number of slots. This assumption is made only for the sake of simplicity to facilitate the analysis.

The slot-pole structure defined in Figure 3-22 is taken as a representation of the region of one stator slot in a SPM machine; regardless of radial or axial flux type (only one airgap is assumed for both cases). The stator area is assumed to be square, and the rotor area is rectangular with a cross section equal to half the stator cross section. Both regions are assumed to be filled with material with the same average density (see Table 3-8).

In Figure 3-22, τ_u is the slot pitch, which determines the other dimensions necessary to calculate torque and weight. For a given amount of poles, the slot pitch is the same for both

radial and axial cases, and determined by the outer machine radius R_o with equation (3-5). For radial flux machines, the stator and rotor regions together have the approximate form of a rectangular box as shown in Figure 3-22 (end windings are ignored). This assumption is valid given the constraint for the minimum pole number, which makes the difference between slot pitch at the airgap and at the outer radius negligible ($< 5\%$). For radial flux machines, the slot pitch also influences performance since it determines the length of the torque arm and the airgap area through equation (3-6). For axial flux machines, it has no effect on performance, and is only calculated at the outer radius with the objective of limiting the axial length of the machine (see equation (3-9)).

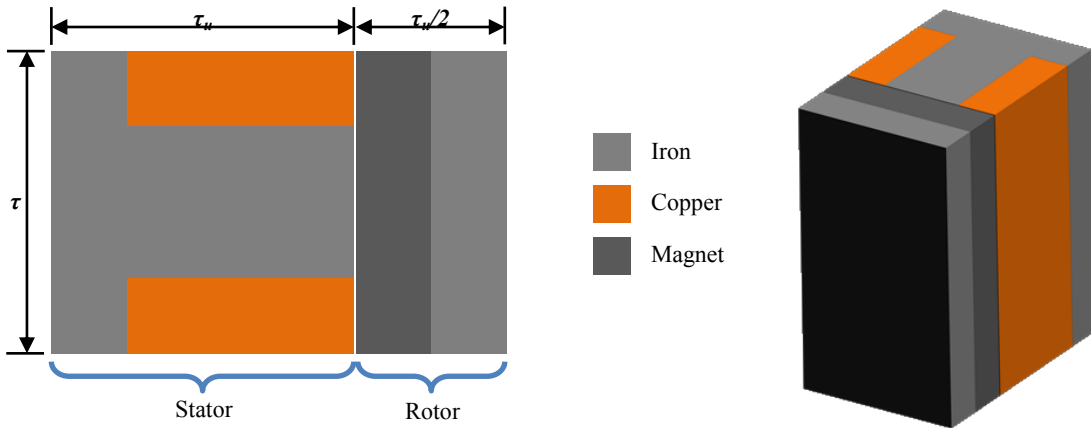


Figure 3-22: Assumed slot/pole structure: cross-section (left), isometric view (right)

Besides the slot pitch, an airgap shear stress σ_t needs to be assumed to calculate torque. Since no magnetic design is done for this analysis the value of σ_t remains unknown. Nevertheless, it is assumed that the airgap length and current loading for both radial and axial flux machines is the same. Under this assumption, the airgap shear stress is the same for both cases provided that the pole number is also the same.

The torque and mass for radial and axial flux machines can then be calculated and compared using equations (3-10), (3-11) and (3-12). The constraints listed in Table 3-9 are defined for this purpose. These were gathered using information presented in Table 2-6 and Table 3-8, plus the assumptions made in the paragraphs above.

Table 3-9: RFPM vs. AFPM machine model constraints

<i>Constraint</i>	<i>Observation</i>
$R_o = 0.7m$	Outer machine radius
$n = 350rpm$	Rotational speed
$0 < L_{RFPM} \leq 0.25m$	Active length (RFPM machine)
$0 < L_{AFPM} \leq 0.7m$	Active length (AFPM machine)
$\rho_{av} = 8 \times 10^3 kg/m^3$	Average material density
$75kg \leq m_{act} \leq 100kg$	Active mass range
$f_{max} = 1kHz$	Maximum electrical frequency
$25 \leq p \leq 172$	Number of pole-pairs range

Table 3-10: RFPM vs. AFPM machine model equations

Eq.	RFPM	AFPM	Description
(3-4)	$N_s = 2p$		Number of slots
(3-5)	$\tau_u = \frac{2\pi R_o}{2p}$		Slot pitch
(3-6)	$R_g = R_o - \tau_u$	-	Airgap radius (RFPM)
(3-7)	$R_{i,RFPM} = R_o - \frac{3}{2}\tau_u$	-	Rotor inner radius (RFPM)
(3-8)	-	$R_{i,AFPM} = R_o - L_{AFPM}$	Machine inner radius (AFPM)
(3-9)	-	$L_{axial} = \frac{3}{2}\tau_u \leq 0,25m$	Machine axial length (AFPM)
(3-10)	$T_{RFPM} = 2\pi R_o^2 (1 - \pi/p)^2 L_{RFPM} \sigma_t$	$T_{AFPM} = \frac{\pi}{2} (2R_o - L_{AFPM})^2 L_{AFPM} \sigma_t$	Torque
(3-11)	$m_{act,RFPM} = \frac{3\pi^2 R_o^2 L_{RFPM} \rho_{av}}{p} (1 - 3\pi/4p)$	$m_{act,AFPM} = \frac{3\pi^2}{2p} (2R_o - L_{AFPM}) R_o L_{AFPM} \rho_{av}$	Active mass
(3-12)	$\left. \frac{T}{m_{act}} \right _{RFPM} = \frac{2p}{3\pi} \frac{(1 - \pi/p)^2}{(1 - 3\pi/4p)} \frac{\sigma_t}{\rho_{av}}$	$\left. \frac{T}{m_{act}} \right _{AFPM} = \frac{p}{3\pi} \frac{(2R_o - L_{AFPM})}{R_o} \frac{\sigma_t}{\rho_{av}}$	Gravimetric torque density

From equation (3-12), the gravimetric torque density in RFPM machines depends only on the number of pole pairs for a given material density and airgap shear stress. This is not the case for AFPM machines, where it also depends on the active length L_{AFPM} . In an AFPM machine constructed with the active length equal to the machine outer radius (a complete disk), the gravimetric torque density depends only on the pole pair number. Using equation (3-12) a ratio of the two gravimetric torque densities is defined:

$$\frac{T/m_{act}|_{RFPM}}{T/m_{act}|_{AFPM}} = 2 \frac{(1 - \pi/p)^2}{1 - 3\pi/4p} \frac{R_o}{2R_o - L_{AFPM}} \quad (3-13)$$

With equation (3-13) it's possible to find the number of pole pairs p , and AFPM machine active length L_{AFPM} , for which an RFPM machine has a higher gravimetric torque density than an AFPM machine. The result is independent from the material density and airgap shear stress, provided they have the same value in both cases. A graphical solution is presented in Figure 3-23, subject to the boundary conditions defined in Table 3-9. The deep blue region represents the area where the constraints for active mass or pole-pair number are not met. The other colored regions give the corresponding values for equation (3-13), depending on p and L_{AFPM} . From the preliminary results, it is *likely* that a RFPM machine has a higher gravimetric torque density *for a pole number equal to 80 and higher*. Furthermore, due to the weight and frequency constraints the full active length possible for an AFPM machine is never achieved, reaching a maximum value of about 45cm.

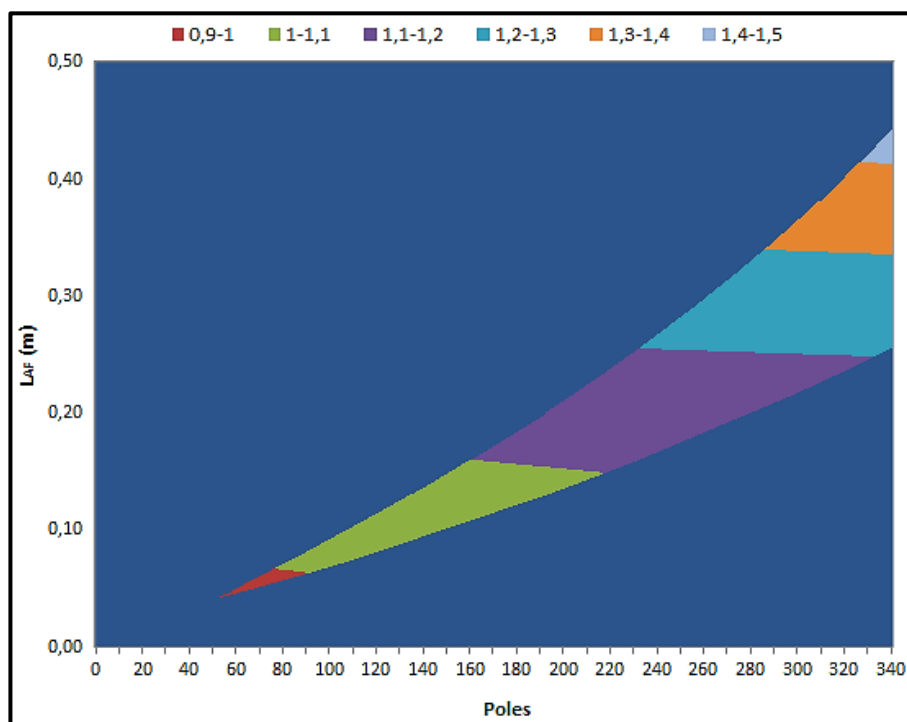


Figure 3-23: Solution of equation (3-13) subjected to constraints in Table 3-9

This model compares RFPM and AFPM machines based on a SPM machine structure. The study however, also considers FSPM machines and HTS DC-excited synchronous machines. For the sake of comparability, these two topologies are also assumed to be RFPM machines. For FSPM machines, given their composition and structure, it is also likely that a radial flux design gives a higher gravimetric torque density than an axial flux design. For the case of HTS DC-Excited synchronous machines, this is uncertain given the lighter materials used for the cryostat, and the unknown amount of iron required to maximize the gravimetric torque density.

3.7 Chapter Summary

In this chapter the main design aspects for an electrical drive for aerospace applications have been reviewed: materials, fault-tolerance measures and actual machine topologies. The more expensive cobalt steel and NdFeB magnets are preferred due to their use in aerospace applications and high performance-to-weight ratio. The question of whether lighter aluminum windings are suitable for this application remains, and depends on the feasibility of the thermal management. This problem is examined in subsequent chapters. One aspect considered less in traditional electrical machine design is the structural weight, since it's less critical in other fields than in aerospace. Materials with a high UTS-to-mass-density ratio are key in achieving the lightest design possible. In this sense, structural steel does not perform as well as titanium, aerospace-grade aluminum or beryllium, and achieves only half the performance of the latter three. Which material is most suitable is evaluated in the structural analysis and design of the experimental setup in Chapter 7.

Regarding fault-tolerance, at machine level it is important to consider the modularity and phase isolation in the machine. The phase isolation must not only be electrical, but if possible, also thermal and magnetic, which can be achieved to a good extent by using concentrated windings. Additionally, the modularity reduces the degree of overrating needed in case of a fault, but at the expense of a higher amount of redundant components.

Parting from the fault tolerance guidelines, different PM and HTS machines were initially reviewed focusing on the absolute torque and shear stress performance under similar conditions. However, for a final selection the ease of implementation was also considered, as the validation of one of the topologies is to be conducted on an experimental setup. This selection considers a compromise between performance, manufacturability and proven operation. From this perspective TFPM, MGPM and HTS bulk flux-concentrating machines were ruled out. As final choices, **SPM** (benchmark), **FSPM** (iron-based) and **HTS DC-excited synchronous** (superconductor-based) machines were taken.

As a next step, various machines related to aerospace with a high gravimetric power or torque density were presented for future medium and large passenger aircraft. It should be noted, that all HTS designs presented are partly superconducting machines with a superconducting inductor. Commercially available conventional machines as well as under-research topologies exhibiting high torque density were reviewed. Research from NASA is focusing in conventional and cryogenic non-superconducting machines for the near future, but only intermediate results are available with no final prototypes. An important conclusion from all this research is that aerospace electric propulsion is still at a very early development stage. At conceptual design level, the number of publications is very limited for electric aircraft propulsion, with even less available literature on already constructed and tested prototypes.

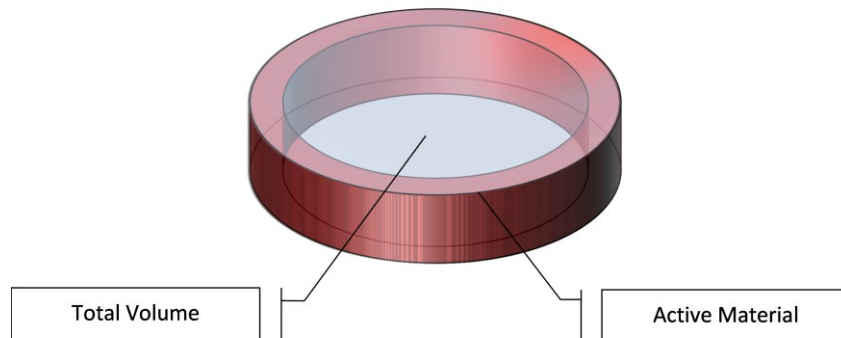


Figure 3-24: Space envelope for a ring-type motor

From the afore-mentioned review, the question about the best machine choice for the application of main helicopter propulsion arose: radial flux vs. axial flux. A simplified analysis indicated that, for the dimensions and constraints given, an RFPM machine is more likely to have a higher gravimetric torque density. From equation (3-12), but also due to the low-speed/high-torque requirement, a high pole number is preferable. This generally implies a ring-type motor as suggested in Figure 3-24. Active material should be located at large diameters, since the total amount of material is to occupy 5% of the total volume. This yields the maximum airgap diameter possible, guaranteeing the largest torque arm and airgap area.

Chapter 4

Surface Permanent Magnet Machines as a Benchmark

This fourth chapter concentrates on SPM machines, which is the first topology selected in the previous section. Since the working principle of SPM machines is well known, and it was reviewed in Chapter 3, this chapter starts directly with the performance study.

First, an explanation and FEM validation of the model employed for performance calculations is presented. This includes geometry definition, assumptions, performance calculation and weight. Important assumptions for this analysis are that frequency-dependent losses in magnet and core material are considered to be low and thermally manageable. This can be achieved with thin core laminations with narrow hysteresis loops and well-studied magnet segmentation strategies.

Afterwards, the alternative of using aluminum windings instead of the traditional copper windings is examined in terms of losses and weight. Furthermore, potential configurations are studied and compared based on their total mass for the required performance. From this comparison, the most important mass driving parameters are identified for different machine components, allowing the choice of a final configuration.

The final design is optimized. Provisions for structural support are made to come to a prediction of the gravimetric torque density of a candidate air-cooled SPM machine.

4.1 Analytical Model

The purpose of this analytical model is the fast and relatively accurate calculation of performance, weight, torque density and efficiency. The focus lays in fractional-slot SPM machines with a ratio of air-gap diameter to outer diameter near one. The model is used to compare different topologies and other design parameters: number of phases, slot and pole number, winding material. Model inputs are basic geometric dimensions, as well as electromagnetic parameters and material properties. Since it's not intended as an optimization tool, it must provide realistic results that can lead to conclusions while remaining simple and easy to implement.

4.1.1 Main Parameters

As mentioned above, one of the main model assumptions is an airgap diameter very close to the outer diameter of the machine (only 5% of the total volume is occupied by active material). In order to simplify the calculations, the stator and rotor geometries are linearized as can be seen in Figure 4-1, where the main dimensions are also presented.

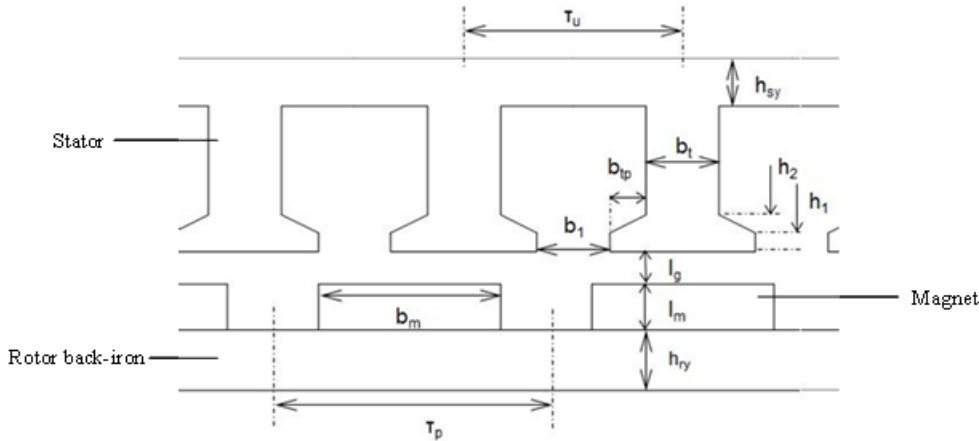


Figure 4-1: Main machine dimensions

From Figure 4-1 the following parameters are defined:

- k_w : winding factor
- λ_m : number of modules
- m_{ph} : number of phases
- L : active length
- D_o : outer machine diameter
- l_g : airgap length
- l_m : magnet height
- d_m : magnet coverage of pole pitch in pu
- k_f : slot fill factor
- J : RMS conductor current density
- B_r : magnet remanent flux density
- k_s : slot opening factor
- N_{ph} : turns per phase
- n_n : nominal rotor speed
- T_n : nominal torque
- v_l : winding type (1 for single layer, 2 for double layer)
- h_1 : Tooth thickness 1
- h_2 : Tooth thickness 2

This model estimates a fractional slot machine with a number of modules λ_m , a total number of slots N_s , and a total number of poles p . Each module is a base machine, for which the slot-pole combination is feasible and the winding factor is known. The winding factor, previously calculated, remains therefore the same as in the base design. Winding

factors for diverse configurations, and the method used to obtain them can be found in [153]. Finally, the target values for electric and magnetic loading are required (*specific values depend on core material and cooling, see 4.3.1*):

B_t^* : maximum allowable peak flux density in stator teeth

B_y^* : maximum allowable peak flux density in stator and rotor yoke

A_s^* : maximum allowable RMS linear current density

4.1.2 Dimensions, Loading and Performance Calculation

With the basic design parameters defined, all the dimensions of the machine can be determined. For this, an iterative process is defined, which takes initial geometry values to calculate a full set of physical dimensions. With the machine's dimensions, further performance parameters are calculated. This is done iteratively, where magnetic and electrical loading are calculated in separate loops, until their target values defined by B_t^* , B_y^* and A_s^* are reached. An overview of this is given in Figure 4-2, and a more thorough explanation of each of the steps is given in the following sections.

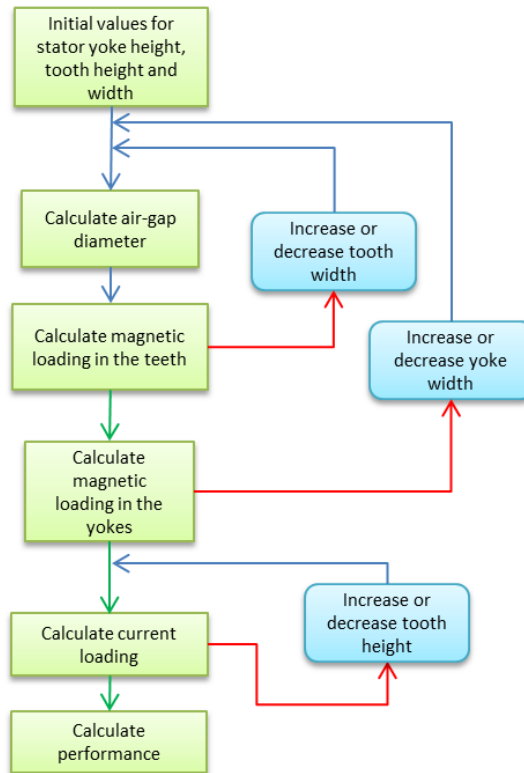


Figure 4-2: Iterative process to determine SPM machine dimensions

Stator, Rotor and Windings

Starting with the air-gap diameter D_g , its value is not initially known, and is dependent on the stator yoke height h_{sy} and the tooth height h_t (see equation (4-1)). The yoke height is related to the pole magnetic flux, which is dependent on the magnet height and width. The

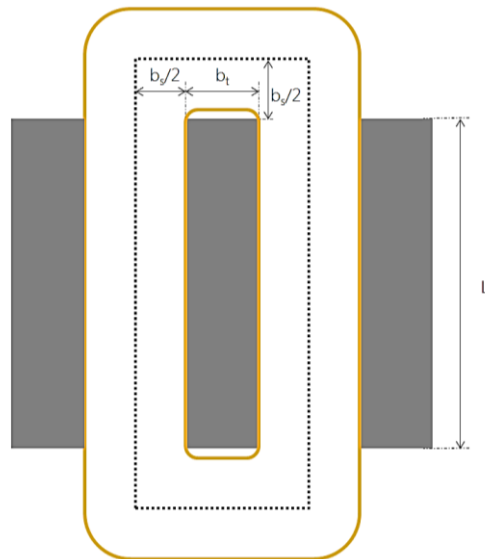
magnet width however depends on the air-gap diameter of the machine, resulting in a circular reference. To address this iteratively, initial values for the tooth height h_t , tooth width b_t , and stator and rotor yoke heights h_{sy} and h_{ry} are selected. The air-gap diameter is then calculated, followed by all geometric dimensions using the equations in Table 4-1.

Table 4-1: Equations for physical dimensions of SPM machine

<i>Eq.</i>	<i>Definition</i>	<i>Parameter description</i>
(4-1)	$D_g = D_o - (2h_{sy} + 2h_t + l_g)$	Airgap Diameter
(4-2)	$\tau_u = \frac{\pi D_g}{N_s}$	Slot pitch
(4-3)	$b_s = \tau_u - b_t$	Slot width
(4-4)	$b_1 = k_s b_s$	Slot opening
(4-5)	$b_{tp} = \frac{b_s - b_1}{2}$	Tip overlength
(4-6)	$\tau_p = \frac{\pi D_g}{2p}$	Pole pitch
(4-7)	$b_m = d_m \tau_p$	Magnet coverage
(4-8)	$l_w = 2(l_e + L)$	Winding turn average length (see dotted line in Figure 4-3)
(4-9)	$l_e = b_t + \frac{2b_s}{v_l}$	End-winding length
(4-10)	$L_w = N_{ph} l_w$	Phase wire length

The windings are concentrated around the teeth, and can be either single (if allowed by the slot/pole combination) or double layer: they are either wound around every second tooth, or around every tooth respectively. Although the winding configuration doesn't affect the current loading, it affects the end winding length. This in turn affects the total weight of the windings, further influencing the gravimetric torque density. A schematic of a coil around a tooth is shown in Figure 4-3 for single layer winding configuration.

Figure 4-3: Schematic of three stator teeth, one winding and the related dimensions for a single layer configuration.



Magnetic Loading

The next step is the calculation of the magnetic loading in the air-gap and teeth. If the maximum flux density is too low/high compared to the target value B_t^* , the tooth width is adjusted respectively. Once the target value is achieved, the same procedure is applied for the flux densities in stator and rotor yokes.

In order to calculate the air-gap flux density some assumptions are made. The actual air-gap l_g is replaced with the equivalent airgap g to account for slotting (see equation (4-11)). Also, the magnetic circuit of the machine is considered to be non-saturated and linear with a very high permeability. This renders an iron reluctance significantly lower than that of the air-gap. More detailed approaches to predict the magnetic field distribution with great accuracy that also take saturation into account can be implemented [154][155]. They were however deemed unnecessary for the purpose of the model.

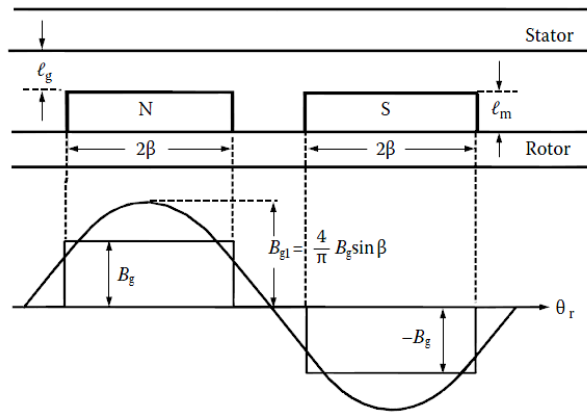


Figure 4-4: Flux density distribution in the air-gap [101]

The fundamental wave component of the airgap flux density is calculated from the rectangular flux density distribution at the magnets’ surface (see equation (4-12)). This flux density has an amplitude given by (4-16), from which the average and peak values of the fundamental can also be calculated (see Table 4-2) [101].

The calculated flux densities act as a guideline to ensure that there is no heavy saturation in the iron, in order to maintain the model’s accuracy. Should this be the case, the saturated parts can be made thicker (higher b_t or h_{sy} , h_{ry}) or the magnetic excitation can be decreased (lower l_m , d_m or higher l_g).

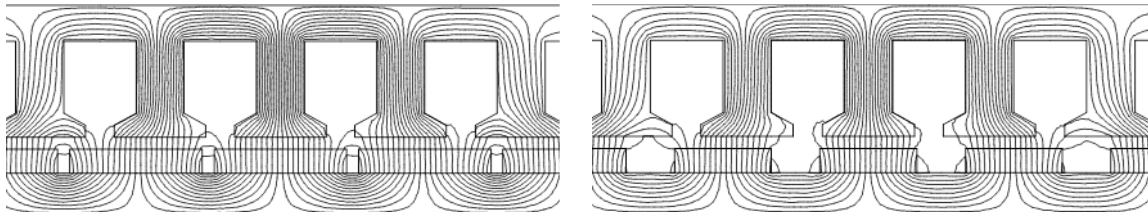


Figure 4-5: Exemplary magnetic flux lines for equations (4-18) and (4-19) with $b_m / \tau_u = 1.15$ (left) and $b_m / \tau_u = 0.8$ (right)

Table 4-2: Equations for magnetic loading calculation of SPM machine

<i>Eq.</i>	<i>Definition</i>	<i>Parameter description</i>
(4-11)	$g = C \cdot l_g$	Equivalent airgap, with C as the Carter factor [83]
(4-12)	$B_m = \frac{B_r}{1 + \frac{\mu_{rm} g}{l_m}}$	Peak flux density at magnet surface
(4-13)	$B_{m1} = \frac{4}{\pi} B_m \sin\beta = \frac{4}{\pi} B_m \sin\left(\frac{d_m \pi}{2}\right)$	Fundamental peak flux density at magnet surface
(4-14)	$\bar{B}_m = d_m B_m$	Average flux density at magnet surface
(4-15)	$B_g = k_\sigma B_m$	Airgap peak flux density (accounting for pole leakage with $k_\sigma = 0.95$)
(4-16)	$B_{g1} = \frac{4}{\pi} B_g \sin\beta$	Fundamental peak flux density at airgap
(4-17)	$\bar{B}_g = d_m B_g$	Average flux density at airgap
(4-18)	$B_t = \frac{b_m}{b_t} B_g, \quad b_m < \tau_u$	Tooth flux density depending on magnet width b_m and slot pitch τ_u . For (4-18) all magnet flux goes into the tooth, while for (4-19) only the portion covered by the slot pitch goes into the tooth (see Figure 4-5).
(4-19)	$B_t = \frac{\tau_u}{b_t} B_g, \quad b_m \geq \tau_u$	
(4-20)	$B_{sy} = \frac{\tau_p}{2h_{sy}} \bar{B}_g$	Stator yoke flux density
(4-21)	$B_{ry} = \frac{\tau_p}{2h_{ry}} \bar{B}_m$	Rotor yoke flux density

Electrical Loading

After the adjustment of the previous parameters, the tooth height can also be adjusted to achieve the desired linear current density A_s^* for a given conductor current density J . Increasing the tooth height yields more slot area and therefore higher total current and linear current density.

Table 4-3: Equations for electrical loading calculation of SPM machine

<i>Eq.</i>	<i>Definition</i>	<i>Parameter description</i>
(4-22)	$S_s = k_f (b_s h_t - 2h_1 b_{tp} - h_2 b_{tp})$	Total conductor area per slot
(4-23)	$S_c = \frac{N_s S_s}{m_{ph} (2N_{ph})}$	Area of one conductor
(4-24)	$I_{ph} = S_c J$	RMS phase current
(4-25)	$A_s = \frac{m_{ph} (2N_{ph} I_{ph})}{\pi D_g}$	Linear current density

The number of turns per phase influences only the phase current and the back-EMF, but not the linear current density. Current loading is only influenced by the conductor current density in the slots and the slot fill factor (see Table 4-3).

Electromagnetic Torque

The final performance is calculated with the airgap shear stress using (4-26) [83]. Once this is calculated, the machine's torque can be obtained as the product of shear stress, airgap surface area and torque arm length. These equations are summarized in Table 4-4.

Table 4-4: Equations for electromagnetic torque calculation of SPM machine

<i>Eq.</i>	<i>Definition</i>	<i>Parameter description</i>
(4-26)	$\sigma_t = \frac{k_w B_{g1} A_s \cos\varphi}{\sqrt{2}}$	Airgap shear stress
(4-27)	$T_e = \sigma_t \frac{\pi D_g^2 L}{2} k_{end}$	Electromagnetic torque

The term k_{end} in (4-27) corresponds to the airgap end-effect, which causes a flux density decrease in the active region of the machine. Its value is assumed to be 0.95 here and depends on the ratio of active length to airgap diameter and also on the air-gap length.

Table 4-5: Equations for weight calculation of SPM machine

<i>Eq.</i>	<i>Definition</i>	<i>Parameter description</i>
(4-28)	$V_{ry} = \pi(R_{ry}^2 - R_i^2)L$	Rotor yoke volume
(4-29)	$R_{ry} = \frac{D_g}{2} - \frac{l_g}{2} - l_m$	Rotor yoke outer radius
(4-30)	$R_i = R_{ry} - h_{ry}$	Rotor yoke inner radius
(4-31)	$V_m = d_m \pi (R_{ro}^2 - R_{ry}^2)L$	Total magnet volume
(4-32)	$R_{ro} = \frac{D_g}{2} - \frac{l_g}{2}$	Rotor outer radius
(4-33)	$V_{st} = N_s (b_t h_t + 2b_{tp} h_1 + b_{tp} h_2)L$	Total stator teeth volume
(4-34)	$V_{sy} = \pi(R_o^2 - R_{sy}^2)L$	Stator yoke volume
(4-35)	$R_o = D_o/2$	Stator outer radius (stator yoke outer radius)
(4-36)	$R_{sy} = R_o - h_{sy}$	Stator yoke inner radius
(4-37)	$V_w = m_{ph} L_w S_c$	Total winding volume
(4-38)	$m_i = \rho_i V_i$	Mass of part i according to the respective material density

4.1.3 Weight

The final step is the weight calculation in order to compare different configurations. With this estimation, the gravimetric torque density is calculated to determine whether a configuration is in the desired specification limits. First the volume of each part is calculated, followed by the mass according to the material selection. All equations used for this are summarized in Table 4-5, and the densities are chosen from the materials in 3.1.

4.1.4 Electromagnetic Model Verification

Although the model is not intended for geometry optimization, it should be accurate enough for geometry input parameters in a reasonable range. Since the geometry parameters are numerous, the model accuracy cannot be tested for all of them. Airgap length and magnet length, which define the excitation strength and the saturation in the core, were chosen for this. **Vacoflux 50** is assumed as core material (see Figure 3-1) and **Vacodym 872 TP** as magnet material.

The configuration used for verification is the 12slot/16pole base configuration, with 7 modules for a total of 84 teeth and 112 poles. Further geometry inputs are given in Table 4-6. Since the stator geometry remains constant, adjusting the magnet height and the airgap length has an impact on the saturation levels in the teeth. The estimated saturation is given for each combination of magnet height and air-gap length, as well as for the electromagnetic torque. The yoke thicknesses are selected so that they remain unsaturated.

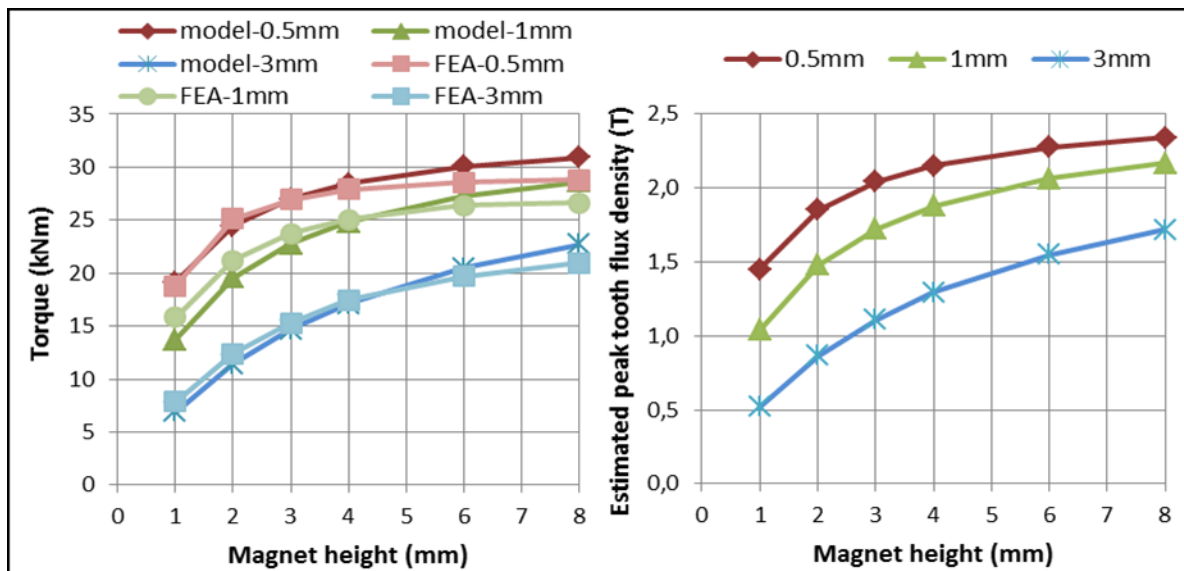


Figure 4-6: Electromagnetic torque vs. magnet height and airgap length from FEM simulations compared to the analytical model (left), and maximum tooth flux density vs. magnet height and airgap length from analytical model (right)

The matching between model and finite element predictions for the selected range is good (see Figure 4-6). Higher deviation is observed at higher saturation levels for small airgap lengths and large magnet height. This is expected, since the assumed permeability in the analytical model is infinite, therefore neglecting any drop in magnetomotive force in the

core. The cobalt iron magnetization curve indicates that saturation starts at 2.35T, so the closer the core flux densities come to this point, the greater the deviation becomes.

Obtaining accurate results therefore depends on the saturation in the core. For core iron not heavily saturated, the core reluctance is very low compared to airgap and magnet, so that iron behavior can be linearly approximated. When the core is heavily saturated however, its permeability drops significantly. Consequently, its reluctance increases and becomes comparable to that of magnet and airgap. In this case, assuming infinite permeability can yield significant error. Only tooth saturation has been checked, but the same principle applies to stator and rotor yokes.

Table 4-6: Parameters for verification of SPM machine model

<i>Constraint</i>	<i>Description</i>
$R_o = 0.7m$	Outer machine radius
$L = 0.25m$	Active length
$h_t = 15mm$	Tooth height
$\tau_u = 51.4mm$	Slot pitch
$d_m = 0.95$	Magnet coverage
$k_s = 0.6$	Slot opening factor
$J = 8 A_{RMS}/mm^2$	RMS conductor current density
$b_t = 20 mm$	Tooth width

4.2 Winding factors and Slot/Pole Combinations

The winding factor is of great importance for the machine performance as it is proportional to the produced torque [156]. As known from electrical machine theory, it is the product of the distribution factor k_d , the pitch factor k_p and the skewing factor k_{sk} [157].

$$k_w = k_d k_p k_{sk} \quad (4-39)$$

For the purpose of this study the skewing factor is assumed to be unity, while the other two are determined from the slot/pole combination. As explained in 3.3, the number of slots and poles must differ by a maximum of two, so that maximum flux-linkage is achieved. Out of the possible combinations four are selected for further investigation:

- **12slots/10poles, 3 phases, $k_w = 0.933$** : popular choice with high torque density and efficiency [157], [158]
- **21slots/22poles, 3 phases, $k_w = 0.953$** : maximum possible winding factor for 3-phase double-layer systems, but with unbalanced magnetic pull
- **24slots/22poles, 6 phases, $k_w = 0.983$** : system with highest winding factor overall for both single- and double-layer cases
- **12slots/16poles, 3 phases, $k_w = 0.866$** : selected as a *basis for comparison* with the FSPM machine proposed in Chapter 5 due to similar winding factor

These combinations are intended for implementation in a final machine comprised of modules with separate power electronics. Also, two of the mentioned combinations can be implemented with single layer windings, allowing a slightly greater winding factor.

However, there are other criteria that should be taken into account before further decisions are made. Some of the main advantages of single layer, apart from the higher winding factor, are the higher fault tolerance and the easier construction. On the downside, the single layer setup leads to longer end-windings (affecting both weight and efficiency) and to a richer space harmonic content (increasing iron and magnet eddy current loss). Furthermore, the rich harmonic content yields a lower torque quality and higher ripple, in exchange for a marginally better winding factor. Since the focus lies mostly on torque performance and quality, and since double layer configurations also offer a certain degree of fault tolerance, only double layer configurations are considered.

4.3 Topology comparison

4.3.1 Basic Assumptions

To compare the selected topologies fairly, certain parameters are kept constant (see Table 4-7). The model calculates the output torque for each topology and pole number, and adjusts the active length to achieve nominal output torque on all designs. The final calculations on weight, gravimetric torque density and shear stress are then performed. Additional parameters not listed in this section are found in Table 2-6 and Table 2-7.

Core and magnet material remain unchanged: **Vacoflux 50** (0.1mm laminations) and **Vacodym 872 TP** respectively. Additional criteria for the magnetic loading are:

- Maximum peak flux density in teeth $B_t^* \leq 2.2T$
- Maximum peak flux density in yokes $B_y^* \leq 2T$
- Maximum RMS linear current density $A_s^* \leq 40A_{RMS}/mm$

Table 4-7: Input parameters for topology comparison

<i>Parameter</i>	<i>Value</i>
Airgap length (mm)	1
Magnet height (mm)	3
Magnet coverage	0.75
Slot fill factor	0.6
Slot opening factor	0.6
Power factor	1
Operating temperature (°C)	100

4.3.2 Aluminum vs. Copper Windings

Winding material is a parameter that must remain constant in all compared topologies. The following comparison is carried out to complete the parameter set needed to go further.

Despite inferior conductivity, aluminum, with its low density (one third of copper), is considered as a possibility to increase torque density due to reduced winding weight. The comparison is done assuming equal heat generation rate per volume for aluminum and copper, at the reference temperature given in Table 4-7:

$$P_{Al}^* = P_{Cu}^* \Rightarrow \rho_{e,Al} J_{Al}^2 = \rho_{e,Cu} J_{Cu}^2 \Rightarrow \frac{J_{Al}}{J_{Cu}} = \sqrt{\frac{\rho_{e,Cu}}{\rho_{e,Al}}} \quad (4-40)$$

According to this, the current density in aluminum must be 77% that of copper. Taking **10A_{RMS}/mm² for copper** as a reference results in a current density of about **8A_{RMS}/mm² for aluminum**. The loss relationship between two machines of the same type, dimensions and performance can be determined from the conduction loss in one slot of the machine. Having assumed equal linear current densities, and also momentarily assuming equal air-gap diameters, the total Ampere-turns per slot must also be equal:

$$A_{s,Al} = A_{s,Cu} \Rightarrow \frac{J_{Al} S_{s,Al}}{\pi D_{g,Al}} = \frac{J_{Cu} S_{s,Cu}}{\pi D_{g,Cu}} \Rightarrow J_{Al} S_{s,Al} = J_{Cu} S_{s,Cu} \quad (4-41)$$

The loss ratio between both machines of the same performance is:

$$\frac{P_{Al}}{P_{Cu}} = \frac{Q \rho_{e,Al} J_{Al}^2 S_{s,Al} L}{Q \rho_{e,Cu} J_{Cu}^2 S_{s,Cu} L} = \frac{\rho_{e,Al} J_{Al}}{\rho_{e,Cu} J_{Cu}} = \frac{\rho_{e,Al}}{\rho_{e,Cu}} \sqrt{\frac{\rho_{e,Cu}}{\rho_{e,Al}}} = \sqrt{\frac{\rho_{e,Al}}{\rho_{e,Cu}}} \quad (4-42)$$

Equation (4-42) indicates 30% greater conduction loss in aluminum windings for the same performance output using the same base configuration. This is verified using the analytical model, by calculating the winding conduction loss for both cases for a *pole pair range between 75 and 125*. The lower limit is taken from 3.6.2, while the upper limit guarantees tooth widths no smaller than 5mm, which is considered as a structural limit.

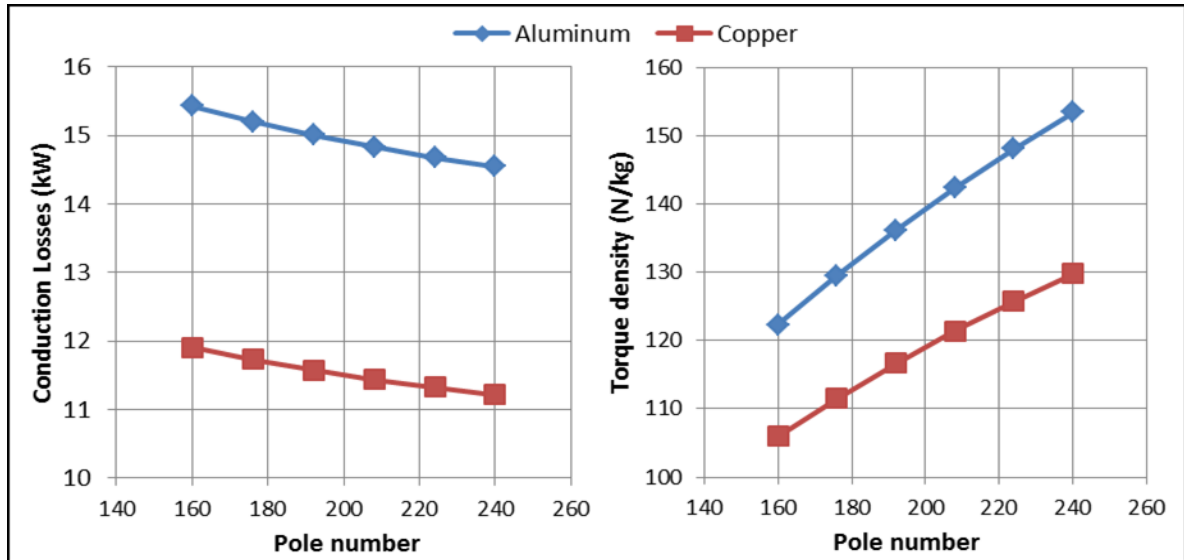


Figure 4-7: Conduction loss (left) and torque density (right) comparison for 12/16 double layer machines with Al and Cu windings

The torque density for the two materials is also compared in Figure 4-7. Aluminum has a significantly lower density, but this advantage is reduced by the need for 30% more winding material to maintain the same loading. This results in a slot area increase by the same amount, and an increase in core weight due to longer teeth. Despite this, aluminum offers a noticeable difference in terms of torque density, with an advantage between 15% and 18%.

4.3.3 Comparison between Topologies

Having already investigated the effects of winding material, the analytical model is used to compare topologies. The main axes of the comparison are torque density, shear stress, and finally total weight. Each graph contains the results for designs based on all four topologies. The topologies are coded as follows: *number of slots / number of poles of the base design*. Table 4-8 presents an overview of different characteristics, dimensions and performance results for the selected machines for a total pole number of around 200 poles. Once again, the comparison focuses on the pole region between 75 and 125 pole pairs as in 4.3.2. Regarding conductor current density a value of $8A_{RMS}/mm^2$ in aluminum windings is taken as suggested from the previous section.

Table 4-8: Comparison of different topologies in the 200-pole-number region

<i>Parameter</i>	<i>12/10</i>	<i>21/22</i>	<i>24/22</i>	<i>12/16</i>
Slot number	240	189	216	144
Pole number	200	198	198	192
Winding factor	0.933	0.953	0.983	0.866
Phases	3	3	6	3
Air-gap diameter (mm)	1366	1369	1368	1371
Active length (mm)	230	231	222	262
Flux density fundamental (T)	0.93	0.90	0.92	0.88
Tooth width (mm)	5.8	5.8	5.9	5.9
Slot height (mm)	13.1	11.8	12.4	10.9
Stator yoke height (mm)	3.2	3.2	3.2	3.2
Rotor yoke height (mm)	3.2	3.2	3.2	3.2
Shear stress (kPa)	24.4	24.1	25.2	21.2
Magnet mass (kg)	16.9	17.1	16.3	19.3
Mass (kg)	121.2	112.5	113.4	120.5
Torque density (Nm/kg)	135.3	145.7	144.7	136.1

Gravimetric Torque Density

In terms of torque density, the 21/22 3-phase and 24/22 6-phase topologies exhibit the best performance with the other two designs following at a short distance. Figure 4-8 indicates that the topologies with the highest winding factor do not necessarily exhibit the highest torque density.

Torque depends on winding factor, rotor volume, linear current loading and magnetic flux density fundamental. The current loading remains constant, whereas the magnetic flux density fundamental and the air-gap diameter vary only slightly. Turning to the shear stress, it is an indicator of torque per rotor volume. So in terms of volumetric torque density, the machines with high winding factor are very torque-dense and require lower active length for the same outer diameter. However, the weight depends largely on the core dimensions, strongly influencing the final gravimetric torque density. The gravimetric torque density is therefore the result of a complex interplay between more parameters additional to shear stress. This aspect is examined further in the next section. From this section, the observed behavior can be summarized in the following points:

- High winding factors yield high shear stress but not necessarily high gravimetric torque density
- Gravimetric torque density is proportional to the number of poles / machine modules
- 12/16-based machines exhibit high gravimetric torque density despite having a low winding factor

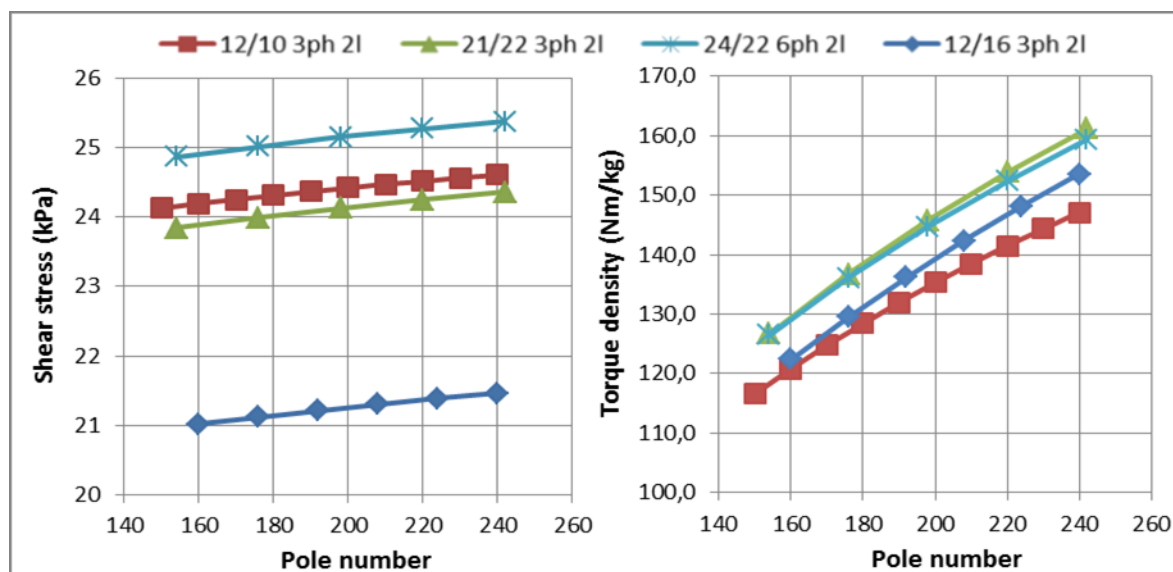


Figure 4-8: Shear stress (left) and torque density (right) for the considered topologies

Mass Distribution

The final variable for assessment is the total active mass of the machine shown in Figure 4-9. The specifications require a total mass of 150kg, corresponding roughly to 100kg of active mass, with an optimized lightweight support structure. The minimum mass achieved is 102kg with the 21-22 design for 242 poles. This indicates that the mass specification could be satisfied with a direct-drive SPM FSCW machine, when only electromagnetic considerations are taken into account.

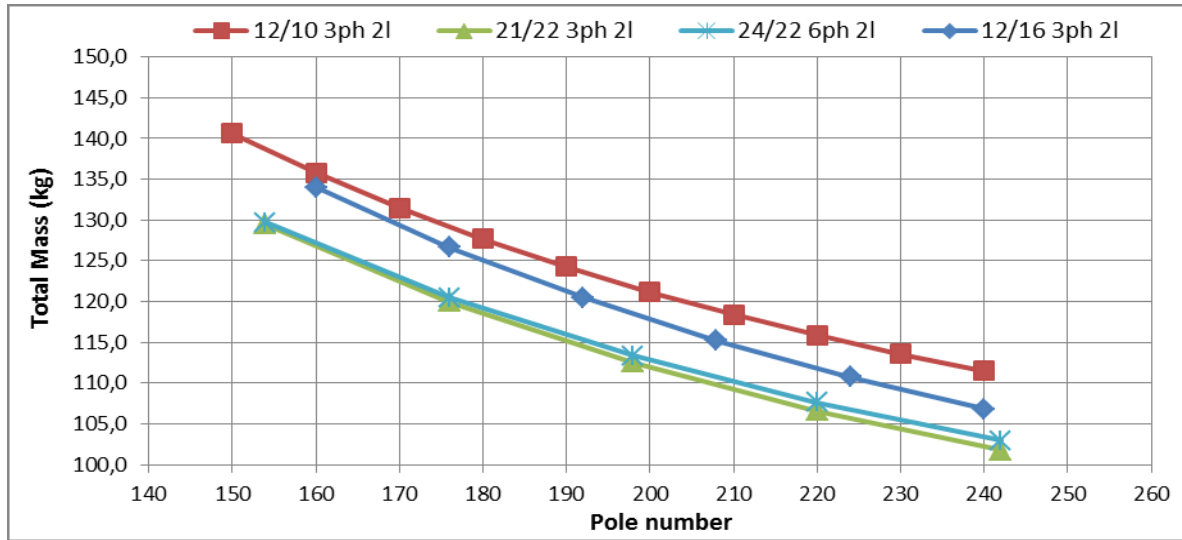


Figure 4-9: Total mass as a function of pole number

As expected, the drivers for the mass of a machine are not straightforward. As already observed, relevant parameters, e.g. winding factor, are not necessarily an indication of the gravimetric torque density. Nevertheless, at first instance *the total mass is inversely proportional to the number of poles / machine modules* as suggested by (3-11) (see Figure 4-9). To further clarify this, the total mass is broken down into rotor and stator mass.

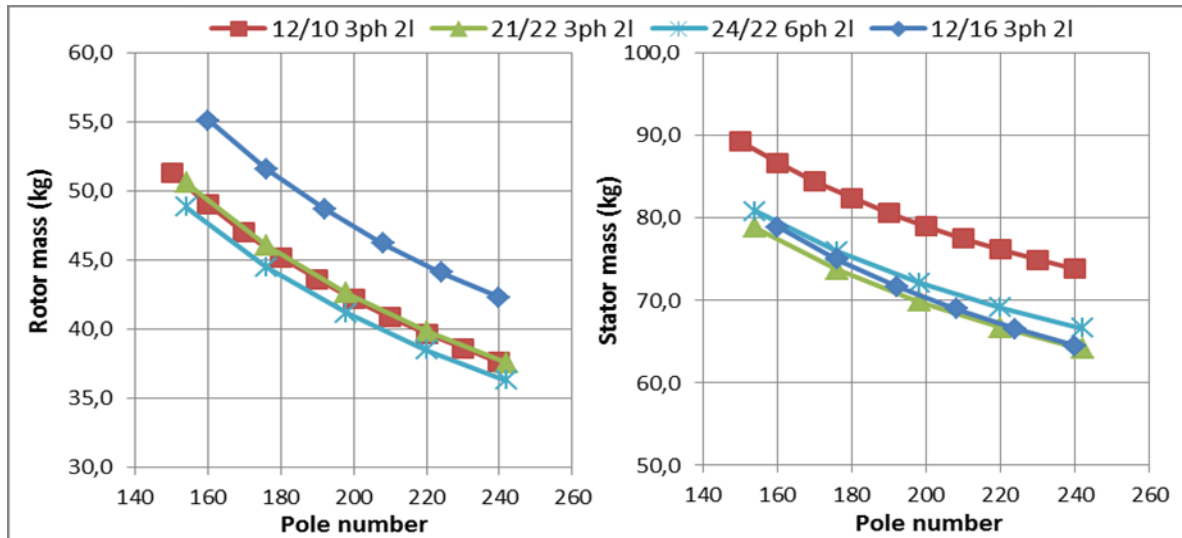


Figure 4-10: Rotor mass (left) and stator mass (right) as a function of pole number

From Figure 4-10, it is clear that rotor and stator have different mass drivers: 12/16-based configurations have clearly higher rotor mass but 12/10-based configurations have higher stator mass. Regarding the rotor mass, it is noticed that the difference between configurations follows the difference in shear stress: the higher the shear stress, the lower the mass due to shorter active length. Since current loading is the same for all machines, the difference depends on winding factor and magnetic field fundamental amplitude. A further parameter influencing rotor mass is the square of the airgap radius:

$$m_{rotor} \propto \frac{R_g^2}{p \sigma_t} = \frac{R_g^2}{p k_w B_{g1} A_s \cos \phi} \quad (4-43)$$

In the case of the stator, the relationship is more complex and follows the preliminary conclusions of the previous section. In order to better characterize it, the stator mass is broken down into core mass and winding mass. They are shown separately in Figure 4-11. Although this separation was done using aluminum windings, a similar analysis can be done for copper windings, under the same conditions, observing similar tendencies. It becomes clear that the main contributor to the overall mass is the core material in the stator, with the winding mass contributing between 15% and 25% to the total stator mass. Although the winding mass follows a tendency similar to the rotor, it shall be seen that it is determined by additional parameters as is also the core mass.

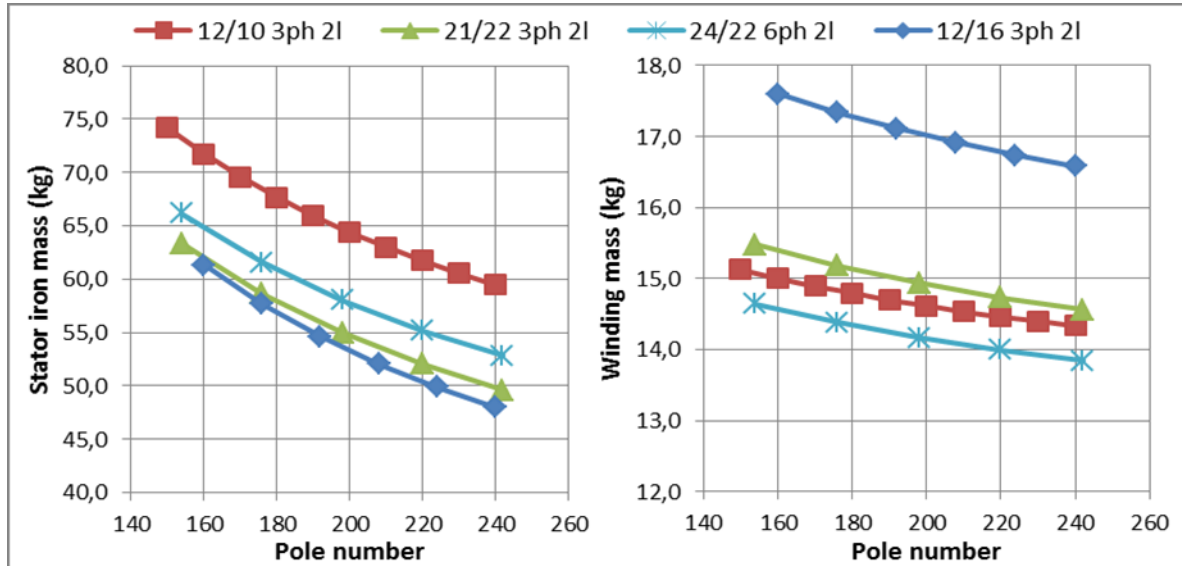


Figure 4-11: Stator mass as a function of pole number: core (left) and windings (right)

The core and windings mass are proportional to the respective mass density of the material used and the volume occupied. For both stator core and windings, the parameters influencing their volume in each dimension have to be identified first: depth d_i (radial direction), width w_i (azimuth direction) and height l_i (axial direction):

$$m_i \rho_i = V_i \propto d_i w_i l_i \quad (4-44)$$

For both windings and core, the axial length of each part is inversely proportional to the shear stress in the same manner as the rotor. It must be noted that *this approximation ignores the volume of the end windings*. This is considered acceptable since the analysis has the objective of identifying the most important parameters influencing winding volume,:

$$l_{core}, l_{winding} \propto \frac{1}{\sigma_t} = \frac{1}{k_w B_{g1} A_s \cos \phi} \quad (4-45)$$

In the same manner, the depth of both winding and core material is approximately proportional to the radial depth of the stator: stator outer radius minus airgap radius. For the

core volume, this implies ignoring the back-iron volume in the slot region, as well as the additional mass from the tooth tips. The bulk of the tooth volume and the back-iron volume behind the teeth are considered much more relevant:

$$d_{core}, d_{winding} \propto R_o - R_g \quad (4-46)$$

The only difference between the two components rests in their width: one slot pitch can be divided in a core material region (the tooth) and a winding material region (the slot itself). The tooth width as a percentage of slot pitch can be determined using the tooth flux density (in this case $2.2T$), the average airgap flux density, the pole pitch and the slot pitch according to (4-2), (4-6), (4-7), (4-18) and (4-19) as follows:

$$\frac{b_t}{\tau_u} = \frac{\frac{B_g}{B_t} b_m}{\tau_u} = d_m \frac{B_g N_s}{B_t 2p} \quad \text{for } b_m < \tau_u \quad (4-47)$$

$$\frac{b_t}{\tau_u} = \frac{B_g}{B_t} \quad \text{for } b_m \geq \tau_u \quad (4-48)$$

Also, using (4-3) the slot width as a percentage of slot pitch can be written as:

$$\frac{b_s}{\tau_u} = \frac{\tau_u - b_t}{\tau_u} = 1 - \frac{b_t}{\tau_u} \quad (4-49)$$

From these expressions, the total tooth volume and winding volume are influenced in the azimuth direction according to the following proportionality relationships:

$$w_{core} \propto \frac{b_t}{\tau_u} \quad (4-50)$$

$$w_{winding} \propto 1 - \frac{b_t}{\tau_u} \quad (4-51)$$

Replacing the previous expression in (4-44) results in the following proportionality relationships for winding and core material, for the case where τ_u is more than b_m :

$$m_{core} \propto \frac{R_o - R_g}{p k_w B_{g1} A_s \cos \phi} \left(\frac{d_m N_s B_g}{2p B_t} \right) \quad (4-52)$$

$$m_{winding} \propto \frac{R_o - R_g}{p k_w B_{g1} A_s \cos \phi} \left(1 - \frac{d_m N_s B_g}{2p B_t} \right) \quad (4-53)$$

In equal manner, for the case where τ_u is less than b_m :

$$m_{core} \propto \frac{R_o - R_g}{p k_w B_{g1} A_s \cos \phi} \left(\frac{B_g}{B_t} \right) \quad (4-54)$$

$$m_{winding} \propto \frac{R_o - R_g}{p k_w B_{g1} A_s \cos \phi} \left(1 - \frac{B_g}{B_t} \right) \quad (4-55)$$

Equations (4-52) to (4-55) deliver an important result. The stator mass depends not only on usual parameters like winding factor, rotor radius and pole number, but also on the slot/pole combination itself, the airgap flux density and the magnet coverage:

- For $\tau_u > b_m$, these are machines, for which the product $d_m N_s$ is less than the number of poles (combinations with fewer total slots than total poles are **all** in this category). The lower the value of the $d_m N_s$ product is, the lower the stator core mass and the higher the slot area tend to be. This explains why machines based on a 12/16 configuration have a lighter stator than machines based on a 12/10 configuration. All machines investigated in this chapter belong to this category.
- For $\tau_u \leq b_m$: all remaining possibilities fall in this category and are machines with more total slots than total poles *and* a high magnet coverage, so that the ratio $d_m N_s / 2p$ is higher than one. Comparing (4-52) with (4-54) for a fixed number of poles and same airgap flux density, the expression in parenthesis is always higher for this case. This indicates that combinations in this category tend to have a higher stator core mass and less slot area in comparison to the category above.

The previous analysis should be handled with care. It only gives a broad idea about the mass difference between different configurations, and is still bounded to the assumptions mentioned previously. It helps identify further important criteria for the design of machines with a high torque density and high pole number. Detailed comparisons and exact differences can only be obtained through complete modeling of all machine details. There, small differences in core dimensions can have a considerable impact on the final weight.

4.4 Analysis of 12/16 as Base Configuration

As mentioned in 4.2, special attention is given to the 12/16 topology due to the resemblance with the FSPM machine chosen for implementation in the following chapter. The most important reasons for this choice are equal winding factor, similar frequency and similar dimensions, combined with its good overall performance characteristics.

As seen already, increasing the pole number improves the torque density of a design at the expense of higher electrical frequency and smaller features, e.g. tooth and yoke width. If done without restriction, the size of teeth and yokes become structurally unfeasible. To avoid this, a strict lower limit of 5mm for the tooth width is set. This results in the final configuration 168/224 with a nominal operating frequency of 653.3Hz.

4.4.1 168/224 Machine Characteristics and Mechanical Considerations

Table 4-9 lists the basic dimensions and performance characteristics of the 168/224 machine. Additional parameters not listed remain unchanged, and are to be taken from 4.3.1 and 4.3.2. The obtained total active mass is 110.7kg at nominal performance.

This design however, only takes into account electromagnetic considerations, leading to a mechanically weak core design. For a more realistic mass, certain additions to the design need to be taken into account: yoke height has been increased to 5mm and holes have been

added for bolt connections in stator and rotor (see Figure 4-12). For these features the following assumptions are considered:

- Support bolts with a radius r_h of 2.5mm
- Clearance d around the holes of 3.5mm

The value of a in Figure 4-12 is further determined by:

$$a = \min(b_t/2, h_{sy}) \quad (4-56)$$

The support titanium bolts employed are non-magnetic. Therefore, in the case of the stator yoke, holes must be placed in such a way that the flux path is not obstructed and the path reluctance is not increased. In the case of the rotor, the hole is located in the middle of each pole, where the flux is split in two paths and the flux density is the lowest. To minimize the extra mass, the hole is placed at a distance d from the magnet. **After adding thicker yokes and support holes the total active mass rises considerably to 162kg, lowering the gravimetric torque density to a little over 100Nm/kg.**

Table 4-9: Overview of initial and optimized 168/224 SPM machines

Parameter	Initial	Optimized
Air-gap diameter (mm)	1372	1372
Active length (mm)	260	242
Flux density fundamental (T)	0.88	0,94
Tooth width (mm)	5	5.3
Slot height (mm)	10.9	11.1
Stator yoke height (mm)	2.8	2.9
Rotor yoke height (mm)	2.8	2.9
Shear stress (kPa)	21.4	23
Core mass (kg)	74.9	72.9
Winding mass (kg)	16.7	15.8
Magnet mass (kg)	19.2	11.9
Active mass (no support) (kg)	110.8	100.6
Torque density (Nm/kg)	148.1	163.1

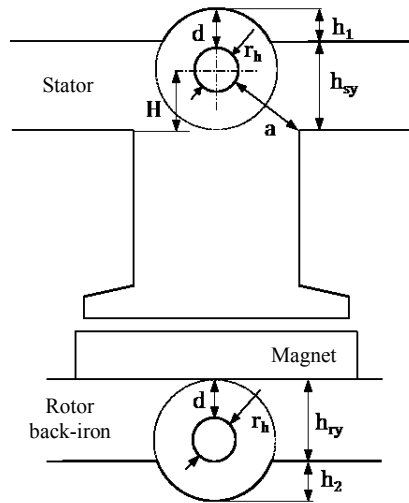


Figure 4-12: Illustration of holes and additional material required for support bolts for SPM machines

4.4.2 Potential for Mass Reduction

The previously calculated 162kg are considered unacceptable, so possibilities for mass reduction are investigated. The independent variables **airgap length** l_g , **magnet height** l_m and **magnet coverage** d_m are considered for this analysis. Previous flux density level guidelines and the minimum tooth width constraint are maintained.

As mass cannot be reduced by an airgap length increase, only smaller airgap lengths are considered: 0.3mm, 0.5mm and 1mm. Furthermore, the magnet height is swept in 1mm steps from 1mm to 5mm, and the magnet coverage in 0.1 steps from 0.65 to 0.95.

The total mass increases with a magnet coverage higher than 0.65 and a magnet height greater than 3mm (see Figure 4-13). In this region, changes in airgap length below 0.5mm do not affect performance considerably. A much more pronounced increase in total mass is observed in all cases for small magnet heights of 1mm. Because of this the magnetic loading is very low, and the mass increases at a much higher rate due to the active length needed to fulfill the performance requirement. Between these two extremes, there is an optimum point for a magnet height of 2mm. Here, the best compromise between total mass and airgap sensitivity is found for a magnet coverage of 0.75. A magnet coverage of 0.65 could offer a slightly lower mass for an airgap length of 0.3mm. However, for this point the manufacturing precision of the magnets, as well as the precision of the magnet mounting on the surface of the rotor would be critical. The mass reduction for a 0.5mm airgap is 10%, and in principle allows fulfilling the active mass requirement.

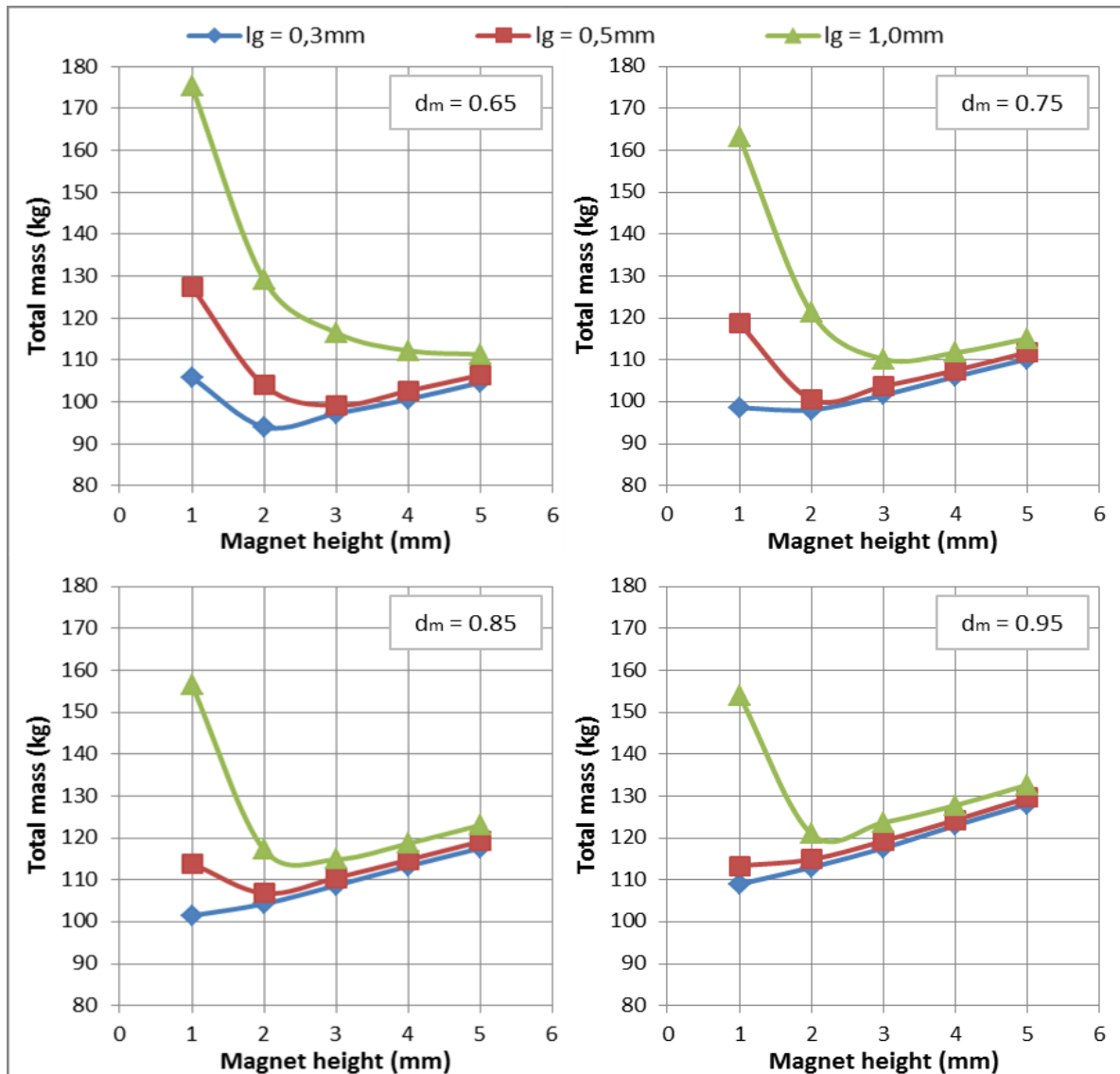


Figure 4-13: Mass as a function of airgap length, magnet height and magnet coverage

Linear and conductor current density are determined based on the thermal loading guideline given in [83]. According to this guideline, the product JA_s is unaffected by machine size and power rating. Therefore, for each value of current density, a maximum linear current loading exists that maximizes shear stress. For air-cooled PMSM machines, this guideline suggests a maximum value for the product JA_s as follows:

- $JA_s|_{max,Cu} = 42.25A_{RMS}^2/m^3$ for copper windings
- $JA_s|_{max,Al} = 32.5A_{RMS}^2/m^3$ for aluminum windings

The maximum current loading is varied to obtain an optimum, while preserving this thermal loading (see Figure 4-14). The minimum at $45A_{RMS}/mm$ is very close to the current value, and does not reduce mass significantly. The current value of $40A_{RMS}/mm$ is therefore maintained to make results more comparable to the designs in the following chapters.

The main parameters of the final design are listed in Table 4-9. Additionally, from this section the following values are taken:

- $l_g = 0.5mm$
- $l_m = 2mm$
- $d_m = 0.75$
- $A_s = 40A_{RMS}/mm$

A demagnetization calculation was performed for all designs discussed throughout the chapter. For the final design, this calculation yielded demagnetization currents at least one order of magnitude higher than the nominal phase current. This step was important given the small magnet height, and it guarantees high enough safety margin for overloading.

The final step is adding the necessary support mass. **Following the guidelines explained before, the total active mass including support is 142kg, yielding a final gravimetric torque density of 115Nm/kg.**

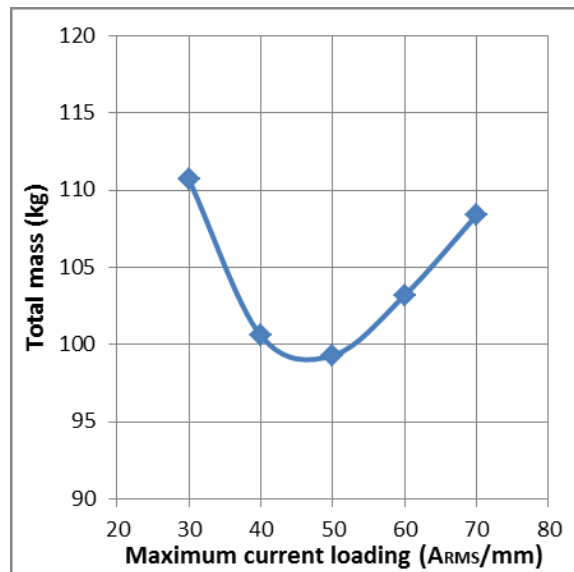


Figure 4-14: Total mass as a function of maximum current loading

4.5 Chapter Summary

The analysis of SPM machines for the proposed helicopter main rotor drive was the main objective of this chapter. A simple yet reliable machine model was proposed and validated for this purpose, which allowed drawing the following key conclusions:

- The use of aluminum windings and the resulting higher conduction loss are justified, since the thermal load remains acceptable, and the advantage in gravimetric torque density is of at least 15% for ring-type machines.

- The rotor mass is mostly determined by shear stress and airgap radius, whereas for the stator mass these parameters in addition to the slot/pole combination itself and magnet coverage play also a crucial role.
- The stator iron core is the component with the highest mass. For a fixed number of poles, a slot/pole combination with fewer slots than poles plus high winding factor tends to have the lowest stator iron mass.

Based on these findings, the machines based on the 21/22 3-phase topology show the lowest mass, closely followed by combinations based on the 24/22 6-phase topology. Nevertheless, as a benchmark for further comparison, a combination based on the third-ranked 12/16 3-phase topology was the final choice: a 168/224 machine. This configuration proved to have a good torque density despite having a relatively low winding factor of 0.87.

With this design the active mass requirement of 100kg can be fulfilled after optimization. Nevertheless, provisions for installation and structural stability add significant mass to the final design (ca. 40%). Not considering this mass would be unrealistic: at such pole pair numbers the yokes, teeth and magnets become so small, that additional mass must be added in order to support the machine. This highlights the increasing importance of structural support with increasing pole pair number. Furthermore, this shows that, increasing torque density in this manner is not only limited by frequency-dependent core losses and airgap requirement. Structural requirements also play an important role.

Final design specifications are summarized in Table 4-9 and section 4.4.2. The desired performance was achieved with a total weight of 142kg, an airgap length of 0.5mm, and a thermal loading adequate for air-cooling. This yields a final gravimetric torque density of 115Nm/kg, a value clearly not within specifications. In a final design including structural support, this will surely mean a weight penalty.

Chapter 5

Flux Switching Permanent Magnet Machines

As an iron based alternative to SPM machines, FSPM machines are examined in this chapter. The working principle and most important features of this topology were presented in 3.3.3. This chapter focuses on quick and simple modelling of FSPM machines that does not incur in long simulation times. The objective is to make an a priori performance estimation of a given configuration based on a one-time initial input from FEM simulations. FEM verification of the model shows that it can be used with silicon and cobalt steel without significant modifications. With this model, the performance sensitivity to two important design parameters is investigated: airgap length and split ratio. Further, the active mass is analyzed for potential configurations given the required performance.

Additionally, a topology variation is presented, in which the magnetic loading of FSPM machines is increased using Halbach arrays: the Halbach-FSPM machine. For this new topology, the gravimetric and volumetric torque density is analyzed, and the conditions under which it brings a weight advantage are determined.

At the same time, adequate mechanical considerations are made, and their impact on performance is analyzed. Lastly, an optimized final design is obtained, and a prediction of the final gravimetric torque density is given.

5.1 Analytical-Numerical Hybrid Model

Although rather simple in construction, analytical electromagnetic design of FSPM machines is not a simple task due to their working principle. A performance prediction based solely on the power equation and machine dimensions is not possible without the use of complex magnetic equivalent circuit (MEC) models or FEM calculations. There are three main reasons, why a linear approximation is inaccurate:

1. Double saliency makes the accurate description of flux paths and airgap permeances a complex task in any MEC analysis [112, 159, 160, 161, 162, 163].
2. Core material has a nonlinear characteristic

3. Back-iron and stator teeth show partial saturation due to flux concentration

Several studies have made efforts in this sense for FSPM machines. In [114] the different winding and stator/rotor pole configurations were studied. There, the plausible optimal configurations for conventional all-poles-wound machines were identified to be those with the number of rotor poles close to the number of stator poles. Similar analysis were done for C-Core FSPM machines in [164], concluding that the optimal combination has a number of rotor poles close to twice the number of stator poles. In [165], a comparison of stator-mounted permanent magnet machines based on the general power equation is made, and where the validity of the power equation is verified.

In all cited studies, the airgap flux density or flux linkage are variables that cannot be estimated analytically without considerable effort. The objective of this section is to provide an expression for calculating this variable as a function of the airgap length and the split ratio of the machine. There are three main assumptions on which the analytical-numerical hybrid model is based. These are explained below.

Machine Parameters

Same as in the original FSPM machine design, stator teeth, magnet height and stator back-iron are chosen equal to each other [165]:

$$b_{ts} = l_m = h_{sy} = \frac{\pi R_o SR}{2k_m N_s} \quad (5-1)$$

where b_{ts} is the stator tooth thickness, l_m is the magnet height and h_{sy} the stator back-iron thickness. The variable k_m is equal to 1 for conventional FSPM machines, and to 2 for C-Core FSPM machines. N_s is the number of stator poles distributed evenly around the machine periphery. These parameters are written as a function of the split ratio SR , defined as the ratio of airgap radius R_g to stator outer radius R_o . Figure 5-1 depicts these quantities. Furthermore, for maximum torque, the optimal rotor tooth width b_{tr} , rotor tooth height l_{tr} and rotor yoke thickness h_{ry} are chosen as one third of the rotor pole pitch. They are therefore a function of the number of rotor poles N_r [164, 166]:

$$b_{tr} = l_{tr} = h_{ry} = \frac{2\pi R_o SR}{3N_r} \quad (5-2)$$

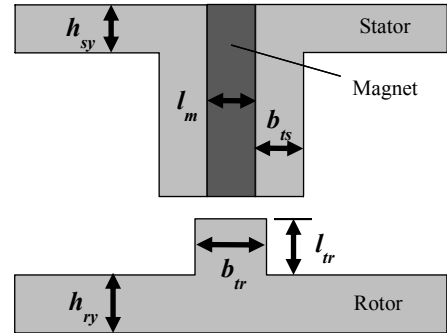


Figure 5-1: FSPM machine main dimensions

Stator/Rotor Pole Combination

There are many rotor/stator pole combinations possible in FSPM machines [114, 164, 166, 167]. For the model development, 3-phase all-poles-wound configurations are considered. These provide a balanced symmetrical back-EMF with a low second harmonic component. This condition together with equations (5-1) and (5-2) guarantee a sinusoidal operation as indicated in [113, 114, 164]. A summary is presented in Table 5-1.

Table 5-1: Stator/Rotor Pole Combinations

<i>FSPM Machine Type</i>	N_s	N_r
Conventional	12	10, 11, 13, 14
C-Core	6	11, 13

Machine configurations multiples and not multiples from those shown in Table 5-1 (with 3 or more phases) can be calculated using this model. Examples are 6-phase 24/20 and 24/22 configurations for conventional FSPM machines [167]. Some examples for C-Core FSPM machines are the 3-phase 12/22 and 6-phase 12/23 configurations.

Power Equation (Sinusoidal Operation)

The electrical power equation for FSPM machines is the same as for brushless AC machines due to its sinusoidal flux linkage, back-EMF and current [165]:

$$P_e = \frac{m_{ph}}{2} \hat{e}_{ph} \hat{i}_{ph} \quad (5-3)$$

where m is the number of phases, and \hat{e}_{ph} and \hat{i}_{ph} the peak phase back-EMF and peak phase current respectively. The peak phase back-EMF can be written as follows:

$$\hat{e}_{ph} = k_w N_{ph} \phi_g \omega_e = k_w \frac{N_s N_c}{m_{ph}} \phi_g N_r \omega_m \quad (5-4)$$

where ω_m is rotor angular speed, N_c number of turns per coil, ϕ_g the peak flux linkage per turn and k_w the winding factor. Equation (5-3) can be rewritten as follows assuming $i_d = 0$:

$$P_e = \frac{1}{2} \omega_m N_r N_s N_c \phi_g k_w i_q \quad (5-5)$$

5.1.1 Airgap and Magnet Flux Density

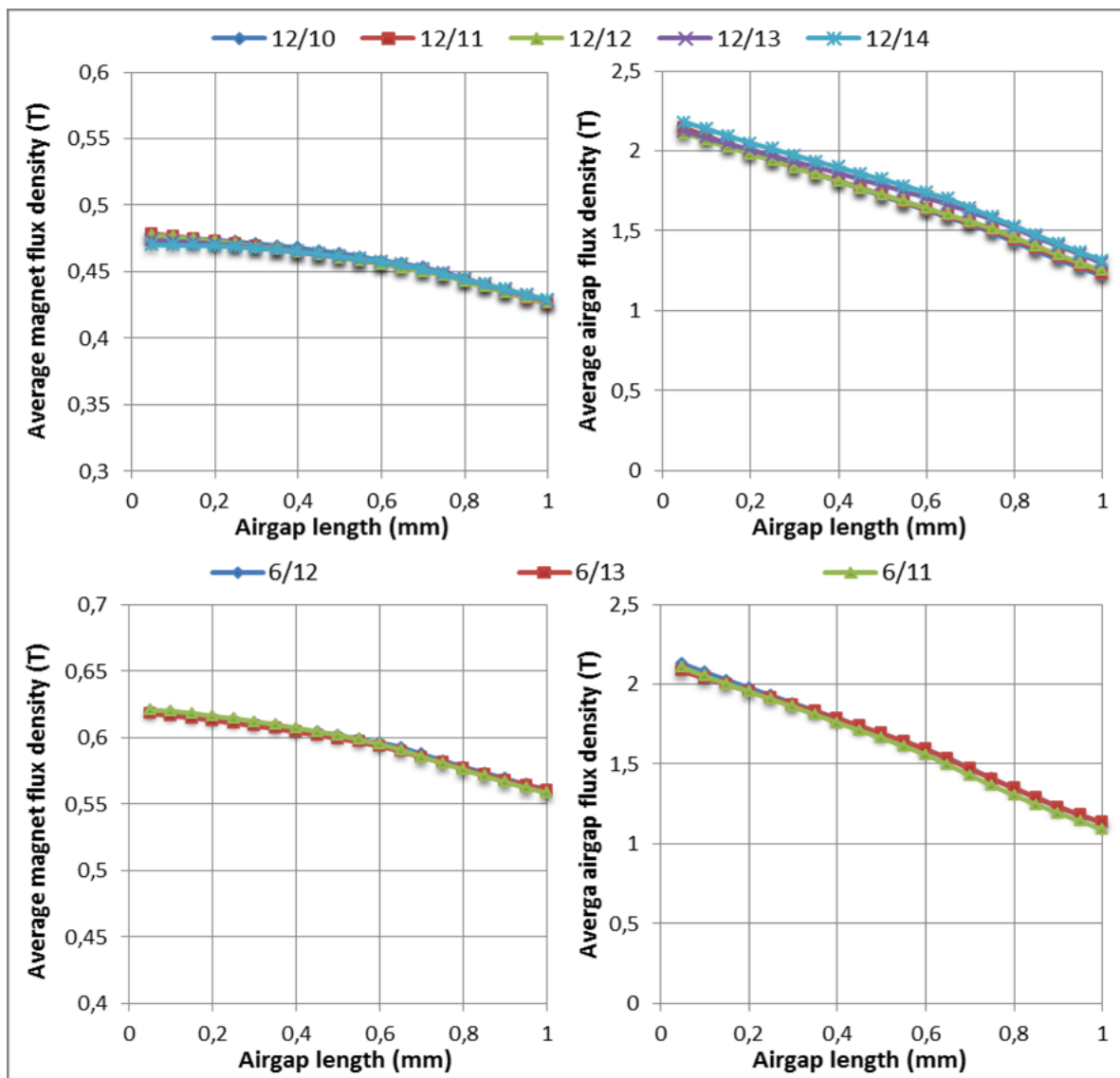
The objective of this first analysis is to determine how the airgap and magnet flux densities at the ***d*-position** vary as a function of airgap length and rotor pole number.

This is done using 2D FEM simulations for the 3-phase configurations proposed in Table 5-1, and for the respective 1-phase configurations (rotor pole number equal to stator pole number in **maximum flux linkage position**). Basic parameters for the ideal machines are summarized in Table 5-2. **M350 silicon steel** is *initially* taken as core material, together with **Vacodym 872 TP** as magnet material. Silicon steel is chosen at this point for a general development of the model, so that it can be used for multiple designs. Later on, cobalt steel is addressed as an alternative material. Remaining parameters are calculated with (5-1) and (5-2), while winding parameters are not relevant at this point.

Magnet flux density is measured along the magnet width, and airgap flux density along the overlapping region between stator and rotor teeth (see flux line diagrams in Figure 5-3). The results in Figure 5-2 show a high sensitivity to airgap length. A reduction of the airgap length by an order of magnitude (1mm to 0.1mm), causes an increase in airgap flux density of 70% and 85% for the conventional and C-core FSPM machines respectively. Regarding the operational flux density of the magnets, an increase of 10% in both cases is observed. Although significant, this increase is not as high as for the airgap flux density.

Table 5-2: Main machine parameters for conventional and C-Core ideal machines

Parameter Name	Symbol	Conventional FSPM	C-Core FSPM
Outer stator radius	R_{so} (mm)	45	
Active length	L (mm)	25	
Outer rotor radius	R_{ro} (mm)	27.5	29.25
Split ratio	SR	0.6	0.65
Stator poles	N_s	12	6
Rotor poles	N_r	10, 11, 12, 13, 14	11, 12, 13

Figure 5-2: Magnet and airgap flux densities at the d -axis as a function of airgap length and rotor pole number for conventional (top) and C-Core (bottom) machines

The flux density dependence on the rotor pole number is, on the other hand, much less pronounced. This means that, for the calculation of the maximum flux linkage of an FSPM machine, all flux paths product of the stator/rotor pole combination must not be considered in detail. Instead, a 1-phase machine with a much simple MEC model can be assumed. The effect of stator/rotor pole combination can then be incorporated with equation (5-5). This is an important finding for the development of this model.

5.1.2 Magnetic Equivalent Circuit

This section introduces a simplified MEC model to predict the flux linkage and machine performance. Such prediction is only valid in the linear region of the machine, before the torque constant becomes nonlinear due to heavy saturation.

Due to the topology characteristics, some iron regions in the machine show some saturation even in the absence of armature current (mostly in the stator teeth). With a traditional MEC model, a reliable flux density prediction is complex and time consuming (see 5.1). This can be overcome by using auxiliary nonlinear elements to characterize such behavior in the simplified MEC model.

The first step in the model development is the simplification to a 1-phase machine. From Figure 5-2, the rotor pole number does not have significant influence on airgap and magnet flux density. For a 3-phase machine, these parameters can therefore be investigated by assuming a 1-phase machine with equal number of stator and rotor poles (half the number of stator poles for C-core machines). This makes all airgap permeances equal (see Figure 5-3), so they can be described using a simple lumped-parameter function (leakage ignored):

$$\mathcal{P}_g = \mu_o \frac{b_{ts}L}{l_g} = \mu_o S_{AR,g}L \quad (5-6)$$

where l_g is the airgap length and $S_{AR,g}$ the aspect ratio of the airgap permeance.

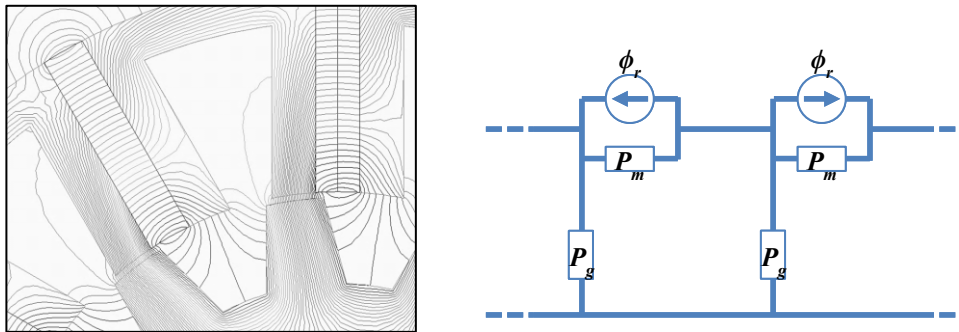


Figure 5-3: Exemplary flux line diagram of two rotor poles and two stator poles (left), and the respective MEC (right) for a 1-phase machine in maximum linkage position

Similarly, the magnet permeance is formulated as a function of its aspect ratio $S_{AR,m}$:

$$\mathcal{P}_m = \mu_o \mu_{rec} \frac{R_o(1 - SR)L}{l_m} = \mu_o \mu_{rec} S_{AR,m}L \quad (5-7)$$

Assuming lumped elements for airgap and magnet, and infinitely permeably iron (as in the MEC model in Figure 5-3), would lead to inaccurate flux densities of several Tesla at

the airgap and in the iron. On the other hand, an accurate MEC model would use many L-shaped sub-networks linked together (each consisting of a series and a parallel element), to represent the magnet and iron regions. For the air/vacuum region, complex permeance formulas would be used as in [112, 159, 161]. As mentioned before, setting up and iteratively solving such a problem is a complex and time consuming task. An intermediate solution between the two scenarios is then proposed below as a compromise.

As a second step in the development, the iron nonlinearity must be incorporated in the model, to take into account the inherent partial saturation of the machine. This is done with a single L-shaped network consisting of two nonlinear permeance elements. These are introduced between magnet and airgap permeances: one placed in parallel and one in series (see shaded elements in Figure 5-4). These elements are placed between the airgap and the equivalent circuit of the magnet, since it is there where the partial saturation takes place. It could be argued that the series element represents the magnetic voltage drop along the iron and the parallel element the flux leakage, but this is not always the case. The L-shape network topology is chosen primarily because it's the simplest version of more complex representations, and not because it represents the above mentioned quantities.

Assuming a 1-phase machine allows further simplification down to a machine with two stator poles as shown on the right of Figure 5-4. This MEC model consists now of the magnet equivalent circuit on the left and an airgap permeance on the right, connected to a two-port L-shaped network made of nonlinear elements.

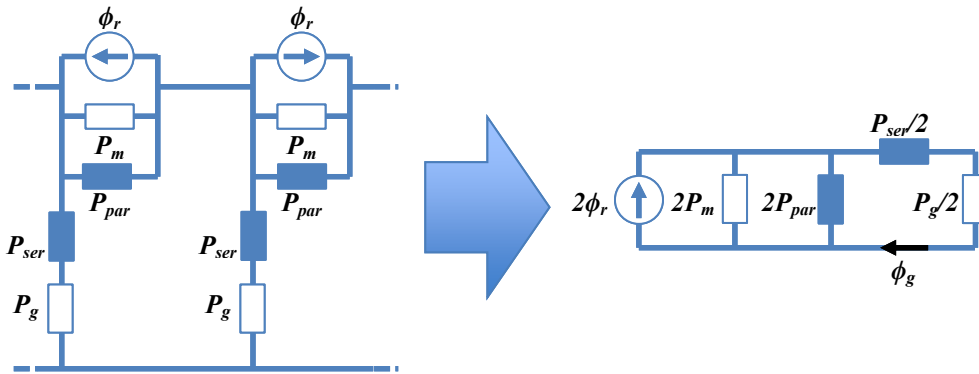


Figure 5-4: Complete (right) and simplified (left) MEC model for 1-phase FSPM machines including nonlinear elements

Using circuit theory, analytical expressions for these two elements can be formulated from the simplified MEC model in Figure 5-4. For the parallel and series elements respectively, the following expressions can be written:

$$\mathcal{P}_{par} = \frac{\mathcal{P}_m}{2} \frac{2\phi_m - \phi_g}{\phi_r - \phi_m} \quad (5-8)$$

$$\mathcal{P}_{ser} = \frac{\phi_g \mathcal{P}_g \mathcal{P}_m}{\mathcal{P}_g (\phi_r - \phi_m) - 2\mathcal{P}_m \phi_g} \quad (5-9)$$

where the airgap and magnet permeances are given by (5-6) and (5-7), and the airgap flux ϕ_g , the magnet operational flux ϕ_m , and the magnet remanent flux ϕ_r are given by

$$\phi_g = B_g b_{ts} L \quad (5-10)$$

$$\phi_m = B_m R_o (1 - SR) L \quad (5-11)$$

$$\phi_r = B_r R_o (1 - SR) L \quad (5-12)$$

All the above-defined quantities can be readily calculated with the machine's physical parameters, except the airgap flux density B_g and magnet flux density B_m . These two quantities must be calculated first using FEM simulations for different airgap length and split ratio values. Through numerical regression of the obtained data, equations for the parallel and series nonlinear permeances can be obtained in a final step.

5.1.3 Nonlinear Permeances

To calculate \mathcal{P}_{par} and \mathcal{P}_{ser} , data from FEM simulations is used. For a 1-phase C-Core FSPM machine and using the machine parameters in Table 5-2, B_g and B_m are obtained for different values of split ratio and airgap length. The split ratio is varied from 0.5 to 0.8 in steps of 0.05, and the airgap length from 0.05mm to 1mm in steps of 0.05mm. This is done here only for C-Core FSPM machines, but it is also valid for conventional FSPM machines.

Figure 5-5 shows the data from the FEM simulations: the airgap length has a strong impact on the airgap flux density, but its influence on the magnet flux density is small. On the other hand, the magnet flux density is strongly dependent on the split ratio but only lightly on the airgap length. The dependence of each quantity is mostly a function of the associated permeance, i.e. of the aspect ratio ($S_{AR,g}$ or $S_{AR,m}$), with little cross-dependence.

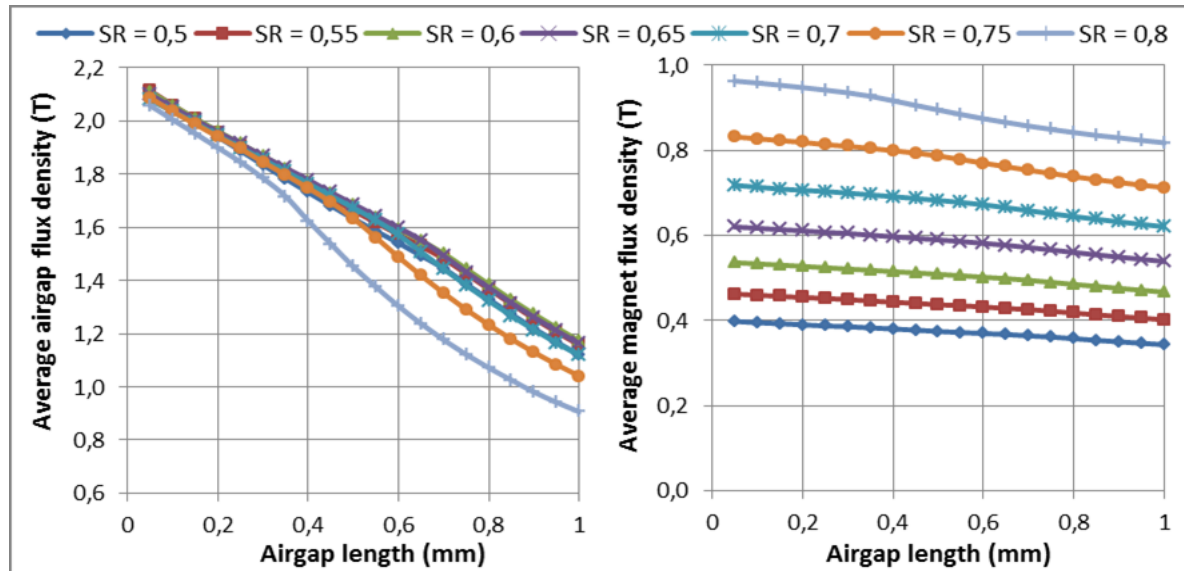


Figure 5-5: Average airgap flux density (left) and average magnet flux density (right) as a function of airgap and split ratio for ideal 1-phase 6/12 C-Core FSPM machine

So that the model can predict the flux linkage independent of machine dimensions, all equations are written as a function of dimensionless quantities: the aspect ratio of the airgap permeance and magnet permeance as defined in (5-6) and (5-7). These quantities determine the operating point of the core material by carrying intrinsic information about the

machine's airgap length and split ratio. Following this logic, \mathcal{P}_{par} and \mathcal{P}_{ser} are calculated and plotted normalized to the active length L in Figure 5-6. The obtained curves can be represented with analytical functions. The exponential function for \mathcal{P}_{par} and the Cauchy function for \mathcal{P}_{ser} are appropriate fits.

$$\frac{\mathcal{P}_{par}}{L} = K_1 e^{f_1 S_{AR,g} + K_2} + f_2 \quad (5-13)$$

$$\frac{\mathcal{P}_{ser}}{L} = f_3 \frac{f_4^2}{(AR_g - f_5)^2 + f_4^2} + f_6 \quad (5-14)$$

where K_1 and K_2 are constants and f_1 to f_6 are functions of $S_{AR,m}$ (see Table 5-3).

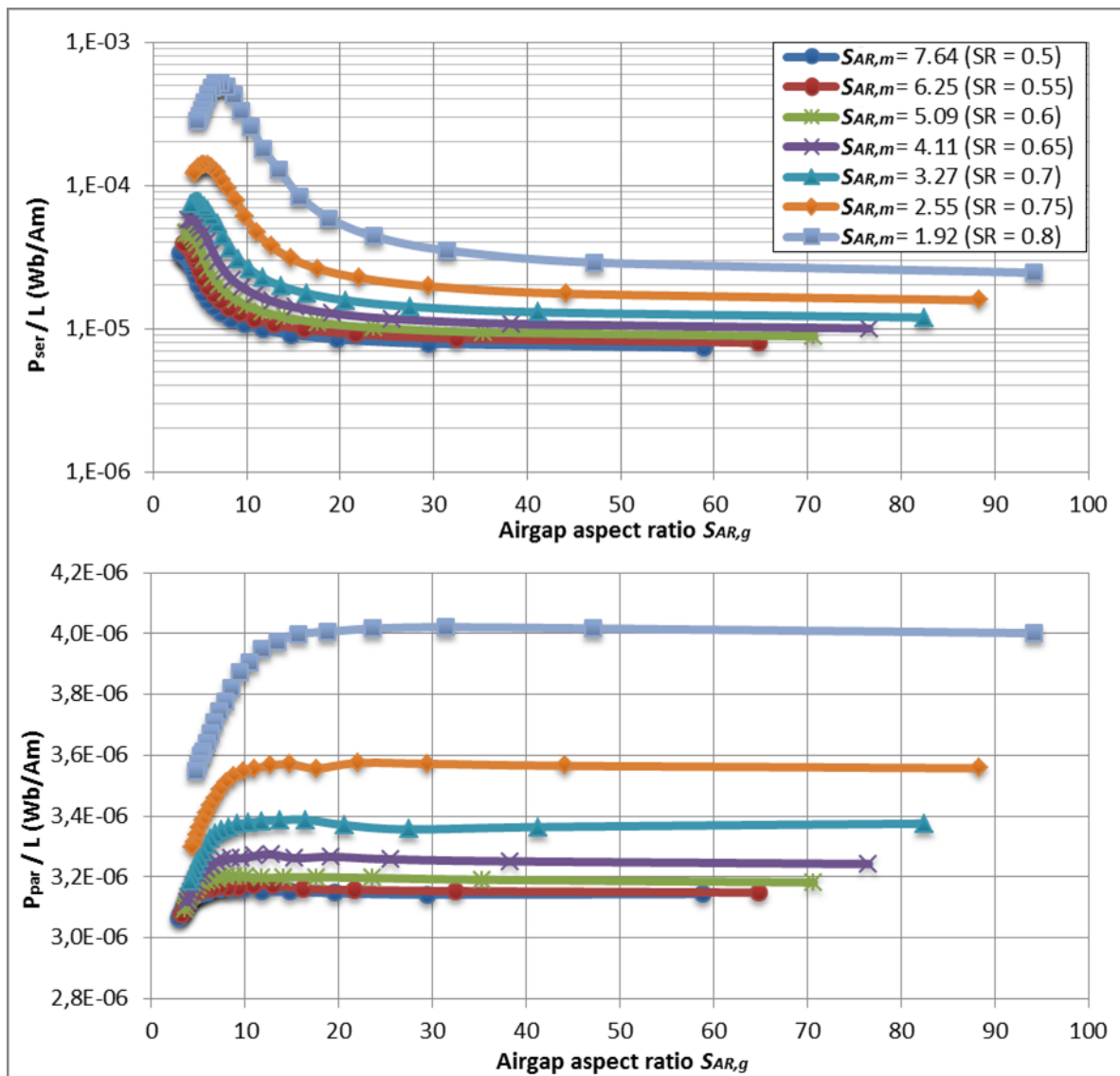


Figure 5-6: \mathcal{P}_{ser} (top) and \mathcal{P}_{par} (bottom) as a function of airgap and magnet permeance aspect ratio for ideal 1-phase 6/12 C-Core FSPM machine

Table 5-3: Constants and functions used in equations (5-13) and (5-14)

Constant / Function	Value / Expression
K_1	-4.7
K_2	-15
f_1	$0.3547 - 0.3422S_{AR,m} + 0.0165S_{AR,m}^2$
f_2	$4.4565 \times 10^{-6}S_{AR,m}^{-2} - 6.844 \times 10^{-7}S_{AR,m}^{-1} + 3.159 \times 10^{-6}$
f_3	$0.04014S_{AR,m}^{-4} - 0.03373S_{AR,m}^{-3} + 0.01069S_{AR,m}^{-2} - 0.00131S_{AR,m}^{-1} + 7.8648 \times 10^{-5}$
f_4	$1.958 + 0.8163S_{AR,m} - 0.2388S_{AR,m}^2 + 0.02397S_{AR,m}^3 - 9.144 \times 10^{-4}S_{AR,m}^4$
f_5	$5.7223S_{AR,m}^{-2} + 7.2608S_{AR,m}^{-1} + 1.8411$
f_6	$8.8459 \times 10^{-5}S_{AR,m}^{-2} - 1.3888 \times 10^{-5}S_{AR,m}^{-1} + 7.8508 \times 10^{-6}$

Coefficient functions f_1 to f_6 are fitted to polynomial functions. With these expressions the flux linkage can be recalculated using circuit theory from the simplified MEC model:

$$\phi_g = 2\phi_r \frac{2\mathcal{P}_{par} + \mathcal{P}'_g}{2\mathcal{P}_m + 2\mathcal{P}_{par} + \mathcal{P}'_g} \cdot \frac{\mathcal{P}'_g}{2\mathcal{P}_{par} + \mathcal{P}'_g} \quad (5-15)$$

with

$$\mathcal{P}'_g = \frac{\mathcal{P}_g \mathcal{P}_{ser}}{2(\mathcal{P}_g + \mathcal{P}_{ser})} \quad (5-16)$$

For the ideal 1-phase 6/12 C-Core FSPM machine, estimations within $\pm 5\%$ of the FEM simulation values were confirmed. It should be noted, that this can only be guaranteed within the region bounded by the magnet and airgap aspect ratios as specified in Figure 5-6.

5.1.4 Electromagnetic Model Verification

Using FEM simulations two very different example machines, defined in Table 5-4, are used for model validation. The machines proposed are ideal, and they were defined only for the purpose of the validation based on the guidelines from the previous sections. For both of them, the electromagnetic torque was calculated based on (5-5), and compared to the results from FEM simulations in Figure 5-7:

$$T_e = \frac{1}{2} N_r N_s N_c \phi_g k_w i_q = k_T i_q \quad (5-17)$$

where k_T is the torque constant.

The model results are in good agreement with the FEM results in the linear region of the torque characteristic, with a maximum deviation of 5%. Saturation effects start becoming strong at $100A_{RMS}$ for both machines, which equates to a linear current loading of $40A_{RMS}/mm$. From previous investigations in literature [114, 167], it is found that C-Core FSPM machines become strongly saturated at around this current loading. Furthermore, the torque constant was calculated and compared to the torque constant obtained using (5-17). For both machines, the model prediction is very accurate with a 4% difference for Machine 1 and only 1% difference for Machine 2.

Table 5-4: Test machine parameters used for model validation

Parameter Name	Symbol	C-Core Machine 1	C-Core Machine 2
Outer stator radius	R_{so} (mm)	700	
Active length	L (mm)	100	1000
Outer rotor radius	R_{ro} (mm)	678.5	485
Split Ratio	SR	0.97	0.7
Airgap	l_g (mm)	0.5	5
Stator poles	N_s	84	12
Rotor poles	N_r	182	23
Turns per coil	N_c	10	50
Number of phases	m	3	6

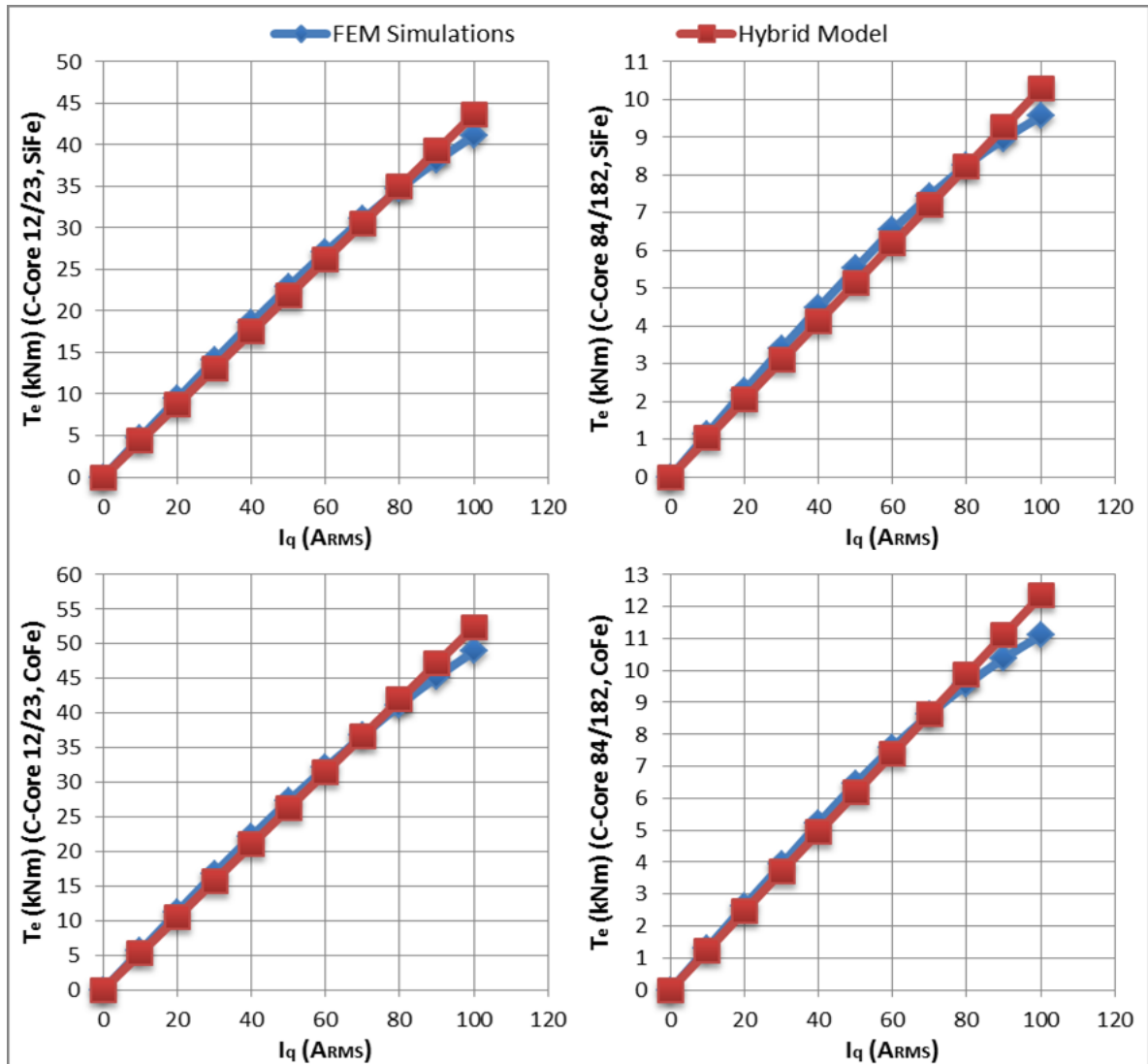


Figure 5-7: Torque for test machines using silicon steel (top) and cobalt steel (bottom)

FSPM machines operate in partial saturation even at low current loadings. Therefore, the use of an alternative material (e.g. cobalt steel, can be incorporated by adjusting the torque constant from the model by the percentage difference in saturation flux density between the two materials (20% according to Figure 3-1). This accounts for the difference in saturation and can be used as rule of thumb for predictions with different materials (see Figure 5-7).

5.2 Electrical Loading, Torque and Weight

Following the same approach from Chapter 4, all quantities needed to predict the gravimetric torque density of FSPM machines are listed in the tables below.

Table 5-5: Equations for electrical loading and weight calculation of FSPM machine

<i>Eq.</i>	<i>Definition</i>	<i>Parameter description</i>
(5-18)	$R_{sy} = R_o - h_{sy}$	Stator yoke inner radius
(5-19)	$S_s = k_f b_{ts} (R_{sy} - R_o SR) (4k_m - 3)$	Total conductor area per slot
(5-20)	$S_c = \frac{N_s S_s}{m(2N_{ph})}$	Area of one conductor
(5-21)	$I_{ph} = S_c J$	RMS phase current
(5-22)	$A_s = \frac{m(N_{ph} I_{ph})}{\pi R_o SR}$	RMS linear current density
(5-23)	$R_{ry} = R_o SR - l_g - l_{tr}$	Rotor yoke outer radius
(5-24)	$R_i = R_{ry} - h_{ry}$	Rotor yoke inner radius
(5-25)	$V_{ry} = \pi(R_{ry}^2 - R_i^2)L$	Rotor yoke volume
(5-26)	$V_{rt} = N_r b_{tr} l_{tr} L$	Total rotor teeth volume
(5-27)	$V_m = N_s l_m R_o (1 - SR)L$	Total magnet volume
(5-28)	$V_{st} = 2N_s b_{ts} R_o (1 - SR)L$	Total stator teeth volume
(5-29)	$V_{sy} = \left(\pi(R_o^2 - R_{sy}^2) - N_s h_{sy} (2b_{ts} + l_m) \right) L$	Stator yoke volume
(5-30)	$l_e = \frac{b_{ts}(4k_m - 3)}{2} + 2b_{ts} + l_m$	End-winding length
(5-31)	$V_w = mN_{ph} 2(l_e + L)S_c$	Total winding volume
(5-32)	$m_i = \rho_i V_i$	Mass of part <i>i</i> according to the respective material mass density and volume

For the electromagnetic performance, only the electromagnetic torque T_e is used. T_e is now written as a function of the number of phases m and winding turns per phase N_{ph} :

$$T_e = \frac{m}{2} N_r N_{ph} \phi_g k_w i_q = k_T i_q \quad (5-33)$$

5.3 Topology Selection: Winding Factor and Slot/Pole Combinations

The previous section focused on the C-Core FSPM machine for the development of the hybrid model. This choice prevails over conventional FSPM machines for the rest of this study due to the following reasons:

- Less core and magnet material are needed automatically reducing weight and cost, since only half the stator teeth are present
- Linear region of C-Core FSPM machines fits within the loading guidelines set for this study ($A_s = 40 A_{RMS}/mm$; $JA_s|_{max,Al} = 32.5 A_{RMS}^2/m^3$)

From the possible combinations for C-Core FSPM machines, those that comply with the hybrid model assumptions are taken. These combinations fulfill the criteria of balanced sinusoidal operation with low THD:

- **6slots/11poles, 3 phases, $k_w = 0.866$** : as a 96/176 machine (16 modules)
- **6slots/13poles, 3 phases, $k_w = 0.866$** : as a 84/182 machine (14 modules)
- **12slots/23poles, 6 phases, $k_w = 0.966$** : as a 96/184 machine (8 modules)
- **12slots/25poles, 6 phases, $k_w = 0.966$** : as a 84/175 machine (7 modules)

From the choices, the latter two could also be proposed as 3-phase systems, although with lower winding factor. As a reminder, in FSPM machines the number of rotor poles equates to the number of pole pairs in a SPM machine. Same as before, final designs using these combinations comprise multiple number of modules, each with a separate power electronics converter.

5.4 Topology Comparison

5.4.1 Basic Assumptions

In Table 5-6, a list of the parameters kept constant for comparison is given. In contrast to Chapter 4, the pole number is not varied, since it is already known that torque density increases with increasing pole number. Instead, a fixed pole number is chosen based on the frequency constraint set in Chapter 3, limiting the number of poles to 172. This is treated as a soft constraint and a pole number above this value is permitted, since it is considered that the additional frequency-related losses are manageable. Furthermore, for the 12/25-based

machine, an odd number of machine modules are allowed despite the possible unbalanced magnetic pull. As is explained in Chapter 7, the machine implementation principle proposed there allows overcoming this problem.

For the purpose of comparison, core and magnet material remain unchanged: **Vacoflux 50** (0.1mm laminations) for the core material, and **Vacodym 872 TP** for the magnet material. For the winding material aluminum is taken.

Table 5-6: Input parameters for topology comparison

<i>Parameter</i>	<i>Value</i>
Outer machine radius (mm)	700
Airgap length (mm)	0.5
Linear current density (A_{RMS}/mm)	≤ 40
Conductor current density (A_{RMS}/mm^2)	≤ 8
Slot fill factor	0.75
Power factor	1
Operating temperature ($^{\circ}C$)	100

5.4.2 Comparison between Topologies

Using the hybrid model and assumptions proposed, the performance of all four designs is compared in the same way as in Chapter 4 (see Table 5-7). Main axes of comparison are torque density, average shear stress and total weight (adjusted for nominal performance).

Table 5-7: Comparison of different topologies

<i>Parameter</i>	<i>6/11</i>	<i>6/13</i>	<i>12/23</i>	<i>12/25</i>
Slot number (Stator pole number)	96	84	96	84
Pole number (Rotor pole number)	176	182	184	175
Winding factor	0.866	0.866	0.966	0.966
Phases	3	3	6	6
Split ratio	0.976	0.975	0.976	0.976
Active length (mm)	153	127	131	119
Stator dimensions: b_{is}, l_m, h_{sy} (mm)	5.6	6.4	5.6	6.4
Rotor dimensions: b_{ir}, l_{ir}, h_{ry} (mm)	8.1	7.8	7.8	8.2
Slot height (mm)	11.2	11.1	11.2	10.4
Electrical frequency (Hz)	1027	1062	1073	1021
Average shear stress (kPa)	35.8	43.1	41.7	45.9
Mass (kg)	120.9	102.8	101.8	96.6
Torque density (Nm/kg)	135.9	159.9	161.1	170.1

From Table 5-7, the split ratio for optimum torque density for all topologies is the same for the specified airgap length and loading, i.e. 0.975. Additional weight differences are caused by the difference in stator/rotor poles and winding factor.

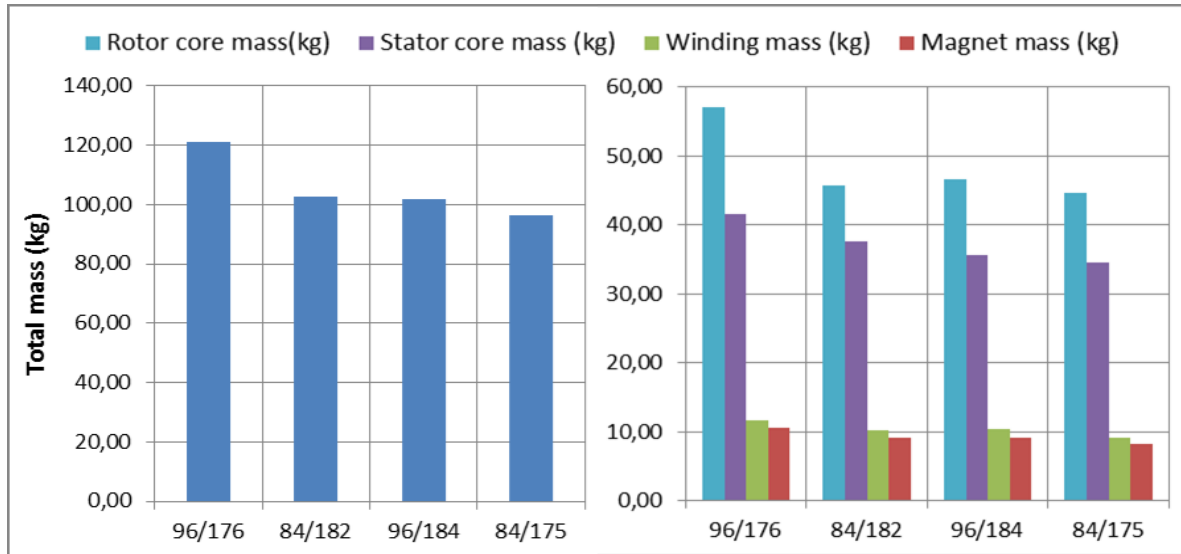


Figure 5-8: Total mass (left) and mass distribution (right) for the chosen topologies

The first and second topologies, with the lowest winding factors, have more mass in all components (see Figure 5-8). Analog to SPM machines, FSPM configurations with more rotor poles than stator poles exhibit higher torque density (lower weight). For C-Core FSPM machines, the same principle applies but for more rotor poles than twice the stator poles ($N_r > k_m N_s$). Torque is proportional to rotor volume, number of poles and loading (magnetic and electric). Taking into account this proportionality, an **approximate** relationship for the weight comparison of different machines can be written as follows:

$$m_{total} \propto \frac{SR^2}{k_w B_g A_s \cos \phi N_r} \frac{k_m N_s}{N_r} \quad (5-34)$$

Equation (5-34) should be handled with care, as it only gives a broad idea of the mass difference between different configurations. Detailed comparisons and exact differences can only be achieved through complete modeling of all machine details, since small differences in core dimensions can have a noticeable impact on the final weight.

5.5 Analysis of 6/13 C-Core Machine as Base Configuration

Compared to configurations with a 6-teeth stator (6/11 and 6/13), configurations with a 12-teeth stator (12/23 and 12/25) exhibit the highest torque density. Considering the experimental setup however (only one segment is manufactured, see Chapter 7), the 6/13 C-Core configuration is selected. The choice is based on the following features in comparison to the 12-teeth stator configurations:

- A comparable torque density
- A stator segment requiring half the active material

The design presented in Table 5-7 was calculated to deliver the target performance from the beginning and does not need recalculation.

5.5.1 84/182 Machine Characteristics and Mechanical Considerations

Using FEM simulations, the 84/182 design proposed is adjusted for leakage, model accuracy, and optimized for torque. This leads to an increase in the active length and consequently in weight. Table 5-8 lists the resulting modified parameters.

Table 5-8: Overview of initial and optimized 84/182 FSPM machines

<i>Parameter</i>	<i>Initial</i>	<i>Corrected</i>
Active Length (mm)	127	130
Stator tooth width (mm)	6.4	7.6
Magnet height (mm)	6.4	7.6
Stator yoke height (mm)	6.4	6.5
Average shear stress (kPa)	43.1	40.2
Core mass (kg)	83.3	86.8
Winding mass (kg)	10.3	10.6
Magnet mass (kg)	9.2	11.2
Active mass (no support) (kg)	102.8	108.6
Torque density (Nm/kg)	159.9	151.1

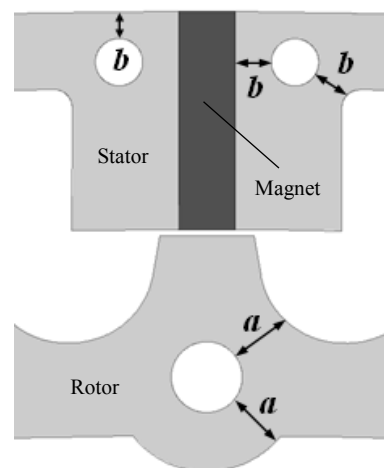


Figure 5-9: Illustration of holes and additional material required for support bolts for FSPM machines

Furthermore, in the same manner as for SPM machines, provisions for structural support are added. In the case of FSPM machines, the dimensions of the different structures do not reach the 5mm limit set for SPM machines due to the frequency constraint. The consequence of this, together with the higher average shear stress, is that the additional weight needed for support is not as high as for SPM machines. The additional mass is calculated based on the parameters depicted in Figure 5-9 with the following values:

- Stator support bolts with 2mm radius and a clearance a of no less than 2.5mm
- Rotor support bolts with 3mm radius and a clearance b of no less than 5mm

The placing of rotor and stator bolts follows the same principle as before: the flux path reluctance may not be increased, and the torque performance must be maintained. **After adding the support holes, the total active mass and length rise to 122kg and 136mm respectively, lowering the gravimetric torque density to a little over 135Nm/kg.**

5.5.2 Potential for Mass Reduction

Section 5.4 showed that FSPM machines develop a higher average shear stress than SPM machines under similar electromagnetic conditions with equal airgap length. Furthermore, the additional weight for structural support is a lower percentage of the total active weight. Despite this, the required gravimetric torque density is not reached with optimized machine dimensions. In contrast to SPM machines, FSPM machines show a high of the airgap flux density to changes in airgap length (see Figure 5-5). This characteristic opens the possibility to improve performance.

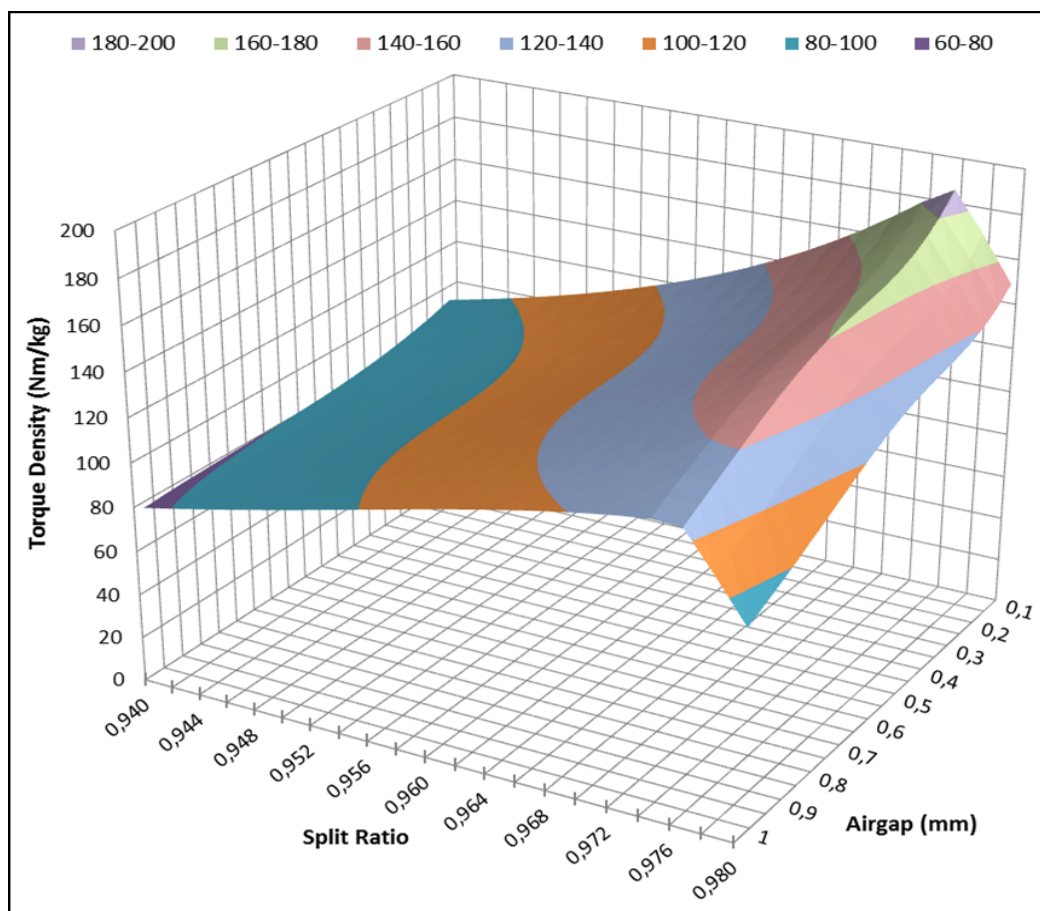


Figure 5-10: Torque density map for initial 84/182 FSPM machine

Figure 5-10 shows the torque map obtained using the hybrid model, with which the optimum split ratio was obtained for the initial 84/182 design. It shows that the gravimetric torque density can be improved, if the airgap length is reduced below 0.5mm. The remaining weight penalty depends on the performance at the final airgap length. A target value of 0.1mm is set, to achieve the highest performance technically possible.

Reducing the airgap below 0.5mm is very challenging and implies a higher-than-average mechanical complexity as explained in [40] and [130]. Guidelines found in literature [169] suggest an airgap length of at least a thousandth of the machine outer radius, i.e. 1.4mm in this case. Such guideline considers manufacturing tolerances, mechanical and thermal expansion, but also mechanical stiffness and stability of the machine frame and shaft. These aspects are the main factors influencing the mechanical design. The resulting components have to withstand and stabilize the magnetic forces between stator and rotor, which tend to close or expand the airgap [110]. Chapter 7 addresses this problematic in detail, and for the time being it is assumed that an airgap length below 0.5mm is achievable.

If successful, a 0.1mm airgap length would yield a torque density of up to 150Nm/kg, resulting in a final weight of 109kg and an active length of 122mm. Although a considerable improvement, the next section explores a further possibility for mass reduction by means of a topology modification.

5.6 Halbach-FSPM Machine

This section proposes an alternative topology that makes use of Halbach arrays in order to improve machine power and torque. The design principle of the new topology is introduced and two implementation alternatives are presented.

5.6.1 Flux Enhancement Principle

From (5-33), the electromagnetic torque is proportional to airgap magnetic flux ϕ_g . Formulated analytically, the airgap magnetic flux equals the magnetic flux from the magnets minus the leakage flux:

$$\phi_g = k_\sigma \phi_m = k_\sigma B_m(SR, l_g)(1 - SR)R_o L \quad (5-35)$$

where $B_m(SR, l_g)$ is the operational flux density of the magnet as a function of split ratio and airgap length. k_σ is the flux leakage coefficient (accounted for by the nonlinear permeance element \mathcal{P}_{par} proposed in 5.1.3). From Figure 5-5, the split ratio affects B_m strongly but B_g only slightly. Therefore, a split ratio increase does not reduce the airgap magnetic loading considerably, despite the resulting magnet material reduction. A higher torque can then be achieved for a fixed machine volume, since a longer torque arm and greater airgap area can be realized. Additionally, if the airgap magnetic loading can be increased, the machine performance is further improved. To achieve this without reducing airgap length an approach is developed by exploiting the following machine features:

- Every stator core has a fixed “magnetic polarity” (flux lines of a magnet are either all going in or coming out of every core)
- The “magnetic polarity” changes from one core to the next one
- The area on the back-side of the stator is not used for any purpose

These features open the possibility to enhance the magnetic flux in each core piece by using Halbach arrays placed on the back-side of the stator (see Figure 5-11).

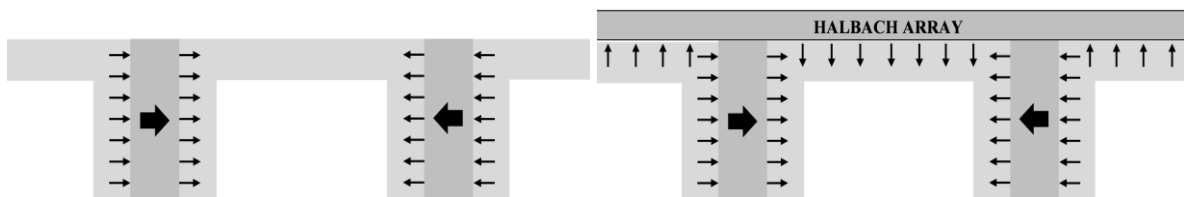


Figure 5-11: Flux line directions within one stator piece for an unmodified machine (left), and a machine with a Halbach array (right)

On the back of the machine, magnet material can be placed and protected between the stator and motor housing. Mechanically, material placed here is not subjected to stress or centrifugal force. Magnetically, the Halbach array injects flux of the corresponding polarity into each stator piece. A percentage of the flux then comes from the embedded magnet mass in the stator, while the rest comes from the Halbach array:

$$\phi_{g,new} = k_{\sigma}^* \phi_m + k_{\sigma,array} \phi_{array} \quad (5-36)$$

where ϕ_{array} is the Halbach array flux, $k_{\sigma,array}$ is the array flux leakage coefficient and k_{σ}^* is the new magnet flux leakage coefficient in the presence of the Halbach array.

The new leakage coefficient k_{σ}^* has a smaller value than the previous k_{σ} , since leakage through the back surface of the machine does not take place. This is an important advantage of placing a Halbach array around the machine, besides the increase in total flux.

The leakage paths and flux line diagram in Figure 5-12 show considerable leakage through the back of the machine. By using a Halbach array, this type of leakage is eliminated as the machine is magnetically “sealed” by the array. The remaining field outside the machine is the weak-side field of the Halbach array, plus the array leakage occurring at the axial ends of the stack (quantified by $k_{\sigma,array}$). This leakage however is not visible in the flux line diagrams in Figure 5-12, since a 3D simulation is required to visualize it, as well as the leakage on top and bottom of the magnets.

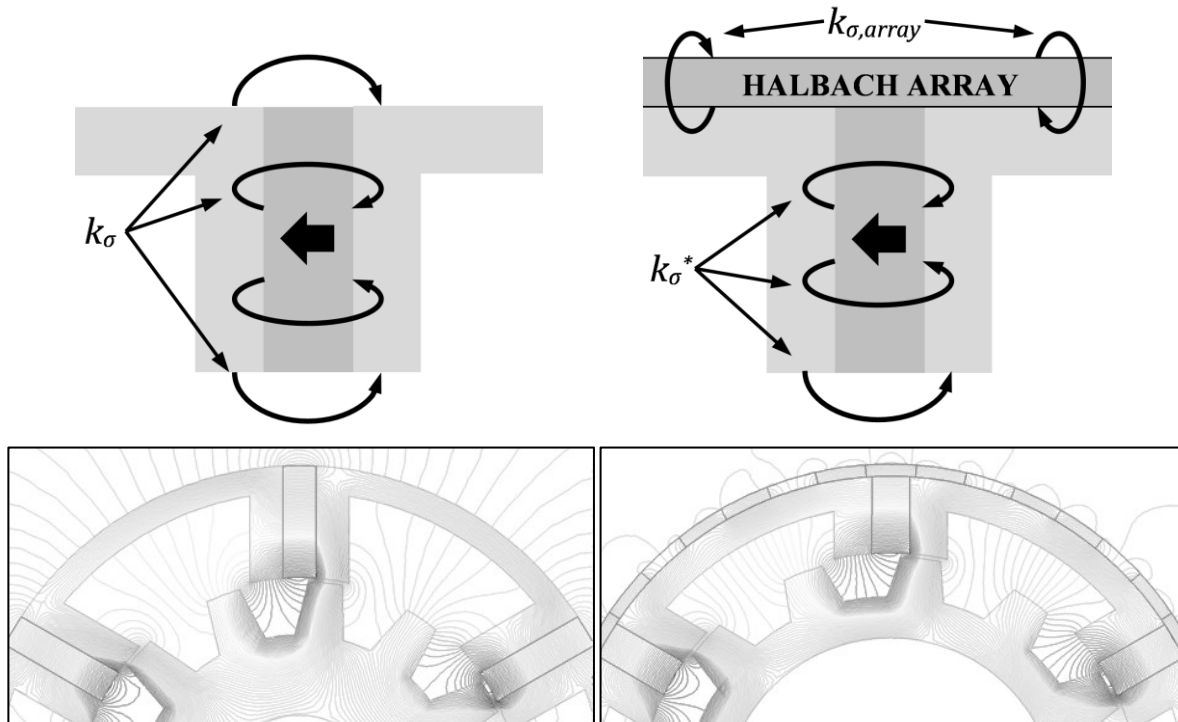


Figure 5-12: Leakage flux paths without Halbach array (top left) and with Halbach array (top right), and exemplary 2D FEM flux line diagrams of a 6/13 FSPM machine without Halbach array (bottom left) and with Halbach array (bottom right)

The addition of a Halbach array increases the total radius of the machine by the array thickness D . Accordingly, the split ratio must be corrected by this amount:

$$SR_{new} = \frac{R_{ro}}{R_o + D} \quad (5-37)$$

With the basics of the flux enhancement principle explained, the next section goes into detail about the Halbach array configuration.

5.6.2 Halbach Arrays in Free Space

This section analyses an alternative array configuration. Compared to the traditional Halbach array, the alternative potentially makes better use of magnet material for the particular use in FSPM machines. As a starting point, from [169] the peak flux density of a linear Halbach array of wavelength λ_1 in *free space* is given by:

$$B_{peak,1} = B_r \frac{\sin(\pi/N_{array})}{\pi/N_{array}} \left(1 - e^{-\frac{2\pi D}{\lambda_1}}\right) e^{-\frac{2\pi y}{\lambda_1}} \quad (5-38)$$

where N_{array} is the number of blocks per wavelength, and y the perpendicular distance to the array surface on the strong side. For an array height L (equal to the machine axial length), the array flux over a distance of a quarter of a wavelength can be calculated by integrating equation (5-38):

$$\phi_{array,1} = L \int_0^{\lambda_1/4} B_1(x) dx = L \int_0^{\lambda_1/4} B_{peak,1} \sin\left(\frac{2\pi}{\lambda_1} x\right) dx = \frac{\lambda_1 L}{2\pi} B_{peak,1} \quad (5-39)$$

A second array with wavelength λ_2 equal to half the initial wavelength λ_1 is assumed. Integrating over an equal distance i.e. half of λ_2 , the array flux is given by equation (5-40). A graphical representation of both cases is shown in Figure 5-13.

$$\phi_{array,2} = L \int_0^{\lambda_2/2} B_2(x) dx = L \int_0^{\lambda_2/2} B_{peak,2} \sin\left(\frac{2\pi}{\lambda_2} x\right) dx = \frac{\lambda_2 L}{\pi} B_{peak,2} \quad (5-40)$$

with

$$\lambda_1 = 2\lambda_2 \quad (5-41)$$

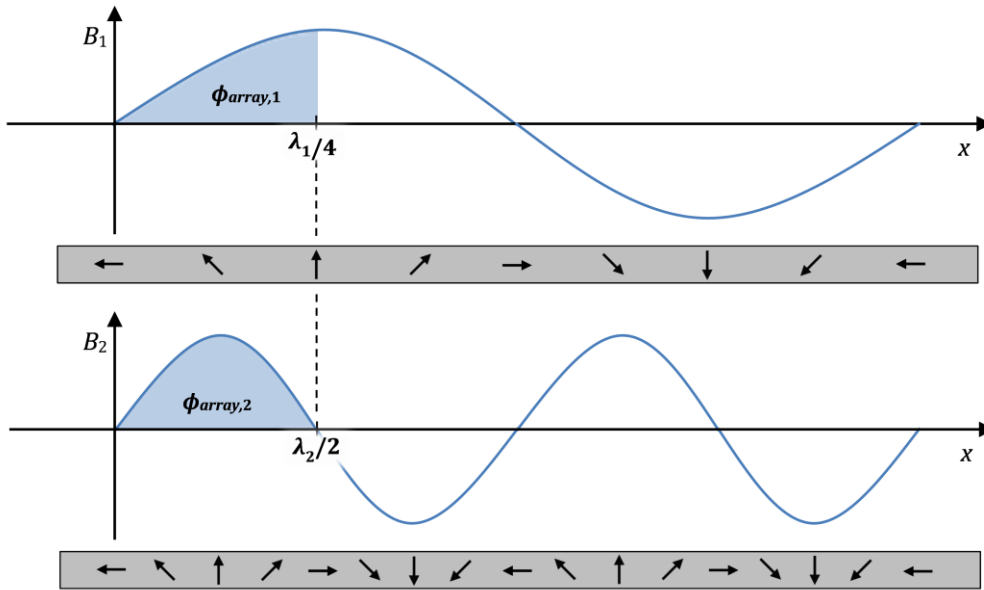


Figure 5-13: Depiction of equations (5-39) and (5-40) with the respective Halbach array polarization sequences

By replacing (5-41) in (5-40), and gathering all other terms in a single factor K (equal in both cases), the calculated flux in equations (5-39) and (5-40) takes the following form at the array surface ($y = 0$),:

$$\phi_{array,1} = K(1 - e^{-z}) \quad (5-42)$$

$$\phi_{array,2} = K(1 - e^{-2z}) \quad (5-43)$$

with

$$z = \frac{2\pi D}{\lambda_1} \quad (5-44)$$

$$K = \frac{1}{2\pi} L \lambda_1 B_r \frac{\sin(\pi/N_{array})}{\pi/N_{array}} \quad (5-45)$$

The flux difference between (5-42) and (5-43) depends on the exponential term only (all other variables being equal). Dividing then (5-43) by (5-42) results in:

$$\phi_{array,1} \leq \phi_{array,2} \quad \text{for all } z \quad (5-46)$$

Equation (5-46) delivers an interesting result: $\phi_{array,2}$ is always higher than or equal to $\phi_{array,1}$ over a length $\lambda_1/4$. Over such distance, more flux is obtained from an array with wavelength λ_2 making more efficient use of the array material. For the use in FSPM machines, this feature can be exploited to minimize the additional weight from the Halbach array. This is explained more in detail in the following section.

5.6.3 Use of Halbach Arrays with Wavelength λ_2 on FSPM Machines

Based on the previous discussion, the wavelength λ_1 of a Halbach array is set equal to twice the length of the outer pitch of one stator pole. The hypothetical Halbach array is placed on the back of the machine such that the respective polarities of Halbach array and embedded magnets coincide. Each Halbach array pole encompasses the length of a U-shaped iron core (C-shaped in C-core machines), as observed on the left of Figure 5-14.

From (5-46) it is known that for a length of $\lambda_1/4$, a Halbach array with wavelength λ_2 provides more magnetic flux than a Halbach array with wavelength λ_1 . However, using a traditional Halbach array with wavelength λ_2 in the proposed case of a FSPM machine would be pointless. This is because a complete wavelength λ_2 would encompass the length of one U-shaped iron core. The iron core would provide a magnetic short circuit path for the magnetic flux of the array, rendering it useless as no flux enhancement would occur.

In order to take partial advantage of the higher flux of an array with wavelength λ_2 , a 180° phase reversal of the flux density profile is attempted at the middle of each slot. This can be done by rearranging the magnet blocks, so that a flux density profile similar to the one shown on the right of Figure 5-14 is achieved. The magnet arrangement is also shown, where it can be seen that at the point of phase reversal the magnet block with 90° polarization direction is suppressed to smoothen the transition to the adjacent array. This minimizes the boundary effects between two the arrays placed next to each other. FEM simulations in Figure 5-15 show the resulting profile of the proposed arrangement, where such boundary effects are observed.

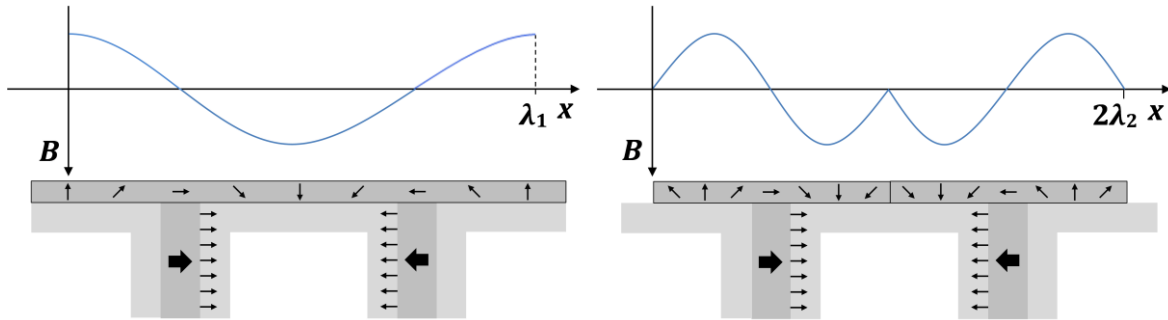


Figure 5-14: Flux enhancement in one stator core piece by means of one Halbach magnetic pole (left) and two Halbach magnetic poles (right). Field profiles are shown along the machine-array boundary or x -coordinate on the strong-side of the array

The objective is to obtain more flux from two poles belonging to arrays with wavelength λ_2 , than from one pole of a traditional Halbach array with wavelength λ_1 . However, the closed form solution presented in equation (5-38) does not apply to Halbach arrays placed in this alternative manner. This makes equation (5-46) invalid.

If the advantage of Halbach arrays with wavelength λ_2 still exists in such an arrangement, it must be quantified using FEM simulations. These simulations also allow taking into account the machine iron core. Due to its high permeability, the core makes the analytical prediction of the resulting flux density an even more complicated task. For different values of z (see equation (5-44)), both arrangements shown in Figure 5-14 are simulated in the presence of silicon steel. The total array flux corresponding to one stator core piece (over a length $\lambda_1/2$) is calculated. The boundary effects and presence of iron reduce the overall advantage of $\phi_{array,2}$ over $\phi_{array,1}$ as follows:

$$\phi_{array,1} \leq \phi_{array,2} \leq 1.2\phi_{array,1} \quad (5-47)$$

for

$$0 < D \leq 0.065\lambda_1 \quad \text{or} \quad 0 < D \leq 0.13\lambda_2 \quad (5-48)$$

Equations (5-47) and (5-48) give the conditions for profile choice: the alternative magnet arrangement with phase shift should be used for arrays no thicker than 13% of λ_2 . In this interval, $\phi_{array,2}$ is higher than $\phi_{array,1}$ by as much as 20%, making more efficient use of magnet material. Beyond this thickness, the traditional Halbach array is recommended.

Figure 5-15 shows the resulting flux density profile for the alternative Halbach array in the presence of the machine iron core. From there, mainly three aspects are worth noticing:

- **Boundary effects between arrays:** simulations show abrupt field gradient changes and flux density reversal at the middle of the slot, i.e. at 0° , 60° and 120° . Here, phase reversal between arrays takes place along 19% of the outer stator pole pitch, with a lowest negative value of 60% the maximum flux density.
- **Zero-flux-density regions:** these regions are centered at the stator pole axis i.e. at 30° and 90° and spanning for ca. 6° . They correspond to the magnets embedded in the iron cores. For the Halbach array, this represents a permeability modulation causing zero normal flux density. All flux from the array travels tangentially from one core piece to the next, through the magnet block with 90° polarization (polarization parallel to that of embedded magnet).

- Flux density ripple:** the overall flux density profile presents a marked sinusoidal fundamental plus a higher harmonic component. This content is of the same order as the number of blocks per array wavelength, in this case 8th order. This 8th order ripple is product of the varying permeability that each block “sees” in the presence of the machine core. The modified flux excitation results in a redistribution of the flux of each block towards its edges (edges are path with the least magnetic reluctance). Since this happens for every block, a pronounced ripple is observed at the boundary between every two blocks of an array. Here, additional flux concentration takes place.

However, the aforementioned aspects have no effect on machine performance. Of importance here is the flux enhancement obtained from the arrays and not the profile shape or harmonic content. In this aspect, the alternative Halbach array configuration (constrained by equation (5-48)) provides a moderate advantage over the traditional one. In terms of machine performance, the advantage of this configuration is quantified in the next section.

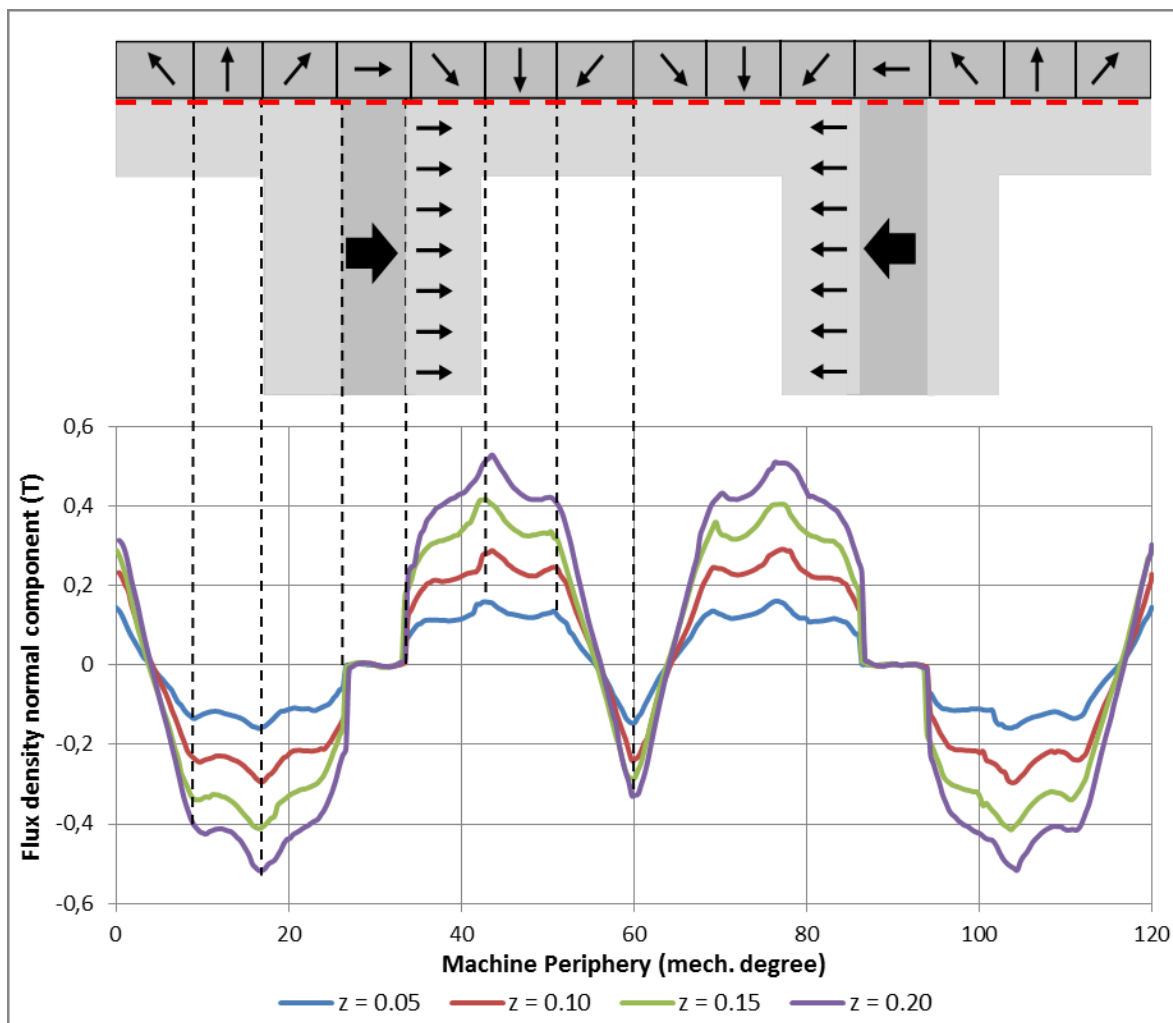


Figure 5-15: Flux density normal component measured on red dotted line at machine-array boundary along 120° of machine periphery ($y = 0$ and $N = 8$)

5.7 Analysis of a 84/182 Halbach-FSPM Machine

This section compares the unmodified FSPM machine with the Halbach-FSPM machine. It makes further mechanical considerations to determine under which conditions the use of Halbach arrays is justified.

5.7.1 Use of Flux Enhancement and Further Mechanical Considerations

Using the technique explained in the previous section, the implementation on an ideal design as defined in 5.5.1 and 5.5.2 is examined. For different array thicknesses and airgap length values, the volumetric and gravimetric torque densities are obtained with FEM simulations. The thickness is varied up to 6% of λ_2 , which according to (5-48), suggests the use of the alternative Halbach array with wavelength λ_2 . The results are shown in Figure 5-16 normalized to the optimal values obtained without a Halbach array:

$$\frac{T_e}{(V_{act}, m_{act})} \Big|_{norm} = \frac{T_e / (V_{act}, m_{act}) \Big|_{opt, D \neq 0}}{T_e / (V_{act}, m_{act}) \Big|_{opt, D = 0}} \quad (5-49)$$

The total torque increase with array use depends on the airgap length of the machine. Without array, the magnetic loading is low for long airgap lengths, so its use contributes considerably to the output torque: up to 17% for a 1mm airgap and an array thickness of 3mm. With decreasing airgap the magnetic loading increases, most leakage is eliminated, and the machine becomes increasingly saturated, even without array. At such point the maximum array contribution is for a thickness of 2mm, yielding a torque increase of 4%.

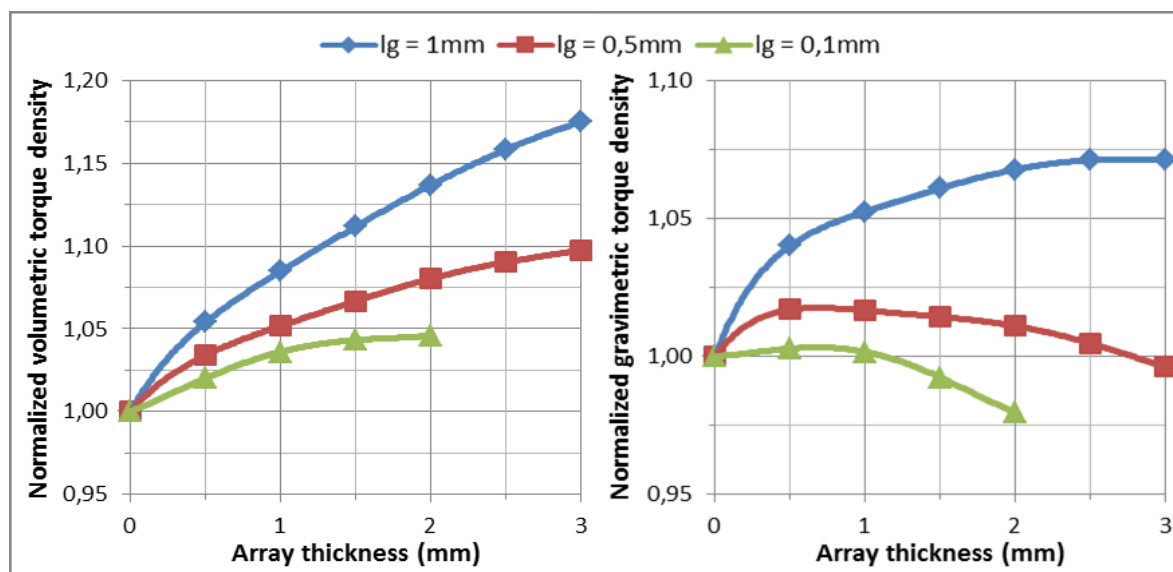


Figure 5-16: Normalized volumetric (left) and gravimetric (right) torque density for a 84/182 Halbach-FSPM machine

For the case of the gravimetric torque density, the use of a Halbach array is less effective. The additional mass from the array offsets the torque improvement more rapidly with increasing array thickness. In the case of a 1mm airgap, an increase of 7% can be obtained. However, for very short airgap lengths the gravimetric torque density remains constant, or drops below the normalization value. Under such conditions, the use of the Halbach array is not justified, since it does not contribute to the machine's performance or is even deterrent to it.

These simulation conditions, however, do not take into account any mechanical or manufacturing considerations. In particular, the mechanical alignment needed between single C-shaped iron cores at the required airgap radius is critical. At such radius and short airgap length, not only the precise manufacturing of the airgap profile is required for every C-shaped core. Also, a precise alignment between cores is necessary such that a constant airgap radius can be guaranteed along the machine's circumference. Consequences of improper alignment vary from unacceptable local airgap clearance, to increased torque ripple and possible vibrations. This is possible even for a long airgap length, as was observed in 5.1 from the discussion on performance sensitivity to airgap length variation.

A solution to this issue has already been presented in [107], and is shown in Figure 3-8: the use of thin bridges to link the stator cores at the outer surface ensures the alignment between them, since they are cut as a single piece. A bridge thickness of 1mm was recommended by the core material manufacturer Vacuumschmelze that acted as development partner for this study. This is considered a reasonable compromise to guarantee manufacturing tolerances and mechanical stability at the intended machine size.

Using such bridges, however, increases the flux leakage in a normal FSPM machine without Halbach array. The effect on torque density is a decrease of about 15 Nm/kg for all airgap lengths (see Figure 5-17). Under these conditions, the use of flux enhancement with Halbach arrays compensates the flux lost to leakage through the bridges.

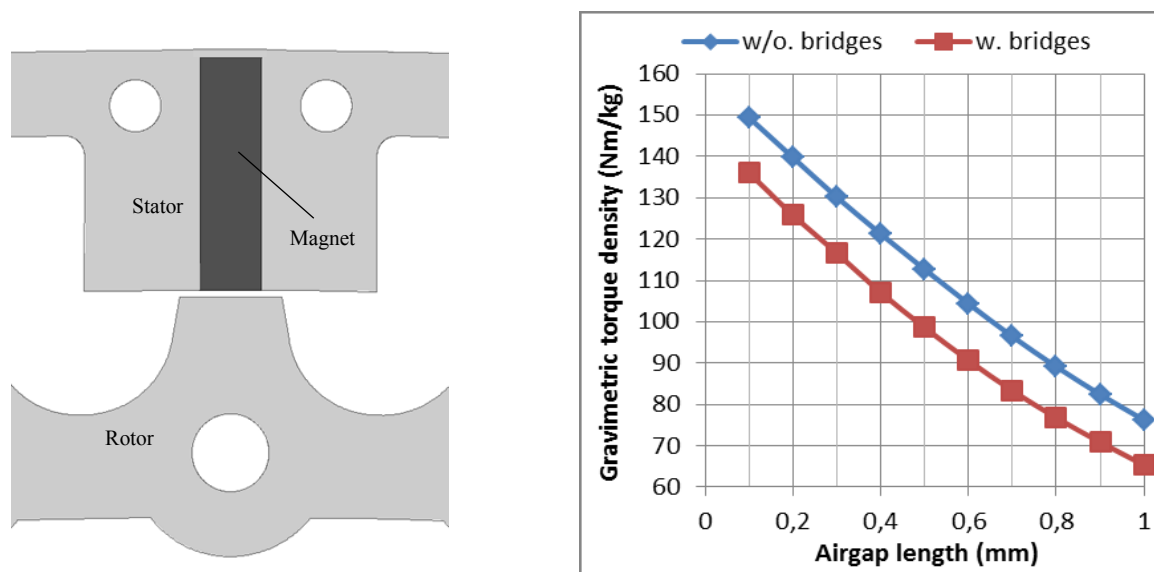


Figure 5-17: Illustration of 1mm bridges at outer surface (left) and gravimetric torque density as a function of airgap length for both cases (**no Halbach array**) (right)

The use of bridges is simulated using an array thickness of 2.5mm (see Figure 5-18). The Halbach array increases again the torque density close to specification values. For a 1mm airgap the improvement with array is of 19%, going down to 12.5% for a 0.1mm airgap. Differences in gravimetric torque density between the two cases are rather constant with little airgap length dependency. A minimum and maximum difference of 14Nm/kg and 19Nm/kg is observed at 1mm and 0.4mm, respectively.

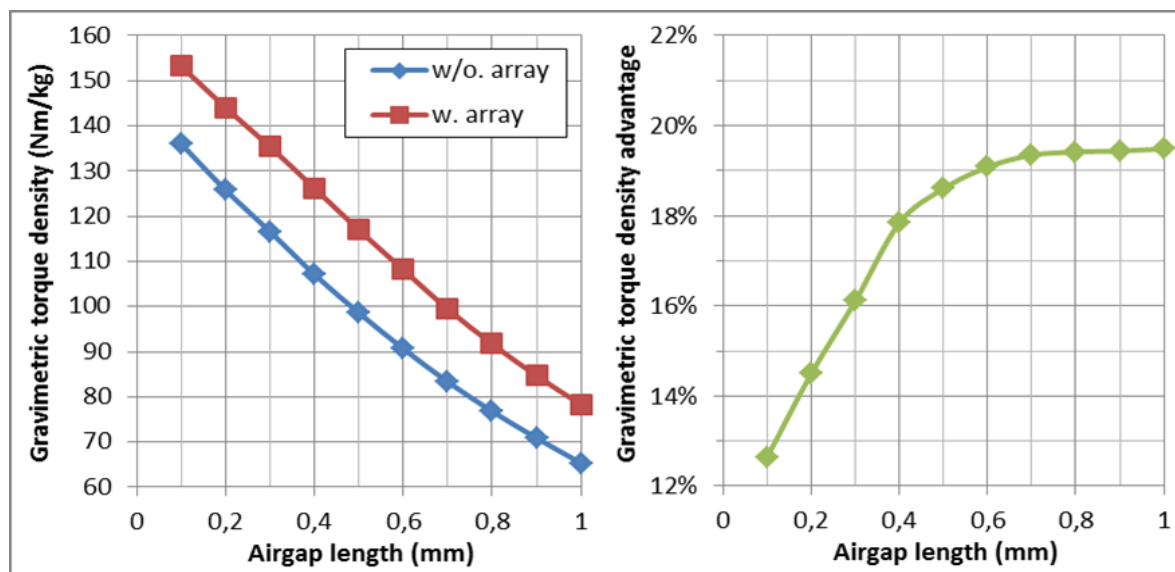


Figure 5-18: Gravimetric torque density for normal FSPM and Halbach-FSPM machines with bridges (left), and the respective gravimetric torque density advantage of a Halbach-FSPM machine (right) for an array thickness of 2.5mm

5.7.2 Final Machine Parameters

Given the findings of the previous section the design proposed in 5.5.2 is modified accordingly. The tooth, yoke and magnet dimensions have been optimized to deliver maximum torque, and the axial length has been adjusted to match the specified performance. The optimization was performed for a target airgap length of 0.1mm.

From the resulting dimensions, it is worth noticing that the use of the Halbach array reduces the amount of magnet mass embedded between cores down to 80% of its original value. This is beneficial from a point of view of magnet eddy current loss, as less material is exposed to the changing fields at the airgap. The tooth width is increased by 40% from its original value to maximize flux linkage, while the stator yoke remains at its original value. The slot area also remains the same as the total width of a stator pole is the same as for an optimized configuration without Halbach array. The rotor tooth and yoke dimensions remain the same and are determined by (5-2).

A single 6/13 segment of the machine in its final version is depicted in Figure 5-19. Main parameters and its corresponding values are listed in Table 5-9. Additional parameters not listed remain unchanged from Table 5-6. **Key parameters are the total active mass including support, which settled at 108kg, yielding a final gravimetric torque density of 152Nm/kg. This amounts to 93% of the target value.**

Table 5-9: Final Machine Parameters

<i>Parameter</i>	<i>Final Value</i>
Machine outer radius (mm)	700
Stator iron outer radius (mm)	697.5
Array thickness (mm)	2.5
Inner stator radius (mm)	679.5
Corrected split ratio	0.97
Active length (mm)	110
Airgap length (mm)	0.1
Stator tooth width (mm)	9.0
Magnet height (mm)	4.8
Stator yoke height (mm)	6.5
Average shear stress (kPa)	51.4
Core mass (kg)	82.9
Winding mass (kg)	8.4
Magnet mass (embedded) (kg)	6.3
Magnet mass (array) (kg)	10.0
Active mass (w. support) (kg)	107.6
Torque density (Nm/kg)	152.5

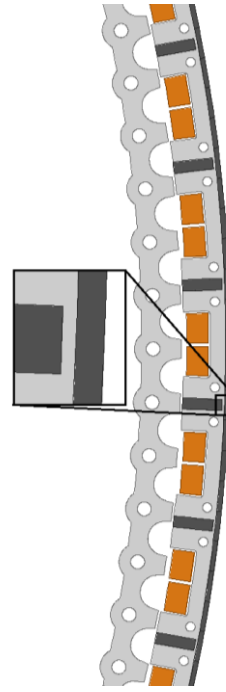


Figure 5-19: Illustration of one segment of final Halbach-FSPM 84/182 machine design

5.8 Chapter Summary

The analysis of FSPM machines for the proposed helicopter main rotor drive was the main objective of this chapter. Due to their characteristic double saliency the development of a new modeling technique was required, that allows the quick assessment of different machine configurations. The proposed analytical-numerical hybrid technique uses an initial input from FEM simulations to characterize airgap and magnet flux densities in the machine. It uses the aspect ratio of the magnet and airgap MEC elements to approximate the torque capability in the linear region. This is regardless of its size and rotor/stator pole configuration. With this model, the torque density of different FSPM C-core machines was studied and the following conclusions were drawn:

- Shear stress and split ratio are direct mass drivers for all machine components, which is also the case for SPM machines
- For a fixed number of rotor poles, FSPM machine configurations with less stator poles than rotor poles (twice the number of stator poles for C-Core FSPM machines) exhibit a higher torque density and therefore a lower weight
- FSPM machines have a high performance dependence on airgap length due their double saliency and low machine reluctance (higher than for SPM machines)

- For an equal airgap length of 0.5mm, same winding factor and same electrical loading, FSPM machines exhibit higher shear stress values than SPM machines resulting in shorter active length
- For the given application, achieving an airgap length smaller than 0.5mm can bring an active weight reduction of up to 12%, if mechanical issues can be overcome

From these findings, machines based on the 12/25 6-phase topology show the lowest mass, closely followed by combinations based on the 12/23 6-phase topology. For comparison and prototyping purposes, a combination based on the 6/13 3-phase topology was selected: the 84/182 machine which ranked in third. This configuration makes a good compromise between torque density and implementation cost, since only one 6/13 segment must be manufactured. Nevertheless, if a complete machine were to be implemented, the alternative based on the 12/25 6-phase machine would be a better choice.

One important finding is that, the additional structural mass needed in FSPM machines is a much lower percentage of the total active mass than for SPM machines. Only 12% additional mass is needed in the former compared to 42% in the latter. For FSPM machines, the magnet, tooth and yoke dimensions were all clearly above the 5mm limit for mechanical stability set in Chapter 4. Because of this, it was necessary to add neither additional mass solely for the purpose of increasing the machine stiffness nor connections for the structural support. Such was not the case for SPM machines, where the yoke thicknesses had to be doubled, so that structural connections could be implemented. The additional mass in SPM machines had no electromagnetic function; only structural, resulting in a significant increase in the final active mass.

Furthermore, a new topology called Halbach-FSPM machine was proposed. In this topology the magnetic loading is increased, by reducing flux leakage and injecting new flux into the machine. Besides the use of the traditional Halbach array, an alternative arrangement was proposed that makes better use of the magnet material. This arrangement applies for arrays with a thickness of up to 13% of the outer stator pole pitch.

In Halbach-FSPM machines with unlinked cores, the proposed technique increases the torque capability and volumetric torque density for all studied configurations. This is more pronounced on machines with high reluctance ($l_g = 1\text{mm}$), for which a maximum improvement of ca. 18% was observed. For the gravimetric torque density on the other hand, the technique is useful for designs with a high reluctance only, where a maximum advantage of 7% was obtained.

Incorporating further mechanical considerations in the form of bridges between cores (for manufacturing precision and mechanical stability) deems the use of Halbach arrays advantageous for all airgap lengths. The enhanced leakage through the bridges is compensated completely by the array flux. The additional improvement achieved in this case is of at least 12%, and up to 19%, for short and long airgap lengths respectively.

Final design specifications are summarized in 5.7.2, for which the desired performance was achieved with a total weight of 107.6kg, and a thermal loading adequate for air cooling. This yields a final gravimetric torque density of 152Nm/kg, a value that is very close to specifications.

Chapter 6

High Temperature Superconducting Synchronous Machines

Having studied two iron-based machine topologies, this chapter turns to the study of a machine design using superconducting materials. In 3.6 the HTS DC-excited synchronous machine was selected over bulk flux-concentrating machines. Herein, two alternatives are predominant [46, 137]: salient and non-salient multi-pole machines, with conventional and airgap armature windings respectively. This chapter focuses on determining the adequate material distribution within the machine that yields the highest gravimetric torque density. This results automatically in the selection of either a salient or a non-salient topology, with cold HTS field windings and normal conducting armature windings.

As a starting point, a brief comparison of the HTS material choices is made with YBCO as the material of choice. Then, a simplified 2D machine model is proposed, that reflects the active components of an HTS machine. With this model, the optimization problem is set, observing the field and current density dependence of HTS wire. The objective is to find the highest magnetic loading possible per overall unit mass for a fixed pole pair number. The optimization result gives the most important design parameters: tooth and yoke thicknesses, HTS coil width and depth, and the HTS engineering current. With the resulting 2D profile, a best-case performance and weight prediction is made. For the time being, this results in an insufficient gravimetric power/torque density of HTS machines for the specified application (cold mass operating at 20K).

6.1 Simplified Machine Model and Assumptions

Given the additional complexity of incorporating a cryogenic cooling system, the scope of the design procedure is limited to a simplified performance assessment. Besides electromagnetic considerations, only basic cryogenic and mechanical considerations are made. For this purpose, some assumptions have been made about the parts operating at both cryogenic and room temperature. These assumptions help simplify the modeling, but without incurring in significant deviations or performance overestimation. The result of this is a best-case prediction of the gravimetric torque density.

6.1.1 HTS Operating Temperature and Cryostat

HTS materials, with their relatively high critical temperatures (see Table 3-6), are in principle easy to use with LN₂-cooling. However, operation at such temperatures (77K or 65K for subcooled LN₂) brings disadvantages for this application:

- Suboptimal performance, since operation at lower temperatures is a number of times superior
- Cooling equipment (cryocoolers or cryogenic bath) serves the purpose of cooling only, and is otherwise dead weight that must be considered as “active mass”

In the scenario of HTS operation at 20K, a cooling system using LH₂ can be devised. As reviewed briefly in 2.3, LH₂ is already considered as an alternative propellant for future aircraft, which make use of turboshaft-driven HTS machines. Such scenario is adopted here to simplify the problem, and exclude the cooling scheme from the machine design. This implies a deviation from 2.4, where Diesel fuel is used as main propellant and Diesel engines as main powerplant. For the purpose of the study of this particular topology, this is considered acceptable.

From [170], it is reasonable to assume a cryostat thickness of 50mm for operation at 20K (two and a half times the thickness for operation above 60K). Within such volume, all thermal insulation elements are housed: vacuum chamber, spacers, support, multi-layer insulation (MLI), and radiation shields. Composite materials are chosen for a potential construction, since they not only have zero eddy current losses but are also light in weight.

6.1.2 HTS Material: YBCO vs. MgB₂

Among HTS materials, YBCO and MgB₂ are considered as the best alternatives, since they offer the best compromise between the different parameters shown in Table 3-6. YBCO tape from SuperPower and MgB₂ wire from Hyper Tech Research are chosen for this comparison. Compared to MgB₂, YBCO features an engineering current density 5 times higher (at 20K in a 2T perpendicular magnetic field), and a mass density 3 times higher [134] [136].

The resulting weight advantage for YBCO is of about 50% at 20K and 2T (see Table 6-1). This ratio of engineering current density to mass density suggests that a MgB₂ coil needs five times more conductor area than a YBCO coil to achieve a certain magnetomotive force. This leads to a 50% higher weight, which outweighs the price and manufacture advantages of MgB₂, at least for this application. Consequently, the material of choice is SuperPower YBCO HTS tape.

Table 6-1: YBCO vs. MgB₂ in terms of weight and performance at 20K in 2T perpendicular magnetic field

<i>Parameter</i>	<i>YBCO</i>	<i>MgB₂</i>
Engineering current density J_{eng} (A/mm ²)	1225	265
Mass density ρ (g/cm ³)	8.3	2.6
Ratio J_{eng} / ρ (Amm/g)	1.48×10^5	1.01×10^5

6.1.3 Simplified Machine Model

For this problem, the initial machine geometry represents the cross section of one pole of a synchronous machine as shown in Figure 6-1. The outer iron region represents the armature iron yoke of height h_{ay} depicted as a slot-less structure. The total electromagnetic airgap l_g is the sum of the airgap between rotor and stator (2mm) plus the cryostat wall thickness h_k . This sum is adjusted by the Carter factor to take into account armature slotting yielding the equivalent airgap length g (see 6.1.4). The HTS field windings are assumed to be racetrack windings, and are initially mounted on an iron core. Such core has a tooth half width h_{ft} and a yoke thickness h_{fy} . The HTS windings also have a depth $h_{d,HTS}$ and width $h_{w,HTS}$. Since the model is only two-dimensional, end windings are ignored.

To make an *initial layout* the following conditions are set:

- The HTS coil is placed such that its front outer edges coincide with the inner cryostat wall **and** its rear outer edges with the boundaries of the half pole region
- h_{ay} , h_{ft} , h_{fy} , $h_{d,HTS}$ and $h_{w,HTS}$ have all the same initial value l (the basic length)
- The basic length l is defined as one fourth of the total field coil width w_f

Based on these conditions and the geometric relation depicted, an expression for l can be obtained from the relations between the different parameters:

$$l = \frac{\lambda}{\lambda + 1} (R_o - g) \tag{6-1}$$

with

$$\lambda = \frac{1}{2} \frac{1}{\sqrt{1 + \frac{1}{4} (1 + 2 \tan \beta)^2}} \tag{6-2}$$

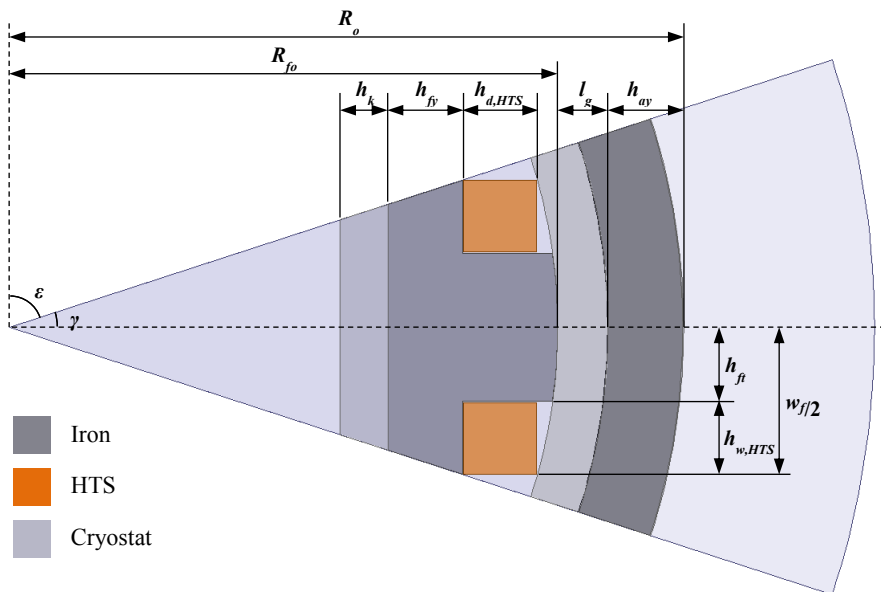


Figure 6-1: Simplified model of a HTS synchronous machine with 5 pole pairs

Equations (6-1) and (6-2) indicate that besides outer machine radius R_o and equivalent airgap length, l is only dependent on the number of pole pairs p through the angle ε :

$$\varepsilon = 90^\circ - \gamma = 90^\circ - \frac{180^\circ}{2p} \quad (6-3)$$

The initial layout sets the value of the outer field radius R_{fo} , which now remains constant for a fixed number of poles. The cryostat region at the airgap remains therefore at a fixed position, acting as a reference for the other parameters h_{ay} , h_{ft} , h_{fy} , $h_{d,HTS}$ and $h_{w,HTS}$. After the initial setup is made, these parameters can be optimized according to the following:

- A change in the armature yoke thickness h_{ay} results in a change of the armature outer edge position, while the inner edge remains fixed. The armature yoke can only be made thinner, so that its outer edge does not go beyond R_o . As h_{ay} is made smaller, the reduced portion between the yoke's outer edge and R_o is automatically replaced by composite material. This accounts for structural support of the armature windings in the case of an ironless armature ($h_{ay} = 0$).
- Both HTS coil and field tooth are centered at the dotted line in Figure 6-1. Increasing the HTS coil width $h_{w,HTS}$ decreases the coil bore leaving the coil outer surface fixed. The tooth half width h_{ft} and $h_{w,HTS}$ are complementary and equal only at first for the purpose of making the initial layout. However, for optimization they are independent of each other, which could lead to either overlapping of the two regions or regions without material. In the first case HTS material has priority, and in the second the void space is filled with composite material to account for the possibility of an ironless tooth ($h_{ft} = 0$).
- An increase in $h_{d,HTS}$ increases the HTS coil thickness towards the center of the machine leaving the front coil surface fixed at the airgap cryostat wall (this increases the length of the field tooth in equal manner).
- The field yoke is placed directly behind the HTS coil and its thickness h_{fy} is measured from the rear coil surface (i.e. the reference position for the field yoke is determined by $h_{d,HTS}$). The field yoke can only be made thinner and the discarded material is automatically replaced by composite material. This allows for a structural support of the windings in the case of an ironless field ($h_{fy} = 0$).

6.1.4 Armature Winding and Mechanical Airgap

During optimization (see 6.2) no electrical loading is assumed and the armature is represented only by the armature yoke. Nevertheless, a winding configuration must be defined to account for slotting in the effective airgap length by means of the Carter factor.

The winding selected for the armature is the simplest "least distributed" full-pitch 3-phase configuration with a **unity winding factor** and

$$q = 1 \text{ slot/pole} \cdot \text{phase}$$

An illustration of the winding setup for two stator poles is presented in Figure 6-2. This selection is preferred over a more compact fractional slot concentrated winding. The justification for this is the inferior heat loss on the electromagnetic shield, product of the

reduced harmonic content of the magnetomotive force. These losses were found to be one order of magnitude lower for the selected distributed winding compared to the “least concentrated” 3/2 fractional slot winding [171].

Furthermore, for the purpose of the calculation of the Carter factor a slot opening equivalent to one third of the slot pitch and a mechanical airgap of 2mm are assumed.

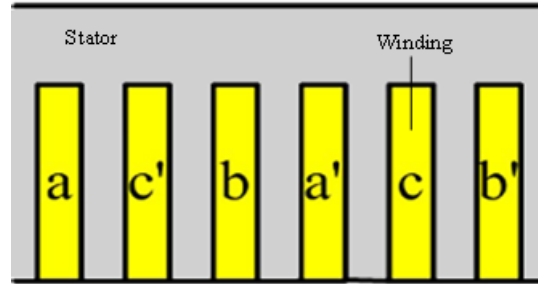


Figure 6-2: Distributed full pitch armature winding ($q = 1$) corresponding to two poles [187]

6.2 Optimization Problem

After setting the initial layout the optimization problem can be defined and solved. For this purpose, a built-in optimization function in ANSYS Maxwell[®] using a sequential nonlinear programming algorithm is employed. Parting from the initial layout, an optimized 2D layout of the machine’s cross-section is obtained. From the result, a preliminary mass can be calculated by means of extrusion of the 2D profile into a 3D model. The weight of the machine’s components is therefore not calculated directly, but instead their cross-section is calculated. The optimization function, which considers the cross-section of the machine and the resulting torque output, is explained further in the following section.

6.2.1 Figure of Merit

The maximum gravimetric torque density is determined by the construction parameters that control a machine’s weight and performance: yoke and tooth thicknesses, and HTS coil width and depth. These are considered in the torque density optimization through the inclusion of the machine’s cross-section in the problem formulation. Since zero electrical loading is assumed during optimization, the problem focuses on maximizing the coil flux linkage per unit of overall active mass. Alternatively, this can be written in the form of airgap magnetic loading divided by the product of cross-section and mass density:

$$\frac{T}{m_{act}} = \frac{\sqrt{2}k_w A_s B_{g1} \pi (R_{fo} + l_g)^2 L}{\sum_i C_i \rho_i L} = k_w A_s F \quad (6-4)$$

with

$$F = \frac{\sqrt{2} B_{g1} \pi (R_{fo} + l_g)^2}{\sum_i C_i \rho_i} \quad (6-5)$$

where B_{g1} is the peak flux density of the fundamental seen at the armature, and C_i and ρ_i are the cross-sectional area and mass density of component i respectively (see Table 6-2). **The figure of merit F describes the distribution of core, HTS and glass fiber reinforced plastics (GFRP) that yields the airgap flux density B_{g1} .** HTS end windings are ignored, and GFRP support and cryostat are considered active materials, since without them HTS operation is not possible at all. The other parameters in (6-4) describe the winding

configuration: armature electrical loading A_s and winding factor k_w (A_s does not include k_w to avoid an underestimation of the thermal loading as explained 3.3.3).

Table 6-2: List of materials considered for optimization

<i>Material</i>	<i>Corresponding Parts</i>	<i>Mass Density (g/cm³)</i>
Vacoflux 50	Armature core, Field core	8.12
GFRP	Armature support, Field support, Cryostat	1.95 ^{*1}
HTS	Field coils	6.65 ^{*2}

^{*1} GFRP is assumed to be S-glass Epoxy Composite

^{*2} The **effective** mass density of the HTS coils is calculated assuming axial and racetrack aluminum support, and an HTS fill factor $k_{f,HTS}$ of 0.7 with 4mm YBCO wire [134, 136, 171]

6.2.2 Problem Formulation

The optimization of the figure of merit F gives an answer to the question of whether an ironless machine is the best choice or not. Furthermore, the optimal HTS coil dimensions and critical current density are also obtained from it. The optimization is then formulated as a minimization problem:

$$\max F = \min -F \quad (6-6)$$

The HTS coil anisotropy is considered by constraining the perpendicular component of the magnetic field (see Figure 3-13). The critical current dependence on this field component is taken into account by first calculating the maximum peak flux density perpendicular to the tape wire within the HTS region:

$$B_{max,\perp} = \max_{C_{HTS}} |B_{\perp}(x, y)| \quad (6-7)$$

With the maximum perpendicular magnetic field calculated, the critical engineering current density J_{eng}^c for the HTS region is obtained from the HTS critical curve at 20K.

$$J_{eng}^c = k_{f,HTS} \frac{I_c(B_{max,\perp})}{A_{tape}} \quad (6-8)$$

where the fill factor $k_{f,HTS}$ accounts for the coil aluminum support as mentioned in Table 6-2. Finally, the optimization variables k_j are coefficients that control the values of h_{ay} , h_{fy} , $h_{d,HTS}$ and $h_{w,HTS}$ as a percentage of the basic length l (all k_j have an initial value of 1):

$$h_j = k_j l \quad (6-9)$$

with

$$0 \leq k_j \leq 1 \quad \text{for } k_{ay} \text{ and } k_{fy} \quad (6-10)$$

and

$$0 \leq k_j \leq 2 \quad \text{for } k_{ft}, k_{d,HTS} \text{ and } k_{w,HTS} \quad (6-11)$$

As a reminder, all dimensions still follow the modeling guidelines set in 6.1.3 regarding structural mass and material prioritization.

6.2.3 Optimization Results

The optimization procedure is run for selected pole number values starting at ten poles in steps of ten. For each step an optimal material distribution is found. One important first result from the optimization is that the field circuit is ironless for all pole pair number values p (all iron is replaced by GFRP):

$$k_{ft} = 0 \quad \text{and} \quad k_{fy} = 0 \quad \text{for all } p \quad (6-12)$$

The figure of merit F is plotted as a function of the pole number in Figure 6-3. Since gravimetric torque is proportional to F at constant current loading, both decrease in the same manner with increasing pole number. As the airgap length is basically the same for all pole numbers, the leakage increases rapidly with pole number as the pole pitch decreases.

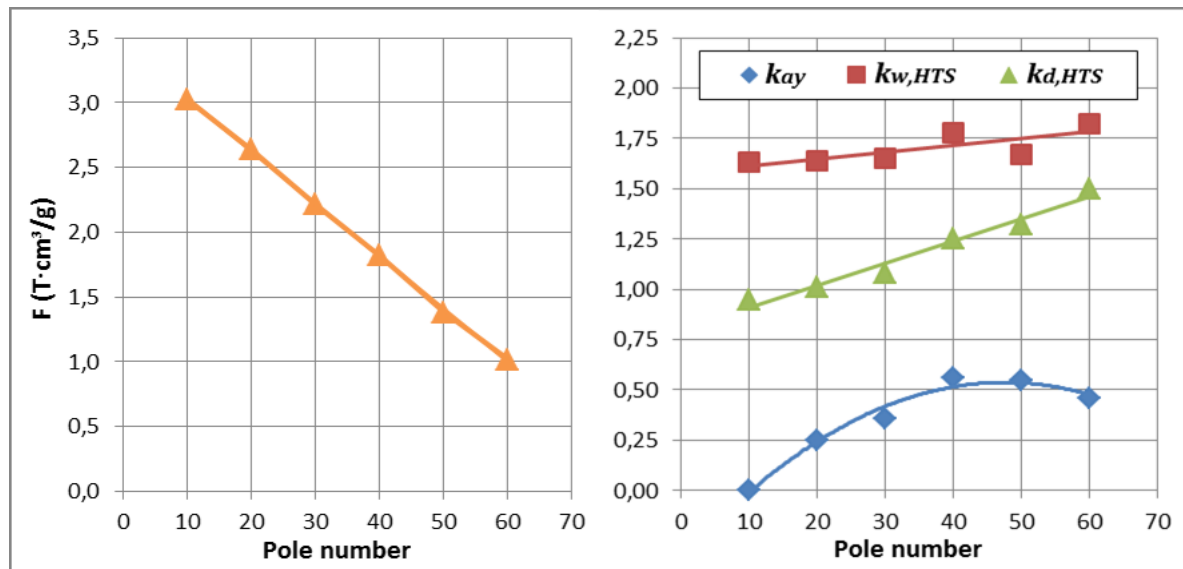


Figure 6-3: Figure of merit optimization results (left) and corresponding values of the optimization variables with trend lines (right)

Furthermore, below 10 poles the machine is completely ironless with $h_{ay} = 0$. From that point on the armature yoke thickness increases up to a maximum value of ca. 55% of l between 40 and 50 poles. The HTS coil width coefficient $h_{w,HTS}$ increases only slightly with pole number in an apparently linear manner. Its value ranges from 160% to 180% of l as the pole number increases, yielding in average 85% coverage of the pole pitch by HTS material. In equal fashion, the HTS coil depth $h_{d,HTS}$ increases seemingly linear with pole number, although more pronounced than $h_{w,HTS}$. Starting roughly at unity, its value rises up to 150% of l at 60 poles. In summary, the addition of HTS and iron material attempts to compensate for the lost performance product of the enhanced leakage as the pole number increases. In the case of HTS material, the tendency is straightforward since adding material increases the field's magnetomotive force, therefore helping to increase F . Regarding the armature yoke, material is added to reduce the machine's reluctance as the pole number increases. This is done until the yoke weight starts to outweigh the reduction in reluctance, point after which the yoke thickness starts being reduced.

It can be concluded that the gravimetric torque density decreases with increasing pole count in HTS machines with cold field windings. This is contrary to the tendency observed in iron-based machines. According to this, a machine with ten poles or less should be considered for further analysis. Nevertheless, the length constraint in the axial direction must be revised. The reason is that machines with a low pole number might require an axial length longer than the 250mm allowed. A minimum active length of 50mm is assumed, in order to provide reasonable length for the coil support. With this guideline, and knowing that the cryostat thickness h_k is 50mm, the total axial length must satisfy:

$$50\text{mm} + 2h_k + 2k_{w,HTS}l = L_{tot} \leq 250\text{mm} \quad (6-13)$$

Equation (6-13) is plotted in Figure 6-4, from which a pole number of 40 would be the minimum appropriate for further investigation. For that pole number, the maximum engineering current density for the HTS region is $450\text{A}_{\text{RMS}}/\text{mm}^2$. This value must be further scaled down to account for the safety factor. This is explained further in the next section where the machine performance prediction is made.

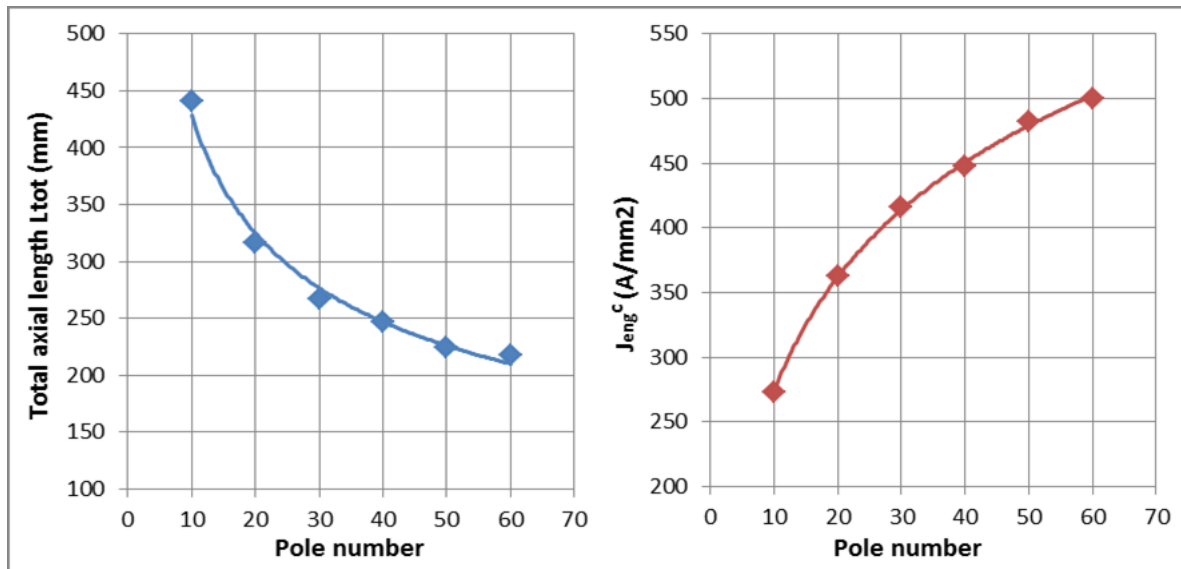


Figure 6-4: Estimated total axial length (left) and engineering critical current density (right) for the studied pole number domain

6.3 Best-case Performance Prediction

Once the optimization of the HTS, iron and support materials is completed, an estimation of the gravimetric torque density can be done. Firstly, the maximum engineering current for the HTS coils must be adjusted by a safety factor $k_{s,HTS}$ to minimize the probability of superconductor quench and insure operability:

$$J_{eng} = k_{s,HTS} J_{eng}^c(B_{max,\perp}) \quad (6-14)$$

This safety factor is chosen to be 0.8 allowing 25% overload before reaching normal conductivity. From Figure 6-4, the application of the safety factor results in an operational

engineering current density of $360A_{RMS}/mm^2$. This current density reduction yields an equal decrease of the calculated figure of merit F , as a consequence of an equally lower peak flux density at the armature:

$$F_{eng} = k_{s,HTS}F \quad (6-15)$$

From (6-4), multiplying F_{eng} by a current loading of $40A_{RMS}/mm$ equates to assuming the presence of a thin current sheet on the inner side of the armature yoke. This current loading has been the guideline throughout this work, and its assumption allows an initial estimation of the maximum achievable gravimetric torque density:

$$\frac{T}{m_{act}} < k_w A_s F_{eng} \quad (6-16)$$

This is written as an inequality, since there are a number of approximations involved, which would not allow the final gravimetric torque density to reach that maximum value. These approximations are summarized as follows:

- Shear stress is produced homogeneously at the airgap regardless of the position along the 50mm active length of the machine (i.e. end-effects are ignored)
- Additional mass corresponding to the end-windings of the HTS coils is not taken into account
- Armature winding, although made of aluminum wire, is not yet incorporated, as well as the armature slotted structure
- The cryostat's top and bottom walls are not taken into account (this is however partly offset by the model representation of the cryostat as a solid region)

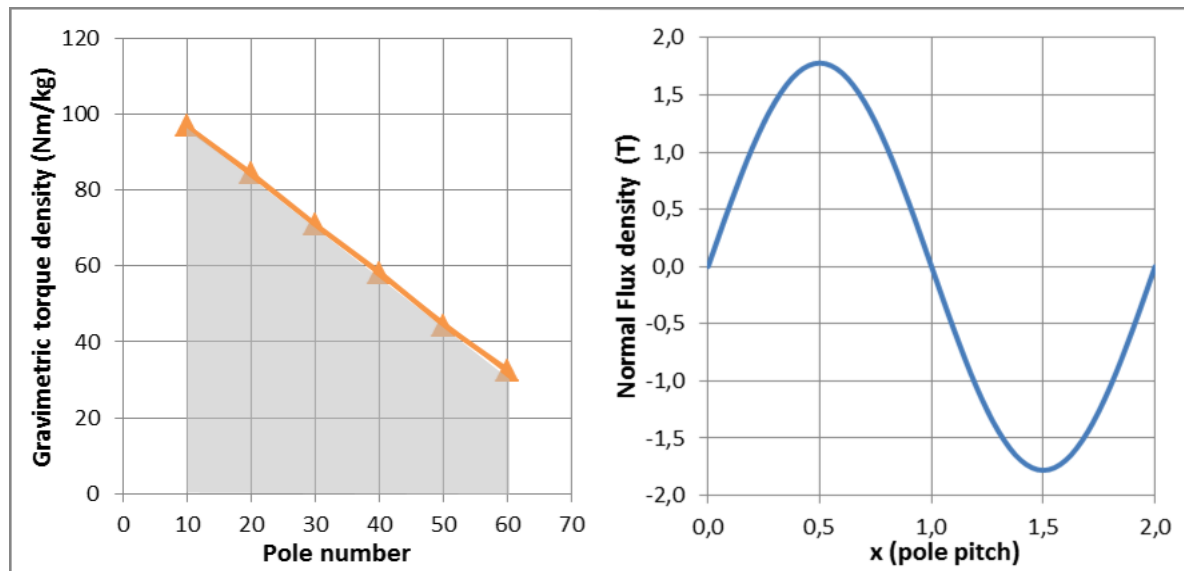


Figure 6-5: Realizable gravimetric torque density presented as shaded region (left) and no-load airgap flux density distribution for two pole pitches (right)

Figure 6-5 shows inequality (6-16) graphically, with the shaded area representing the feasible region. A theoretical maximum of slightly less than 100Nm/kg can be achieved with a low pole number. However, for 40 poles (constrained by (6-13)) **the gravimetric torque density is below 60Nm/kg. The maximum torque obtained is 10100Nm, roughly 60% of the required value. The projected weight is NO LESS THAN 175kg.** Due to these results, no further design steps are pursued. It is already clear from preliminary data that the required weight and torque cannot be achieved. These figures indicate that with the current performance of HTS wire at 20K, it is unlikely that a machine with an HTS field circuit can deliver the required performance for a helicopter propulsion application.

Nevertheless, with the flux density at the armature (see Figure 6-5) and the assumed current loading, the airgap shear stress is found to be around 50kPa. Although this is only a maximum *theoretical* value, this result is worth mentioning, since it highlights the potential of HTS machines. Indeed, this a very high shear stress considering the current loading assumed and the length of the airgap. Further progress in this field will possibly allow reaching even higher airgap force densities at even lower weights in the future.

6.4 Chapter Summary

This chapter focused on the study of HTS machines for the application of helicopter propulsion, with the HTS DC-excited synchronous machine as the topology of choice. Using YBCO tape wire and assuming an operating temperature of 20K, a simplified machine model was proposed as a starting point. Such model reflects the basic regions of a superconducting machine, which could be considered as “active material”: armature iron, field iron, HTS coils, cryostat and alternative GFRP support.

Taking into account the anisotropy of HTS wire, the basic machine structure is optimized to produce the highest magnetic loading possible with the lowest amount of overall material. From such optimization, it was concluded that an ironless field circuit (therefore non-salient) is the lightest choice possible for the pole number region considered. However, only for low pole numbers the machine is completely ironless (less than 10); the amount of armature iron increases with pole number until a maximum is reached at 40 poles.

The optimal material distribution allows calculating an ideal best-case performance. This reveals that even without space envelope constraints, only two thirds of the target value for gravimetric torque density can be met at a low pole number. Taking into account the limited axial length further lowers the prediction to one third of the requirement value. In such case, there is a weight penalty of at least 75%, and a maximum output torque of two thirds of the required value.

Chapter 7

Comparison, Experimental Validation and Conceptual Structure

The objective of this chapter is the laboratory implementation of an experimental setup based on one of the studied topologies. This allows the validation on a partial one-segment implementation of the followed design methodology and construction principles.

In a first step, the resulting machines from the studied topologies are revisited and briefly compared based on performance and preliminary efficiency. The Halbach-FSPM design is chosen and further analyzed, in order to validate that a full-machine implementation would indeed fulfill the key performance requirements.

As a next step, the experimental setup is introduced starting with the differences between the implemented single segment and a segment in a full machine. The mechanical support design based on air bearings is introduced, as well as the cooling approach using compressed air and forced convection. As explained in Chapter 5, the mechanical aspect requires particular attention, not only due to the machine's low mass, but also due to the small airgap. An experimental setup is developed parting from the proposed construction principle, emphasizing on proof of concept and not on final implementation. With such experimental setup, the most relevant performance parameters are validated.

With the experimental results, a conceptual full-prototype design is proposed to make a final weight prediction. This serves as starting point for future recommendations and work.

7.1 Design Comparison and Selection

The studies performed in Chapter 4, Chapter 5 and Chapter 6 gave an idea of the physical limits of each topology in terms of electromagnetic performance. SPM and FSPM machines are currently better candidates for a helicopter main rotor direct-drive, while HTS machines offer more room for future improvement. Table 7-1 summarizes the parameters considered for the comparison of all three designs.

An estimation of the DC-conduction and core loss are included for SPM and Halbach-FSPM machines. For the core loss calculation, 0.1mm **Vacodur 49** laminations were taken

assuming **Vacstack** production technology. This material has similar magnetic properties as **Vacoflux 50**, with additional mechanical strength. Regarding magnet material in the SPM machine, each magnet was segmented circumferentially in 5 pieces and the losses calculated according to [169]. For the Halbach-FSPM machine, the magnet segmentation was done only in radial direction using 4 segments [172], while the magnet array on the back of the machine is composed of 8 blocks per stator pole. Magnet axial segmentation was assumed in neither case for the sake of simulation simplicity. Loss calculations were not performed for the HTS machine, since the armature design was not completed due to inferior torque performance.

The summarized data is discussed focusing on gravimetric torque density, additional structural mass and efficiency. Based on this argumentation a final choice is made.

Table 7-1: Comparison of studied machine topologies

<i>Parameter</i>	<i>SPM</i>	<i>Halbach-FSPM</i>	<i>HTS</i>
Electromagnetic torque (kNm)	16.4	16.4	< 10.1
Final mass (kg)	142	108	> 175
Electrical frequency (Hz)	653.3	1061.7	116.7
Gravimetric power density (kW/kg)	4.3	5.5	< 2.1
Equivalent shear stress (kPa)	23.1	51.4	< 50
Airgap radius (mm)	686	679.5	672
Mechanical airgap length (mm)	0.5	0.1	2.0
Active length (mm)	242	110	250
Conduction loss P_{Al} (kW)	14.2	8.5	N/A
Core loss P_{Fe} (kW)	2.6	5.2	N/A
Magnet eddy current loss P_M (kW)	1.5	1.2	N/A
Array eddy current loss $P_{M,array}$ (kW)	N/A	0.9	N/A
Miscellaneous loss (kW)	5	5	N/A
Efficiency η	96.2%	96.7%	N/A

Gravimetric torque density

Both iron-based machines fulfill the torque requirement. The HTS machine however achieves only 62% of the minimum volumetric torque density needed. From all machines, the Halbach-FSPM design has the lowest mass and the smallest weight penalty, product mostly of higher shear stress at the airgap. As a consequence, the SPM machine has more than twice the active length than the FSPM machine, together with 30% additional mass.

Although the shear stress value for the HTS machine is also close to 50kPa, this is a best-case estimation only. Furthermore, despite of having the maximum active length allowed (250mm), only a maximum of 50mm actually produce torque. This amounts to only half of the active length of the FSPM machine, strongly limiting performance. Also, the cryostat and support regions (considered as “active”) make a significant contribution to the total active mass. Such regions are obviously not present in iron-based variants. The resulting weight penalty of the preliminary design is of at least 75%.

Summarizing the above, the Halbach-FSPM machine shows the highest gravimetric torque density (ca. 92% of the target value, albeit at a very short airgap length), while the other two alternatives incur in considerable weight penalty.

Additional structural mass

Before addition of support mass, the FSPM machine has practically the same *electromagnetic* mass as the SPM machine: ca. 100kg. The similar mass and the difference in active length imply that FSPM machines are bulkier and therefore have a bigger cross-section. This permits combining the material's electromagnetic function with a structural support function. The additional cross-section needed for structural purposes is a smaller percentage of the total cross-section, therefore limiting the additional weight required. Such is not the case for SPM machines: the structural feasibility requires much more additional area *for support purposes only* (ca. 30% of the total). In this respect FSPM machines have an advantage with respect to SPM machines.

Also from a structural point of view, a bulkier machine with a short active length and large cross-section has higher mechanical stiffness. This is an important feature for thin ring-type machines with a short airgap length. It helps maintain a constant airgap clearance by preventing deformation or deflection along the active length. Such deformation is product of the attractive magnetic forces between rotor and stator.

Efficiency

Regarding DC losses, the SPM machine has almost twice the losses as the FSPM machine: with twice the active length, the winding length is accordingly longer. For AC losses, the electrical frequency of the FSPM machine is 62% higher than for the SPM machine. This is despite having a similar number of rotor poles: 224 and 182 for SPM and FSPM machines respectively. The result is a core loss twice as high and a 68% higher volumetric loss concentration. For the magnet material, the overall loss is also higher by 40%, but the overall loss concentration is the same as for SPM machines. On the other hand, with all magnet material in the stator, the handling of these losses is more manageable for FSPM machines.

Overall, despite q -axis operation at nominal current, the iron-based designs have a high efficiency ($> 96\%$), with a slight advantage for the FSPM topology. For this machine, magnetic loading and frequency are high, while current loading is moderate. The result is a moderately high loss concentration, but in a low amount of total active material. The total loss produced under these conditions is therefore far smaller than the motoring power obtained due to the high pole count and long torque arm. Consequently, in this scenario, the efficiency of ring-type machines is less of a problem (easily above 90%). More critical on the other hand is an efficient transport of the losses out of the machine with the available surface area. In such a machine, extreme loss differences between nominal and maximum operating conditions are difficult to handle (e.g. twice the nominal load or higher). With a low mass, the machine has little thermal capacity to absorb the additional losses for the duration of an extreme transient. Consequently, the power spectrum for the helicopter main rotor application fits adequately in this constraint: the transient (10 sec) and take-off (5 min) power are respectively 15% and 10% higher than the nominal power.

Final Choice

Based on the previous discussion, the Halbach-FSPM machine is used for the experimental setup due to its overall characteristics:

- Gravimetric torque density close to the required value
- Short stack length leading to a stiff construction
- Low additional mass required solely for structural support
- High efficiency with most losses originating from the stator

The design and discussion of the experimental setup is an important step, since it addresses two crucial issues still open:

- Stable construction and operation of a ring-type machine with little total mass
- Adjustment and control of a very small airgap clearance at a high airgap radius

7.2 Halbach-FSPM Machine: Electromagnetic Analysis and Implementation

The focus of this section lays on the implementation principle of a full Halbach-FSPM machine, and the respective electromagnet analysis. This is carried out for the chosen topology, in order to validate the feasibility and performance of a full machine. More importantly, it serves as the basis for the developed experimental setup.

7.2.1 Stator Segmentation and Use of Air Bearings

The designed machine is a large-diameter ring-type flux-switching machine with a small airgap. For manufacture, assembly and operation, a stator segmentation approach is adopted with a total of 14 separately driven segments. Each one constitutes an independent 6/13 FSPM machine supplied by its own power electronics. Segmentation makes fault isolation and redundancy possible, by keeping faults occurring in one segment from affecting the adjacent ones. An electrical fault therefore would affect only 1/14th of the entire machine.

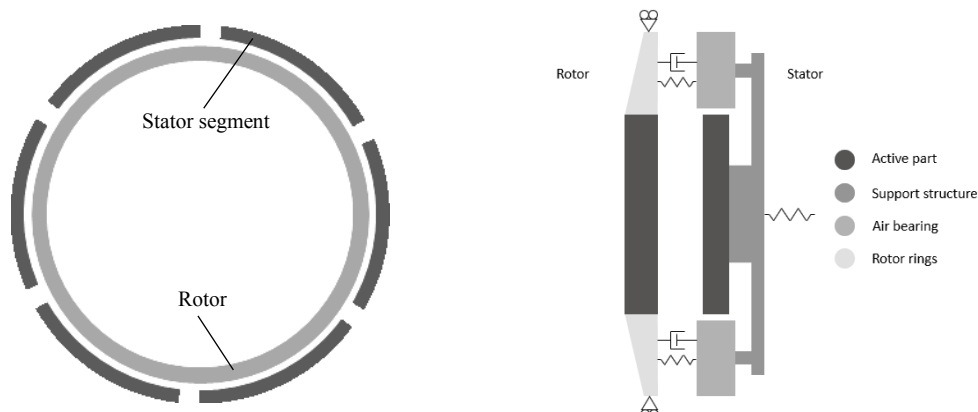


Figure 7-1: Conceptual representation of large diameter machine with 6 stator segments (left) and cross-section of single segment suspended with air bearings (right)

The motor is air-cooled and although the operating current density is relatively low, the use of aluminum windings increases the thermal load by 67% compared to copper. Torque density is achieved by increasing the magnetic loading through reduction of the airgap length down to 0.1mm. However, due to thermal expansion, changes in either the rotor or stator diameter suffice to either make the airgap larger and lower the output torque, or make it smaller and risk stator-rotor contact. The need for an individual segment suspension system arises from this issue. In such system, a segment must be able to individually follow the thermal expansion of the rotor, thus maintaining the airgap length at its set point. This function is achieved through the use of air bearings on each stator segment (see Figure 7-1).

Aerostatic bearings utilize a thin film of pressurized air to provide a very-low-friction high-stiffness interface between two surfaces [174]. The air needed to create the film is supplied through one of the two surfaces through orifices or a porous medium. When a load normal to the film is applied, the film thickness (also called fly height h_{fy}) decreases and the film flow resistance increases. The resulting pressure increase determines a new equilibrium point, where the load can be supported (see Figure 7-2). The observed behavior is linear around the nominal operating point. For porous air bearings with a fly height range of around 10 μm , the air bearing behavior resembles that of a compressed spring.

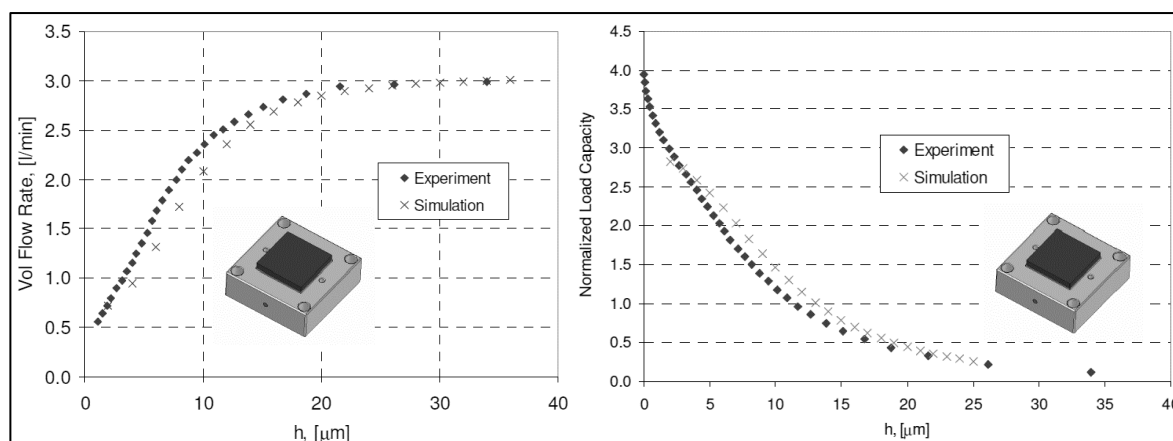


Figure 7-2: CFD simulation and experimental results on porous air bearings for air flow (left) and load capacity proportional to film pressure (right) [175]

For air-bearings to function properly a preloading force is needed, which in the case of the segmented stator, is provided by the magnetic pull between rotor and stator. The force tending to close the airgap is counteracted by the air bearings mounted on the segment's support structure. They push against cylindrical rings attached on top and bottom of the rotor stack (see Figure 7-1). The stator segment can then follow the thermal expansion of the rotor, if attached to the helicopter chassis by a low radial stiffness connection. Such connection must restrain the segment in tangential direction to allow torque transmission. The rotor's weight can also be supported on top and bottom by additional air-bearings (indicated as roller supports). In this manner, the connection to the center shaft transmits only torque and thus remains lightweight. The main purpose of this configuration is the adjustment and control of a very low mechanical airgap at all instants. This requires bypassing the effect of thermal contraction and expansion of the rotor and stator.

7.2.2 Further Electromagnetic Characterization

The electromagnetic analysis in this section characterizes the main parameters of a full implementation. These are used to verify the desired performance of a *potential* full-machine, and also serve as baseline to establish the differences with the experimental setup.

Back-EMF

The armature windings are chosen with 10 turns in series per coil, i.e. 20 turns in series per phase. They are manufactured using anodized aluminum strip wire and preformed into racetrack windings. According to the manufacturer ANOFOL[®], each coil can be manufactured with two sub-coils in parallel, each with two parallel paths (4 parallel paths in total). These choices result in the following machine parameters:

- Phase current I_{ph} : $100A_{RMS}$
- Conductor current density J : $8.5A_{RMS}/mm^2$
- Slot fill factor k_f : 0.73
- Peak phase back-EMF \hat{e}_{ph} : 234V

Manufacturing tolerances and the anodization layers between turns (1% of total coil area) require a slight reduction of the final slot fill factor down to 73%. A corresponding increase in conductor current density is therefore necessary.

Finite element simulations with this winding configuration are shown in Figure 7-3 for all phases in one machine segment. The back-EMF is essentially sinusoidal, but with some parasitic harmonic components, especially of the 5th and 7th order. Since optimization was focused on achieving a high gravimetric torque density, the resulting flux linkage gives rise to these unwanted components. The resulting total harmonic distortion is a little less than 8% for the first hundred harmonic orders.

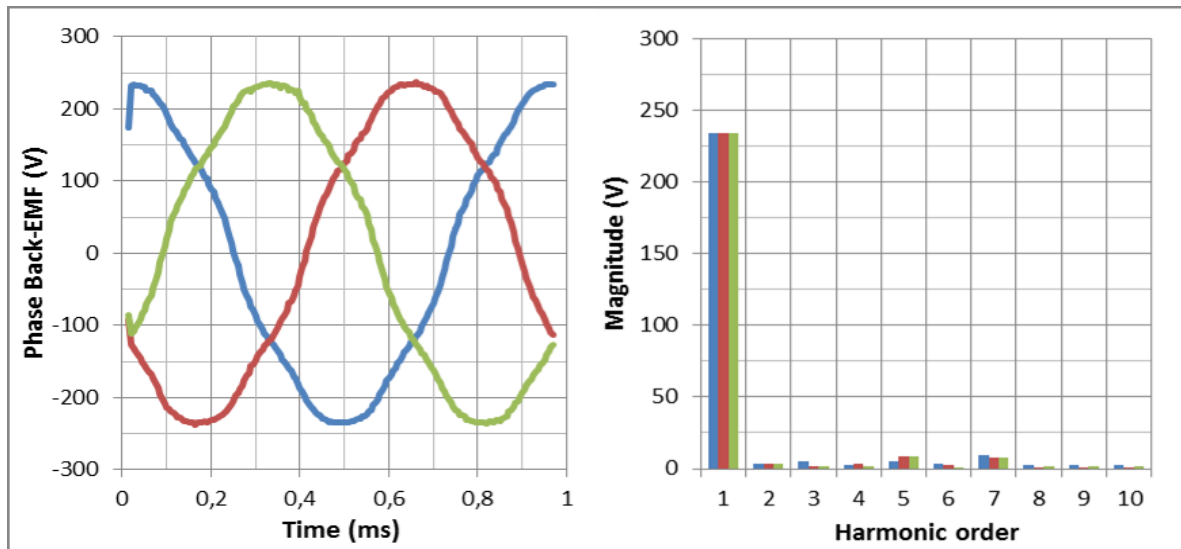


Figure 7-3: Simulation of phase back-EMF for all phases of Halbach-FSPM machine for one electrical period (left), and the respective harmonic spectra (right)

Total Torque

The final torque characteristics are also calculated using finite element simulations for different airgap length values. Figure 7-4 shows such curves, where the strong dependency of the output performance on airgap length can be appreciated. An increase of the airgap length by an order of magnitude (from 0.1mm to 1mm) reduces torque output by a factor of two. For the intended airgap length, the required performance is achieved at $100A_{RMS}$, with a torque ripple of 4.5%.

The effect of saturation is more pronounced for short airgap lengths since the magnetic loading is higher due to low reluctance. At a current loading of $40A_{RMS}/mm$, i.e. $100A_{RMS}$ or nominal phase current, the machine begins to saturate. At 120% of the nominal current, the drop in torque constant is evident for example for a 0.1mm airgap.

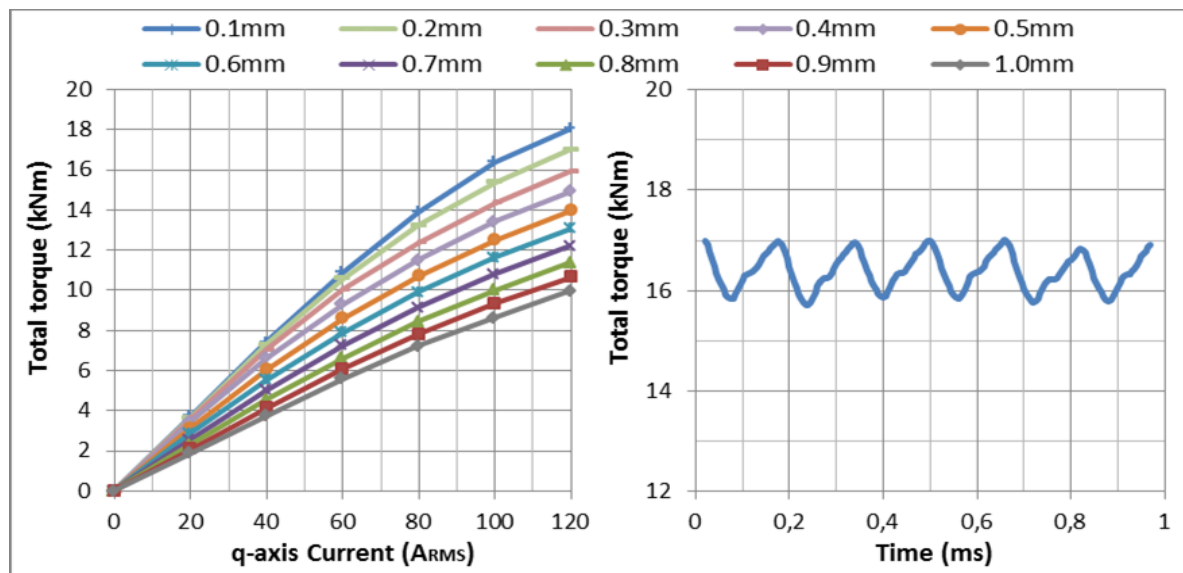


Figure 7-4: Simulated total torque as a function of phase current for different airgap length values (left) and during one electrical period for a 0.1mm airgap (right)

Normal Force per Segment

The normal force is between 5 and 7 times higher than the tangential force. For the design airgap length, a maximum average of 12.5kN is the normal force with a force ripple of 2.7% in no-load conditions (see Figure 7-5). For airgap lengths between 0.1mm and 0.5mm, the average force drops with increasing phase current reaching a minimum at 60% of the nominal current. Beyond this value, the average force increases again. For airgap lengths from 0.5mm upwards, the force always increases with increasing phase current.

There are then two different behaviors of the normal force according to airgap length. This is interpreted as a joint effect of the magnet flux (redirected to produce torque), and the armature reaction product of the applied current. As current is applied, the magnet force is redirected by the magnetomotive force, so that normal force is reduced and tangential force (i.e. torque) increased. The amount of tangential force produced at a certain phase current increases as the airgap length is reduced. Since the machine reluctance is lowered, the magnetic loading increases and consequently the torque constant. At the same time, as

current is applied, the armature reaction always tends to increase the attraction force between rotor and stator. For short airgap lengths, the net effect of these two contributions is a decrease in normal force. For long airgap lengths, since the magnetic loading is low in comparison, the force contribution from the armature reaction always prevails. For high phase currents, as the machine becomes saturated the armature reaction becomes dominant and its contribution to the normal force prevails. Therefore, the normal force in the high-current region increases at roughly the same rate regardless of airgap length.

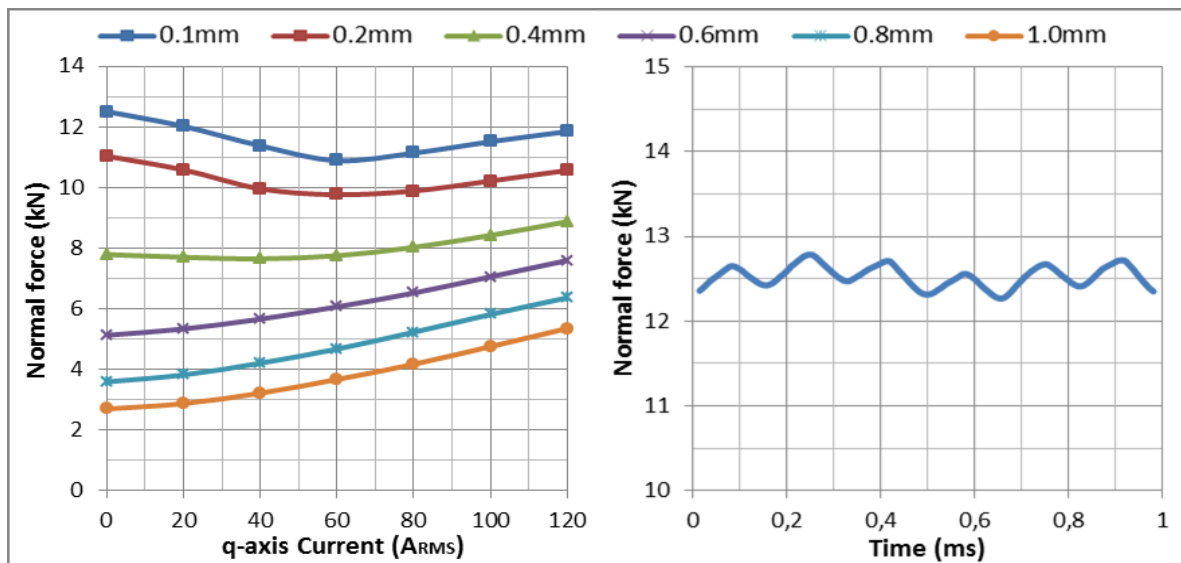


Figure 7-5: Simulation of normal force per segment as a function of phase current and airgap length (left) and during one electrical period for a 0.1mm airgap and no load

The behavior of normal force is also important for determining the air bearing requirement. It gives the magnetic stiffness of a single stator segment (change in normal force as a function of distance), which has an average value of $-10\text{N}/\mu\text{m}$ for all currents.

The lowest normal force as a function of airgap length is 25% of the maximum normal force at 0.1mm. Taking the maximum force (12.5kN) as the maximum operating point, air bearings can be used to maintain separation between stator and rotor. According to Figure 7-2, a 75% decrease in preloading (from 0.1mm to 1mm airgap and no phase current) can be accommodated in the fly height region between $5\mu\text{m}$ and $15\mu\text{m}$. Any change in preloading due to a change in phase current modifies the fly height by no more than one or two micrometers in all cases. This is for any airgap length adjustment.

7.3 Experimental setup

The experimental setup must be developed according to the same principle of separately suspended segments explained in 7.2.1. This includes a tangential support that allows free radial movement to account for thermal expansion and some rotor eccentricity. The objective is the validation of the mechanical functionality, by using a single stator segment without manufacturing a complete machine. For this implementation, the priority is set on

the proof of concept, and not on achieving the required weight. Bulkier structures are therefore allowed where convenient, to reduce manufacturing complexity and cost.

Furthermore, from an electromagnetic point of view, the one segment used for experiments differs slightly from those in a complete machine. This is to account for the absence of neighboring segments. The differences are presented more in detail in the next sections, together with the cooling scheme based on the use of compressed air.

7.3.1 Full Machine vs. Experimental setup: Segment Differences

All the results presented in 7.2.2 assume a complete machine with 14 neighboring segments, with which the expected performance can be achieved. The experimental validation however is done using one segment with outer teeth. These teeth provide a return path for the magnetic flux at the stator ends (see Figure 7-6).

The use of outer teeth has a limited effect in the electromagnetic performance as observed in the generated torque and normal force. Under the same operating conditions explained in 7.2.2, both output torque and normal force exhibit lower average values and have a more pronounced ripple (see Figure 7-7 and Figure 7-8):

- Average torque decrease per segment: 12%
- Torque ripple: 11%
- Average normal force decrease per segment: 6%
- Normal force ripple: 11%

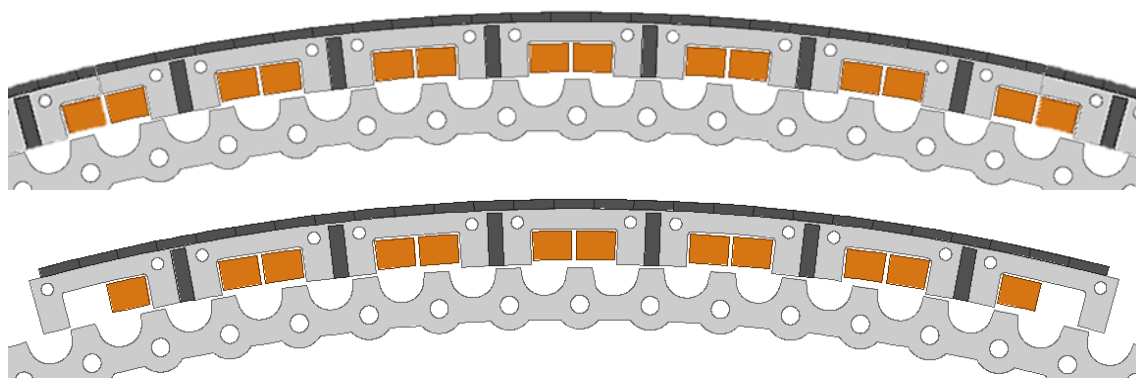


Figure 7-6: Complete machine with segmented stator (top) and segment with outer teeth used in experimental validation

The outer teeth and the absence of magnets in them cause a reduction of the peak flux linkage at the outer coils, since some flux escapes through those teeth. This results in the reduction of the torque capability due to asymmetric and reduced flux linkage at the corresponding phases. Consequently, the increased torque/force ripple is originated at those discontinuities as well. Magnetically, the flux escaping through the outer teeth increases normal force at some positions. On the other hand, the reduced linkage in the adjacent teeth decreases their maximum torque and normal force contribution. These two effects cause the strong variations observed throughout an electrical period [175].

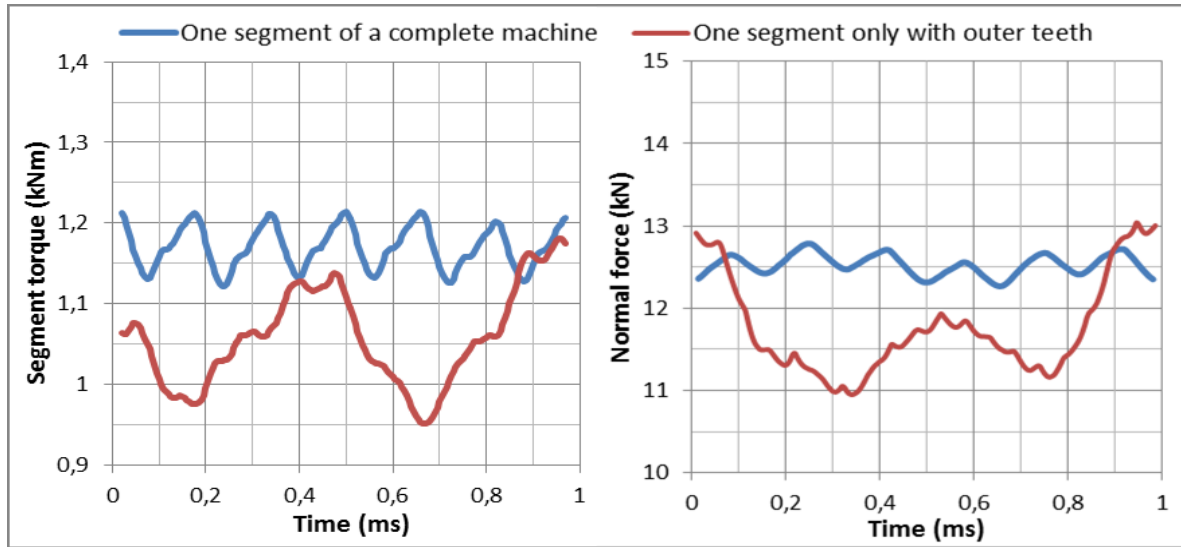


Figure 7-7: Simulation of torque output per segment (left) and normal force per segment (right) for one electrical period, airgap length of 0.1mm and nominal current

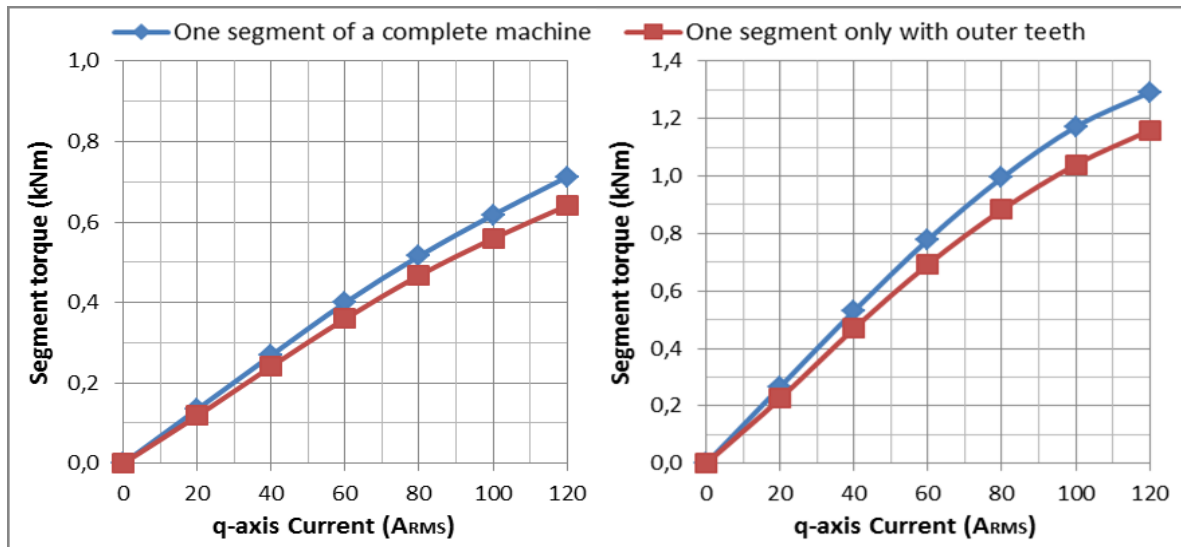


Figure 7-8: Simulation of torque output per segment as a function of phase current for a 1mm airgap (left) and a 0.1mm airgap (right)

A maximum average of ca. 12kN plus 11% of force ripple are observed for a segment with outer teeth. Air bearings must be able to counteract both these static and dynamic components of the attractive normal force. This is still achieved despite the higher force ripple, so that safe operation is possible with a new maximum preloading of 13kN.

Nevertheless, the high average normal force and increased ripple imply that the mechanical stiffness of the segment must be as high as possible. This minimizes stator and rotor deflection along the active length, so that a small airgap can be set. Since normal force increases with decreasing airgap length, the structural stiffness must increase accordingly. This issue and the air bearing dimensioning is examined in greater detail in the next section, where the complete support structure is introduced and analyzed.

Regarding output torque, the achievable performance of the experimental setup lags the required value by 12%. Since the priority is set on proof of concept, this is acceptable from an electromagnetic point of view. However, **this difference is caused by the outer teeth needed in a single-segment implementation. A full machine construction is expected to perform as analyzed in 7.2.2, fulfilling the imposed requirements.**

7.3.2 Support Structure

The support structure designed (see Figure 7-9) serves as a proof-of-concept testbench to verify the air bearing concept, and the feasibility of very small air-gaps. ***It is not a final implementation***, but a platform on which the principle can be validated. The air bearing units (light blue) are off-the-shelf components selected for simplicity and not weight.

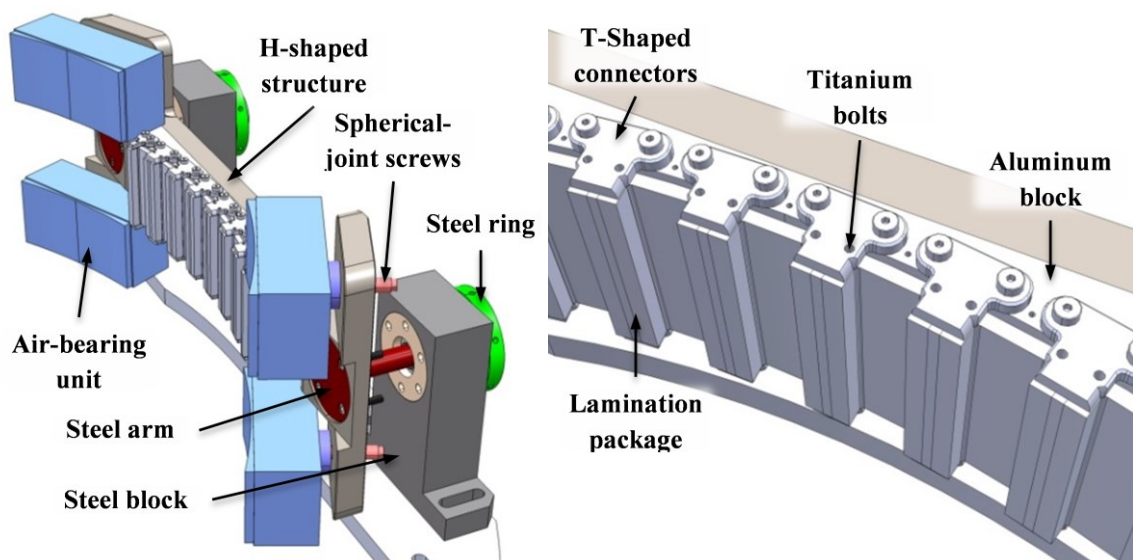


Figure 7-9: Stator support structure (left) and stator with titanium connectors (right)

The stator segment is attached to the rest of the support structure through T-shaped titanium connectors and titanium bolts. The bolts go through holes in the lamination package. The titanium connectors are fixed to a curved aluminum block on the back of the segment. This aluminum block is in turn attached to the H-shaped stainless steel structure that holds the air-bearings. The air-bearings are connected to the H-shaped structure through steel screws with a spherical joint (pink). This joint allows rotation and pivoting, allowing adjustment of the air bearings to the opposing surface. The air bearing arrangement provides support in the radial direction. Axial and tangential restraining is provided by stainless steel arms (dark red) connected to the fixed steel blocks (dark gray).

In the cross-section shown in Figure 7-10, the radial spherical plain bearings supporting the arms of the structure are visible in light gray. Besides the pivoting movement, these bearings allow back and forth sliding of the steel arms through them. At the end of each arm, two steel rings of different diameters (light green and light gray) provide a safety locking function for the complete structure. The airgap length is adjusted through the air bearing screws, thus moving the structure further away or closer to the rotor.

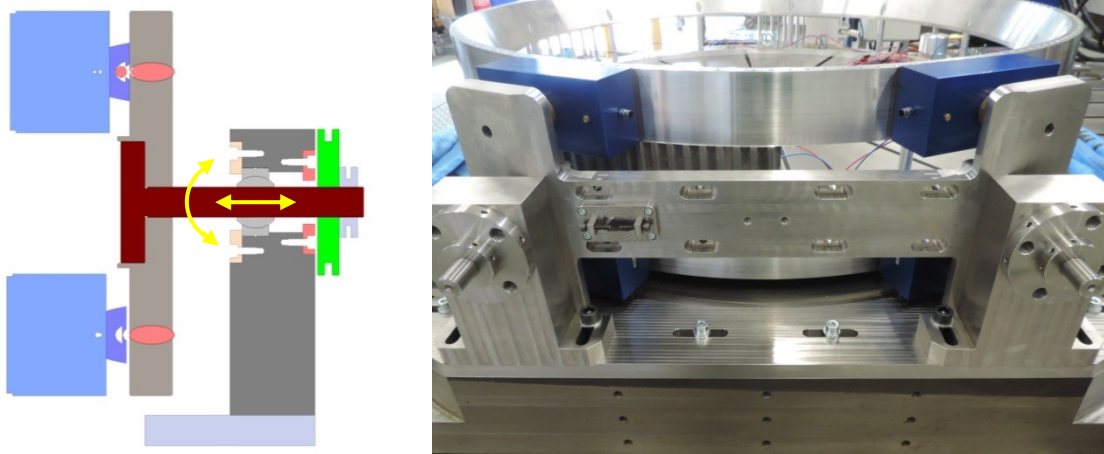


Figure 7-10: CAD cross-section of support structure (left) and actual laboratory implementation (right)

Air Bearing Dimensioning

From the FEM simulations performed, a maximum normal force of 12kN *in average* is found at the smallest airgap setting, i.e. 0.1mm. At this preloading, four air bearing units are used, providing a rated total load of 16kN and a safety factor of 25% (5 μ m fly height and 4.1bar supply pressure). In this configuration, the air bearing system has a total stiffness of -2660N/ μ m. This is two orders of magnitude higher than the magnetic stiffness of the stator/rotor system (ca. -10N/ μ m) as mentioned in 7.2.2.

Due to the difference in stiffness, the preloading force is perceived as constant by the air bearing system, for a fixed setting of the air bearing screws. Any change in the operating point of the air bearing is then unnoticeable for the stator/rotor system. The preloading force is then determined by the adjustment of the airgap length through the air bearing screws. The result is a stable operating fly height between 6.5 μ m and 10 μ m (see 7.2.1).

Compensation for Deviation from Ideal Support

With the use of off-the-shelf air bearings, their placement on the sides of the stator segment is mandatory, since they cannot be accommodated directly on top of it. This results in elastic circumferential deformation of the support structure and stator segment. The

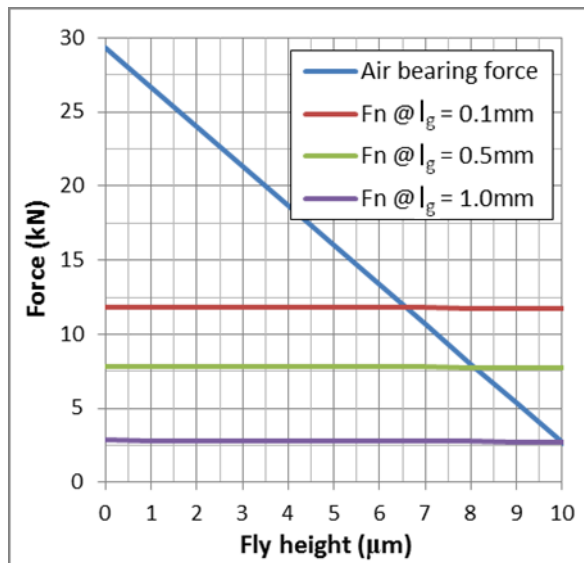


Figure 7-11: Air bearing force and total magnetic force per segment at different airgap lengths

deformation is caused by the construction's low stiffness, thus yielding a distorted airgap profile. The distortion can be many times the shortest airgap length, instead of a 10-20% suggested by related literature [177]. A structural reinforcement prevents this unwanted effect by limiting it to levels that allow accurate measurements of the output torque.

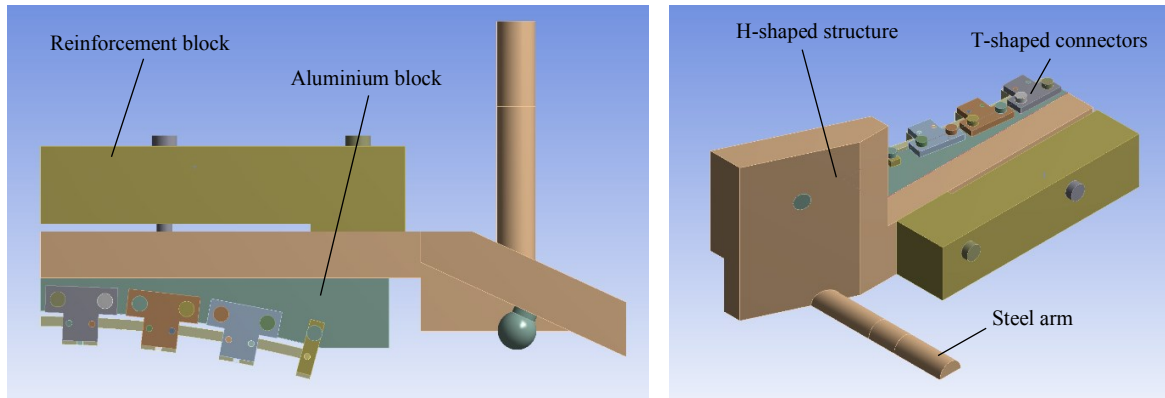


Figure 7-12: Top view (left) and posterior view (right) of reinforced complete structure with 2 planes of symmetry

A steel block (ocher colored in Figure 7-12) with a light C-shape is placed on the back of the original H-shaped support structure, leaving a small 5mm gap between them. Bolts go through block and original support (light brown), and are fastened at the aluminum block (blue-gray). The gap allows tightening of the center bolts, pulling the middle of the structure backwards, thus compensating the unwanted bending. Through bolt pretension, the amount of compensation is adjustable for different airgap lengths and normal forces.

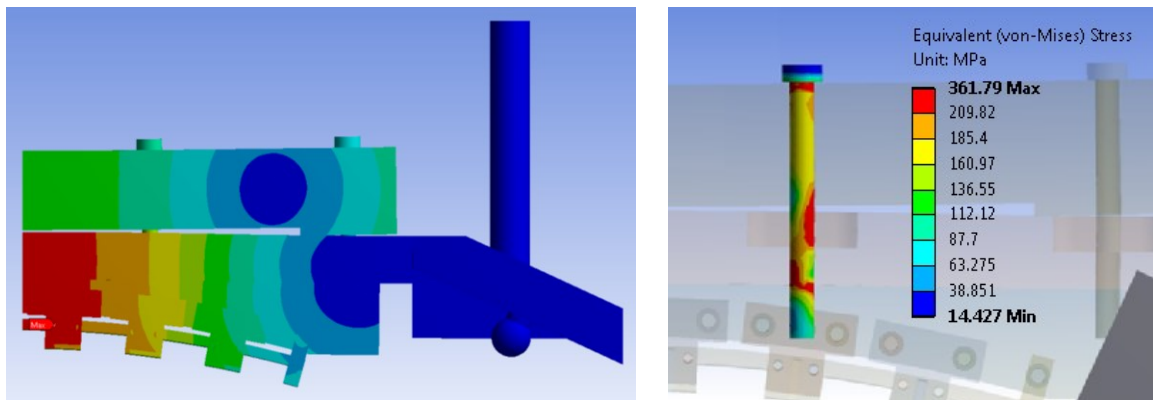


Figure 7-13: Deformation with bolt pretension and no applied normal load (left), and equivalent stress with 10kN normal force and 0.4mm bolt pretension

The reinforcement functionality and airgap distortion are examined by varying bolt pretension for a radial load of 10kN applied uniformly to the stator teeth (see Figure 7-13 and Figure 7-14). By applying pretension, the middle stator region is pulled back, resulting in a uniform airgap profile: for the applied normal force and a 0.1mm bolt pretension, the airgap profile is practically undistorted. The bolts used undergo practically no deformation, since they are class 12.9 alloy steel bolts with 1100MPa of yield strength.

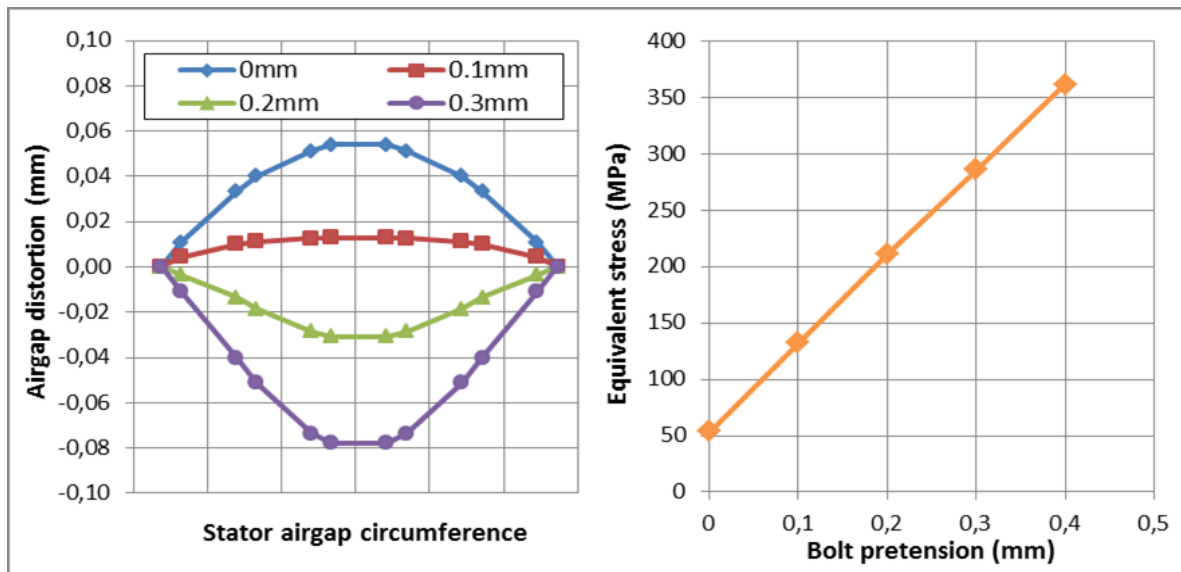


Figure 7-14: Simulation of airgap distortion profiles (left), and maximum bolt equivalent stress as a function of pretension for a 10kN normal force

7.3.3 Air Cooling Scheme

As reviewed in 7.1, the loss concentration in the small amount of active mass can be high and the available cooling area limited. This is despite the low losses with respect to the total power. These conditions call for the application of separate air cooling circuits in different regions of the machine. This way, cooling area and cooling effectiveness are maximized. Table 7-2 lists the electromagnetic losses occurring in rotor and stator active material at nominal load. From the total loss, 87% is present in the stator and the remaining 13% in the rotor. The winding loss accounts for the bulk of the stator loss, ca. 63% (55% of the total).

Table 7-2: Loss distribution in active material

<i>Loss Parameter</i>	<i>Stator</i>	<i>Rotor</i>
Conduction loss P_{Al} (kW)	8.92	N/A
Core loss P_{Fe} (kW)	3.20	2.04
Magnet eddy current loss P_M (kW)	1.15	N/A
Array eddy current loss $P_{M,array}$ (kW)	0.85	N/A
Support bolt eddy current loss (kW)	0.03	0.03
Total loss (kW)	14.15	2.07

There are three available regions in the active material useful for the removal of the aforementioned losses (see Figure 7-15):

- Inner rotor region (light green)
- Outer stator region (light blue)
- Slot and airgap region (light red)

In all three regions, forced convection must be implemented, either movement induced or with compressed air. The *main objective is to determine the effectiveness of forced convection in the third region*, since its geometry is far more complex, and must be studied using 3D Computational Fluid Dynamics (CFD). For the first and second regions, the approximate cooling characteristics can be approximated from relationships presented in literature for flow over simplified geometries.

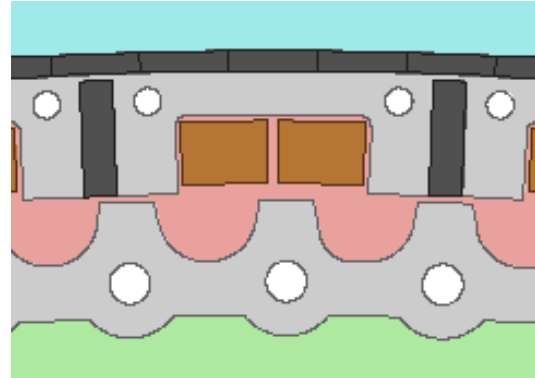


Figure 7-15: Regions available for cooling circuits (in light colors)

Rotor Cooling

In the green region, the rotor movement induces forced convection on the rotor inner wall. The relative free stream air velocity can be assumed to be the rotor linear velocity at that wall (ca. 25m/s). Axial flow is also assumed, so that hot air is transported out of the machine, albeit at a much lower rate (3.5m/s are assumed). Such a ventilation mechanism can be implemented in the final rotor structure by using e.g. fins. This induces air circulation in axial direction. Consequently, the resulting circumferential length L_c covered by an air particle before exiting the rotor region is roughly 75cm. Treating the airflow as over a flat plate, the Reynolds number Re_{Lc} can then be calculated as follows [177]:

$$Re_{Lc} = \frac{\mu L_c}{\nu} = 1216531 \quad (7-1)$$

where μ is the free stream velocity (ca. 25m/s), and ν is the kinematic viscosity of air ($1.53 \times 10^{-5} \text{m}^2/\text{s}$). The flow is considered turbulent, since the result is higher than 5×10^5 , which represents the transition between laminar and turbulent flow. Therefore, the Nusselt number $Nu_{Lc,av}$ for turbulent flow across a flat plate is calculated as follows [177]:

$$Nu_{Lc,av} = (0.037 Re_L^{4/5} - 871) Pr^{1/3} = 1658.4 \quad (7-2)$$

where Pr is the Prandtl number (0.709 for air). With $Nu_{Lc,av}$, the heat transfer coefficient h can be calculated using the conduction coefficient of air k_{air} (0.0262W/m·K) [177]:

$$h = \frac{k_{air} Nu_{Lc,av}}{L_c} = 57.9 \text{W/m}^2 \cdot \text{K} \quad (7-3)$$

Further assuming a rotor temperature of 100°C and an air inlet temperature of 22°C, all the losses from the rotor can be transported out of the machine. The calculations performed assume a simplified flat-plate geometry, but in reality the back of the rotor presents grooves. They are a consequence of the holes for the titanium bolts. Such grooves cause additional turbulence likely yielding an even higher heat transfer coefficient.

Stator Cooling

For the light blue region behind the stator, the use of a compressed air jacket is necessary, since the stator segments are static. A typical value for the heat transfer coefficient is assumed for compressed air cooling [179]: $100 \text{W/m}^2 \cdot \text{K}$. This allows 4.81kW to be

transported out of the machine (35% of all stator loss or 31% of the total loss), under the assumptions of 100°C object temperature and an air inlet temperature of 22°C.

The remaining 8.92kW represent the bulk of all losses produced: 63% of the stator loss or 55% of the total. This remaining loss must be handled through forced convection at the slot and airgap region (light red in Figure 7-15). The cooling structure of Figure 7-16 was developed to guide the air on the coil surfaces, and remove the heat directly from the coils.

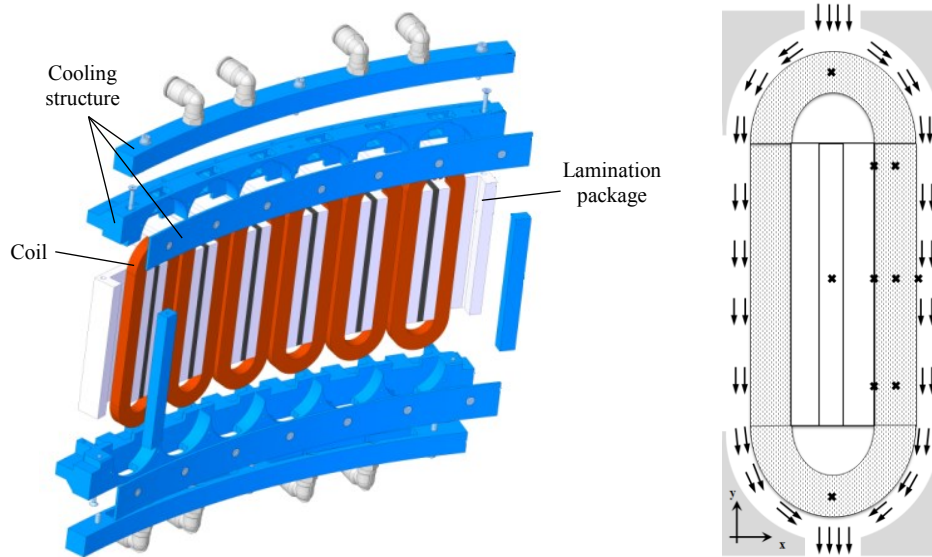


Figure 7-16: Stator segment with structure for air cooling with inlet on top and exhaust on the bottom side (left), and simplified air flow around one coil with x-marked sensor positions (right)

Each segment has its dedicated cooling structure, with four air-inlets supplied by two separate air-circuits for redundancy (see Figure 7-16). The air-inlet and exhaust of the cooling system are made of Duraform HST in the prototype. The final version is made of PEEK, an aerospace certified polymer that can be manufactured in complex shapes. After the inlet, the airstream is directed to the top of each coil head, which is circular in shape to guide the airflow around it. The air flows down to the bottom of the coil. There, it is again concentrated below the lower head of each coil and led to the exhaust. The main flow path of the air can also be seen in Figure 7-16.

An accurate approach to validate the cooling performance of the structure is a simplified CFD heat transfer simulation of one coil. The geometry of one stator tooth, with its corresponding coil and two rotor teeth are simulated. The rotor movement at nominal speed is also considered. Only the coil is considered as a heat source, with heat transfer possible only through the flowing air. The heat conductivity of the stator and rotor iron is set to zero. Therefore, forced convection on the back of rotor and stator cannot influence the cooling of the coil. Additionally, the complex geometry of the cooling structure is not modeled. Instead, the air is assumed to be flowing in a rectangular box surrounding the coil geometry. These simplifications have been made to reduce the modeling and meshing effort, and are considered acceptable in the scope of an initial performance estimation.

Air at 22°C enters from the inlet into the upper part of the segment, and then directed to the upper part of each coil head. The coil heads are round-shaped so that the hydraulic resistance is minimized. The air speeds up as it is compressed in the space around the coil. Additionally, the cooling stream swirls around the rotor teeth, causing turbulent flow and thus increasing the cooling effect as seen in Figure 7-17. An overview of the maximum temperatures achieved with each mass flow is also presented.

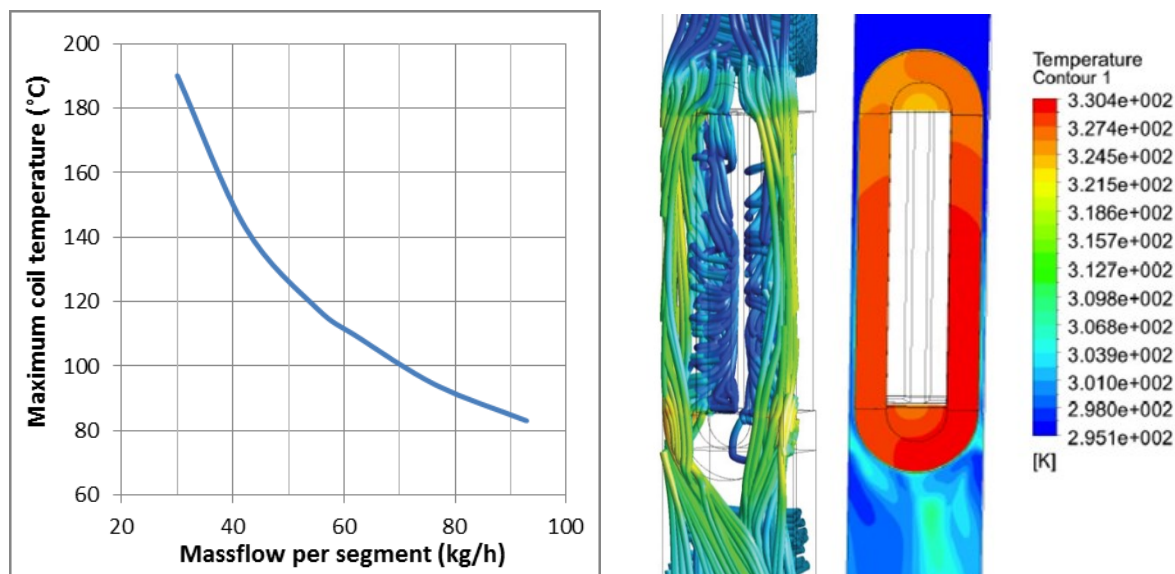


Figure 7-17: CFD simulation of maximum coil temperature as a function of mass flow per segment (left), and 3D CFD simulation of airflow around one coil and coil temperature profile (right)

The actual setup differs from the simulation model in its flow-path. The main difference is the design of the exhaust: in the setup, it concentrates the air from the two sides of the coil into one stream under the lower head of the coil. Initial simulations show that the bulk of the stator loss can be indeed cooled directly from the coils. The intended object temperature of 100°C is achieved with a mass flow per segment of 70kg/h. A lower temperature of 85°C can also be achieved with a mass flow of about 93kg/h.

7.4 Experimental Validation

Through numerical simulations, different aspects of the final Halbach-FSPM design have been analyzed and investigated. Complete verification of the electromagnetic design, cooling system and structural support concept require the construction of a full scale prototype. Due to the high cost and complexity of a complete setup, a modular approach and a partial validation in three phases have been followed. In the first phase, one stator segment and two rotor segments of very high precision were manufactured with cobalt steel laminations. Also manufactured were the support structure and other components for static measurements. The second phase focused on the testing of the cooling circuit, for which the stator segment was taken out of the setup. In a final phase, an entire silicon steel rotor with

lower precision was manufactured and assembled. This was used for rotational testing of the structural support concept and back-EMF measurements at short airgap lengths.

Although further phases were being considered at the moment of writing, the time required for their completion goes beyond the time stipulated for this study.

7.4.1 Phase 1: Static Torque Measurements

In this first phase, torque measurements were performed in standstill on a complete setup. More specifically, the following aspects were of particular importance:

- Torque at q -position
- Gravimetric torque density
- Torque as a function of load angle

As mentioned before, the setup consists of one stator segment and two rotor segments fabricated with an airgap radius tolerance of $\pm 10\mu\text{m}$. At said tolerance, it is possible to configure very short airgap lengths, while the adjustable reinforcement (see 7.3.2) guarantees an airgap profile with very little distortion. The complete setup and the rotor construction with the two rotor segments are presented in Figure 7-18.

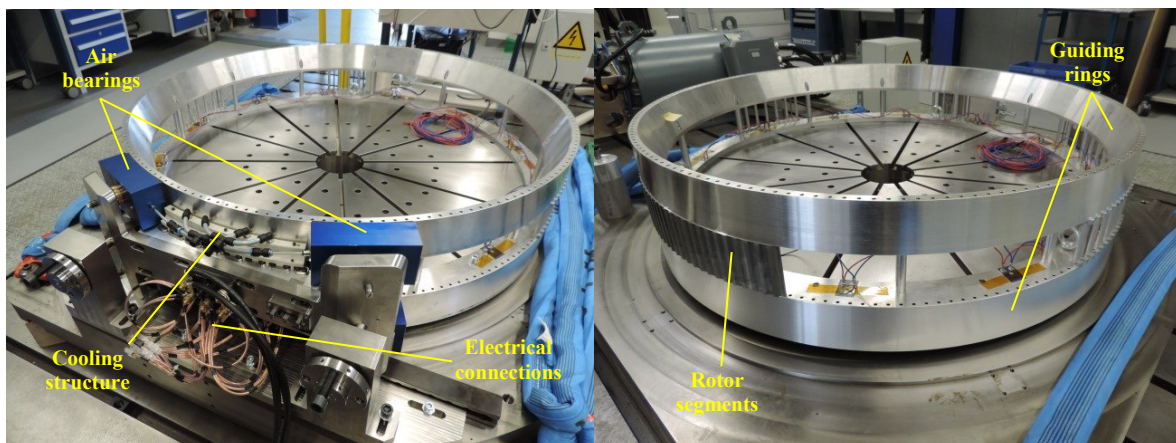


Figure 7-18: Complete setup with stator support structure equipped with air-bearings, electrical connections and cooling structure (left), and rotor with segments placed between the air bearing guiding rings

A schematic representation of the experimental setup is shown in Figure 7-19. The rotor position is fixed using a steel bar of adjustable length attached to a force transducer. The stator segment is energized using a DC current source, resulting in static torque generation. The tangential force at the airgap radius is measured, and then converted to the produced torque. The measurement of torque at different load angles is performed not by changing the fed current, but instead by changing the position of the rotor through the adjustment of the steel bar length. A 1mm increase or decrease in bar length corresponds to a variation of ± 15 electrical degrees. The bar length change is three orders of magnitude lower than to the rotor diameter. Therefore, the steel bar can always be considered tangential to the rotor throughout 180 electrical degrees.

Torque at q-position

Torque characteristics were measured for all airgap lengths, starting at 1mm down to 0.1mm in 0.1mm steps. Phase current was applied in steps of 20A_{RMS} starting at 20A_{RMS} and up to 120A_{RMS} using a DC current source (i.e. up to 120% of the nominal phase current). All experimental and simulation results are presented in Figure 7-20 and Figure 7-21.

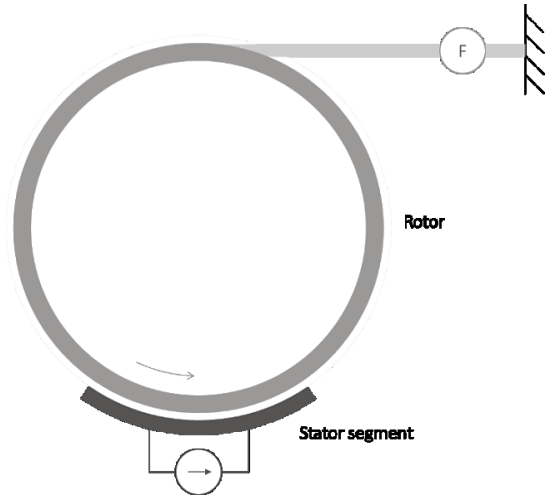


Figure 7-19: Experimental setup for torque measurement

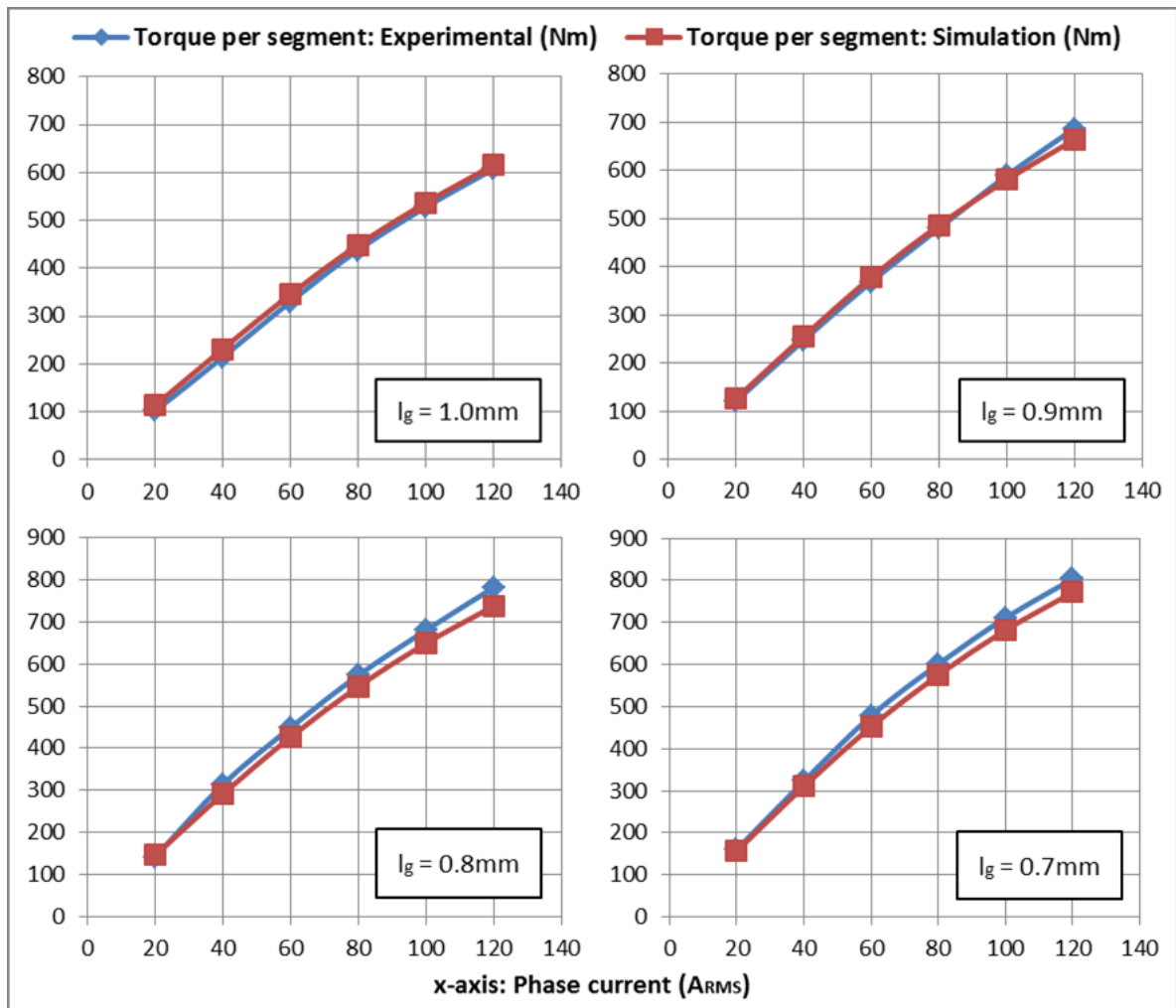


Figure 7-20: Segment torque as a function of phase current for different airgap lengths

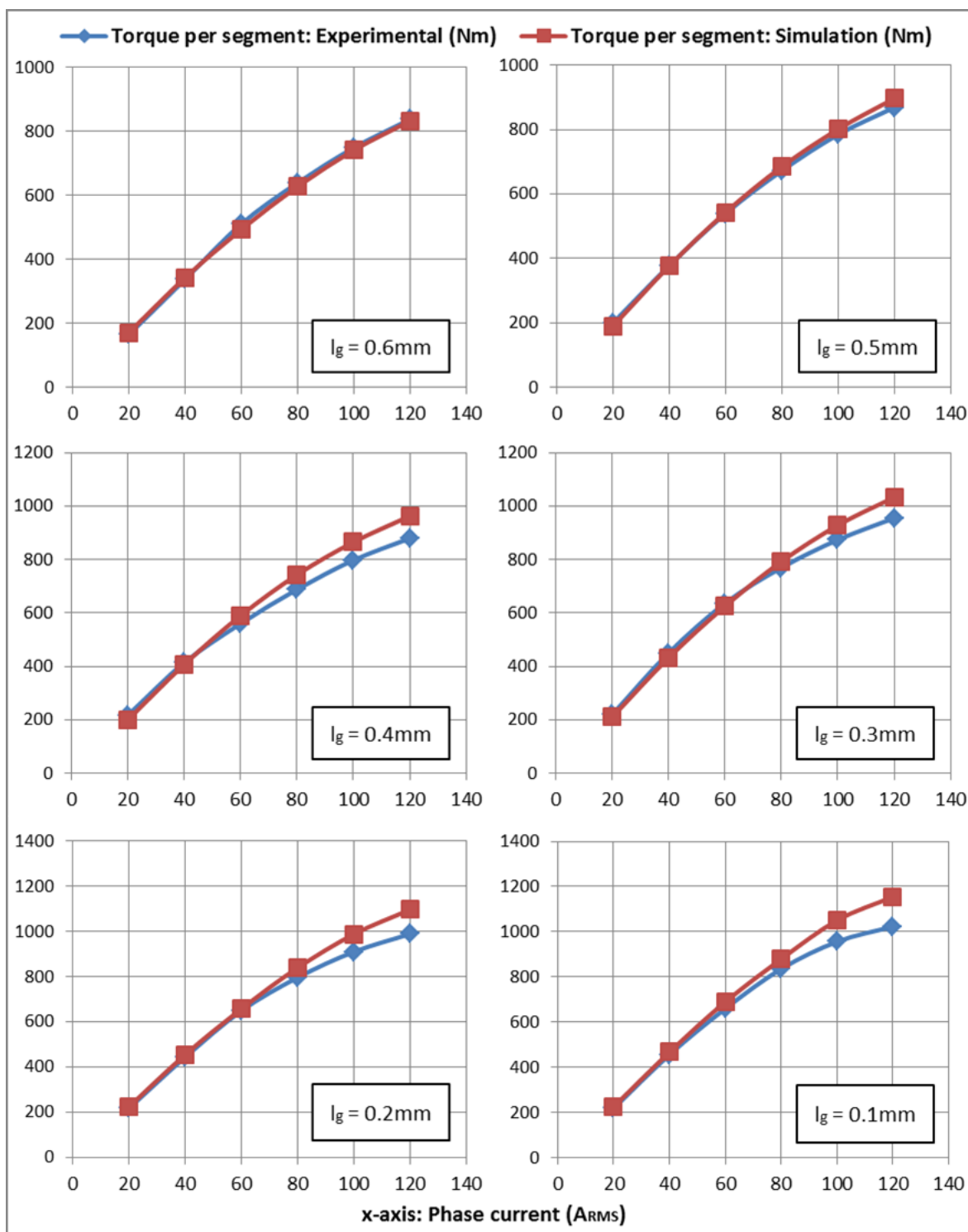


Figure 7-21: Segment torque as a function of phase current for different airgap lengths

All experimental data is in good agreement with results obtained previously from simulations. In some cases, e.g. for an airgap length of 0.8mm, the experimental results

even surpass the simulation results. This is attributed to the precision that can be achieved in the airgap adjustment: $\pm 30\mu\text{m}$. In such cases, the airgap configured was most probably less than the intended value. Such precision was achieved during adjustment by placing precision gauge brass foil (brass foil with high-precision thickness) between rotor and stator. This insured the intended uniform separation along the airgap circumference.

Furthermore, of particular interest is the increased saturation at high current loadings as the airgap is reduced. Starting approximately at a 0.5mm airgap and from $80A_{\text{RMS}}$ upwards, the measured torque characteristic increasingly differs from simulation values. The difference is initially 5% at nominal current and 0.5mm, increasing to 10% at 0.1mm of airgap length for the same current. The good agreement at low phase currents suggests the airgap adjustment is correct and within the achievable tolerance. The enhanced saturation in such scenarios is more likely to be caused by varying material properties in the prototype segment, product of the manufacturing process. Indeed, all simulations were performed assuming a perfectly isotropic material determined by the B-H-curve configured in ANSYS Maxwell[®]. Nevertheless, for the manufactured segment, the cutting process (wire-electro discharge machining) can slightly modify the magnetic properties on the machined edges and immediate vicinity. Although minor, this change becomes important for machines that rely heavily on magnetic reluctance or double saliency for torque production.

Gravimetric Torque Density

With the static torque measurements, the gravimetric torque density at the nominal phase current is calculated for the active mass in the current setup. This mass corresponds to the weight of the stator segment manufactured (with outer teeth), plus the corresponding rotor span (approximately 15 rotor teeth). This amounts to **8.3kg**. The results in Figure 7-22 show an increasing difference between the simulation and experimental values below an airgap length of 0.5mm. This is attributed to enhanced saturation as discussed previously. Performance is additionally limited by end-effects as explained (see 7.3.1). **A maximum gravimetric torque density of 115Nm/kg can be achieved for the current setup.**

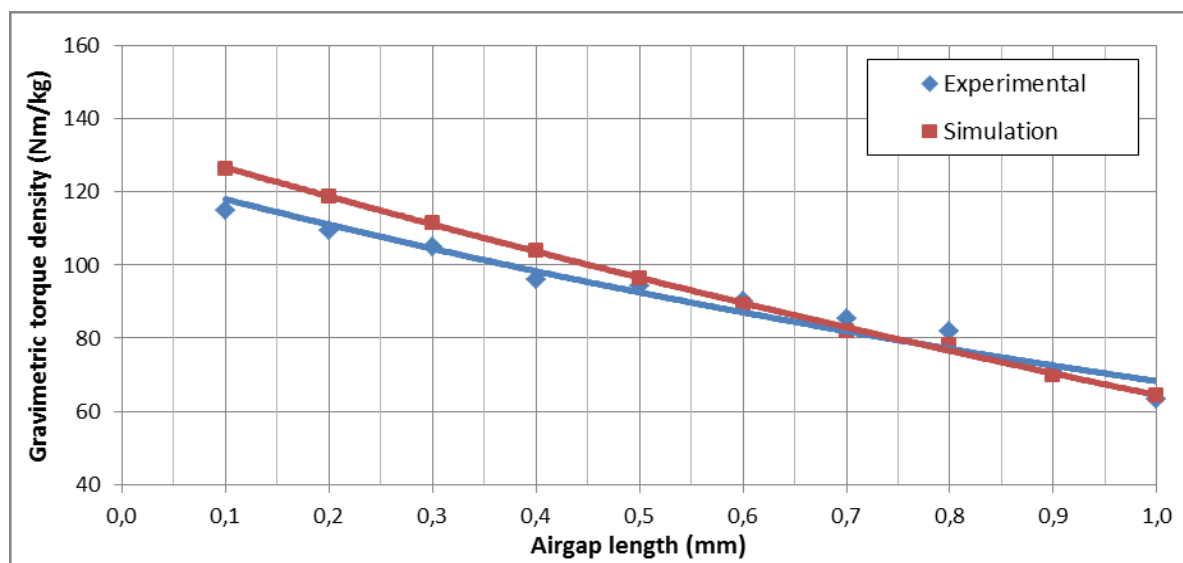


Figure 7-22: Gravimetric torque density as a function of airgap length at $100A_{\text{RMS}}$

Despite the suboptimal performance achieved, there is little difference with the simulation results for the same scenario. This is very important, since it confirms that the procedure and assumptions made throughout the design phase are consistent and valid. Furthermore, **it indicates that the performance-to-active-mass ratio of a complete machine would be very close to the target value set in the requirements definition in Chapter 2.**

Torque as a Function of Load Angle

Torque measurements were conducted by varying rotor position with a constant phase current applied. The experimental setup allowed position changes in steps of 12.8 electrical degrees. The measurement starts at 0 degrees of load angle (q -position), and goes up to 90 degrees ($-d$ -position). A $40A_{RMS}$ phase current was used for some of the smallest airgap lengths considered: 0.1mm, 0.3mm and 0.5mm.

The obtained values for each airgap are shown together with the respective sinusoidal fit (see Figure 7-23). Starting at zero degrees, it matches the q -position-torque presented in the previous section. The experimental data closely follows the sinusoidal fit presented alongside. This suggests no unwanted mechanical behavior that may alter the torque performance: from a static point view the constructed setup is stiff enough to prevent deformation. The airgap control mechanism maintains the desired separation as intended, so that further tests under no-load conditions can be carried out.

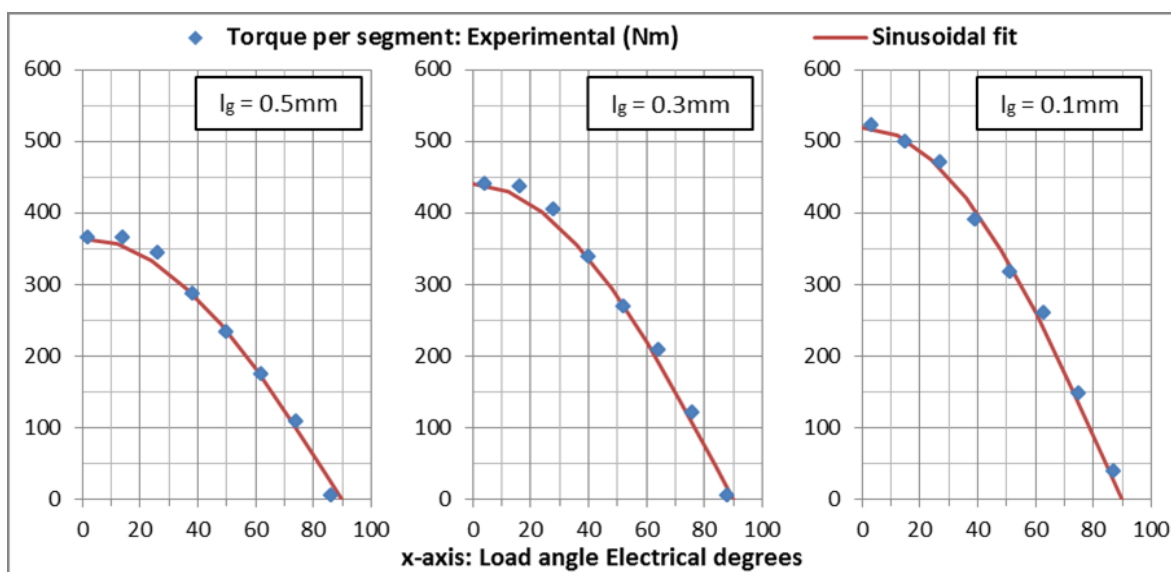


Figure 7-23: Torque as a function of load angle at 40% nominal current for different airgap length configurations

7.4.2 Phase 2: Cooling and Temperature Measurements

The actual stator segment of cobalt steel attached to the aluminum block is used for cooling experiments. The difference between the experimental setup and actual machine operation is the lack of iron and magnet loss which accounts for 35% of the total loss in the stator. Such loss is dissipated through forced convection on the back of the segment (see 7.3.3)

To simulate the rotor presence (without rotation), a 2mm-thick plastic sheet is placed at a distance of 1mm of the inner stator surface. The 1mm separation from the stator is intended as an effective mechanical airgap. This is to take into account the slotted rotor profile, in the same way the Carter factor accounts for permeance variation along the airgap. Thermocouples (k-type) are used to measure the temperature due to their small size, so that airflow disturbances are avoided. Disturbances can cause inaccurate results in the narrow air conduits, if the sensor shape and size is comparable to the conduit size. Temperature is measured at ten points along and across the coil (see Figure 7-16), so that the gradients in the x- and y-directions can be displayed. Inlet temperature remains constant at 22°C. The experimental setup is presented in Figure 7-24.

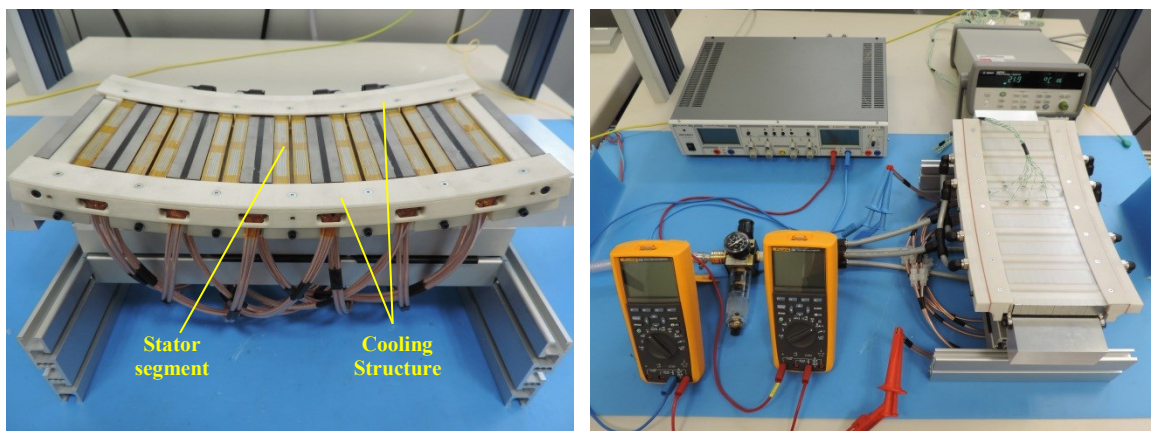


Figure 7-24: Stator segment with cooling structure (left), and experimental setup for cooling experiments (right)

Steady-State Operation

Steady state measurements were taken with a current density of $8.5A_{RMS}/mm^2$, for which a maximum temperature is observed in the middle and lower regions of the coil. Depending on the mass flow, the maximum absolute temperature varies from 195°C to 56°C. In the same manner, the difference between the maximum and minimum temperatures observed decreases with increasing mass flow and ranges from 52°C to 15°C. The temperature increases from the top to the bottom part of the coil. However, the temperature of the bottom head is lower than in the middle and middle-lower regions of the coil. This difference is a result of the reunification of the two air streams from each side of the coil at the bottom of the structure (see Figure 7-16). This was not evaluated in simulations, since the air conduits at the coil heads were not modelled. As the mass flow is decreased, this difference is reduced, since the airstream's speed is lower in overall. A gradient is also measured in the x-direction in the middle region, from the coil edge to the middle of the magnet. The measurements give a temperature profile and an indication of the different heat paths as seen in Figure 7-25. The temperature decreases from the inside of the coil towards its outer edges, since most of the heat flows towards the airstream on the side, front and rear of the coil. The remaining heat flows through the stator, mostly to the teeth faces facing the air-gap, where high forced convection takes place. The magnet is kept at a lower temperature thus avoiding the risk of demagnetization.

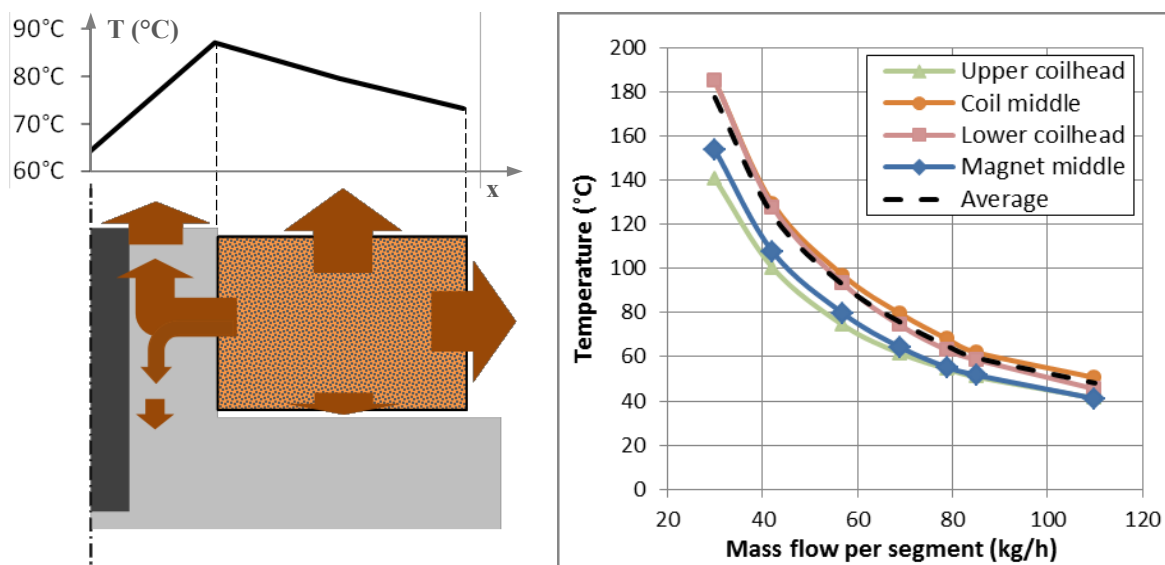


Figure 7-25: Temperature distribution across the coil and stator tooth surface for 69kg/h of mass flow with arrows representing heat paths (left), and steady state experimental temperatures at nominal current and different measurement points (right)

In the design phase, the DC conduction loss has been estimated assuming a uniform coil temperature of 100°C. To obtain this loss level, 55kg/h of airflow per segment are necessary (see Figure 7-25). Furthermore, it is possible to achieve lower operating temperatures and lower conduction loss by increasing the mass flow: an increase up to 85kg/h reduces the average temperature down to 60°C and the conduction loss by 18%.

The left half of Figure 7-26 compares the average coil temperature from simulations with experimental data. The cooling structure at the coil heads improves heat transfer in those regions considerably, making the difference with simulations as high as 30°C at

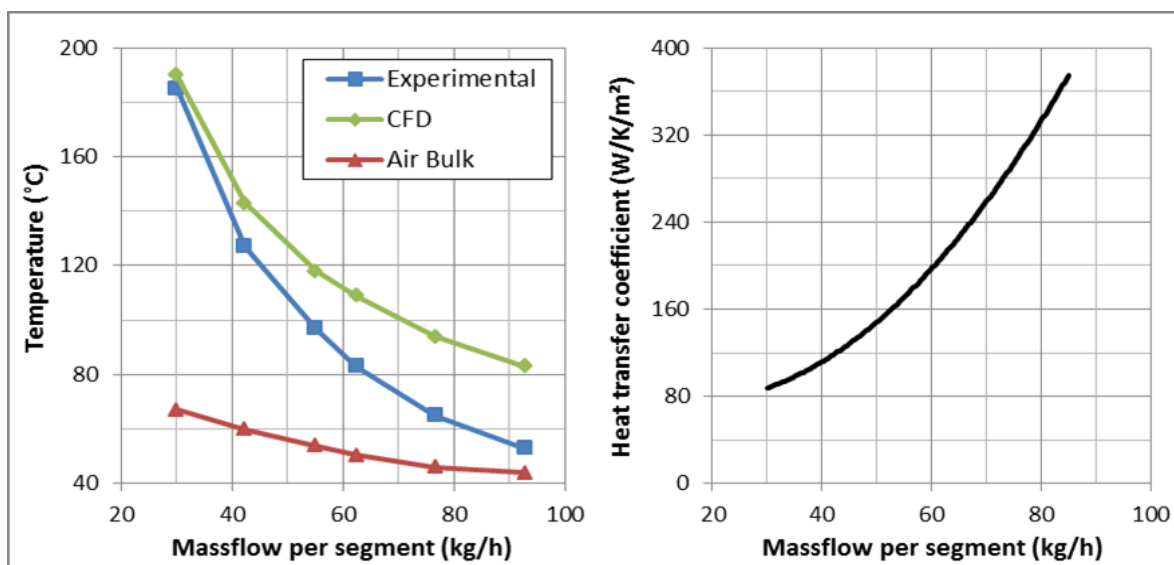


Figure 7-26: Average coil temperatures (CFD and experimental) and air bulk temperature (left) and approximate heat transfer coefficient (right)

90kg/h. This performance could eventually allow reducing the cooling requirements defined for the back of the stator and rotor, and/or allow higher current densities.

With the measured data plus a measurement of the air bulk temperature near the cooling exhaust, an approximate heat transfer coefficient is calculated (see Figure 7-26). Since it is not possible to characterize the heat transfer with complete accuracy in the studied region, the following assumptions were made for the coefficient calculation:

- The area where forced convection takes place is comprised by the coil and tooth surfaces only (including magnet region)
- 5% of the generated loss is considered to be conducted through the stator towards the back of the machine, were only natural convection takes place.

From this estimation, it can be concluded that direct air cooling of the windings allows reaching heat transfer coefficients comparable to those of moderate liquid cooling. Additional cooling circuitry and coolant handling are not needed, and the heat can be directly dissipated through the surrounding air. This makes it a light and practical solution for this application in particular.

Take-Off and Transient Overloading

Apart from steady state operation, tests for take-off and transient operation were also performed (see Table 7-3). Temperatures during these phases need to remain within acceptable limits (see Table 7-4), while minor performance degradation is acceptable. For transient behavior tests, the system was brought to steady state; take-off current was applied for 5 minutes, followed by transient current for 30 seconds. This sequence is considered a worst-case scenario as the transient follows the already overloaded take-off condition.

Table 7-3: Flight phases and machine operational states

<i>Flight phase</i>	<i>Phase current (%)</i>	<i>Duration (s)</i>
Cruise flight / Hovering (Steady state)	100	N/A
Take-Off	115	300
Transient maneuver	125	30

Table 7-4: Maximum operating temperatures for different materials

<i>Material</i>	<i>Maximum operating temperature (°C)</i>
Magnet material	190
Aluminum windings	500
Kapton	400
Durafoam HST ^{*1}	180 ^{*1}
PEEK	250

^{*1} Necessary during development only. Final structure made of PEEK

Results indicate that the effect of transient current is not very relevant due to the time constants of the system (see Figure 7-27). Take-off conditions result in a temperature increase of 16°C in the magnet region, which is well within the acceptable limits. This

temperature rise corresponds to 71% of the final steady state temperature that would be reached under prolonged transient operation. This test was performed under constant airflow of 85 kg/h. However, an airflow control scheme depending on the operation point, inlet air temperature and machine temperature can be considered for later design stages.

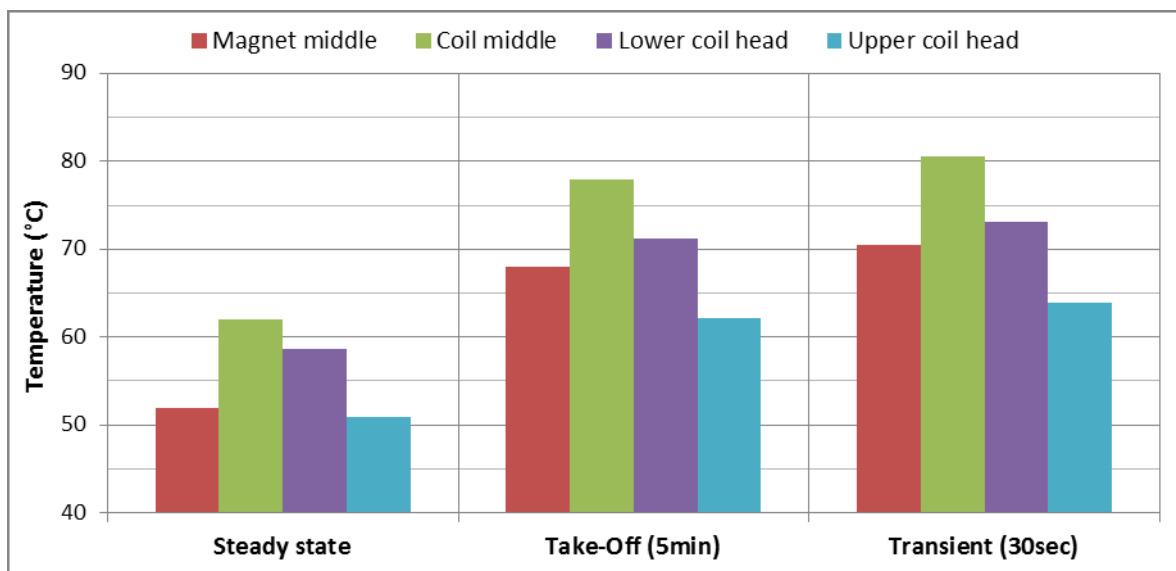


Figure 7-27: Experimental temperatures measured for a mass flow of 85kg/h.

7.4.3 Phase 3: Back-EMF and Structural Support Testing

In the final test phase a complete rotor made of silicon steel was manufactured and assembled. The complete setup was coupled to a driving machine via an aluminum shaft to perform no-load tests in generation mode and examine the following aspects:

- Phase back-EMF
- Stable operation of stator support concept using air bearings



Figure 7-28: Rotor segments before assembly (left), setup coupled to driving machine through aluminum shaft (center), and setup close-up with assembled rotor (right)

For the rotor assembly, 14 segments were manufactured using M270-35 silicon steel, but with a much lower precision compared to the original cobalt steel segments. While the cobalt steel segments were manufactured with an airgap radius precision of $\pm 10\mu\text{m}$, the silicon steel segment manufacture could only guarantee $\pm 100\mu\text{m}$. This constraint allows rotational testing down to an airgap length of 0.2mm without safety concerns.

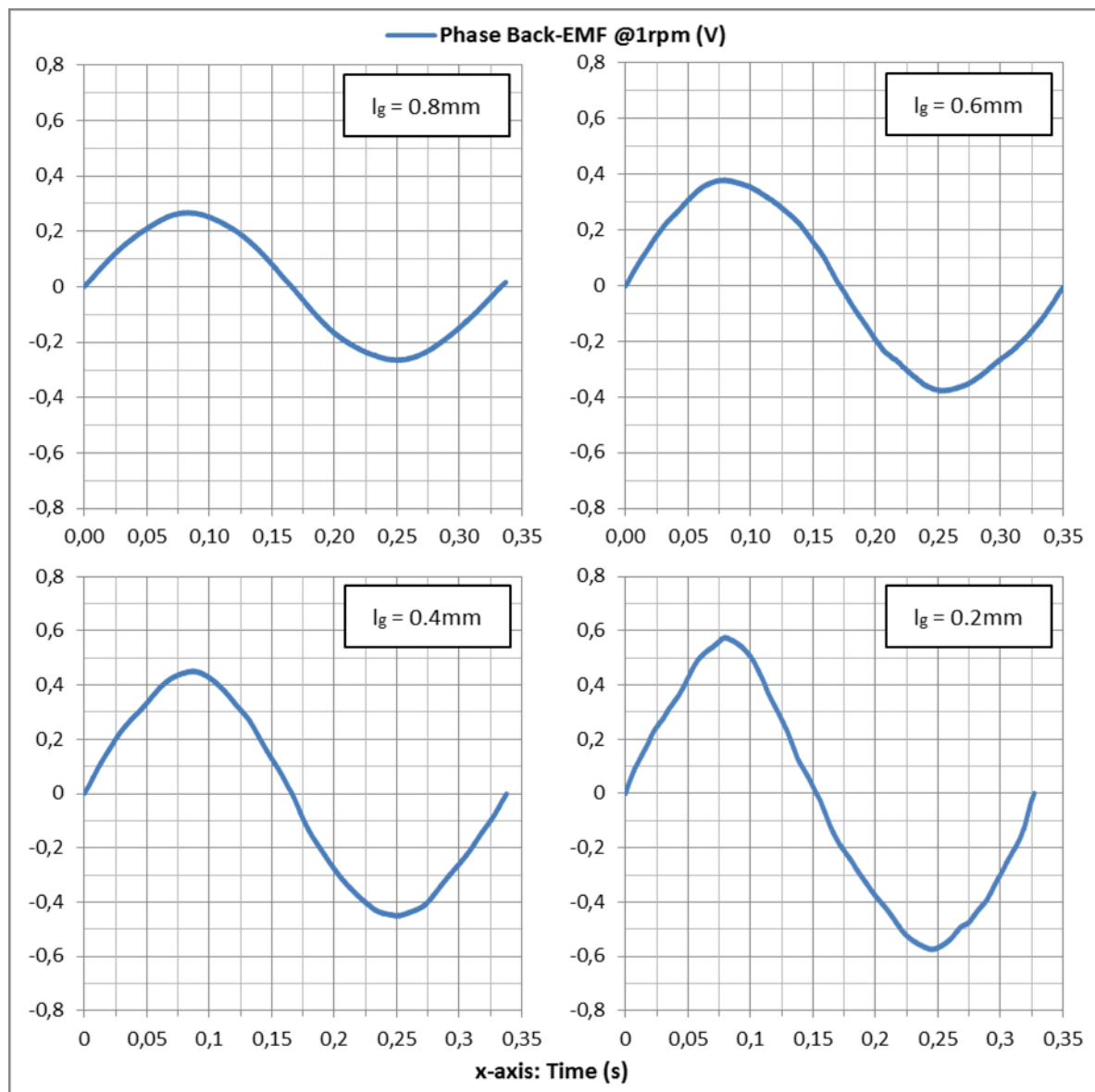


Figure 7-29: Experimental phase back-EMF measured for one electrical period

Phase Back-EMF

Running tests were performed at low speed and no load in generation mode. Starting at an airgap length of 0.8mm, it was consequently reduced down to a final value of 0.2mm in steps of 0.2mm. For each setting, the phase back-EMF was measured at a rotational speed of 1rpm (see Figure 7-30).

The measured waveforms are essentially sinusoidal, but a higher harmonic distortion is evident, when compared to the ideal waveforms of a complete machine (see 7.2.2). Quantified at a little under 9%, this enhanced harmonic distortion is mostly product of the modified flux linkage caused by the outer teeth of the stator segment. Furthermore, the phase back-EMF constant was calculated from the performed measurements and shown in Figure 7-30. There, an increase with airgap length reduction is observed, similar to the one seen for the torque density (and therefore torque constant) in Figure 7-22.

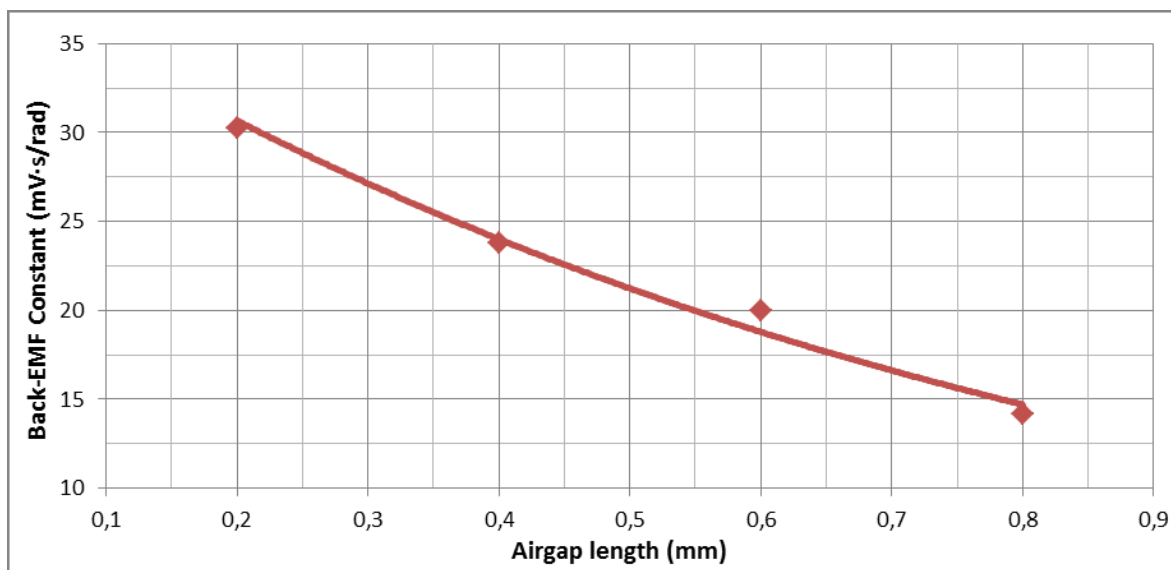


Figure 7-30: Experimental phase back-EMF constant as a function of airgap length

Stable Operation of Stator Support Concept Using Air Bearings

The previous back-EMF investigation is not entirely relevant for the machine evaluation, since the rotor manufacturing precision and material deviate from specifications. More important was the initial confirmation of the airgap control concept at a very low speed.

In a second investigation, the rotational speed was increased up to nominal speed. Although no measurements were performed, the objective was to assess the operational stability of the stator support, even if only under no-load conditions:

- **For an airgap length between 1mm and 0.4mm, the experimental setup was tested successfully at nominal speed (350rpm) for 60 seconds**
- **For an airgap length of 0.2mm, the experimental setup was tested successfully at 85% of the nominal speed (300rpm) for 30 seconds**

This test was only assessed qualitatively, and no relevant measurements could be performed at the time, so that its success could be quantified. However, the operation during the mentioned time is a relevant milestone of this study. The correct functioning of the support concept is vital for achieving the required torque density with air cooling, and is a major step for the further development of the concept.

7.5 Conceptual Stator Support Structure

The available support structure was only meant as a proof of concept, since its weight is inadequate as explained in 7.3. With a total target mass of 150kg and an ideal active mass of 100kg, the entire structural mass must not surpass 50kg. In this section, a design principle for an adequate structure based on air bearings is proposed and analyzed, based on the observed experimental behavior. The design objective is to set a base for further development and optimization, and not to design an optimized final structure. The methodology uses a weight model to estimate the performance-to-weight ratio of the complete machine as a function of airgap length.

7.5.1 Design Methodology

From the previous investigations, the following aspects are highlighted and must be reflected in the proposed structure:

- Distributed support
- Air bearings placement on top and bottom of each stator segment
- Stiff air bearing connections
- Use of alternative high-stiffness lightweight materials
- Improved stiff connections

The support structure is comprised of six brackets (one on every stator tooth), each one connected to the stator segment through titanium pins. The pins must be further secured with nuts on top and bottom of the connector to increase overall stiffness and prevent sliding. Figure 7-31 shows a cross-section of one bracket of the proposed concept.

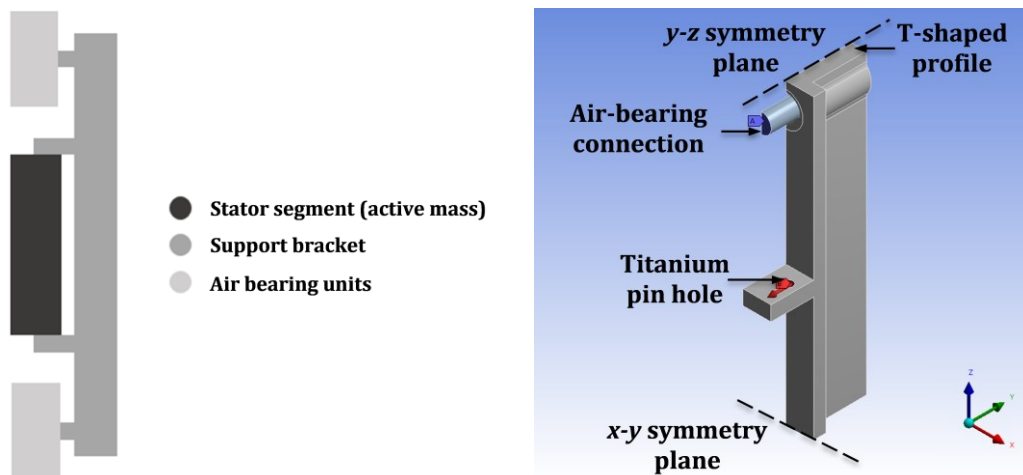


Figure 7-31: Cross-section of proposed structure (left), and load setup for finite element analysis of initial not-optimized bracket with two planes of symmetry (right)

A T-shaped bracket is chosen to fulfill two contradicting requirements at the same time: provide low mass but a high stiffness to avoid airgap deflection. Using a frictionless

support for the air bearing connector, a reduced Ansys model of the bracket was simulated with the load applied at the pin holes. An initial shape optimization was then performed (see Figure 7-32 and Figure 7-33). The material used initially is stainless steel 1.4305.

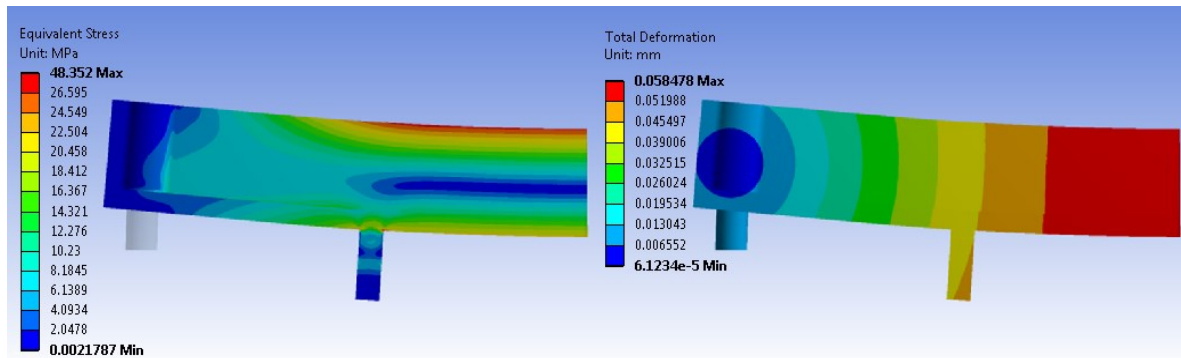


Figure 7-32: Simulated initial equivalent stress (left) and deformation (right)

The equivalent stress under load indicates the vital regions contributing to the structure stiffness, while the deformation is the measure of the actual shape. Material in low-stress regions can be removed and, depending on deformation, additional material should be added to high-stress regions. The stress distribution indicates that the bracket is more stressed in the area of the connector. High stress concentration is also found on the lower part of the screw thread of the air-bearing connector.

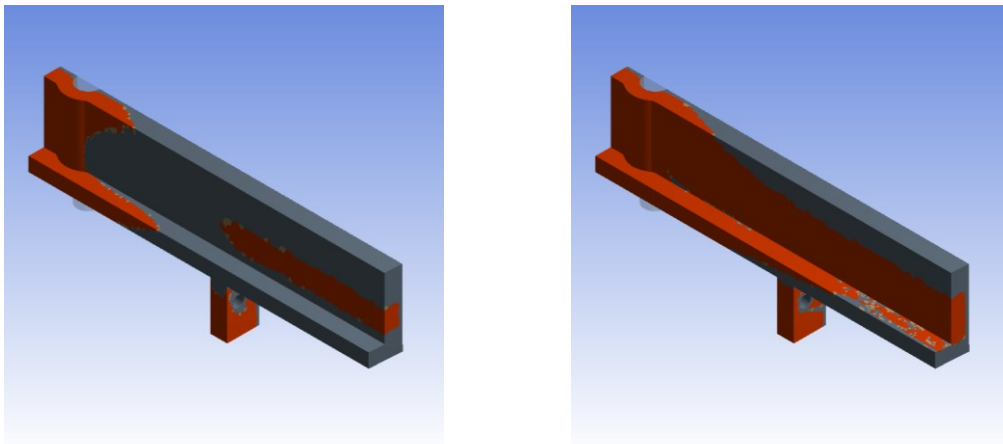


Figure 7-33: Geometry optimization for 30% (left) and 60% (right) weight reduction

The red regions in Figure 7-33 indicate the material that can be removed with little effect on the structural stiffness. In a second iteration 30% of the material is taken away from the low stress areas and the equivalent stress distribution is recalculated. The final result is shown on the left of Figure 7-35. There, titanium strips with fixed ends are also attached to the back to restrict tangential movement, when tangential force is applied. Titanium is used for the strips due to its high strength to weight ratio. The air bearings should support the structure in the radial direction and counteract the normal force, while the strips on the back counteract the torque (see Figure 7-34). The strips must have the necessary thickness only, so that stress remains within acceptable limits but without incurring in overweight: 10mm wide and 1.5mm thick strips are used to counteract the torque at nominal conditions.

The redesigned bracket exhibits a good stress distribution with few unutilized areas (see left of Figure 7-35). With this bracket, an entire support structure for one stator segment with six brackets is put together. Following, it is simulated under similar conditions as for the experimental setup. All brackets are connected to two concave air-bearings on top and bottom of the stator segment. Stiffness in tangential direction is guaranteed by connecting each bracket to the adjacent ones through bridges. This way, tangential forces don't cause large deformation between the brackets. The titanium strips, assuming only tensile loading, show a maximum equivalent stress of 30MPa, well below the 880MPa yield strength.

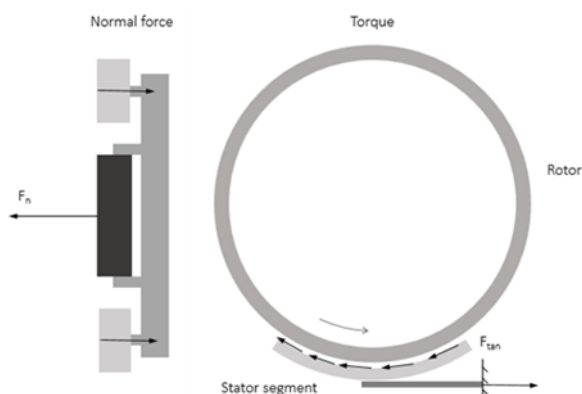


Figure 7-34: Support concept in the normal and tangential directions

The titanium strips, assuming only tensile loading, show a maximum equivalent stress of 30MPa, well below the 880MPa yield strength.

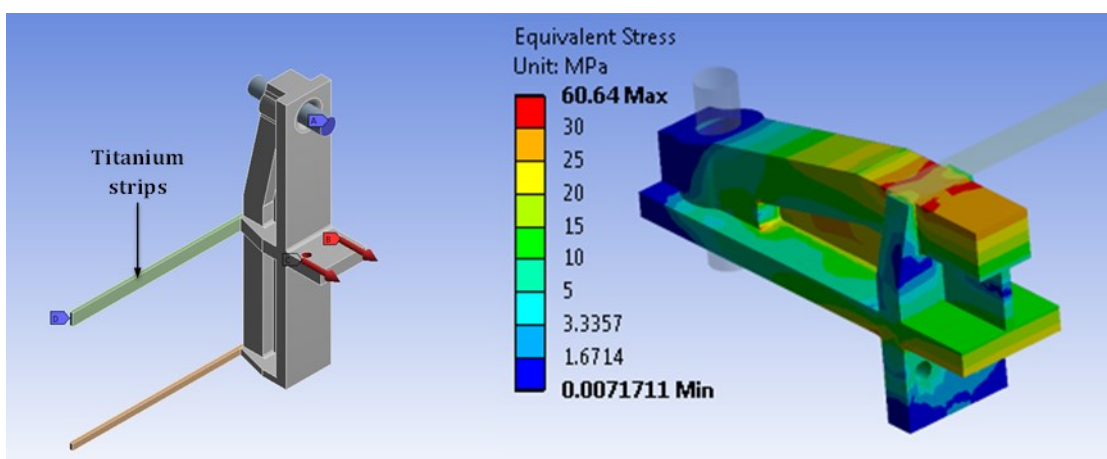


Figure 7-35: Redesigned bracket with strips supporting tangential loads (left), and simulated equivalent stress distribution on the surface and inside the bracket (right)

7.5.2 Stiffness and Weight

Besides stainless steel, an alternative material considered is a beryllium-aluminum alloy for aerospace applications with the brand name Beralcast[®]. This alloy has a very high stiffness to weight ratio with a Young's modulus of 202GPa. This is equivalent to stainless steel but with a quarter of the mass density (see Table 3-4). The Vacodur 49 lamination package is modeled as an orthotropic material in [175] according to the principle proposed in [179].

The structure stiffness is tested under a uniform radial force of up to 20kN applied to the teeth surface. The highest deformation is found at the middle of the teeth faces, and on the back of the support structure (see Figure 7-36). The structure shows almost no deformation along the airgap circumference, and most of the deflection is in the axial direction. The structure weight is of 3.55kg per segment when using stainless steel, and 0.97kg when using Beralcast[®]. Such mass is for an active stack length of 110mm, corresponding to the performance of a uniform 0.1mm airgap. At this point the stator segment weighs 4.45kg.

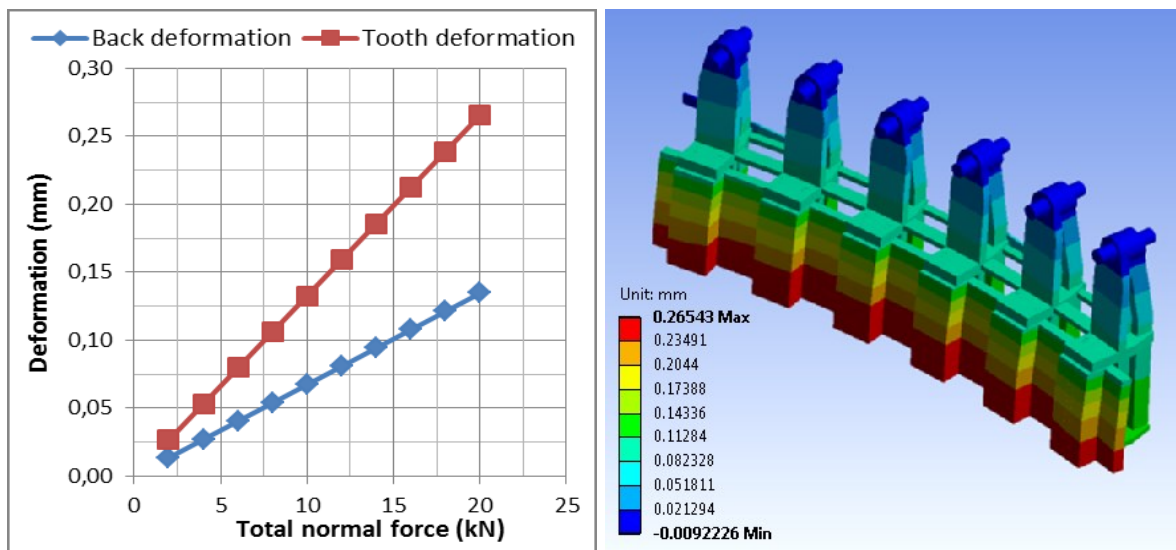


Figure 7-36: Simulation of structural deformation at stator teeth and on the back for a uniform normal force profile (left), and FEM solution for deformation under 20kN of uniform normal force for new support

7.5.3 Deformation Study

The first simulations with uniform force show adequate stiffness at a low mass. A more detailed analysis of the structural performance under no-load and nominal conditions is made with a one-way coupled electromagnetic-structural simulation (see Figure 7-37). Most of the distortion occurs at the outer teeth during nominal operation. The main cause of this behavior lies in the twisting of the structure caused by the produced torque around its own center. The outer teeth do not seem to be stiff enough to bear the nominal load without significant deformation. Furthermore, by simulating four different time instants within one electrical period, it was verified that the center airgap region is much less prone to deformation (see Figure 7-38).

Stronger brackets for the outer teeth should increase the stiffness on the sides and minimize deformation. Half of the maximum deformation takes place at the brackets, while the other half comes from the connectors and the lamination package. This suggests that the package mounting method is crucial to minimize airgap distortion and must be improved. Also, stiffness of the lamination package can be increased in axial and circumferential directions by adding attachment points between the support structure and the back of the stator. In this case, the Halbach array mounted on the back must not be damaged, and the adopted method may not cause excessive losses. Possible solutions include:

- Bolts in radial direction through the lamination package and support structure
- Division of lamination package in two halves and insertion of additional connectors between them

Axial stiffness would improve with either approach, at the same time introducing conduction loss and leakage inductance. It is therefore evident that the segment mounting is not a simple task, regardless of the machine topology, and requires further consideration.

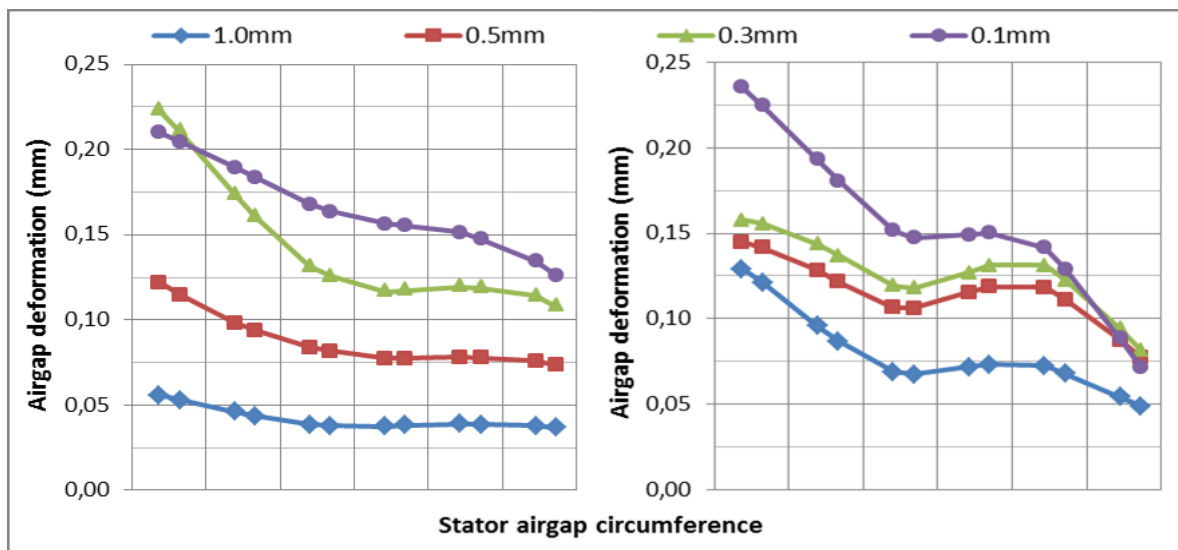


Figure 7-37: Deformation profiles at no-load (left) and nominal load conditions (right)

Airgap profile distortion causes a torque reduction, requiring an active length increase to match rated performance (see Figure 7-38). For a 0.1mm airgap, a 5.4% torque reduction compared to a uniform airgap takes place bringing the total active length up to 115mm (the point where rotor and stator are closest to each other measures 0.1mm). The resulting increase in both active and structural mass is further analyzed in the following sections.

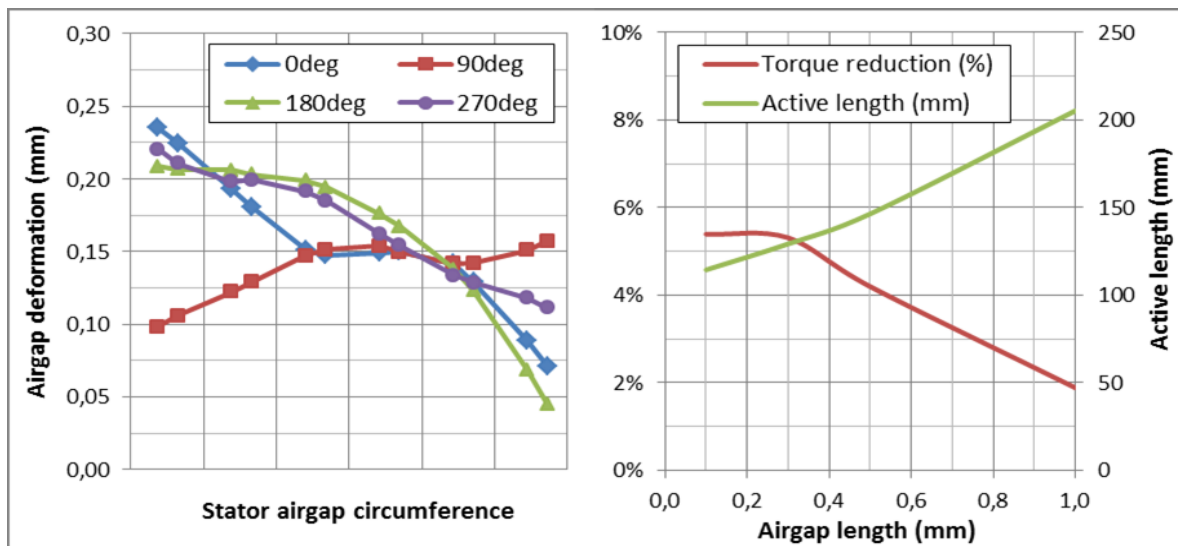


Figure 7-38: Deformation at different rotor positions for a 0.1mm airgap and nominal conditions (left) and airgap length influence on torque and active length (right)

7.5.4 Thermal Expansion

The main purpose of the segmented stator concept with air bearings is to bypass the effect of thermal expansion on airgap length. To achieve this, all rotor components must undergo thermal expansion homogeneously: active mass and air bearing rings. A mismatch in

thermal expansion coefficients between both components would lead to temperature dependent variations of the airgap length. The rotor active part is equally divided in 14 segments sandwiched between the two air-bearing-guiding rings. Each segment is fixed with 13 titanium pins (1 per tooth) that go through the segments and into the rings.

Two candidate materials are considered for ring manufacture: titanium and aluminum. While titanium matches the thermal characteristics of cobalt iron, aluminum is lighter and could also be used if the difference in thermal expansion is acceptable.

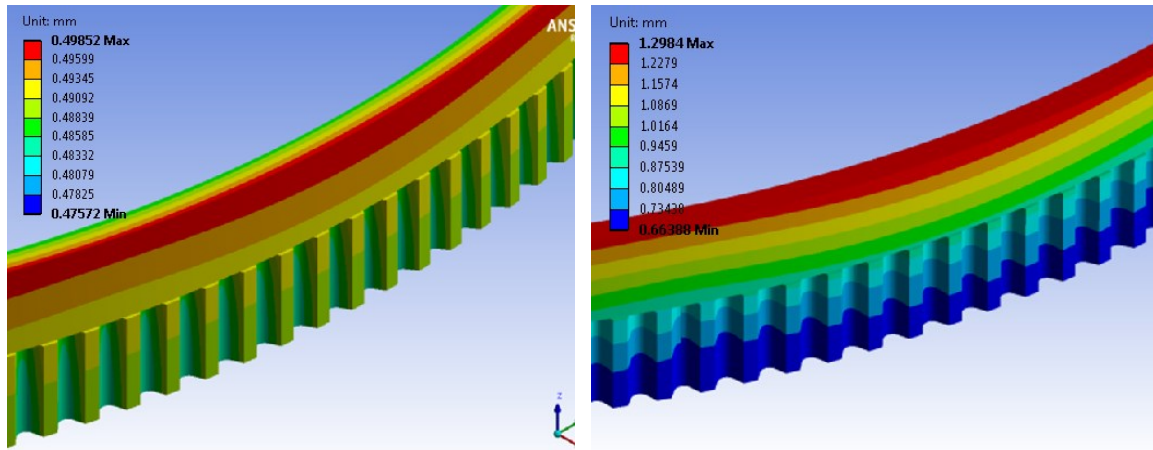


Figure 7-39: Rotor thermal expansion at 100°C with titanium rings (left) and aluminum rings (right)

In the case of aluminum rings, an *airgap length expansion* of about 450 μm at 100°C can be expected, while for titanium rings the increase would be of only 5 μm . From this result it is straightforward that titanium is a more adequate material choice for the guiding rings.

7.5.5 Weight Estimation Model

In a final step, a total weight estimation of the machine including the structural mass is proposed. This section presents a more detailed mass calculation, but should only serve as a first estimation and starting point for further work and optimization. The calculation approximates the electromagnetic-structural interaction. For this, deformation input data from FEM simulations and the performance dependence on airgap length are used. The active length is fixed at 110mm, so the active mass remains at 107.6kg.

Using simulations the relationships for output torque and normal force as a function of airgap length under nominal conditions are defined. For the selected airgap $l_{g,min}$ (this also represents the minimum distance between rotor and stator), the corresponding force profile is applied to the structure resulting in an airgap distortion δ_{dist} . The distortion is defined as half the difference between $l_{g,min}$ and $l_{g,max}$ (maximum distance between rotor and stator). Although a similar characterization of the rotor was not made, a simulation performed for this purpose showed similar behavior as for the stator under nominal conditions. Therefore, the full model considers an average electromagnetic airgap equal to $l_{g,min}$ plus twice the distortion. This accounts for rotor and stator deformation (see Figure 7-40):

$$l_{g,av} = l_{g,min} + 2\delta_{dist} = l_{g,min} + (l_{g,max} - l_{g,min}) \quad (7-4)$$

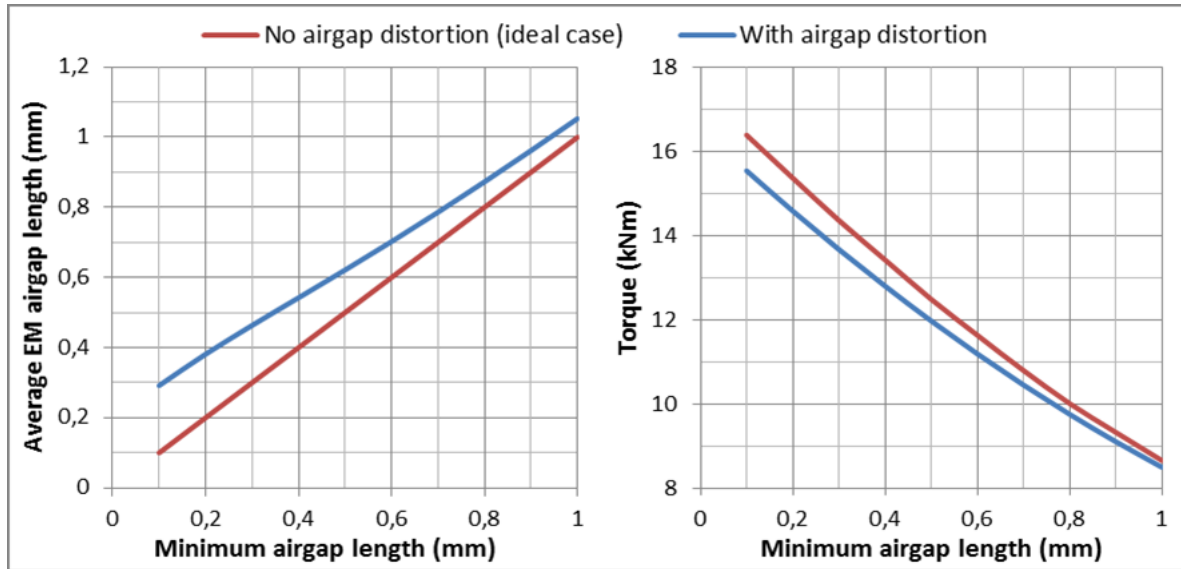


Figure 7-40: Average electromagnetic airgap (left) and output torque (right) as a function of minimum mechanical airgap $l_{g,min}$

The output torque and normal force are calculated using the average airgap. The result is a lower performance, since the average airgap length is always longer than the ideal case. With them, the mass of the following structural components can be calculated:

- Stator air bearings
- Stator support brackets
- Rotor guiding rings
- Rotor air bearings
- Torque transmission structure
- Miscellaneous components: bolts, pins, etc.

Stator Air Bearings

The normal forces of each stator segment are equalized by the air bearing units on top and bottom of it. To fully characterize the air bearing units, a force density per unit mass $F_{m,AB}^*$ and a surface force density $F_{s,AB}^*$ are calculated with data from the custom air bearing manufacturer Aerolas [180]. The air bearing performance is adjusted for a 9bar input pressure. The normal force magnitude determines the air bearing area needed, consequently determining the total weight of the air bearing units m_{AB} (see Figure 7-41):

$$m_{AB} = k_{safe} N_{seg} \frac{F_{n,seg}}{F_{m,AB}^*} \quad (7-5)$$

where N_{seg} is the number of stator segments, k_{safe} the safety factor equal to 1.5, and $F_{n,seg}$ is the normal force per segment. The circumferential span of the air bearing units is the same as the circumferential span per segment l_{seg} . The span is calculated by dividing the airgap

perimeter equally among all segments. Lastly, using the segment span and surface force density, the height of the air bearing units h_{AB} is calculated (see Figure 7-41):

$$h_{AB} = \frac{k_{safe} F_{n,seg}}{2l_{seg} F_{s,AB}^*} = \frac{k_{safe} N_{seg} F_{n,seg}}{4\pi R_g F_{s,AB}^*} \quad (7-6)$$

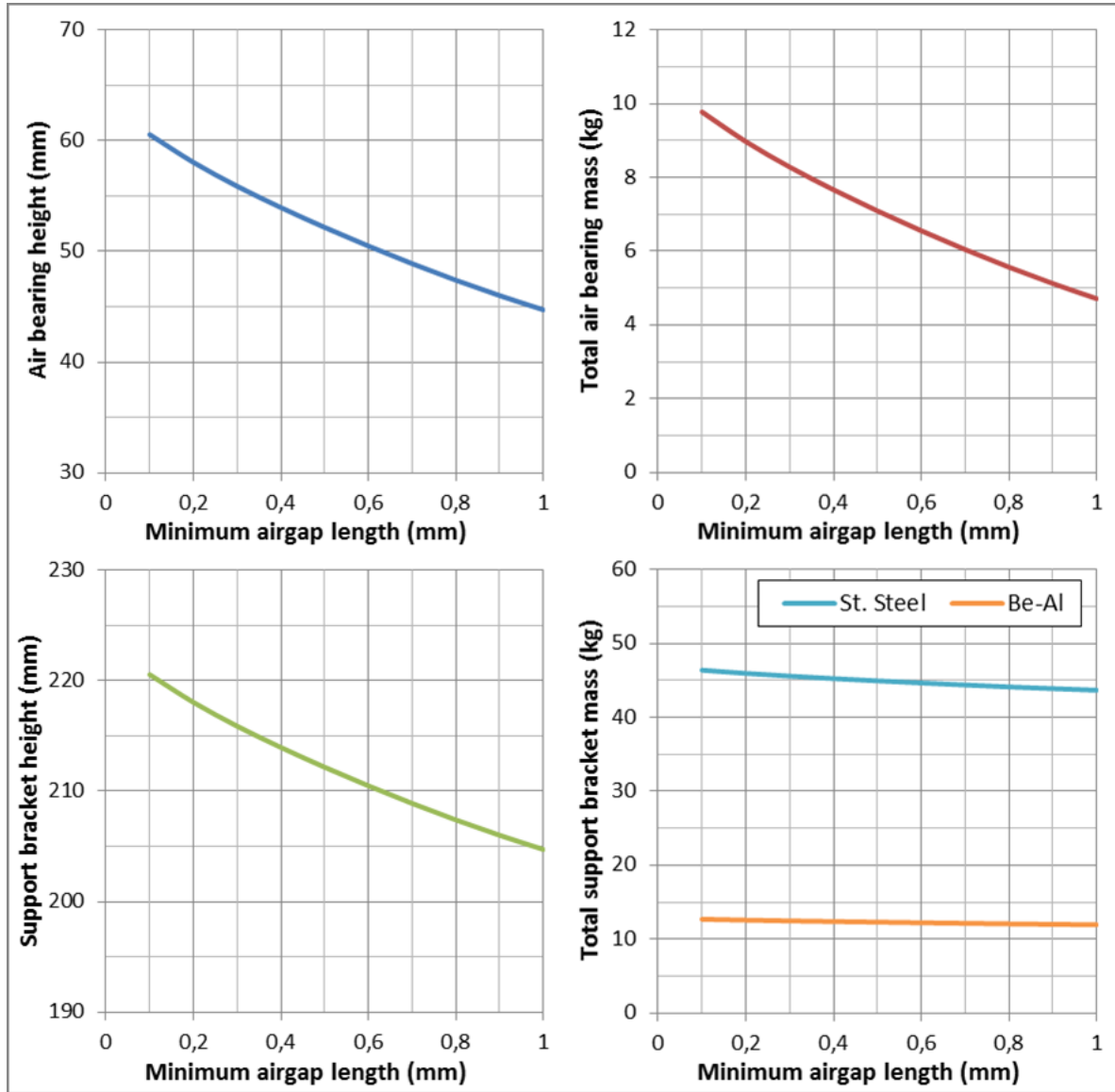


Figure 7-41: Height of each air bearing unit (top left), total mass of the stator air bearings (top right), height of support bracket (bottom left) and total support bracket mass (bottom right) as a function of minimum airgap length

Stator Support Brackets

The volume and mass of the stator support brackets is not calculated analytically, but instead derived from the CAD construction used for FEM simulations. The only parameter for which an analytical expression is presented is the bracket height:

$$h_{br} = L + 2 \left(h_c + \frac{h_{AB}}{2} + 10mm \right) \quad (7-7)$$

where h_c is the height of the coil-head-cooling region. The maximum variation of the total bracket height is 9%, caused solely by the variation of h_{AB} (see Figure 7-41). For the bracket mass calculation stainless steel and Beralcast[®] 310 are both considered.

Rotor Guiding Rings

For the rotor rings, titanium is the material of choice as explained in section 7.5.4. They have a radial thickness d_{ring} of 20mm and their height is equal to the height of the air bearings h_{AB} . The total mass of both rings is calculated and shown in Figure 7-42.

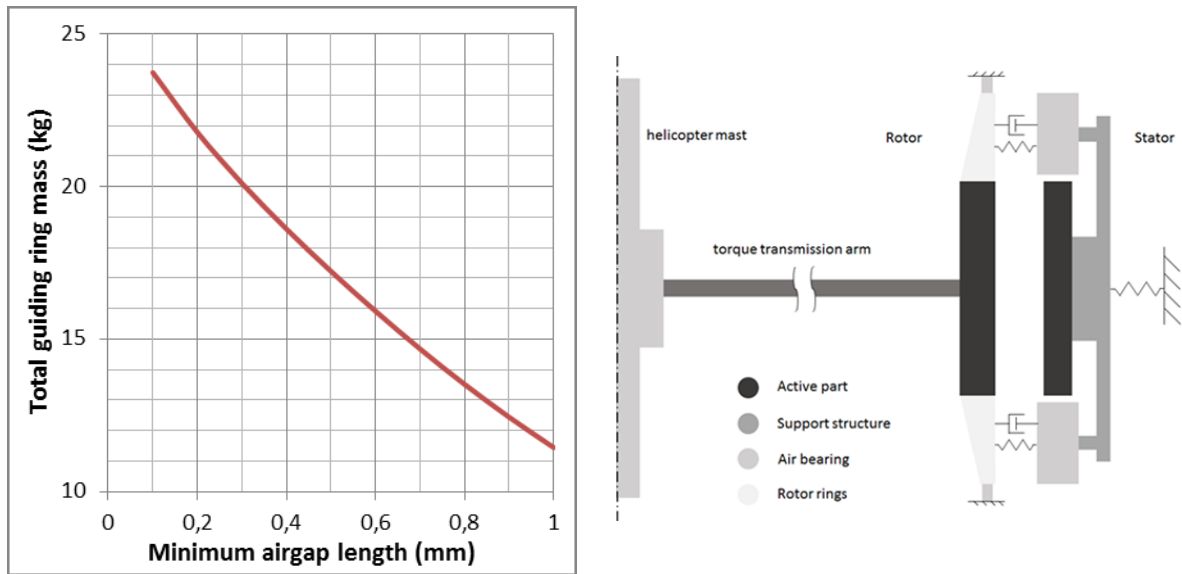


Figure 7-42: Total mass of the rotor guiding rings (left) and cross section of the conceptual machine

Rotor Air Bearings

The rotor weight is supported by air bearings mounted on the bottom side on the frame of the helicopter. Furthermore, with additional air bearings on the top side (see Figure 7-42), the rotor position is locked, and only yaw rotation is allowed during pitch and roll maneuvers. In this manner, the torque transmission arms need only to transmit the rotor torque to the helicopter mast without supporting any weight. These arms must be stiff in the radial direction only.

The mass calculation is done with the following expression:

$$m_{AB,rot} = \frac{k_{safe} k_{red} m_{rotor} g_{acc} (1 + 2a_{mvr})}{F_{s,AB}^*} \quad (7-8)$$

where k_{red} is a redundancy factor with value 1.5, m_{rotor} is the rotor mass, g_{acc} the gravitational acceleration. The parameter a_{mvr} is the acceleration to which the rotor is subjected during maneuvers (assumed to be twice the gravitational acceleration).

Torque Transmission

The mass of the torque transmission structure was estimated at 19.2kg using aerospace grade aluminum spokes and including a 50% safety factor [181]. Assuming further optimization and the use of lightweight high-strength composite materials, a 50% weight reduction could be reached: 10kg for a nominal torque of 16.4kNm. A reduction of the output torque due to airgap distortion causes a proportional reduction of the torque transmission mass.

Total Mass

In a final step, other miscellaneous components are considered in the final mass estimation as a function of minimum airgap length (see Figure 7-43). A stainless steel support structure results in ca. 50% of the total mass being structural mass (between 93kg and 105kg). A maximum total mass variation of ca. 12% between a 1mm airgap and a 0.1mm airgap is observed. The variation is mainly product of the air bearing height change. From this perspective, the choice of Be-Al as structural material is advantageous, since the structural mass represents 40% of the total mass in average (ca. 65kg).

Furthermore, using the estimated torque output with airgap distortion from Figure 7-40, the final torque density is estimated for a Be-Al structure. A maximum value of 87.7Nm/kg is found at the lowest airgap length of 0.1mm (average air-gap of 0.29mm). The corresponding torque at this point is 15.54kNm with a total mass of 177.2kg. A more conservative approach is taken with a 0.5mm minimum airgap (average 0.62mm), resulting in a torque density of 72.4Nm/kg, an output torque of 12kNm and 165kg of total mass.

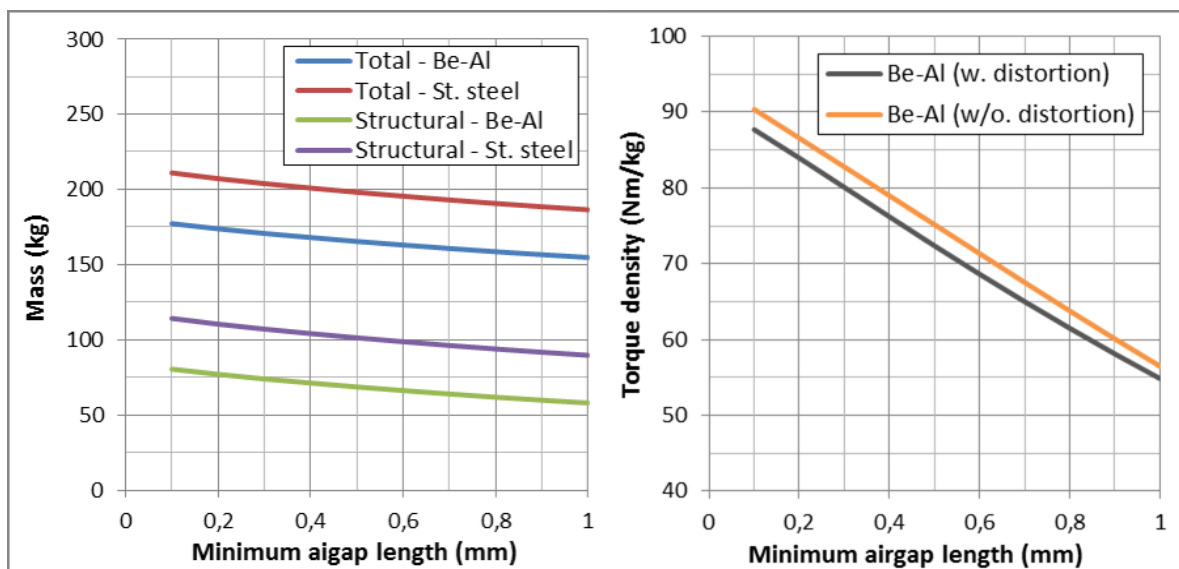


Figure 7-43: Total and structural mass for different materials (left) and torque density using Be-Al with and without airgap distortion (right)

Modeling the airgap deformation as presented in [175] involves a degree of uncertainty in its accuracy, which is owed mainly to the following factors:

- Differences in elasticity between actual material and FEM simulations

- Only one-way coupled simulation possible, neglecting the effect of structural deformation on electromagnetic behavior
- Uncertainty regarding the modeling principle of the orthotropic core
- Rotor not considered in structural analysis (twice the stator distortion assumed)

Nevertheless, electromagnetic simulations without distortion and experimental results showed good agreement, if only in static conditions. This suggests less distortion in the stator lamination package than predicted by the model. It is in this component where the highest deformation is observed. Due to these results and the modeling uncertainty, a second weight estimation was made assuming a uniform airgap profile, i.e. no torque reduction. This represents the absolute best-case scenario for the designed support structure, with only a slight increase in gravimetric torque density (see Figure 7-43).

Although there is an increase in torque output, the total mass increases at the same time, product of higher normal forces. The maximum torque density for a uniform airgap profile is 90.4Nm/kg, yielding a total mass of 181.6kg. The mass distribution and the differences between the two scenarios are presented in Figure 7-44.

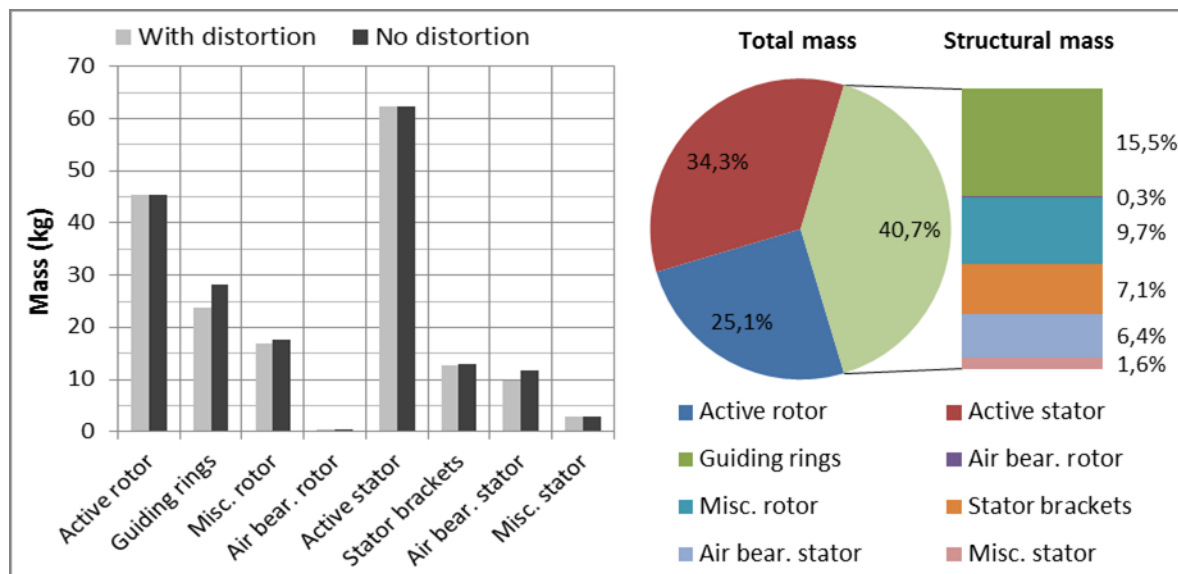


Figure 7-44: Component mass for deformed and uniform airgap profiles and 0.1mm airgap length (left), and mass distribution as a percentage of total mass for a uniform 0.1mm airgap scenario

Considering or neglecting airgap profile distortion has little impact in the total mass distribution. The differences are caused by larger torque and normal forces present in a uniform airgap profile. In the ideal scenario without distortion, the active mass corresponds to 60.3% of the total mass. The stator support brackets along with air bearings and other miscellaneous components correspond to 15.1%, whereas the stator support brackets alone account for 7.1%. The rotor rings and further rotor components however correspond to 25.5% of the total mass, and 63% of the structural mass. Improvement in torque density is expected, if the rotor support structure and especially the rotor rings are optimized.

7.6 Chapter Summary

This chapter revisited the machine topologies considered, and the resulting designs for the specific application of a civilian helicopter main rotor drive. This comparison showed that a Halbach-FSPM design offers a good electromagnetic performance and efficiency at the expense of increased airgap sensitivity.

For such design, a more detailed electromagnetic analysis and the implementation of a segmented stator was proposed. The electromagnetic analysis provided an overview of the machine behavior: it showed the variation of normal force and torque as function of airgap length, current and rotor position. The performance requirements are mostly fulfilled, but it was also noted that normal stress is significantly higher and almost six fold the tangential stress. The resulting normal forces are balanced out directly at the airgap, through the use of air bearings on top and bottom of each segment. This guarantees a constant separation between rotor and each stator segment, regardless of the thermal state of the active components. Experimentally however, the implementation differed from the ideal concept in the following aspects:

- Stator segment manufactured with outer teeth (this closes the magnetic flux path)
- Air bearings positioned on each side of stator and not directly above and below
- Use of four support points (one at each corner) instead of a distributed support

Simulations considering these differences showed a decrease in output torque and an increase in experimental setup mass. This is however acceptable, since the principles of electromagnetic and support design could still be validated with good agreement between simulations and experiments. Static torque and air cooling measurements, together with no-load test runs, showed that fulfilling the overall requirements is possible.

Therefore, the basic design of an improved stator support structure was attempted. This basic design is based on a segmented stator supported on air bearings. The improved structure avoids the drawbacks of the experimental setup, allowing a more unbiased estimation of the final gravimetric torque density. In the design, the shape of the structure was optimized, and its structural stiffness and performance were investigated. A major weight reduction has been achieved, along with an improvement in stiffness characteristics. Potential flaws of the new structure have been pinpointed, and possible improvements have been suggested to minimize the airgap profile distortion. Additionally, the rotor thermal expansion has been investigated in order to identify suitable materials for the air bearing guiding rings. The material choice has an impact on the total machine weight.

The weight model created in the previous steps provided a performance estimation based on the achievable airgap length at nominal conditions. For a fixed active length of 110mm, little difference was found between the ideal and distorted airgap profiles: 90.4Nm/kg and 87.7Nm/kg respectively. The latter however, shows 5.5% less torque output and 2.5% lower mass compared to the former. The ideal case represents the absolute highest possible gravimetric torque density achievable with the present approach. This suggests a weight penalty of at least a 21%. The new structure is but a basis for further work and not a fully optimized design. Further work should focus on lightweight composite material use, more in-depth structural optimization and actual operation.

Chapter 8

Conclusions and Recommendations

This last chapter reviews the most important findings of this work. The review takes place in the context set by the thesis objectives and research question (Chapter 1, sections 1.3.2 and 1.3.3), and is presented in three separate topics: considerations for electrical main aircraft propulsion, topology selection and comparison, and distributed design approach. Additionally, it lists the technical and scientific contributions achieved throughout the thesis, and comments on the areas that remain open in a list of recommendations.

8.1 Considerations for Electrical Main Aircraft Propulsion

An initial objective of this thesis was to identify the key performance drivers and limitations in the design of electrical drive systems for aerospace propulsion. To address this, a review of the current panorama of aircraft using electrical machines for propulsion is presented in Chapter 2 and Chapter 3. This showed a clear preference for Permanent Magnet (PM) systems at present, while clearly emphasizing on superconducting machines in the medium to long term. Regarding the latter however, examples beyond the conceptual phase were not found at the time of writing. For the research question this means that a reliable estimation can only be made for iron-based PM machines for the time being. While a prediction can be made for superconducting machines, this will not reflect the technological maturity that still needs to be achieved in that field.

Thanks to the higher feasibility of PM machines, identifying key performance indicators was possible based on the available literature. It was observed that the highest airgap shear stress values among electrical machines are linked to the use of magnet material. Nevertheless, these vary from topology to topology: ca. 40kPa for the Surface Permanent Magnet (SPM) machines and up to 100kPa for Transverse Flux PM (TFPM) machines. Therefore, for a fixed type of cooling, *shear stress serves as a first key performance indicator* for the evaluation of electrical machine topologies. In this regard, no concrete values are found for superconducting machines. However, the findings from Chapter 6 show that airgap flux densities of several Tesla should be possible in the future. This means that higher shear stress values than for PM machines are possible at low current loadings and long airgap lengths, which opens new possibilities for electrical aircraft propulsion.

As a *second key performance indicator* for a topology pre-selection, *torque-to-volume ratio* provided an initial overview of the state of the art. It was established however, that the reviewed iron-based examples must comply with the assumption given in (2-1) in order for them to be comparable. For the reviewed examples, (2-1) insured similar iron content per machine volume making the volumetric torque density (ca. 50kNm/m^3 in average) roughly proportional to the gravimetric torque density. Therefore, it can be taken as a direct indicator of the torque capability per unit mass for a certain topology. Further, the review also showed that under the conditions of (2-1), the volumetric torque density was roughly equal in value to the airgap shear stress (ca. 50kPa in average).

Additional to the selection of key performance indicators, other important points were observed in the preliminary phase of this work. These contributed the broad guidelines to the design approach, which set the development framework for subsequent sections:

- Based on the above numbers, plausible power-to-weight ratios are of a few kW/kg at best ($< 6\text{kW/kg}$ @4000rpm in average), which translates into a torque-to-weight ratio of a few Nm/kg ($\sim 10\text{Nm/kg}$). Such figures necessarily imply a low pole number and a split ratio of 60% to 70%, resulting in a machine with high iron content. At that performance, solutions for applications with moderate take-off weights ($> 2\text{t}$) are only possible with a constellation “electrical machine plus gearbox”. This solution comes with a lower reliability and higher maintenance costs than a direct-drive solution. As a consequence, a candidate design for rotary wing applications may not profit from the torque amplification possible with a gearbox, despite the high power-to-weight ratios that can be achieved at high rotational speeds. Instead, a direct-drive solution without gearbox should be pursued as stated in the requirements.
- The previous inevitably leads to the constraints identified in material properties as reviewed in Chapter 3 (copper/aluminum resistivity, iron saturation, magnet remanent flux density, frequency-dependent losses of all materials). These limit the amount of power that can be generated through electromagnetic torque. Such physical limits are rather well-defined for traditional materials. Only marginal improvements are possible, and these are usually accompanied by a trade-off in another property. Superconductivity potentially offers significant improvement of more than one order of magnitude in resistivity and producible magnetic flux density. This comes at the expense of a complex cryogenic operating environment. As a conclusion of this: unless superconductivity is used, a candidate solution can only be achieved through the synergy of marginal advantages from all materials in the appropriate property trade-off (e.g. high remanent flux density of magnets vs. high maximum operating temperature).
- Apart from the material limitations and the performance indicators used for topology evaluation, the level of customization was identified to play an important role in the final weight. Current demonstrators rely mostly on off-the-shelf and/or low-customization PM machines, focusing on their integration as a single discrete component. This results in additional weight stemming from features necessary for machine operation. Focusing on a highly-customized highly-integrated design helps avoid additional weight, product of design

integration and tailoring to the target application. Such is the case of for example the machine casing, some structural components and even electromagnetic mass that serves structural purposes only.

- As specified in Chapter 1, the key performance indicators and limiting aspects discussed above serve as boundary conditions for the main rotor drive of a EC135 civilian helicopter. Such low-speed/high-torque direct-drive application requires an approach similar to the one used in wind turbines: improvement of the torque-to-weight ratio by means of a rotor pole number increase. Such approach is only possible as long as the following aspects are within realizable and/or controllable limits:
 - Amount of AC/DC losses of the machine
 - Maximum operational frequency of power electronics
 - Physical size and precision of the machine parts
 - Required structural support

This section can be summarized in a design philosophy: A potential machine must sum up the advantages in different aspects (electromagnetic, structural, and thermal), without disregarding physical limits or being conservative. It must pursue higher distribution of the machine parts, and higher integration with its surroundings. Finding such physical and integration limits for different machine topologies was essential for the study's success.

8.2 Topology Selection and Comparison

The second objective of this thesis was to perform a selection of candidate topologies based on the already defined performance indicators. In this sense, the use of the volumetric torque density and airgap shear stress as figures of merit proved to be useful as a first evaluation indicator. Nevertheless, for further consideration, less obvious aspects also had to be brought into the selection process: design complexity, hands-on experience and operating record. The selection ruled out Magnetically-Geared PM (MGPM) machines and TFPM machines due to complexity and reliability, and favored SPM machines and Flux-Switching PM (FSPM) machines. For High-Temperature Superconducting (HTS) machines similar analysis and principles could not be applied directly due to insufficient design literature available. However, some operating experimental examples of DC-excited synchronous HTS machines could be found. Also, some literature is available giving an average volumetric torque density for superconducting synchronous machines of ca. 100kNm/m^3 . This allowed their inclusion in the final selection next to SPM and FSPM machines, but also highlights that despite favorable performance indicators, subtle factors like previous experience play an important role in the selection process.

With the second thesis objective fulfilled, the third objective could be addressed: make a comparison of the candidate topologies through a preliminary design, while fulfilling the performance requirements of the target application. In decreasing order, the gravimetric torque density of the final designs, with the corresponding pole pair number and its limiting factor are the following (weight of structural support not considered):

	<i>Torque Density</i>	<i>Pole pair number</i>	<i>Limiting factor</i>
• FSPM machine:	150Nm/kg	182 pole pairs	Frequency
• SPM machine:	115Nm/kg	115 pole pairs	Yoke/tooth width
• HTS machine:	< 60Nm/kg	20 pole pairs	Axial length

The comparison of the gravimetric torque density related to the final active mass clearly showed the differences in performance between topologies, by revealing unexpected mass drivers specific of each design. In this sense, the development of this objective brought with it further findings relevant to the first thesis objective:

- Despite the noticeable performance difference between SPM and FSPM machines, both topologies showed a similar gravimetric torque density when not considering structural provisions (i.e. similar raw active mass). While SPM machines have a longer axial length, FSPM machines have wider features (teeth, yokes, etc.). This implies a high machine reluctance / low airgap shear stress vs. low machine reluctance / high airgap shear stress, respectively. Precisely this difference makes the addition of structural mass less detrimental to the total active weight in FSPM machines: a low reluctance implies a high machine cross-section with wide machine features, which serve both electromagnetic and structural purposes.
- The iron-based SPM and FSPM machine designs showed the expected increase in gravimetric torque density as a function of increasing pole number. Such was not the case of HTS machines, where the maximum torque-to-weight ratio was observed at the lowest pole number considered (10 poles). The constant electromagnetic airgap length of HTS machines (due to the cryostat), makes the airgap flux density decrease rapidly as the pole number increases. This causes the machine reluctance and pole leakage to increase. In the other designs the electromagnetic airgap length could be reduced accordingly as the pole number was increased. In this manner the machine airgap flux density could be maintained as constant as possible.

The next priority of this work was to perform a detailed electromagnetic design based on an FSPM machine, due to its advantages compared to the other two topologies. The final FSPM machine design as presented was only possible by means of a topology modification, which resulted in the Halbach-FSPM machine. This modification uses Halbach arrays to reduce flux leakage. In some cases an enhancement of the magnetic loading of the electrical machine was also observed, which increased the gravimetric torque density. For the volumetric torque density, an improvement was observed in all cases.

With the new topology, the leakage stemming from the connection bridges between C-cores could be completely compensated, restoring the gravimetric torque density. These connection bridges are absolutely necessary in the manufacturing process of the stator as a single piece. They guarantee the precision of the airgap curvature needed for a 0.1mm airgap length. Ergo, this modification makes FSPM machines competitive candidates in applications, where ring-type direct-drive machines are an ideal solution: It allows a

simplified one-piece stator construction, without the detrimental effects in performance, caused by the magnetic short circuit between the single iron cores. Furthermore, thanks to this manufacturing advantage, very short airgap lengths relative to the airgap radius could be achieved by means of a segmented design.

8.3 Distributed Design Approach

The fifth objective was to make structural considerations for the finished electromagnetic design focusing on a lightweight support. These comprised mechanical and thermal aspects, crucial when dealing with a very small mechanical airgap (smaller than $D_g/1000$). From the mechanical side, the approach of stator segmentation and independent mounting of the resulting segments was adopted successfully. The resulting key features of this approach are:

- Prevention of an increase in airgap length, product of a greater thermal expansion in the stator than in the rotor
- Variable independent positioning of all stator segments in radial direction, through the use of sliding mechanical joints attached to each stator segment

These two aspects permitted adjusting a constant airgap length between rotor and stator regardless of thermal expansion. This was achieved through the use of air bearing units attached to the stator segments, which compensate the attractive normal forces between rotor and stator. The approach considerably reduces the support mass needed to counteract normal forces. These forces are therefore controlled locally in a distributed manner, and are not transmitted to the rotor axis through the rotor structure. The result is a simplified structural design, since only torque transmission must be accounted for.

On the thermal side, the cooling principle proposed removes the bulk of the heat losses directly at the source. By flushing each winding individually with cool air from one end to the other, there was no need to transport heat losses to another dissipation surface. This made the back-iron surface available for the dissipation of magnet and core losses, so that temperature could be held below design values on all components. By cooling the machine through different areas and as near as possible to the loss sources, operating points with high loss concentrations can be handled for extended periods of time with air cooling.

Finally, the last objective was the implementation of a partial experimental set-up for model and performance validation. The setup was successfully developed and tested based on a stator segmentation approach with floating segments. The principle proved to be effective in laboratory experiments, where the measured output torque matched simulation values for all cases down to an airgap length of 0.1mm. Additionally, no-load runs of the machine at nominal speed were successful down to an airgap length of 0.2mm, when using a rotor manufactured with an airgap radius tolerance of ± 0.1 mm. In the same manner for the cooling system, all tests showed temperatures below the desired operating point of 100°C at all measurement points, for a reasonable cooling effort. This suggested an overloading capability that can be sustained through very demanding operating phases like take-off, without significant temperature increase. In summary, the experimental set-up was developed in a manner that permitted verification of the performance obtained from

analytical models and simulations. Despite not giving priority to lightweight construction and concentrating on proof-of-concept, it provided evidence on the feasibility of the proposed ideas and their reliable validation.

The successful experimental verification of the structural support and cooling principles paved the way for the development of an analytical model to estimate the final gravimetric torque density of a complete machine. This model was not part of the original thesis objectives, but resulted essential to the evaluation of the research question. It focused on the mechanical design, by replacing the bulky support structure of the experimental setup with:

- lightweight stator brackets made of beryllium-aluminum alloy
- titanium air bearing guiding rings

Preliminary results indicate that the implementation of floating stator segments can improve the gravimetric torque density of the construction up to ca. 90Nm/kg (ca. 180kg of total mass). Compared to maximum values of the state of the art, found mainly in wind turbines (ca. 40Nm/kg), this represents a considerable improvement. Despite this achievement, for the purpose of propulsion of rotary-wing aircraft, the weight penalty involved is of around 20% for the studied FSPM C-core configuration.

As mentioned previously, the model development focused on mechanical design while the electromagnetic configuration remained unchanged. The reason for this is that tangential and normal force profiles were only available for the implemented Halbach-FSPM design (based on a 6/13 C-core machine). However, for configurations with higher winding factors, e.g. a 12/25 C-core variant (see Chapter 5), a reduction of the weight penalty down to ca. 15% is possible. Its complete elimination on the other hand, is unlikely. Further improvement also demands a more detailed model and a simultaneous optimization of electromagnetic, structural and thermal objectives.

8.4 Contributions

General Contributions

- *Scientific contribution:* with respect to the research question, this thesis indicates that for the application of main helicopter propulsion, it is very likely to incur into a weight penalty with air-cooled direct-drive ring-type machines. For iron-based electrical machines, under the above mentioned conditions, this sets a soft limit for the gravimetric power and torque density at ca. 3.3kW/kg and 90Nm/kg respectively (section 7.5.5).
- *Technical contribution:* this thesis addresses the application of electrically propelled rotary-wing air transport, an application not investigated before at the level of detail presented. Although some demonstrators exist, there is no particular attempt to go beyond 4-passenger fixed-wing transport and into a more civilian-oriented application. Because of this, this work serves as an initial guideline for the design of electrical propulsion drives for rotary-wing aircraft with a MTOW of 3t or lower. At the same time, it also serves as a starting point for future research of the same aircraft application with higher MTOWs.

- *Scientific contribution:* in the context of the previous contribution, this thesis proposes a systematic approach for finding a solution. It first makes a selection of electrical machine topologies based on potential performance and ease of manufacture. It then goes on to point out the most relevant weight drivers: for iron-based ring-type designs, it identifies the addition of structural support provisions as a weight driver more critical for SPM machines than for FSPM machines (sections 4.4.1, 5.5.1 and 7.1). For superconducting machines with a cold rotor, it shows how increasing the pole number has the opposite effect on torque-to-weight ratio as it does on iron-based designs (section 6.3).
- *Technical contribution:* this thesis proposes the first considerations for high-power/low-weight machines with low to medium rotational speed. It highlights the importance of the mechanical and structural considerations, not only within the electromagnetic active mass, but also at the support structure itself: in iron-based machines, it proposes a new support structure that allows increasing performance and reducing total weight at the same time. For superconducting machines, it broadly integrates the distribution of the support mass in the optimization of the electromagnetic mass.
- *Scientific contribution:* this thesis provides a topology comparison in equality of loading, cooling and construction conditions, showing that iron-based solutions are for the time being the best alternative for the addressed application. Nevertheless, it also notes the special attention required in airgap control, since iron-based designs are unavoidably ring-type machines with a small airgap and high airgap radius.

Contributions of chapter 2

- *Scientific contribution:* A general picture of the current panorama for electrical propulsion in aerospace is given based on actual demonstrators. Up to now this picture was not very clear due to the infancy of the field. Although a wide range of rotational speeds are observed, with mostly a low torque-to-weight ratio, the limit of 4kW/kg in gravimetric power density is rarely exceeded regardless of rotational speed (section 2.5).

Contributions of chapter 3

- *Scientific contribution:* Chapter 3 shows analytically that a radial flux machine tends to offer a higher gravimetric torque density than an axial flux machine for a pole number higher than 80 (section 3.6.2). This is valid for iron-based machines with a high aspect ratio, i.e. diameter-to-axial-length ratio (machines with a pancake-like space envelope).

Contributions of chapter 4

- *Scientific contribution:* in Chapter 4 an approach for the selection of a slot/pole combination to maximize the gravimetric torque density is proposed for SPM machines. For a fixed pole number, guidelines based on the slot/pole

combination itself, the magnet coverage and the slot pitch are defined (section 4.3.3). These parameters affect mostly the total stator weight, which makes the highest contribution to the total active weight. These guidelines give an indication of a higher or lower total mass for a certain design *relative to others*.

- *Scientific contribution:* for each active component of a machine the most relevant weight drivers are defined. The rotor mass is mostly determined by shear stress and airgap radius, whereas for the stator and winding mass these parameters plus the slot/pole combination, magnet coverage and slot pitch play a crucial role in the final active mass. For a fixed number of poles, a slot/pole combination with fewer slots than poles plus high winding factor tends to have the lowest stator iron mass.
- *Scientific contribution:* Chapter 4 shows that aluminum windings help reduce the total machine weight, while maintaining the same volumetric loss density in the winding material (section 4.3.2). This comes however at the expense of additional material needed to maintain electrical loading, resulting also in a higher total loss. The final advantage in gravimetric torque density is of 18%.

Contributions of chapter 5

- *Scientific contribution:* Chapter 5 proposes a modeling method for FSPM machines based on an analytical-numerical hybrid model. In it, the two most sensitive parameters are considered: split ratio and airgap length (section 5.1). For an arbitrary FSPM machine configuration, this model allows making an a priori flux linkage estimation that can be easily extended to an a priori torque-to-weight ratio optimization. This reveals that, given the constraints imposed for current density and current loading, there is little cross-dependence between split ratio and airgap length. While an optimum split ratio exists, the final performance is determined by the realized airgap for that optimum split ratio (section 5.4.2).
- *Technical contribution:* Chapter 5 proposes a new topology, the Halbach-FSPM machine. Two implementation alternatives are specified depending on the Halbach array thickness relative to the stator pole pitch (sections 5.6 and 5.7). This topology allows increasing the volumetric and gravimetric torque density of FSPM machines depending on the airgap length adjustment. The increase is achieved by enhancing the magnetic flux in the iron cores and by reducing the flux leakage through the back side of the machine. This last feature is the strongest point of this contribution: it allowed the manufacture of the stator segment of a FSPM machine in a single piece with a high split ratio and a very stringent tolerance. This was essential to achieve the required airgap length without loss of performance.

Contributions of chapter 6

- *Scientific contribution:* Chapter 6 proposes a figure of merit and an optimization approach for HTS machines that allows finding the optimum material

distribution within a machine with cold field windings (sections 6.1.3 and 6.2). The figure of merit is defined as the ratio of the peak airgap flux density to the total cross-sectional area of the machine components (proportional to the amount of iron, GFRP and HTS). When this figure of merit is multiplied by the armature current loading the best-case gravimetric torque density is obtained.

- *Scientific contribution:* from the optimization of the figure of merit, it is found that due to the cryostat thickness (i.e. constant airgap length) the torque-to-weight ratio decreases with increasing pole number (section 6.3). With a decreasing pole number, the size of the field windings and the respective MMF increase, so that the armature iron content is reduced until an ironless machine is obtained. The optimum field circuit on the other hand is *always* ironless.

Contributions of chapter 7

- *Technical contribution:* The use of air bearings and the precise positioning they offer as proposed in Chapter 7 provide enhanced control of the airgap length as was proven experimentally (section 7.2.1 and 7.4.1). This method permits decreasing the realizable airgap down to 0.1mm, one order of magnitude lower than recommended guidelines found in literature. The machining tolerances needed for this setup are of the order of a few micrometers ($\pm 10\mu\text{m}$).
- *Technical contribution:* the air cooling approach, based on direct cooling of the windings plus traditional cooling of the back-iron of rotor and stator, notably increases the overloading capability of the machine (sections 7.3.3 and 7.4.2). With the use of compressed air at the stator and movement-induced forced convection at the rotor, loss densities usually corresponding to liquid cooling ($11A_{\text{RMS}}/\text{mm}^2$ - $13A_{\text{RMS}}/\text{mm}^2$ in copper) are manageable. The specified maximum temperature of 100°C can also be achieved, as long as the air at the inlet is filtered and has the appropriate temperature (ca. 22°C).
- *Technical contribution:* the experimental setup as proof of concept of the floating stator support structure effectively maintains the adjusted airgap length. This is regardless of the rotor-stator attraction and thermal expansion (section 7.2.1, 7.3.2 and 7.4). The local treatment of normal forces and the possibility of variable stator positioning present a new approach to machine design not documented by the state of the art. This opens up new possibilities into better material utilization and lightweight design (section 7.5).

8.5 Recommendations

- From the designs proposed it was clear that the magnetic loading was at the maximum achievable for both iron-based and HTS machines. Given the air cooling constraint, it was in principle not possible to aspire to a higher current loading and conductor current density values ($40A_{\text{RMS}}/\text{mm}$ and $8A_{\text{RMS}}/\text{mm}^2$ for aluminum). After observing the results of the thermal experiments, it seems more

plausible to use higher current loadings, which would however decrease the magnetic loading as a consequence of the higher operating temperature. Finding a compromise between the two, in order to come closer to achieving the application requirements, is a possibility that should be explored. Should such analysis not provide considerable improvement, a change to liquid cooling should be considered, since this would surely allow a higher loss density than presented here. In this context, a new solution must consider the additional mass needed for storage, distribution and coolant. Additionally, new variables like reliability and problem scenarios (e.g. leakage) must be considered and analyzed thoroughly. This would apply to SPM machines, conventional FSPM machines and the conventional armature in HTS machines. Not C-core FSPM machines though, since for these the saturation limit was already achieved using air cooling.

- The study done on HTS machines showed that their full potential cannot be achieved with the space envelope specified for main rotor helicopter propulsion. Applications with a more cylindrical design are perhaps better suited for their use than those where pancake-like space envelopes are imposed. Completely ironless designs are however possible with the appropriate HTS operating current, as was observed in the lower pole number range. Also, a six fold improvement in HTS material performance is anticipated by suppliers at the operating conditions considered in this thesis (20K and 2T). In principle, a considerable improvement in shear stress would be realizable, bringing the present design much closer to the required torque- and power-to-weight ratios. A reevaluation of this approach for a helicopter main rotor application using HTS is attractive and recommendable in the future as their performance further develops in time.
- The design approach considered in all three cases focused on the electromagnetic and mechanical aspects, while ignoring the electrical side. Operation in the base region is required for maximum torque, combined with a high phase current per module at a high electrical frequency. These demanding conditions make the design of power electronics a less than trivial task, which can have a considerable impact in the final system weight. Accurately considering the sizing of power electronics in the design process is therefore an important aspect that should be addressed.
- The final machine presented, including the stator structure concept, is a first iteration that still needs to be refined. Further development of the support structure is recommended, since it was observed that asymmetric bracket shapes (with more robust edges) might be necessary. These asymmetric brackets would provide a more uniform airgap profile at nominal operation, but would also have a slightly higher mass. Therefore, choosing a machine with fewer segments (7-segment 6-phase FSPM machine) and a higher winding factor would not only improve performance and fault tolerance: with fewer segments per machine, the support mass would be less, since reinforcement would be needed at fewer places, in turn reducing the weight penalty.

- With the partial setup available for laboratory experiments only measurements in stationary conditions were possible. However, mechanical behavior should be investigated in terms of vibrations and dynamic operation in further experimental phases, and considering further iterations of the machine concept.

References

- [1] European Commission, "The 2020 climate and energy package," European Commission, [Online]. Available: http://ec.europa.eu/clima/policies/index_en.htm. [Accessed 1 July 2014].
- [2] OECD, "www.oecd.org," 2014. [Online]. Available: <http://www.oecd.org/sti/ind/48350231.pdf>. [Accessed 4 June 2014].
- [3] N. Cumpsty, *Jet Propulsion*, Cambridge University Press, 2003.
- [4] C. A. Luongo, M. P. J., T. Nam, D. Mavris, H. D. Kim, G. V. Brown, M. Walters and D. Hall, "Next Generation More-Electric Aircraft: A Potential Applications for HTS Superconductors," *IEEE Transactions on Superconductivity*, pp. 1055-1068, June 2009.
- [5] Ward's, "wardsauto.com," Ward's, 2014. [Online]. Available: <http://wardsauto.com/2014-wards-10-best-engines>. [Accessed 4 June 2014].
- [6] A. S. Gohardani, G. Doulgeris and R. Singh, "Challenges of future aircraft propulsion: A review of distributed propulsion technology and its potential application for the all electric commercial aircraft," *Progress in Aerospace Sciences*, pp. 369-391, 2011.
- [7] Rolls-Royce plc, *The Jet Engine*, London, England: Rolls-Royce Technical Publications, 2005.
- [8] C. C. Chan, "The State of the Art of Electric, Hybrid, and Fuel Cell Vehicles," *Proceedings of the IEEE*, pp. 704-718, April 2007.
- [9] "Wikipedia: Energy density," Wikimedia Foundation, Inc, 3 June 2014. [Online]. Available: http://en.wikipedia.org/wiki/Energy_density. [Accessed 4 June 2014].
- [10] S. Stückl, J. van Toor and H. Lobentanz, "Voltair - The all electric propulsion concept platform - A vision for atmospheric friendly flight," in *Proceedings of the 28th International Congress of the Aeronautical Sciences*, Brisbane, Australia, 2012.
- [11] F. Buysschaert, P. Hendrick and S. Newman, "Conventional helicopters: an adaptiveness study for more electric and alternative propulsion technologies," *Proceedings of the Institution of Mechanical Engineers, Part G: Journal of Aerospace Engineering*, pp. 1078-1094, September 2012.

- [12] M. Soimar, "The Challenges of CVTs in Current Heavy-Duty Powertrains," *Diesel Progress - North American Edition*, pp. 68-77, April 2000.
- [13] United States Environmental Protection Agency, "Medium and Heavy Duty Diesel Vehicle Modeling Using a Fuel Consumption Methodology," 2004. [Online]. Available: <http://www.epa.gov/otaq/models/ngm/may04/crc0304c.pdf>. [Accessed 11 June 2014].
- [14] MAN Diesel, "MAN Diesel Turbo," May 2009. [Online]. Available: http://www.mandieselturbo.com/files/news/files0f16119/tech_paper_low_speed.pdf. [Accessed 11 June 2014].
- [15] United States Department of Energy, "Motivations for Promoting Clean Diesels," in *Tools & Incentives for Green Diesel Technology: Lower Emissions, Higher Profits*, Chicago, USA, 2006.
- [16] P. Jänker, F. Hoffmann, V. Kloeppel and J. Stuhlberger, "Helicopter Hybridisation - The Key for Drastic Reductions of Fuel Burn and Emissions," in *American Helicopter Society 67th Annual Forum*, Virginia Beach, USA, 2011.
- [17] P. Jänker, J. Stuhlberger, F. Hoffmann, G. Niesl and V. Kloeppel, "The Hybrid Helicopter Drive - A Step to New Horizons of Efficiency and Flexibility," in *European Rotorcraft Forum*, Paris, France, 2010.
- [18] C. Campbell, E. Dittman, J. MacRae, C. Ehringer, A. Stone, K. Lake and S. Haskins, "Design of a Hybrid Electrical Propulsion System," in *Proceedings of the 52nd AIAA/ASME/ASCE/AHS/ASC Structures, Structural Dynamics and Materials Conference*, Denver, USA, 2011.
- [19] A. Datta and W. Johnson, "Requirements for a Hydrogen Powered All-Electric Manned Helicopter," in *AIAA Aviation Technology, Integration and Operations Conference*, Indianapolis, USA, 2012.
- [20] C. Friedrich and P. Robertson, "Hybrid-Electric Propulsion for Aircraft," in *11th International Energy Conversion Engineering Conference*, San Jose, USA, 2013.
- [21] S. Durkee and A. Muetze, "Conceptual Design of an Electric Helicopter Powertrain," in *Proceedings of the 5th IET International Conference on Power Electronics, Machines and Drives*, Brighton, UK, 2010.
- [22] J. Felder, H. Kim and G. Brown, "Turboelectric Distributed Propulsion Engine Cycle Analysis for Hybrid-Wing-Body Aircraft," in *AIAA Aerospace Sciences Meeting including the New Horizons Forum and Aerospace Exposition*, Orlando, USA, 2009.
- [23] A. M. El-Rafaie, "Motors/Generators for Traction/Propulsion Applications: A review," *IEEE Vehicular Technology Magazine*, pp. 490-497, March 2013.
- [24] P. E. Kakosimos, A. G. Sarigiannidis, M. E. Beniakar, A. G. Kladas and C. Gerada, "Induction Motors versus Permanent Magnet Actuators for Aerospace Applications," *IEEE Transactions on Industrial Electronics*, pp. 4315-4325, August 2014.
- [25] D. Fodorean, M. Ruba, L. Szabo and A. Miraoui, "Comparison of the Main Types of Fault-Tolerant Electrical Drives used in Vehicle Applications," *Proceedings of the International Symposium on Power Electronics, Electrical Drives, Automation and Motion*, pp. 895-900, June 2008.

- [26] A. M. El-Rafaie, "Fault-tolerant permanent magnet machines: A review," *IET Electrical Power Applications*, pp. 59-74, January 2011.
- [27] H. Polinder, F. F. van der Pijl, G.-J. de Vilder and P. J. Tavner, "Comparison of Direct-Drive and Geared Generator Concepts for Wind Turbines," *IEEE Transactions on Energy Conversion*, pp. 725-733, September 2006.
- [28] M. Liserre, R. Cárdenas, M. Molinas and J. Rodríguez, "Overview of Multi-MW Wind Turbines and Wind Parks," *IEEE Transactions on Industrial Electronics*, pp. 1081-1095, April 2011.
- [29] K. M. Rahman, N. R. Patel, T. G. Ward, J. M. Nagashima, F. Caricchi and F. Crescimbeni, "Application of Direct-Drive Wheel Motor for Fuel Cell and Hybrid Electric Vehicle Propulsion System," *IEEE Transactions on Industry Applications*, pp. 1185-1192, September / October 2006.
- [30] B. Mecrow and A. Fraser, "The Challenges of Direct-Drive In-Wheel Motors," in *Extreme Machines Seminar*, Derby, UK, 2013.
- [31] S. Wu, L. Song and S. Cui, "Study on Improving the Performance of Permanent Magnet Wheel Motor for the Electric Vehicle Application," *IEEE Transactions on Magnetics*, pp. 438-442, January 2007.
- [32] W. Fei, P. Luk and K. Jinupun, "A New Axial Flux Permanent Magnet Segmented-Armature-Torus Machine for In-Wheel Direct Drive Applications," *39th IEEE Power Electronics Specialists Conference*, pp. 2197-2202, June 2008.
- [33] W. Fei, P. Luk, B. Xia and D. Wu, "Design Improvement of Outer-Rotor Permanent Magnet Flux Switching Machine for Direct-Drive Urban Electric Vehicle Propulsion," *39th Annual Conference of the IEEE Industrial Electronics Society*, pp. 7319-7324, November 2013.
- [34] A. Mitcham, G. Antonopoulos and J. Cullen, "Favourable slot and pole number combinations for fault-tolerant PM machines," *IEE Proceedings on Electrical Power Applications*, pp. 520-525, September 2004.
- [35] A. El-Rafaie, "Fractional-Slot Concentrated-Windings Synchronous Permanent Magnet Machines: Opportunities and Challenges," *IEEE Transactions on Industrial Electronics*, pp. 107-121, January 2010.
- [36] F. Magnussen and H. Lendenmann, "Parasitic Effects in PM Machines with Concentrated Windings," *IEEE Transaction on Industry Applications*, pp. 1223-1232, September/ October 2007.
- [37] A. El-Rafaie, T. M. Jahns and D. W. Novotny, "Analysis of Surface Permanent Magnet Machines with Fractional-Slot Concentrated Windings," *IEEE Transactions on Energy Conversion*, pp. 34-43, March 2006.
- [38] P. B. Reddy, A. M. El-Rafaie, K.-K. Huh, J. K. Tangudu and T. M. Jahns, "Comparison of Interior and Surface PM Machines Equipped with Fractional-Slot Concentrated Windings for Hybrid Traction Applications," *IEEE Transactions on Energy Conversion*, pp. 593-602, Spetember 2012.
- [39] J. Tangudu and T. Jahns, "Comparison of Interior PM Machines with Concentrated and Distributed Stator Windings for Traction Applications," in *Proceedings of the*

- IEEE Vehicle Power and Propulsion Conference*, Chicago, USA, 2011.
- [40] D. Bang, H. Polinder, G. Shrestha and J. Ferreira, "Review of Generator Systems for Direct-Drive Wind Turbines," in *Proceedings of the European Wind Energy Conference & Exhibition*, Brussels, Belgium, 2008.
- [41] M. P. H. Dubois and J. Ferreira, "Comparison of Generator Topologies for Direct-Drive Wind Turbines," in *Proc. 2000 Nordic Countries Pow. and Indust. Elec.*, 2000.
- [42] P. Masson, T. Nam, T. Choi, P. Tixador, M. Waters, D. Hall, C. Luongo and D. Mavris, "Superconducting Ducted Fan Design for Reduced Emissions Aeropropulsion," *IEEE Transactions on Applied Superconductivity*, pp. 1662-1668, June 2009.
- [43] R. Qu, Y. Liu and J. Wang, "Review of Superconducting Generator Topologies for direct-Drive Wind Turbines," *IEEE Transactions on Applied Superconductivity*, p. Art. 5201108, June 2013.
- [44] G. Snitchler, "Progress on High Temperature Superconductor Propulsion Motors and Direct-Drive Wind Generators," *Proceedings of the International Power Electronics conference*, pp. 5-10, June 2010.
- [45] Airbus Group, "PSAM Report for Airbus: Final Outcomes," EADS UK Limited, United Kingdom, 2014.
- [46] P. Masson and C. Luongo, "HTS Machines for Applications in All-Electric Aircraft," in *IEEE Power Engineering Society General Meeting*, Tampa, USA, 2007.
- [47] Clean Sky Joint Undertaking, "Clean Sky Joint Undertaking," Clean Sky Joint Undertaking, [Online]. Available: <http://www.cleansky.eu/>. [Accessed 2 July 2014].
- [48] Wankel SuperTec GmbH, "www.wankelsupertec.de," [Online]. Available: http://www.wankelsupertec.de/Downloads/WST_KKM350.pdf. [Accessed 4 July 2014].
- [49] G. Cantore, E. Mattarelli and C. A. Rinaldini, "A new design concept for 2-stroke aircraft Diesel engines," *Proceedings of the 68th Conference of the Italian Thermal Machines Engineering Association*, pp. 739-748, January 2014.
- [50] Siemens, "www.siemens.com," Siemens, 20 June 2011. [Online]. Available: http://www.siemens.com/press/de/pressemitteilungen/?press=/de/pressemitteilungen/2011/corporate_communication/axx20110666.htm. [Accessed 7 July 2014].
- [51] Flight Design, "www.flightdesign.com," Flight Design, 13 March 2009. [Online]. Available: <http://www.flightdesign.com/index.php?page=home&n=126&y=2009>. [Accessed 7 July 2014].
- [52] Flight Design, "www.flightdesign.com," 9 April 2010. [Online]. Available: <http://flightdesign.com/files/Press%20Release/AERO%202010/FD%20-%20Press%20Releases/updated/Press%20release%20FD%20Hybrid%20E.pdf>. [Accessed 7 July 2014].
- [53] Flight Design, "www.flightdesign.com," Flight Design, 2014. [Online]. Available: <http://www.flightdesign.com/index.php?page=product&p=60>. [Accessed 7 July 2014].

- [54] Flight Design, "www.flightdesign.com," 2009. [Online]. Available: <http://www.flightdesign.com/index.php?page=pressroom&n=26&y=2009>. [Accessed 16 July 2014].
- [55] PC-Aero, "PC-Aero," PC-Aero, 2014. [Online]. Available: <http://www.aircraft-certification.de/>. [Accessed 14 July 2014].
- [56] Flytec AG, "www.flytech.ch," [Online]. Available: http://www.flytec.ch/de/e-drive/e-drive-systeme/hpd-135/downloads.html?file=tl_files/downloads/e-drive/Bedienungsanleitung_HPD_V1_1_21-1-11.pdf. [Accessed 14 July 2014].
- [57] R. Colyer, "Progress in electrically-propelled aircraft," *International Aegean Conference on Electrical Machines and Power Electronics*, pp. 357-362, September 2007.
- [58] Lange Aviation, "www.lange-aviation.com," Lange Aviation, 2013. [Online]. Available: http://www.lange-aviation.com/htm/deutsch/produkte/antares_20e/antrieb.html. [Accessed 15 July 2014].
- [59] EASA, "easa.europa.eu," 31 January 2006. [Online]. Available: http://easa.europa.eu/system/files/dfu/EASA-TCDS-E.015_Lange_Flugzeugbau_EA42_series_engines-01-31012006.pdf. [Accessed 15 July 2014].
- [60] Institut für Flugzeugbau der Universität Stuttgart, "www.ifb.uni-stuttgart.de," August 2013. [Online]. Available: http://www.ifb.uni-stuttgart.de/egenius/page_Aircraft/. [Accessed 15 July 2014].
- [61] Carbon Composites e. V., "www.carbon-composites.eu," [Online]. Available: http://www.carbon-composites.eu/sites/carbon-composites.eu/files/anhaenge/gruppen/12/12/14/08.voit-nitschmann_rudolf.pdf. [Accessed 15 July 2014].
- [62] Daily Mail, "www.dailymail.co.uk," October 2011. [Online]. Available: <http://www.dailymail.co.uk/sciencetech/article-2045101/Taurus-G4-Electric-plane-wins-biggest-prize-aviation-history.html>. [Accessed 15 July 2014].
- [63] Pipistrel, "www.pipistrel.si," Pipistrel, [Online]. Available: <http://www.pipistrel.si/news/taurus-g4-is-flying-at-the-nasa-gfc>. [Accessed 15 July 2014].
- [64] Pipistrel, "www.pipistrel.si," [Online]. Available: <http://www.pipistrel.si/plane/taurus-electro/overview>. [Accessed 15 July 2014].
- [65] Airbus Group, "www.airbusgroup.com," [Online]. Available: <http://www.airbusgroup.com/service/mediacenter/download/?uuid=48b1bd2c-a428-4c65-82e5-ed3e923bd142>. [Accessed 15 July 2014].
- [66] A. Chandra, "All set for the future," *Force*, pp. 54-55, November 2013.
- [67] Airbus Group, "www.airbusgroup.com," [Online]. Available: http://www.highflyer.airbus-group.com/04_2013_efan_and_ethrust.html#article_06_01. [Accessed 15 July 2014].

- [68] N. Lapena-Rey, J. Mosquera, E. Bataller and F. Orti, "First Fuel-Cell Manned Aircraft," *Journal of Aircraft*, vol. 47, no. 6, pp. 1825-1835, November-December 2010.
- [69] UQM Technologies, "www.uqm.com," 2014. [Online]. Available: <http://uqm.com/products/full-electric/prototype/passenger-vehicles/>. [Accessed 16 July 2014].
- [70] G. Romeo, E. Cestino and F. Borello, "More/All Electric Aircraft Based on Fuel Cell Energy System: The Enfica-FC Experience," in *Proceedings of the 28th International Congress of the Aeronautical Sciences*, Brisbane, Australia, 2012.
- [71] B. Mecrow, J. Bennett, A. Jack, D. Atkinson and A. Freeman, "Very High Efficiency Drives for Solar Powered Unmanned Aircraft," in *Proceedings of the International Conference on Electrical Machines*, Algarve, Portugal, 2008.
- [72] Airbus Helicopters, "www.airbushelicopters.com," 2011. [Online]. Available: http://www.airbushelicopters.com/site/en/press/Eurocopter-innovation-puts-the-focus-on-safety-with-the-world-s-first-flight-of-a-hybrid-helicopter-combining-an-internal-combustion-engine-and-an-electric-motor_823.html. [Accessed 16 July 2014].
- [73] Sikorsky, "www.sikorsky.com," 2014. [Online]. Available: <http://www.sikorsky.com/Innovation/Technologies/Firefly+Technology+Demonstrator>. [Accessed 16 July 2014].
- [74] C. Snyder, J. Berton, G. Brown, J. Dolce, N. Dravid, D. Eichenberg, J. Freeh, C. Gallo, S. Jones, K. Kundu, K. Geiselhart and A. Kascak, "Propulsion Investigation for Zero and Near-Zero Emissions Aircraft," NASA Glenn Research Center, Cleveland, USA, 2009.
- [75] D. Verstraete, "Long range transport aircraft using hydrogen fuel," *International Journal of Hydrogen Energy*, vol. 38, pp. 14824-14831, September 2013.
- [76] G. Brown, "Weights and Efficiencies of Electric Components of a Turboelectric Aircraft Propulsion System," in *AIAA Aerospace Sciences Meeting including the New Horizons Forum and Aerospace Exposition*, Orlando, USA, 2011.
- [77] I. Pazdera, P. Prochazka, D. Cervinka and B. Klima, "Electrical drivetrain of the small airplane and mutual interaction of this drivetrain," *IEEE Industrial Electronics Conference*, pp. 4624-4629, November 2013.
- [78] M. Ehsani, Y. Gao, S. Gay and A. Emadi, *Modern Electric, Hybrid Electric, and Fuel Cell Vehicles: Fundamentals, Theory and Design*, Boca Raton, USA: CRC Press LLC, 2005.
- [79] Airbus Helicopters (formelry Eurocopter), "Eurocopter EC135 Technical Data," Airbus Helicopters (formerly Eurocopter).
- [80] European Aviation Safety Agency, "Type-Certificate Data Sheet No. R.009 for EC135," European Aviation Safety Agency, Cologne, Germany, 2014.
- [81] W. L. Soong, "Sizing of Electrical Machines," *Power Engineering Briefing Note Series (School of Electrical and Electronic Engineering, University of Adelaide)*, pp. 17-18, September 2008.

- [82] K. Atallah, J. Rens, S. Mezani and D. Howe, "A Novel "Pseudo" Direct-Drive Brushless Permanent Magnet Machine," *IEEE Transactions on Magnetics*, pp. 4349-4352, November 2008.
- [83] J. Pyrhönen, T. Jokinen and V. Hrabovcová, *Design of Rotating Electrical Machines*, West Sussex, United Kingdom: John Wiley & Sons, Ltd., 2008.
- [84] STEINERT Elektromagnetbau GmbH, "www.anofol.de," [Online]. Available: http://www.anofol.de/fileadmin/downloads/ANOFOL_6-Seiter_engl.pdf. [Accessed 8 Sept. 2014].
- [85] D. Askeland, P. Fulay and W. J. Wright, *The Science of Engineering Materials*, Stamford, USA: Cengage Learning, 2010.
- [86] J. Pelleg, *Mechanical Properties of Materials*, Springer, 2012.
- [87] D. Edelstahlwerke, *1.4305 X8CrNiS18-9 stainless steel datasheet*, 2008.
- [88] I. A. A. Corp., *Beralcast - Castable Beryllium-Aluminum Alloys*.
- [89] B. Mecrow, A. Jack, J. Haylock and J. Coles, "Fault-tolerant permanent magnet machine drives," *IEEE Proceedings in Electrical Power Applications*, vol. 143, no. 6, pp. 437-442, November 1996.
- [90] O. Thorsen and M. Dalva, "A Survey on Faults on Induction Motors in Offshore Oil Industry, Petrochemical Industry, Gas Terminals and Oil Refineries," *IEEE Transactions on Industry Applications*, vol. 31, no. 5, pp. 1186-1196, September 1995.
- [91] W. Cao, B. Mecrow, G. Atkinson and J. Bennet, "Overview of Electric Motor Technologies Used for Electric Aircraft," *IEEE Transactions on Industrial Electronics*, vol. 59, no. 9, pp. 3523-3531, September 2012.
- [92] L. Mhango and R. Perryman, "Analysis and simulation of a high-speed two phase AC drive for aerospace applications," *IEE Proceedings on Electric Power Applications*, vol. 144, no. 2, pp. 149-157, March 1997.
- [93] C. Koechli, B. Fussell, S. Prina and D. James, "Design optimization of induction motors for aerospace applications," *Conference Record of the 2004 Industry Applications Conference*, pp. 2501-2505, October 2004.
- [94] I. Hansen, "Aerospace induction motor actuators driven from a 20kHz power link," *Fourth International Conference on Power Electronics and Variable-Speed Drives*, pp. 488-491, July 1990.
- [95] E. Ganev, "High Performance Electric Drives for Aerospace More Electric Architectures Part I -- Electric Machines," in *IEEE Power Engineering Society General Meeting*, 2007.
- [96] A. Jack, B. Mecrow and J. Haylock, "A Comparative Study of Permanent Magnet and Switched Reluctance Motors for High-Performance Fault-Tolerant Applications," *IEEE Transactions on Industry Applications*, vol. 32, no. 4, pp. 889-895, July 1996.

- [97] A. Hofmann, K. Kasper and R. D. Doncker, "High speed switched reluctance drives: a promising alternative to power electric vehicles," *IEEE 8th International Conference on Power Electronics and ECCE Asia*, pp. 169-175, May/June 2011.
- [98] M. Cinar and F. Kuymcu, "Design and Drives Simulation of an In-Wheel Switched Reluctance Motor for Electric Vehicle Applications," *IEEE International Electric Machines & Drives Conference*, pp. 50-54, May 2007.
- [99] H. Li and Z. Chen, "Overview of different wind generator systems and their comparisons," *IET Renewable Power Generation*, vol. 2, no. 2, pp. 123-138, 2008.
- [100] A. Jack, B. Mecrow and C. Weiner, "Switched reluctance and permanent magnet motors suitable for vehicle drives," *International Conference on Electric Machines and Drives*, pp. 505-507, May 1999.
- [101] R. Krishnan, *Permanent Magnet Synchronous and Brushless DC Motor Drives*, CRC Press, 2010.
- [102] T. Heikkila, *Permanent magnet synchronous motor for industrial inverter applications - analysis and design*, Lappeenranta: Acta Universitatis Lappeenrantaensis, 2002.
- [103] C. Gerada, K. Bradley, C. Whitley and G. Towers, "High Torque Density PM Machines for High Performance Operation," *Proceedings of the 33rd Annual Conference of the IEEE Industrial Electronics Society*, pp. 210-215, November 2007.
- [104] A. Jack, B. Mecrow, P. Dickinson, D. Stephenson, J. Burdess, J. Fawcett and T. Evans, "Permanent magnet machines with powdered iron cores and pre-pressed windings," *Conference Record of Industry Applications Conference*, pp. 97-103, October 1999.
- [105] N. Bianchi, M. Pre, G. Grezzani and S. Bolognani, "Design considerations on fractional-slot fault-tolerant synchronous motors," *IEEE International Conference on Machine and Drives*, pp. 902-909, May 2005.
- [106] Z. Zhu, „Fractional slot permanent magnet brushless machines and drives for electric and hybrid propulsion systems,“ *COMPEL: The International Journal for Computation and Mathematics in Electrical and Electronic Engineering*, Bd. 30, Nr. 1, pp. 9-31, 2011.
- [107] J. T. Chen and Z. Z. Q., "Comparison of All-and Alternate-Poles-Wound Flux-Switching PM Machines Having Different Stator and Rotor Pole Configurations," *IEEE Transactions on in Industry Applications*, pp. 1406-1415, July/August 2010.
- [108] J. Paulides, B. Gysen, K. Meesen, Y. Tang and E. Lomonova, "Influence of Multiple Airgaps on the Performance of Electrical Machines with (semi) Halbach Magnetization," *IEEE Transactions on Magnetics*, pp. 2664-2667, October 2011.
- [109] H. Polinder, B. Mecrow, A. Jack, P. Dickinson and M. Mueller, "Conventional and TFPM Linear Generators for Direct-Drive Wave Energy Conversion," *IEEE Transactions on Energy Conversion*, pp. 260-267, June 2005.
- [110] E. Spooner, P. Gordon, J. R. Bumby and C. D. French, "Lightweight ironless-stator PM generators for direct-Drive wind turbines," *IEE Proceedings on Electrical Power Applications*, pp. 17-26, January 2005.

- [111] J. T. Chen, Z. Q. Zhu, S. Iwasaki and R. Deodhar, "Comparison of losses and Efficiency in Alternate Flux-Switching Permanent Magnet Machines," in *Proceedings of the 19th International Conference on Electrical Machines*, Rome, Italy, 2010.
- [112] Z. Q. Zhu, Y. Pang, D. Howe, S. Iwasaki and R. P. A. Deodhar, "Analysis of Electromagnetic Performance of Flux-Switching Permanent Magnet Machines by Nonlinear Adaptive Lumped Parameter Magnetic Circuit Model," *IEEE Transactions on Magnetics*, pp. 4277-4287, November 2005.
- [113] W. Hua, M. Cheng, Z. Q. Zhu and D. Howe, "Analysis and Optimization of Back-EMF Waveform of a Flux-Switching Permanent Magnet Motor," *IEEE Transactions on Energy Conversion*, pp. 727-733, September 2008.
- [114] J. T. Cheng and Z. Q. Z. Q. Zhu, "Winding Configurations and Optimal Stator and Rotor Pole Combination of Flux-Switching PM Brushless AC Machines," *IEEE Transactions on Energy Conversion*, pp. 293-302, September 2010.
- [115] T. Raminosa, C. Gerada und M. Galea, „Design considerations for a Fault-Tolerant Flux-Switching Permanent-Magnet machine,“ *IEEE Transactions on Industrial Electronics*, Bd. 58, Nr. 7, pp. 2818-2815, July 2011.
- [116] R. Owen, Z. Zhu, A. Thomas, G. Jewell and D. Howe, "Fault-Tolerant Flux-Switching Permanent Magnet Brushless AC Machines," in *IEEE Industry Applications Annual Meeting*, Edmonton, Canada, 2008.
- [117] Y. Wang und Z. Deng, „A Multi-tooth Fault-Tolerant Flux-Switching Permanent Magnet Machine with Twisted-Rotor,“ *IEEE Transactions on Magnetics*, Bd. 48, Nr. 10, pp. 2674-2684, October 2012.
- [118] A. S. Thomas, Z. Q. Zhu and G. W. Jewell, "Comparison of flux switching and surface mounted permanent magnet generators for high-speed applications," *IET Electrical Systems in Transportation*, pp. 111-116, April 2011.
- [119] A. S. Thomas, Z. Q. Zhu and G. W. Jewell, "Comparison of flux switching and surface mounted permanent magnet generators for aerospace applications," in *Proceedings of the 5th International Conference on Power Electronics, Machines and Drives*, Brighton, UK, 2010.
- [120] W. Hua, M. Cheng, Z. Q. Zhu, W. Zhao and X. Kong, "Comparison of electromagnetic performance of brushless motors having magnets in stator and rotor," *Journal of Applied Physics*, 2008.
- [121] K. Atallah and D. Howe, "A Novel High-Performance Magnetic Gear," *IEEE Transactions on Magnetics*, vol. 37, no. 4, pp. 2844-2846, July 2001.
- [122] K. Atallah, S. Calverley, R. Clark, J. Rens and D. Howe, "A New PM Machine Topology for Low-Speed, High Torque Drives," in *International Conference on Electrical Machines*, 2008.
- [123] S. Gerber and R.-J. Wang, "Torque Capability Comparison of Two Magnetically Geared PM Machine Topologies," *IEEE International Conference on Industrial Technology*, pp. 1915-1920, February 2013.

- [124] R.-J. Wang, L. Brönn, S. Gerber and P. Tlali, "Design and Evaluation of a Disc-Type Magnetically Geared PM Wind Generator," *Fourth International Conference on Power Engineering, Energy and Electrical Drives*, pp. 1259-1264, May 2013.
- [125] S. Gerber and R.-J. Wang, "Design of a Magnetically Geared PM Machine," *Fourth International Conference on Power Engineering, Energy and Electrical Drives*, pp. 852-857, May 2013.
- [126] P. Rasmussen, T. Andersen, F. Jorgensen and O. Nielsen, "Development of a High-Performance Magnetic Gear," *IEEE Transactions on Industry Applications*, pp. 764-770, May/June 2005.
- [127] L. Jian, K. T. Chau and J. J. Z., "A Magnetic-Geared Outer-Rotor Permanent-Magnet Brushless Machine for Wind Power Generation," *IEEE Transactions on Industry Applications*, pp. 954-962, May/June 2009.
- [128] J. Wang and K. Atallah, "Modeling and Control of "Pseudo" Direct-Drive Brushless Permanent Magnet Machines," *Proceedings of the International Electric Machines and Drives Conference*, pp. 870-875, May 2009.
- [129] K. lu, P. Rasmussen and E. Ritchie, "Design Considerations of Permanent Magnet Transverse Flux Machines," *IEEE Transactions on Magnetics*, pp. 2804-2807, October 2011.
- [130] M. R. Dubois, H. Polinder and J. A. Ferreira, "Influence of Air Gap Thickness in Transverse Flux Permanent Magnet (TFPM) Generators for Wind Turbine Applications," in *IEEE Researchers Symposium in Electrical Power Engineering*, Leuven, Belgium, 2002.
- [131] M. Mueller, "Electrical generators for direct drive wave energy converters," *IEE Proceedings on Generation, Transmission and Distribution*, pp. 446-456, July 2002.
- [132] A. S. Abd-Rabou, H. M. Hasanien and S. M. Sakr, "Design development of permanent magnet excitation transverse flux linear motor with inner mover type," *IET Electric Power Applications*, pp. 559-568, August 2010.
- [133] Y. Iwasa, *Case Studies in Superconducting Magnets: Design and Operational Issues*, Springer US, 2009.
- [134] S. S. Kalsi, *Applications of High Temperature Superconductors to Electric Power Equipment.*, John Wiley & Sons. IEEE Press., 2011.
- [135] K. Vinod, R. Kumar and U. Syamaprasad, "Prospects for MgB₂ superconductors for magnet application," *Superconductor Science and Technology*, 2007.
- [136] SuperPower Inc., "www.superpower-inc.com," 2012. [Online]. Available: <http://www.superpower-inc.com/content/hts-motors-and-generators>. [Accessed 10 October 2014].
- [137] G. Klaus, M. Wilke, J. Fraunhofer, W. Nick and H.-W. Neumuller, "Design Challenges and Benefits of HTS Synchronous Machines," in *IEEE Power Engineering Society General Meeting*, Tampa, USA, 2007.
- [138] P. Masson, P. Tixador and C. Luongo, "Safety Torque Generation in HTS Propulsion Motor for General Aviation Aircraft," *IEEE Transactions on Applied*

- Superconductivity*, pp. 1619-1622, July 2007.
- [139] C. Oberhauser and H. Kinner, "Some Considerations in the Design of a Superconducting Alternator," *Advanced Cryogenic Engineering*, pp. 161-167, January 1967.
- [140] Advanced Magnet lab, "almsuperconductivity.com," 2014. [Online]. Available: <http://almsuperconductivity.com/applications/aml-product-platforms/>. [Accessed 10 October 2014].
- [141] J. F. Gieras, *Advancements in Electrical Machines*, Springer, 2008.
- [142] H.-W. Neumüller, W. Nick, B. Wacjer, M. Frank, G. Nerowsky, J. Fraunhofer, W. Rzdaki and R. Hartig, "Advances in and prospects for development of high-temperature superconductor rotating machines at Siemens," *Superconductor Science and Technology*, February 2006.
- [143] H. Ohsaki, Y. Terao and M. Sekino, "Wind Turbine Generators using Superconducting Coils and Bulks," *Journal of Physics: Conference Series*, 2010.
- [144] G. Brown, R. Jansen and J. Trudell, "High Specific Power Motors in LN2 and LH2," in *Cryogenic Engineering Conference*, Chattanooga, USA, 2007.
- [145] G. Brown, A. Kascak, B. Ebihara, D. Johnson, B. Choi, M. Siebert and C. Buccieri, "NASA Glenn Research Center Program in High Power Density Motors for Aeropropulsion," NASA Glenn Research Center, Cleveland, USA, December 2005.
- [146] D. Eichenberg, C. Gallo, P. Solano, W. Thompson and D. Vrnak, "Development of a 32inch diameter levitated ducted fan conceptual design," NASA Glenn Research Center, Cleveland, USA, 2006.
- [147] T. Woolmer and M. McCulloch, "Analysis of the Yokeless and Segmented Armature Machine," *IEEE International Electric Machines & Drives Conference*, pp. 704-708, May 2007.
- [148] S. Vun, M. McCulloch and C. Leong, "The Development of an Electromagnetic Analytical Design Tool for Megawatt-Scale YASA Generators," in *IET Conference on Renewable Power Generation*, Edinburgh, Scotland, 2011.
- [149] Yasa Motors, "www.yasamotors.com," October 2013. [Online]. Available: <http://www.yasamotors.com/>. [Accessed 14 October 2014].
- [150] P. Masson and C. Luongo, "High Power Density Superconducting Motor for All-Electric Aircraft Propulsion," *IEEE Transactions on Applied Superconductivity*, vol. 15, no. 2, pp. 2226-2229, June 2005.
- [151] P. Masson, M. Breschi, P. Tixador and C. Luongo, "Design of HTS Axial Flux Motor for Aircraft Propulsion," *IEEE Transactions on Applied Superconductivity*, vol. 17, no. 2, pp. 1533-1536, June 2007.
- [152] P. Masson and C. Luongo, "HTS Machines in All-Electric Aircraft," in *IEEE Power Engineering Society General Meeting*, Tampa, USA, 2007.
- [153] F. Libert und J. Soulard, „Investigation on Pole-Slot Combinations for Permanent-Magnet Machines with Concentrated Windings,“ *Proc. ICEM*, pp. 530-535, 2004.

- [154] Z. Zhu, D. Howe und C. Chan, „Improved analytical model for predicting the magnetic field distribution in brushless permanent magnet machines,“ *IEEE Transactions on Magnetics*, Bd. 38, Nr. 1, pp. 229-238, 2002.
- [155] H. Polinder, J. Sloopweg, M. Hoeijmakers und J. Compter, „Modeling of a Linear PM Machine Including Magnetic Saturation and End Effects: Maximum Force-to-Current Ratio,“ *IEEE Transactions on Industry Applications*, Bd. 39, Nr. 6, pp. 1681-1688, November/December 2003.
- [156] F. Magnussen and C. Sadarangani, "Winding factors and Joule losses of permanent magnet machines with concentrated windings," *Proc. IEEE-IEMDC*, pp. 333-339, June 2003.
- [157] P. Salminen, Fractional slot permanent magnet synchronous motor for low speed application, A. U. Lappeenrantaensis, Ed., Lappeenranta, Finland: Acta Universitatis Lappeenrantaensis, 2004.
- [158] D. L. H. P. J. A. F. Hung Vu Xuan, "Influence of Slot/Pole Number Combinations on Performances of Permanent Magnet Machines with Concentrated Windings for Ship Applications," in *International Conference on Electrical Machines and Systems (ICEMS)*, 2011.
- [159] Y. Chen, Z. Zhu and D. Howe, "Three-Dimensional Lumped-Parameter Magnetic Circuit Analysis of Single-Phase Flux-Switching Permanent Magnet Motor," *IEEE Transactions on Industry Applications*, pp. 1701-1710, November 2008.
- [160] J. Chen and Z. Zhu, "Influence of Rotor Pole Number on Optimal Parameters in Flux-Switching PM Brushless AC Machines by Lumped Parameter Magnetic Circuit Model," *IEEE Transactions on Industry Applications*, pp. 1381-1388, July/August 2010.
- [161] E. Ilhan, B. Gysen, J. Paulides and E. Lomonova, "Analytical Hybrid Model for Flux Switching Permanent Magnet Machines," *IEEE Transactions on Magnetics*, pp. 1762-1765, June 2010.
- [162] B. Gysen, E. Ilhan, K. Meessen, J. Paulides and E. A. Lomonova, "Modeling of Flux Switching Permanent Magnet Machines with Fourier Analysis," *IEEE Transactions on Magnetics*, pp. 1499-1502, June 2010.
- [163] E. Ilhan, M. Kremers, E. Motosca, P. J.J.H. and E. Lomonova, "Spatial Discretization Methods for Air Gap Permeance Calculations in Double Salient Traction Motors," *IEEE Transactions on Industry Applications*, pp. 2165-2172, November/December 2012.
- [164] J. Chen, Z. Zhu, S. Iwasaki and R. Deodhar, "Influence of Slot Opening on Optimal Stator and Rotor Pole Combination Electromagnetic Performance of Flux-Switching PM Brushless AC Machines," *IEEE Transactions on Industrial Applications*, pp. 1681-1691, July/August 2011.
- [165] J. Zhang, M. Cheng, Z. Chen and W. Hua, "Comparison of Stator-Mounted Permanent-Magnet Machines Based on a General Power Equation," *IEEE Transactions on Energy Conversion*, pp. 826-834, December 2009.

- [166] A. Thomas, Z. Zhu, R. Owen, G. Jewell und D. Howe, „Multiphase Flux-Switching Permanent Magnet Brushless Machine for Aerospace Application,“ *IEEE Transactions on Industrial Applications*, Bd. 45, Nr. 6, pp. 1971-1981, November/December 2009.
- [167] M. Cheng, W. Hua, J. Zhang and W. Zhao, "Overview of Stator-Permanent Magnet Brushless Machines," *IEEE Transactions on Industrial Electronics*, pp. 5087-5101, November 2011.
- [168] J. Pyrhönen, H. Jussila, Y. Alexandrova, P. Rafajdus und J. Nerg, „Harmonic loss Calculation in Rotor Surface Permanent Magnets - New Analytic Approach,“ *IEEE Transactions on Magnetics*, Bd. 48, Nr. 8, pp. 2358-2366, August 2012.
- [169] M. Thompson, "Practical Issues in the Use of NdFeB Permanent Magnets in Maglev, Motors, Bearings, and Eddy Current Brakes," *Proceedings of the IEEE*, pp. 1758-1767, November 2009.
- [170] N. Mijatovic, B. Jensen, A. Abrahamsen, V. Zermeno, C. Traeholt and N. Pedersen, "Coil Optimization for High Temperature Superconductor Machines," *IEEE Transactions on Applied Superconductivity*, pp. 1136-1140, June 2011.
- [171] C. Simons, Feasibility study of a superconducting helicopter electric propulsion motor, TUDelft, Ed., Delft, The Netherlands: Institutional Repository of the Delft University of Technology, 2013.
- [172] C. Sanabria-Walter, H. Polinder and J. Ferreira, "High-Torque-Density High-Efficiency Flux-Switching PM Machines for Aerospace Applications," *IEEE Journal of Emerging and Selected Topics in Power Electronics*, pp. 327-336, December 2013.
- [173] J. Magill, K. M. M. Z. J. McManus and M. Hinds, "An Air-bearing Balance with 1-DOF Spin Capability," in *37th AIAA Aerospace Sciences Meeting and Exhibit*, Reno, USA, 1999.
- [174] S. Ng, G. Widdowson and S. Yao, "Characteristics Estimation of Porous Air-Bearing," in *Comsol Multiphysics User's Conference*, Stockholm, Sweden, 2005.
- [175] V. Papanikolaou, Helicopter, Coupled electromagnetic and structural analysis of support structures for the main rotor electric motor of a hybrid, Delft, The Netherlands: Institutional Repository of the Delft University of Technology, 2014.
- [176] A. McDonald, M. Mueller und H. Polinder, „Structural mass in direct-drive permanent magnet electrical generators,“ *IET Renewable Power Generation*, Bd. 2, Nr. 1, pp. 3-15, 2008.
- [177] F. Incropera and D. Dewitt, Introduction to Heat Transfer, John Wiley & Sons, 2002.
- [178] A. Bejan, Convection Heat Transfer, John Wiley & Sons, 1995.
- [179] Y. Gao, K. Muramatsu, M. Hatim and M. Nagata, "The effect of laminated structure on coupled magnetic field and mechanical analysis of iron core and its homogenization technique," *IEEE Transactions on Magnetics*, pp. 1358-1361, June 2011.

- [180] Aerolas, "Al-69-50-HD air bearing datasheet".
- [181] C. Dawson, Mechanical Design of a flux-switching permanent magnet machine for the application of a hybrid helicopter, Ingolstadt, Germany: Ingolstadt University of Applied Sciences, 2012.
- [182] Airliners.net, "www.airliners.net," Airliners.net, 2014. [Online]. Available: <http://www.airliners.net/photo/PC-Aero-Elektra-One/1993152/L/&sid=408d0e54d2924f27a3edbebb6a684cc6>. [Accessed 15 July 2014].
- [183] Coalition for the Commercial Application of Superconductors (CCAS), "www.ccas-web.org," 2014. [Online]. Available: <http://www.ccas-web.org/superconductivity/#image1>. [Accessed 22 September 2014].
- [184] THEVA Dünnschichttechnik GmbH, "www.theva.com," 2012. [Online]. Available: <http://www.theva.com/prod>. [Accessed 9 October 2014].
- [185] H. Polinder and M. Hoeijmakers, "Eddy-Current Losses in Permanent Magnets of a PM Machine," *IEEE Proceedings on Electric Power Applications*, vol. 146, no. 3, pp. 261-266, May 1999.
- [186] Y. Pang, Z. Zhu, D. Howe, S. Iwasaki, D. Deodhar and A. Pride, "Eddy Current Loss in the Frame of a Flux-Switching Permanent Magnet Machine," *IEEE Transactions on Magnetics*, pp. 3413-3415, October 2006.
- [187] Z. Zhu and J. Chen, "Advanced Flux-Switching Permanent Magnet Brushless Machines," *IEEE Transactions on Magnetics*, pp. 1447-1453, June 2010.

Summary

Design of High-Torque-Density Synchronous Drives for Propulsion of Rotary-Wing Aircraft

PhD thesis
By Christian Sanabria von Water

Background

Currently, a top priority cascaded down from EU and global environmental policies is achieving fixed targets in energy efficiency and emissions reduction. In the aerospace context, this requires intensive innovation in the topics of All-Electric- and More-Electric-Aircraft (AEA and MEA). However, in this field, propulsion is still based on conventional propellant combustion in power-dense gas turbines with a poor thermal efficiency. For the time being this is the most reasonable alternative.

Nevertheless, new policies revolve around a “reduced and more efficient fuel burn”. Alternative hybrid propulsion systems are therefore worth considering, if the advantage in efficiency is considerable, and the weight penalty involved is acceptable. In a serial hybrid architecture, Diesel engines generate the electrical energy required while operating efficiently at their sweet spot. The generated energy flows into electrical machines that drive the main aircraft propulsor(s), eliminating the mechanical coupling between the energy source and propellers/rotors. This approach can improve the efficiency of the drivetrain, and allows a more flexible operation and integration than using Diesel engines alone. It also has the advantage of a lower weight compared to an all-electric solution.

The hybrid drivetrain, a more-electric propulsion system, has a higher probability of success. Among its components, Diesel engines are already a tested technology in aircraft. Electrical machines have been investigated for aircraft propulsion, mostly at a conceptual level however. The result of these investigations always points at the same known problem: insufficient power-to-weight ratio of electrical machines in general.

Research Question

This thesis considers both conventional and superconducting machines as candidate topologies for electrical propulsion of rotary-wing aircraft. Its main goal is to take into account specific requirements and machine topologies, and examine them for a specific target application: the main rotor drive of a civilian helicopter of the EC135 class. The feasibility of a solution based on direct-drive electrical machines is analyzed, and a detailed design is performed. Topic-related literature shows, that for any given weight, the

capabilities of electrical machines are placed one order of magnitude below turbofan engines. Due to the power-torque relationship, the same can be assumed for the torque capabilities.

For the case study at hand, a gravimetric power density of 5kW/kg between 300rpm and 400rpm is required. Considering the above, an electrical machine can be initially expected to have a gravimetric power density of 0,5kW/kg. The feasibility assessment should focus on alternative or new construction principles, and/or materials offering any improvement, even if only incremental. Regardless of the purpose (electromagnetic, thermal or structural), possibilities should be considered keeping in mind that their implementation should be aerospace certifiable.

Modelling

The analytical models employed in this thesis are used for electromagnetic performance estimation and weight calculation. Separate models were defined for SPM and FSPM machines, while HTS machines were examined using FEM simulations entirely. A weight estimation model was also developed exclusively for the final design.

The model used for fractional-slot SPM machines is meant for fast and relatively accurate estimation of performance, weight, torque density and efficiency. It assumes that the flux density in the core material is near saturation, and that the ratio of air-gap diameter to outer diameter has a value near one. This allows linearization of rotor and stator geometries to simplify calculations. Model inputs are basic geometric dimensions, as well as electromagnetic parameters and material properties. Since it's not intended as an optimization tool, it must provide realistic results while remaining simple and easy to implement. More detailed design is done using finite element analysis.

For FSPM machines, due to their characteristic double saliency, a new modeling approach was developed allowing quick assessment of different machine configurations. The proposed analytical-numerical hybrid technique uses an initial input from FEM simulations to characterize airgap and magnet flux densities in the machine. It uses the aspect ratio of the magnet and airgap MEC elements to approximate the flux linkage in the linear region. This is regardless of its size and rotor/stator pole configuration. With this model, the torque density of different FSPM C-core machines was studied.

For the different machine topologies weight calculations were used to compare different configurations. The mass of each component was calculated based on the material selection and the volume resulting from the physical parameters, which were also used for electromagnetic modelling.

Finally, a total weight estimation of the final conceptual machine presents a more detailed mass calculation including structural components. The calculation approximates the electromagnetic-structural interaction and the performance dependence on airgap length using input data from FEM simulations. The active length, and therefore the active mass, is fixed. Using simulations, the output torque and normal force as a function of airgap length under nominal conditions are obtained. With them, the mass of the different structural components is calculated (stator air bearings, stator support brackets, rotor guiding rings, rotor air bearings, torque transmission structure and miscellaneous components).

Design

The final design is a large-diameter ring-type flux-switching machine with a very small airgap. For manufacture, assembly and operation, a stator segmentation approach is adopted resulting in 14 separately driven segments. Each one constitutes an independent 6/13 FSPM machine, supplied by its own power electronics. Segmentation makes fault isolation and redundancy possible, by containing faults occurring in one segment from the adjacent ones.

The motor is air-cooled and uses aluminum windings with a moderate current density. Torque density is achieved by increasing the magnetic loading through reduction of the airgap length down to 0.1mm. At this scale, thermal-expansion related changes in either the rotor or stator diameter suffice to either make the airgap larger (decreasing torque output), or make it smaller (risking stator-rotor contact). This calls for a suspension system in which any individual segment is able to follow the thermal expansion of the rotor independently, thus maintaining the airgap length at its set point. This functionality is achieved through the use of air bearings on each stator segment, and a segment support with a low radial stiffness connected to the helicopter chassis. Such connection must restrain the segment in tangential direction to allow torque transmission. The magnetic force tending to close the airgap is counteracted by the air bearings mounted on the segment's support structure.

The experimental setup focused on the validation of the above described mechanical functionality by using a single stator segment. For this implementation, the priority is set on proof of concept and not on achieving the required weight. This way, bulkier structures are allowed where convenient to reduce complexity and cost. The segment support allows free radial movement to account for thermal expansion and some rotor eccentricity. From an electromagnetic point of view, the one segment used for experiments differs slightly from those in a complete machine. The differences account for the absence of neighboring segments, and close the magnetic flux path at the outer teeth.

Results

The models developed gave an idea of the physical limits of each topology in terms of electromagnetic performance. While SPM and FSPM machines are perhaps better candidates for a helicopter main rotor direct-drive for the time being, HTS machines offer more room for future improvement. This comparison showed that a Halbach-FSPM design offers a good electromagnetic performance and efficiency. In such design most losses are generated in the stator facilitating thermal management. On the other hand, it also shows increased performance sensitivity to airgap length changes. It offers the highest gravimetric torque density (ca. 92% of the target value), while the other two alternatives incur in higher weight penalty. Additionally, its short stack length increases the stiffness of the construction, while little additional mass is required solely for structural support.

Verification of the electromagnetic design, cooling system and structural support concept were carried out on the one-segment experimental setup in three phases. In the first phase, the support structure along with one stator segment and two rotor segments of very high precision were manufactured (using cobalt steel). The support structure included air-bearings and other components necessary for mounting and static torque measurements. The second phase focused on the testing of the cooling circuit, for which the stator segment was taken out of the setup. In a final phase an entire silicon steel rotor with lower precision

was manufactured and assembled. This was used for rotational testing of the structural support concept, and back-EMF measurements at short airgap lengths. In all tests good agreement with predicted values was achieved, indicating that the performance-to-active-mass ratio of a complete machine would be very near to the target value.

A performance estimation was made using the conceptual weight model. This prediction indicated that the absolute highest possible gravimetric torque density is of 90Nm/kg. This implies a weight penalty of at least 21%.

Conclusion

This thesis suggests that with air-cooled direct-drive ring-type machines it is very likely to incur into a weight penalty for the application of main propulsion of civilian helicopters. This is however an application not investigated before at the level of detail presented. Therefore, this work serves as a design philosophy and guideline for the development of electrical main propulsion drives for rotary-wing aircraft with a MTOW of 3t or lower. It proposes a systematic approach to a solution, and initial considerations for high-power/low-weight machines with low to medium rotational speed. Furthermore, it highlights the importance of the mechanical and structural considerations for both the electromagnetic mass and the support structure.

Samenvatting

Design of High-Torque-Density Synchronous Drives for Propulsion of Rotary-Wing Aircraft

("Het ontwerp van synchrone aandrijvingen met hoge koppeldichtheid voor de voortstuwing van propellervliegtuigen")

PhD thesis

Door Christian Sanabria von Water

Achtergrond

Momenteel heeft het bereiken van de gestelde doelen voor de verbetering van energie efficiëntie en de vermindering van uitstoot een hoge prioriteit gekregen vanuit de EU en het globale milieubeleid. In de context van luchtvaart vereist dit innovatie op de onderwerpen van volledig elektrisch en meer elektrische vliegtuigen (All-Electric Aircraft; AEA, en More-Electric-Aircraft; MEA). Echter, in dit vakgebied zijn de aandrijvingen nog steeds gebaseerd op de (conventionele) verbranding van gas (met een hoge energiedichtheid) in gas turbines met matige thermische efficiëntie: hetgeen wat momenteel de meest logische technologie is.

Desondanks, doelen nieuwe beleidsstukken op het reduceren van verbruik en het efficiënter verbranden van brandstof. Alternatieve, hybride, aandrijvingssystemen worden interessant als het voordeel in efficiëntie aanzienlijk is en het effect op het gewicht acceptabel is. In een seriële hybride architectuur genereren Diesel generatoren elektrische energie opererend op het punt van optimale efficiëntie. De gegenereerde energie gaat naar efficiënte elektrische motoren die de voortstuwing van het vliegtuig aandrijven. Hierdoor wordt de mechanische overbrenging tussen de energiebron en de voortstuwing geëlimineerd. Deze benadering kan de efficiëntie van de aandrijving verbeteren en zorgt voor een flexibelere operatie en integratie dan het gebruik van een diesel motor, en heeft ook een lager gewicht dan een volledig elektrisch systeem.

De hybride aandrijving, een meer elektrisch aandrijfsysteem (MEA), heeft een hogere kans van slagen. De diesel generator van dit ontwerp is een bewezen technologie in de luchtvaart. Elektrische machines voor de voortstuwing van vliegtuigen zijn vooral onderzocht op een conceptueel niveau, maar kampen met een bekend probleem; onvoldoende vermogen tot gewicht ratio.

Onderzoeksvraag

Deze thesis beschouwt zowel conventionele als supergeleidende machines als kandidaat topologieën voor de elektrische voortstuwing van vliegtuigen. Het hoofddoel is om rekening te houden met specifieke vereisten en machine topologieën, en hen te onderzoeken in een specifieke context; de hoofdaandrijving van een passagiers helikopter van de EC135 klasse gebruikt. De haalbaarheid van een oplossing gebaseerd op direct-drive elektrische machines wordt geanalyseerd en een gedetailleerd ontwerp wordt gemaakt. Literatuur op het onderwerp laat zien dat de prestaties van elektrische machines een orde van grote lager liggen dan schroefturbines in elke gewichtsklasse. Door de relatie tussen vermogen en koppel kan worden aangenomen dat hetzelfde waar is voor het koppel.

Voor deze casus, kan een gravimetrische vermogensdichtheid van 5 kW/kg worden aangenomen voor schroefturbines met snelheden tussen 300 en 400 rpm. Rekening houdende met het bovengenoemde, kan aanvankelijk worden aangenomen dat een elektrische machine in een gravimetrische vermogensdichtheid heeft van 0,5 kW/kg.

Modelleren

De analytische modellen in deze thesis worden gebruikt om elektromagnetische en gewichtsberekeningen uit te voeren en daarmee de prestaties in te schatten. Afzonderlijke modellen werden gedefinieerd voor SPM en SFPM machines. HTS machines werden onderzocht door FEM simulaties toe te passen. Een model dat het gewicht inschat werd ook ontwikkeld voor het uiteindelijke ontwerp.

Het model dat gebruikt werd voor de SPM machine berekeningen is gericht op snelle maar relatief precieze inschatting van prestaties, gewicht, koppeldichtheid en efficiëntie. De gebruikte aannames zijn gefocust op fractional-slot SPM machines met een ratio van luchtspleet diameter tot buitenste rotor diameter ratio in de buurt van één, en een fluxdichtheid in het kernmateriaal dat in de buurt van verzadiging is. Dit staat toe dat de rotor en stator geometrieën gelineariseerd kunnen worden wat berekeningen versimpelt. De inputs van het model zijn simpele geometrische dimensies, de elektromagnetische parameters en de materiaal eigenschappen. Omdat het niet bedoelt was als een optimalisatie tool, moest het realistische resultaten verschaffen die tot conclusies konden leiden zonder dat het te gecompliceerd wordt om te implementeren. Een meer gedetailleerd ontwerp werd gemaakt met behulp van eindige elementen analyse (FEM).

Voor de FSPM machines werd, door de karakteristieke uitstekende polen, een nieuwe modelmatige benadering ontwikkeld dat snelle beoordeling toestaat van verschillende machine configuraties. De voorgestelde analytisch-numerieke techniek gebruikt initiële waarden van FEM simulaties om de eigenschappen van de luchtspleet en de flux dichtheden in de machine te bepalen. Het gebruikt de aspectverhouding van de magneet en de luchtspleet MEC elementen om de koppel te benaderen in het lineaire gebied. Dit werkt ongeacht het formaat en de rotor/stator poolconfiguratie. Met dit model werd de koppeldichtheid van verschillende FSPM C-kern machines bestudeerd.

Voor de bovenstaande machine topologieën werden vergelijkbare gewichtsberekeningen gebruikt om de verschillende configuraties te vergelijken. De massa van elke component is berekend aan de hand van de selectie van de materialen en het volume dat resulteert uit de geometrische parameters die ook gebruikt werden voor de elektromagnetische modellen.

Tot slot werd het totale gewicht van de uiteindelijke conceptuele machine benaderd inclusief de structurele componenten, alhoewel dit alleen een eerste benadering is en verder onderzoek nodig is. De berekening benadert de elektromagnetische-structurele interactie door deformatie data te gebruiken van FEM simulaties en de prestatie afhankelijkheid ten opzichte van de luchtspleet in acht te nemen. De actieve lengte is constant aangenomen waardoor ook de actieve massa vast staat. Gebruikmakend van simulaties werden de verhoudingen tussen de koppel en de normaal kracht als functie van de luchtspleet lengte onder nominale toestanden vastgesteld. Met deze verhoudingen werd de massa van verscheidene structurele componenten uitgerekend (luchtlagers in de stator, ondersteuningsconstructie van de stator, ringen voor de geleiding van de rotor, luchtlagers van de rotor, koppel overbrengingsconstructie en diversen andere componenten).

Ontwerp

Het definitieve ontwerp is een ring-type fluxwisselende machine met een grote diameter en een kleine luchtspleet. Voor productie, montage en operatie is een gesegmenteerde benadering, met in totaal 14 individueel aangedreven segmenten, voor de stator gebruikt. Elk segment is een onafhankelijke 6/13 FSPM machine gevoed door eigen vermogenselektronica. Het segmenteren maakt het isoleren van fouten en redundantie mogelijk door fouten lokaal af te sluiten van naastgelegen segmenten.

De motor is luchtgekoeld en heeft een matige stroomdichtheid in zijn aluminium spoelen. Hoge koppeldichtheid wordt bereikt door de luchtspleetlengte te reduceren tot 0.1mm waardoor de magnetische belasting verhoogd wordt. Op deze schaal resulteren veranderingen in de rotor of stator diameter door thermische expansie tot een significante verandering in de luchtspleetlengte met als gevolg dat het koppel van de machine verandert en er is zelfs risico op contact tussen de stator en rotor. Hierdoor is een ophanging vereist dat in elk individueel segment kan compenseren voor thermische expansie van de rotor, waardoor de luchtspleetlengte constant wordt gehouden. Dit wordt bereikt door luchtlagers te gebruiken voor elk stator segment en elk segment met lage radiale stijfheid te verbinden met het helikopter chassis. Zo'n verbinden beperkt wel het segment in de tangentele richting om koppeloverbrenging mogelijk te maken. De magnetische kracht die de luchtspleet tracht te verkleinen wordt tegen gegaan door luchtlagers gemonteerd op de ondersteuningsconstructie van het segment.

De experimentele opstelling concentreert zich op de validatie van de bovengenoemde mechanische functionaliteit, zonder een complete machine te construeren, door een enkel stator segment te gebruiken. Voor deze implementatie is het bewijs van het concept geprioriteerd en niet het bereiken van het beoogde gewicht. Hierdoor waren omvangrijke constructies toegestaan waardoor complexiteit en kosten laag konden blijven. Het resultaat was een tangentele constructie bij die radiale beweging toestaat ten gevolge van thermische expansie en rotor excentriciteit. Vanuit een elektromagnetisch oogpunt verschilt gebruik van een enkel een segment enigszins met een volledige machine door de afwezigheid van naburige segmenten.

Resultaten

De ontwikkelde modellen resulteerden in een heldere weergave van de fysieke limieten van elke topologie met betrekking tot elektromagnetische prestaties. Hoewel SPM en FSPM

machines momenteel betere kandidaten zijn voor een helikopter aandrijving bieden HTS machines meer perspectief in de toekomst. De vergelijking liet zien dat een Hallbach-FSPM ontwerp goede elektromagnetische prestaties en een hoge efficiëntie heeft, echter gaat dit ten koste van de gevoeligheid voor de luchtspleet. Dit ontwerp biedt de hoogste gravimetrische koppeldichtheid (grotfweg 92% van de beoogde waarde), ten opzichte van de twee alternatieven die een groter effect hebben op het gewicht. Daar komt nog bij dat door de korte stack lengte de stijfheid van de machine hoger is waardoor minder massa nodig is voor de ondersteuningsconstructie.

Verificatie van het elektromagnetisch ontwerp, koelingssysteem en het concept voor de ondersteuningsconstructie werd in 3 fasen uitgevoerd op een experimentele opstelling van één segment. In de eerste fase werd één stator segment en twee rotor segmenten, die met hoge precisie vervaardigd waren uit kobalt staal, samen met de ondersteuningsconstructie, luchtlagers en andere componenten gebruikt voor statische koppelmetingen. De tweede fase focuste op het testen van het koelcircuit waarvoor het stator segment uit de opstelling werd genomen. In de laatste fase werd een compleet silicium stalen rotor met relatief lage precisie vervaardigd en geassembleerd. Deze rotor werd gebruikt voor het testen van de ondersteuningsconstructie en de back-EMF in een roterende opstelling met een kleine luchtspleet. De resultaten uit de testen kwamen goed overeen met de verwacht waarden, wat een indicatie is dat de ratio van prestaties tot de massa van een volledige machine dichtbij de doelstelling zou kunnen komen.

Vanuit het conceptuele gewichtsmodel werd een schatting gemaakt van het absoluut hoogst haalbare gravimetrische koppeldichtheid van de voorgestelde benadering. Er wordt ingeschat dat dit ontwerp een negatieve impact van 21% zou hebben op het gewicht.

Conclusie

Deze thesis geeft aan dat voor luchtgekoelde direct-drive ring-type machines het erg waarschijnlijk is dat ze een negatief effect heeft op het gewicht voor het aandrijven van passagiershelikopters. Echter is dit een toepassing dat in het verleden nog niet gedetailleerd is onderzocht. Deze thesis biedt een richtlijn voor het systematisch ontwerpen van een elektrische voortstuwing voor propellervliegtuigen met een MTOW van 3 ton of lager. Het biedt een eerste blik op hoge vermogens/lage gewichtsmachines met lage tot middelmatige rotatiesnelheid. Bovendien wordt het belang van mechanische en structurele overwegingen benadrukt op het gebied van elektromagnetische actieve massa en de ondersteuningsconstructie.

List of Publications

Journal Publications

1. **C. Sanabria-Walter**, H. Polinder, J.A. Ferreira: “High-Torque-Density High-Efficiency Flux-Switching PM Machine fir Aerospace Applications”, *IEEE Journal of Emerging and Selected Topics in Power Electronics*, August 2013, Vol. 1, No. 4, pp. 327-336.
2. C.A.B.A.E. Simons, **C. Sanabria-Walter**, H. Polinder: “Feasibility study of a superconducting motor for electrical helicopter propulsion”, *Journal of Physics: Conference Series*, May 2014, Vo. 507, No. 3.

Conference Publications

1. **C. Sanabria-Walter**, H. Polinder, J.A. Ferreira, M. Hofmann, P.Jänker: „Torque Enhanced Flux-Switching PM Machine for Aerospace Applications“, *Proceedings of the 20th International Conference on electrical Machines*, September 2012, pp. 2585-2595.
2. **C. Sanabria-Walter**, H. Polinder: “Analytical-Numerical Hybrid Model for Flux-Switching Permanent Magnet Machines”, *Proceedings of the 39th Annual Conference of the IEEE Industrial Electronics Society*, November 2013, pp. 2614-2619.
3. **C. Sanabria-Walter**: “Design of a 600kW ring-type direct-drive Flux-Switching Permanent Magnet machine for aerospace main propulsion”, *Proceedings of the 16th European Conference on Power Electronics and Applications*, August 2014.

Patents

1. **C. Sanabria-Walter**, M. Hofmann, P.Jänker: “Electric machine, in particular for aircraft”, German Patent 10 2011 121 174, April 3 2014.
2. **C. Sanabria-Walter**, F. Hermle: “Elektrische Maschine, insbesondere für Luftfahrzeuge”, German Patent 10 2014 003 956, *submitted on March 3 2014*.

Biography

Christian Sanabria von Walter was born in Bogotá, Colombia in 1981. He received his bachelor and master degrees in electrical engineering from the Los Andes University (Bogotá, Colombia) in 2004 and the Technical University Hamburg-Harburg (Hamburg, Germany) in 2007, respectively.

From 2007 to 2015 he worked in conventional and alternative propulsion concepts for the aerospace industry. First at MTU Aero Engines and then at Airbus Group Innovations, where he worked towards his PhD degree in cooperation with the Delft University of Technology. His main research interests are high-power-density variable-speed synchronous drives for the automotive and aerospace industries.

Since September 2015 he has been a development engineer at Mercedes Benz Cars, multinational division of Daimler AG. His work is focused on general powertrain development for fully electrical vehicles.